

# **Grain Growth in Protoplanetary Disks**

Thesis by  
Laura María Pérez Muñoz

Advisors  
Dr. John Carpenter & Prof. Anneila Sargent

In Partial Fulfillment of the Requirements  
for the Degree of  
Doctor of Philosophy



California Institute of Technology  
Pasadena, California

2013

(Defended October 29, 2012)



© 2013

Laura María Pérez Muñoz

All Rights Reserved



Dedicado a mis abuelas,  
Rosa Irene y Norma Alicia.



## Acknowledgments

This adventure in astronomy would not have been possible without the tremendous amount of encouragement, motivation, and inspiration that I received throughout the years from my dear family and friends, from scientific collaborators near and far, and from my wonderful advisors: John Carpenter and Anneila Sargent. Dear John, your determination to get things right, your deep understanding of radio astronomy, and your superhuman work ethic were invaluable to help me finish this thesis and to provide exciting science for years to come. Thank you for your confidence in me and my abilities, and for always answering “Yes!” every time I went to your office asking “Hi John, do you have a minute?”. Dear Anneila, your passion and knowledge about astronomy, your matter-of-fact demeanor and your great common sense were vital to overcome difficult times, of which there were some during the making on this thesis. Thank you for sharing with me your wisdom, your funny jokes, and your splendid house in Berkeley Avenue, on that summer that Walter and I will always recall as the best summer ever. Without the valuable input of Andrea Isella, who is practically a third advisor on this thesis, this project could not have been completed. Thank you Andrea for sharing with me your vast knowledge on circumstellar disks, radio astronomy and MCMC codes. I also was fortunate to have Claire Chandler from NRAO as a mentor from far away, who provided the opportunity of spending a summer at NRAO in Socorro; it was quite fun and I learned a great deal. Thank you Claire for all you have taught me about cm-wave observations and for trusting me with your beautiful VLA data.

As a radio astronomer in the making, I had the good fortune of driving up many times to beautiful Owens Valley. Up at Cedar Flat I spent more than 140 days and nights observing at the Combined Array for Millimeter-wave Astronomy, and I had the pleasure to work with many passionate people that helped me become a seasoned CARMA observer. My words of appreciation go to all the staff at OVRO and CARMA who keep the telescope running smoothly, and specially to James Lamb and Dave Woody, who enlightened me in the arts of interferometry, Nikolaus Volgenau, who trained me during my first CARMA run and always cared about observers in such a remote location, and Mary Daniel, Cecil Patrick and Terry Sepsey, who always made me feel truly at home when up at CARMA. The early departure of Terry was a shock to all of us, and I deeply wish she

was still here to share with me the joy of completing this thesis. I am grateful to all of the observers that shared observing runs and CARMA adventures with me, especially Kartik Sheth, Jin Koda, Colette Salyk, Ashley Zauderer, Andreea Petric, and David Rebollo. You made all of the sleepless night babysitting a telescope much better. My gratitude goes to the CARMA group at Caltech, in between telecons and observing runs I learned a wealth from you all. In particular, Stuart Corder and Melissa Enoch, who led the way for graduate students to become involved with CARMA, as well as Kartik Sheth, Scott Schnee, Thushara Pillai, and Luca Ricci, whose enthusiasm and knowledge were great to have around. My time at Caltech was made easy by the outstanding staff at the Astronomy Department: Anu Mahabal and Patrick Shopbell, who came to the rescue when I had computer problems; Althea Keith, Sandy Lester, Gita Patel, Gina Armas, and Judith Mack, who simplified my life by helping me with administrative problems; and Efrain Hernández and Engracia Álvarez, who did an excellent job of taming my office mess and whose words of encouragement I received daily. My sincere recognition goes as well to the excellent staff at many places in Caltech: Laura Flower-Kim, Jim Endrizzi, and Daniel Yoder at the International Student Programs; Tess Legaspi at the Registrar’s Office; and especially to Marta Robles and Elvira Serpa, from Chandler Dining Services, whose warmth and cheerful personality always put a smile on my face.

But my love for radio astronomy began before Caltech, during my undergraduate studies at Universidad de Chile. There, Diego Mardones, Guido Garay, and Mónica Rubio (who later became my M.Sc. thesis advisor) provided exciting avenues of research for a novice undergrad. It was thanks to the passion of these professors and many astronomers at Cerro Calán that I became enthralled with astronomy and the “invisible” universe. During this time, I also had the wonderful opportunity of working at Cerro Tololo Inter-American Observatory, under the *Prácticas de Investigación en Astronomía* program, where Malcolm Smith showed me the wonders of infrared observations and quasars. A big thank you to Mónica, Malcolm, Guido and Diego, for your never-ending enthusiasm and for giving me the starting tools to become a researcher in astronomy. During the first four years of this thesis I received funding from a Fulbright-Conicyt fellowship. Without it, I probably would not have even started this project, and I am extremely grateful for their support. The Fulbright staff in Chile, in particular Karina Sapunar, as well as the Fulbright Enrichment Program run by Ann Kerr, were extremely helpful and took good care of me during my years as a visiting scholar. Thank you Ann for all the fun times in Pacific Palisades, JPL, Cabrillo, and the Hollywood Bowl.

And when you are having fun, the long days of thesis work can just fly by. It was thanks to the great atmosphere among graduate students at Caltech that these six years felt very short. I was fortunate enough to have amazing classmates: Matthew Stevenson, Varun Bhalerao, Yacine Ali-Haïmoud, and Walter Max-Moerbeck. You guys were a pleasure to be around, thank you for being great friends. My then-officemates and now-friends: Gwen Rudie and Varun (the Robinson

generation, office 16 in the basement) were fundamental to keep me sane through the long days. Thank you guys for convincing me that I could do this! Sebastian Pineda and Kunal Mooley joined the office later on (the Cahill generation, office 256, with a beautiful view on the second floor), and when I finally moved away the formidable Jackie Villadsen took my desk; I'm sure she will do incredible things from there. Thank you all, including Shriharsh Tendulkar, Ryan Trainor, Swarnima Manohar (Jaaneman!), Ke (Coco) Zhang, Mike Bottom, Melodie Kao, and Allison Strom, for always cheering for me whether the days were cloudy or sunny. I had tons of encouragement as well from the “older” generations: Mansi Kasliwal, who was a fantastic T.A. and then became a great friend, and who happened to have an amazing wedding in Indore, India (thank you Mansi and Setu, it was lovely!), Ann Marie Cody, who along with Tommy shared many India and Pasadena adventures with Walter and I, and of course Karín Menéndez-Delmestre and Thiago Signorini Gonçalves, who are so awesome that they managed to convince me to come to Caltech just over a phone conversation. Thank you guys for showing us L.A., for hosting so many awesome parties and for speaking Spanish with those lovely Puerto Rican and Brazilian accents. Walter and I also had the pleasure to live for the past 2.5 years in the same apartment building as the wonderful Stevenson family: thank you Matthew, Jennifer, Bronson and Edmund, for sharing your family life with us and for all the fun we had together (Camping! The beach! Birthday parties! Soccer!). You guys provided so much support when things got tough; it warms my heart to be “Auntie Laura” for Bronson and Edmund.

And a big thank you to the Chilean community at Caltech: Pancho, Fabian and Carola, Roberto, Rodrigo and Javiera, Daniel and Margarita, Gustavo and Mariana, Solange and Adolfo, Jorge and Jolana, Guille and Isi, and Ruby and Carlos, who provided that home away from home feeling, as well as great conversation, yummy Chilean food and many pisco sours. I also had never-ending encouragement from *mi madrina*, Tiziana Calcagno, and from my dear friend Alessandra Da'Silva Calcagno, who is my sister at heart. A big thank you goes to all of my family in Chile, who always made me feel loved and cared for, despite the 8992 km that separated us. My love and gratitude goes to my brother Carlos, whose zen personality I deeply admire, and to my parents, Carlos and Lilian, whose persevering personality I seem to have inherited. I can't even begin to thank you, *Papi y Mami*, for all your sacrifices, for your endless support and encouragement, and for always telling me that you didn't need anything extra from me — like a Ph.D. — to just love me.

And finally, I would like to thank the handsome young man that started a conversation with me at the top of the stairs in the School of Sciences and Engineering at Universidad de Chile, on my first day of summer school classes. That guy with his beautiful smile, noble personality, and loving kindness ended up stealing my heart and holding my hand throughout this entire adventure: Walter, thank you for everything, you always make it all better. I love you!



## Abstract

The majority of young, low-mass stars are surrounded by optically thick accretion disks. These circumstellar disks provide large reservoirs of gas and dust that will eventually be transformed into planetary systems. Theory and observations suggest that the earliest stage toward planet formation in a protoplanetary disk is the growth of particles, from sub-micron-sized grains to centimeter-sized pebbles. Theory indicates that small interstellar grains are well coupled into the gas and are incorporated to the disk during the proto-stellar collapse. These dust particles settle toward the disk mid-plane and simultaneously grow through collisional coagulation in a very short timescale. Observationally, grain growth can be inferred by measuring the spectral energy distribution at long wavelengths, which traces the continuum dust emission spectrum and hence the dust opacity. Several observational studies have indicated that the dust component in protoplanetary disks has evolved as compared to interstellar medium dust particles, suggesting at least 4 orders of magnitude in particle-size growth. However, the limited angular resolution and poor sensitivity of previous observations has not allowed for further exploration of this astrophysical process.

As part of my thesis, I embarked in an observational program to search for evidence of radial variations in the dust properties across a protoplanetary disk, which may be indicative of grain growth. By making use of high angular resolution observations obtained with CARMA, VLA, and SMA, I searched for radial variations in the dust opacity inside protoplanetary disks. These observations span more than an order of magnitude in wavelength (from sub-millimeter to centimeter wavelengths) and attain spatial resolutions down to  $\sim 20$  AU. I characterized the radial distribution of the circumstellar material and constrained radial variations of the dust opacity spectral index, which may originate from particle growth in these circumstellar disks. Furthermore, I compared these observational constraints with simple physical models of grain evolution that include collisional coagulation, fragmentation, and the interaction of these grains with the gaseous disk (the radial drift problem). For the parameters explored, these observational constraints are in agreement with a population of grains limited in size by radial drift. Finally, I also discuss future endeavors with forthcoming ALMA observations.



# Contents

<b>List of Figures</b>	<b>xvii</b>
<b>List of Tables</b>	<b>xxi</b>
<b>1 Introduction</b>	<b>1</b>
1.1 Protoplanetary Disks Properties . . . . .	4
1.2 Grain Growth in Protoplanetary Disks . . . . .	7
1.3 Current Observational Constraints for Grain Growth in Protoplanetary Disks	9
1.4 Thesis Summary . . . . .	13
<b>2 Radio Interferometric Observations of Circumstellar Disks</b>	<b>15</b>
2.1 Sample Selection . . . . .	16
2.2 CARMA Observations . . . . .	21
2.2.1 Observational setup . . . . .	22
2.2.2 Calibration of CARMA interferometric data . . . . .	25
2.2.3 Astronomical corrections and averaging of CARMA interferometric data . . . . .	26
2.3 VLA Observations . . . . .	27
2.3.1 Observational setup . . . . .	28
2.3.2 Calibration of VLA interferometric data . . . . .	29
2.3.3 Astronomical corrections and averaging of VLA interferometric data	31
2.4 SMA Observations . . . . .	32
2.4.1 Observational setup and calibration . . . . .	32
2.4.2 Astronomical corrections and averaging of SMA interferometric data	33
2.5 Imaging of Interferometric Data . . . . .	34

<b>3 Atmospheric Phase Correction Using CARMA-PACS: High Angular Resolution Observations of the FU-Orionis Star PP 13S*</b>	<b>37</b>
3.1 Introduction . . . . .	38
3.2 Description of C-PACS . . . . .	40
3.2.1 CARMA . . . . .	40
3.2.2 Properties of the atmosphere . . . . .	42
3.2.3 Atmospheric delay corrections . . . . .	43
3.2.4 Atmospheric calibrators . . . . .	44
3.3 Observations and Data Reduction . . . . .	46
3.3.1 CARMA 1.3 mm wavelength observations . . . . .	46
3.3.2 CARMA 1 cm wavelength observations . . . . .	47
3.3.3 Applying 1 cm delays to the 1.3 mm data . . . . .	47
3.4 Application of C-PACS . . . . .	48
3.4.1 3C111 . . . . .	48
3.4.2 PP 13S* . . . . .	51
3.5 Properties of the PP 13S* Circumstellar Disk . . . . .	51
3.6 Conclusions . . . . .	58
<b>4 Modeling Circumstellar Disk Observations</b>	<b>61</b>
4.1 Modeling the Unresolved SED . . . . .	61
4.2 Modeling Resolved Millimeter- and Centimeter-Wave Observations . . . . .	63
4.2.1 Ingredients for the disk structure . . . . .	65
4.3 Disk Structure Fitting Through Markov Chain Monte Carlo . . . . .	79
4.3.1 Finding the best-fit model to our data . . . . .	79
4.3.2 Uncertainties in model parameters . . . . .	81
4.3.3 Uncertainties for $\Sigma(R)$ and T(R) . . . . .	82
4.4 Monte Carlo Fitting of Radial Variations of $\beta$ . . . . .	84
4.5 Maximum Likelihood Estimate Method to Constrain the value of $a_{max}(R)$ .	86
<b>5 Constraints on the Radial Variation of Grain Growth in the AS 209 Circumstellar Disk</b>	<b>89</b>
5.1 Introduction . . . . .	90

5.2	AS 209 Observations . . . . .	92
5.3	Observational Results . . . . .	94
5.4	Modeling Results . . . . .	96
5.5	Discussion . . . . .	102
5.5.1	Radial variations of $\beta$ . . . . .	102
5.5.2	Radial variations of $a_{max}$ . . . . .	103
5.5.3	Summary . . . . .	106
<b>6</b>	<b>Grain Growth in the Circumstellar Disks of DoAr 25 and CY Tau</b>	<b>107</b>
6.1	DoAr 25 . . . . .	107
6.1.1	Observational results . . . . .	109
6.1.2	The effect of C-PACS in the DoAr25 disk . . . . .	112
6.1.3	Modeling of dust continuum emission . . . . .	112
6.1.4	Radial variations of the dust opacity . . . . .	121
6.2	CY Tau . . . . .	124
6.2.1	Observational results . . . . .	126
6.2.2	Modeling of dust continuum emission . . . . .	128
6.2.3	Radial variations of the dust opacity . . . . .	135
<b>7</b>	<b>Conclusions and Future Work</b>	<b>137</b>
7.1	General Results from This Thesis . . . . .	137
7.2	Future Work: Studying Grain Growth with ALMA . . . . .	139
7.3	And the Future is Here: ALMA Early Science Observations of Transitional Disks . . . . .	145
<b>Bibliography</b>		<b>147</b>



## List of Figures

1.1	Schematic illustration for the current framework of low-mass star formation	2
1.2	Disk mass vs. stellar mass for Class II YSOs . . . . .	5
1.3	Observed $10\ \mu\text{m}$ silicate feature for a variety of young stars . . . . .	10
1.4	Dust opacity spectral index, $\beta$ , as a function of the stellar age . . . . .	11
1.5	First observational constraints on the radial variation of $\beta$ . . . . .	12
2.1	Selection criteria, based on the C-band (6 cm) emission, for the circumstellar disks analyzed on this thesis . . . . .	19
3.1	Schematic of the CARMA Paired Antenna Calibration System . . . . .	41
3.2	Location of paired antennas for C-PACS and beam separation at the height of the turbulent layer . . . . .	44
3.3	Comparison between the measured visibility phase for the science array vs. the reference array of antennas, during C-PACS observations . . . . .	49
3.4	Visibility phases versus $uv$ -distance on all paired baselines during C-PACS observations . . . . .	50
3.5	Before and after C-PACS for the circumstellar disk around PP 13S* . . . . .	52
3.6	Increase in flux density and improvement in seeing after application of C-PACS corrections . . . . .	53
3.7	Visibility profile for PP 13S* . . . . .	54
3.8	Model $\Sigma(R)$ for PP 13S* . . . . .	56
3.9	Toomre's instability parameter as a function of the PP 13S* disk radius .	58
4.1	Surface density profile for similarity solution . . . . .	69
4.2	Dust opacity vs. $\lambda$ , for different grain compositions and single particle size	73

4.3	Dust opacity vs. $\lambda$ , for different grain compositions and a particle-size distribution . . . . .	74
4.4	Dust opacity vs. $\lambda$ , for a fixed grain composition and different particle-size distributions . . . . .	75
4.5	Dust opacity spectral index $\beta$ as a function of $a_{max}$ . . . . .	76
5.1	Maps of the continuum emission towards AS 209, observed with SMA (0.88 mm), CARMA (2.8 mm), and VLA (8.0 and 9.8 mm) . . . . .	93
5.2	AS 209 visibility profile . . . . .	95
5.3	Probability distribution functions for the AS 209 model parameters at 0.88 and 2.8 mm . . . . .	98
5.4	Probability distribution functions for the AS 209 model parameters at 8.0 and 9.8 mm . . . . .	99
5.5	Comparison between model and observations for AS 209 . . . . .	100
5.6	Temperature and optical depth profile for AS 209, at observed wavelengths . . . . .	101
5.7	Constraint on $\beta(R)$ for AS 209 (left panel), and normalized dust opacity for $a_{max}$ between 0.1–10 cm (right panel) . . . . .	103
5.8	Constraint on $\Sigma(R)$ and $a_{max}(R)$ for AS 209 . . . . .	105
6.1	Spectral energy distribution for DoAr 25 . . . . .	108
6.2	Maps of the continuum emission towards DoAr 25, observed with SMA (0.88 mm), CARMA (2.8 mm), and VLA (8.0 and 9.8 mm) . . . . .	110
6.3	DoAr 25 visibility profile . . . . .	111
6.4	C-PACS application to A configuration CARMA observations of DoAr 25 . . . . .	113
6.5	C-PACS application to B configuration CARMA observations of DoAr 25 . . . . .	114
6.6	Probability distribution functions for the DoAr 25 model parameters at 0.88 mm . . . . .	116
6.7	Probability distribution functions for the DoAr 25 model parameters at 2.8 mm . . . . .	117
6.8	Probability distribution functions for the DoAr 25 model parameters at 8.0 and 9.8 mm . . . . .	118
6.9	Comparison between model and observations for DoAr 25 . . . . .	119

6.10	Temperature and optical depth profile for DoAr 25, at observed wavelengths	120
6.11	Constraint on $\beta(R)$ for DoAr 25 . . . . .	122
6.12	Constraint on $\Sigma(R)$ and $a_{max}(R)$ for DoAR 25 . . . . .	123
6.13	PdBI observations of CY Tau . . . . .	124
6.14	Constraints on $\beta(R)$ obtained from PdBI observations . . . . .	125
6.15	Maps of the continuum emission towards CY Tau, observed with CARMA (1.3 and 2.8 mm) and VLA (7.1 mm) . . . . .	127
6.16	CY Tau visibility profile . . . . .	128
6.17	Probability distribution functions for the CY Tau model parameters at 1.3 mm	130
6.18	Probability distribution functions for the CY Tau model parameters at 2.8 mm	131
6.19	Probability distribution functions for the CY Tau model parameters at 7.1 mm	132
6.20	Comparison between model and observations for CY Tau . . . . .	133
6.21	Temperature and optical depth profile for CY Tau, at observed wavelengths	134
6.22	Constraint on $\beta(R)$ for CY Tau . . . . .	135
6.23	Constraint on $\Sigma(R)$ and $a_{max}(R)$ for CY Tau . . . . .	136
7.1	Comparison between previous studies and this thesis . . . . .	138
7.2	Compilation of the $a_{max}(R)$ constraints for this thesis disk sample . . . . .	140
7.3	CARMA aperture synthesis image of the 1.3 mm dust continuum emission toward LkCa 15 . . . . .	141
7.4	CARMA visibility profile for LkCa 15 . . . . .	142
7.5	Simulated ALMA Early Science observations of LkCa 15 . . . . .	143
7.6	Visibility profile for the simulated ALMA Early Science observations of LkCa 15 . . . . .	143
7.7	ALMA sample of transitional disks . . . . .	144
7.8	ALMA Early Science observations of the transitional disks surrounding SAO 206462 and SR 21 . . . . .	146



## List of Tables

2.1	Star's coordinates and proper motion . . . . .	20
2.2	Stellar properties . . . . .	20
2.3	CARMA configurations and angular resolutions . . . . .	21
2.4	Observing journal for CARMA observations at 2.8 mm . . . . .	24
2.5	Observing journal for CARMA observations at 1.3 mm . . . . .	24
2.6	VLA configurations and corresponding angular resolution . . . . .	28
2.7	Observing journal for VLA observations in Q- and Ka-band . . . . .	30
2.8	Summary of SMA observations at 0.88 mm . . . . .	33
5.1	Properties of the aperture synthesis imaging of AS 209 . . . . .	94
5.2	Best-fit model parameters and constraints for AS 209 . . . . .	97
6.1	Properties of the aperture synthesis imaging of DoAr 25 . . . . .	109
6.2	Best-fit model parameters and constraints for DoAr 25 . . . . .	115
6.3	Properties of the aperture synthesis imaging of CY Tau . . . . .	126
6.4	Best-fit model parameters and constraints for CY Tau . . . . .	129



# Chapter 1

## Introduction

New generations of stars are formed through the collapse of material inside dense cores within a molecular cloud. The current theoretical framework that describes the process of low-mass star formation, illustrated in Figure 1.1, starts when the self-gravity of a core inside a molecular cloud overcomes its own thermal pressure (top row, Figure 1.1). A rapid runaway contraction follows, which allows this local density enhancement to quickly approach the stellar density and form protostellar object (second row, Figure 1.1). Since the collapsing material possesses some angular momentum, the collapse cannot proceed directly towards the center of the core; a disk of gas and dust surrounding the protostar must be formed by conservation of angular momentum.

The earliest evolutionary stage for which the rotational signature of a disk has been detected in Young Stellar Objects (YSOs) are Class I YSOs, under the phenomenological classification scheme introduced by [Lada & Wilking \(1984\)](#)<sup>1</sup>. This scheme, illustrated in Figure 1.1, defines the class of a YSO by the slope of its spectral energy distribution (SED) at infrared wavelengths ( $\sim 1\text{--}20 \mu\text{m}$ ). [Adams et al. \(1987\)](#) matched this classification scheme to a physical evolutionary sequence that starts with an envelope surrounding a protostar with a disk, and ends with a newly formed pre-main sequence star. The detection of heavily embedded sources, with a lack of emission for  $\lambda < 25 \mu\text{m}$  ([Andre et al., 1993](#)), introduced an additional—and earlier—evolutionary phase, named Class 0 YSOs (second row panels, Figure 1.1). Class 0 YSOs are deeply embedded in the parental cloud, making the central protostar invisible even at infrared wavelengths. The transition from a Class 0 to a Class I object takes less than 0.5 Myr ([Evans et al., 2009](#)), and during this stage there still exists

---

<sup>1</sup>The year I was born.

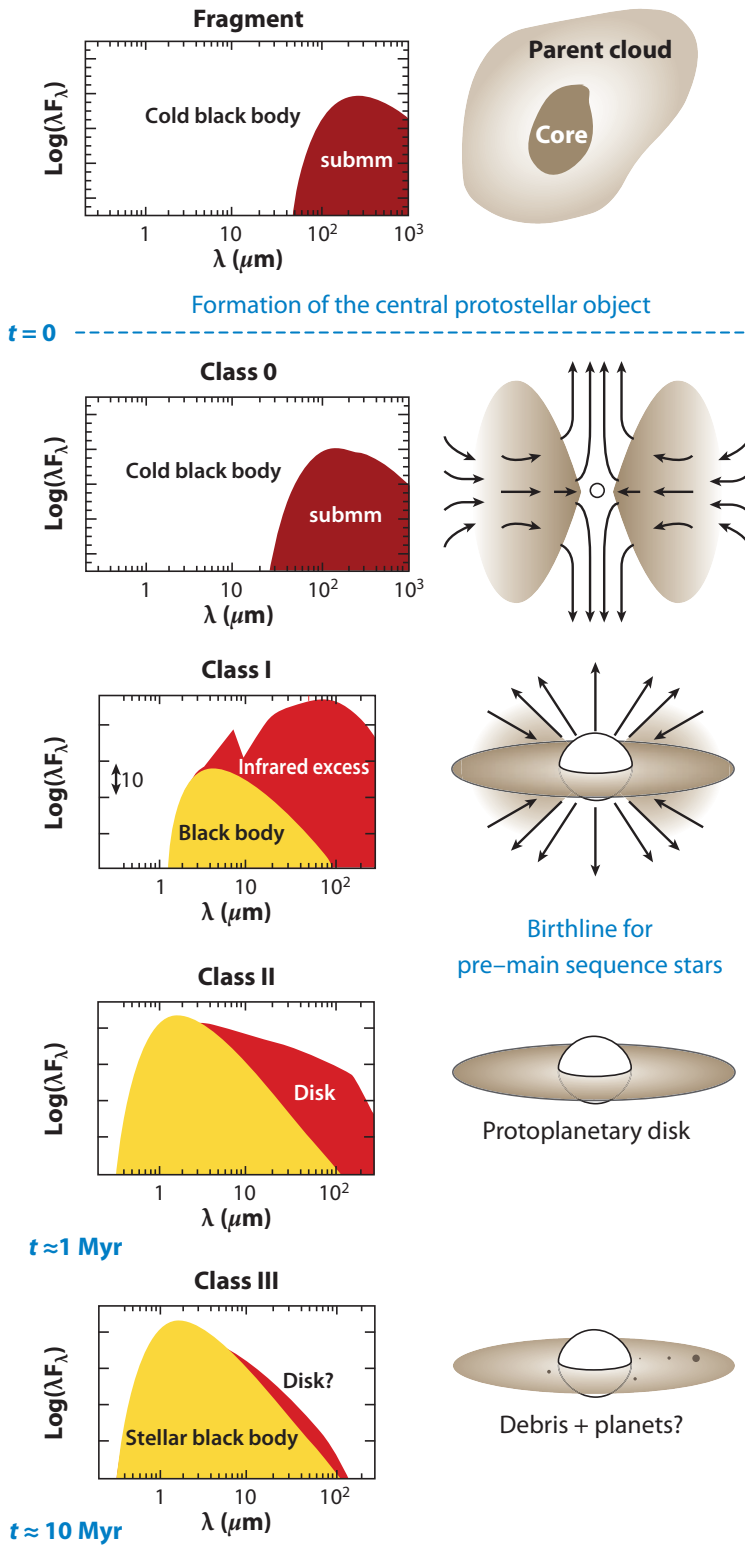


Figure 1.1: (Continued on the following page)

**Figure 1.1:** The current theoretical framework for the formation of a low-mass star (illustration adapted from [Dauphas & Chaussidon, 2011](#)). On the left, a canonical spectral energy distribution for each one of these stages is shown. On the right, an illustration of the main components that characterize each stage is drawn. From top to bottom: a fragment inside a molecular cloud experiences contraction under its own selfgravity (top). Runaway growth ensues and a protostar is formed (Class 0 YSO). Angular momentum is conserved and a disk of material orbiting the star is formed, but the star+disk system is still surrounded by an envelope (Class I YSO). Once the envelope dissipates the central object becomes visible at optical wavelengths, with only a disk surrounding the pre-main sequence star (Class II YSO). Finally, the disk is accreted but collisions between macroscopic bodies may create a *debris* disk (Class III YSO). Credit: Dauphas, N., & Chaussidon, M., Annual Review of Earth and Planetary Sciences, 39, 351, 2011, reproduced with permission © Annual Reviews, Inc.

an envelope of infalling material that surrounds the protostar and the disk, with possible outflowing jets (third row panels, Figure 1.1).

The circumstellar disk and remaining envelope in a Class I YSO serve as a reservoir of mass that slowly feeds the young central star. As accretion proceeds, the envelope is eventually dissipated and the central object becomes optically visible, representing the start of the Class II phase (fourth row panels, Figure 1.1). For Class II YSOs (sometimes also referred to as T-Tauri stars), a large excess of emission over the stellar photosphere (extending from infrared to mm-wavelengths) is still present, but the SED slope at infrared wavelengths is now declining with increasing wavelength (third row, Figure 1.1). The lifetime of the massive circumstellar disks around such systems has been constrained to be a few Myr (e.g., [Strom et al., 1989](#); [Hillenbrand, 2005](#); [Hernández et al., 2007](#)), allowing plenty of time for the formation of planets inside their still-massive circumstellar disks. Once the disk is dissipated, the signatures of accretion and the long-wavelength excess disappear as well, leaving behind a pre-main sequence star that may have a planetary system, known as a Class III YSO (bottom row, Figure 1.1). During this final stage, destructive collisions between small solid bodies may occur. If that is the case, the remnants of these collisions produce some faint—but detectable—excess of emission at infrared wavelengths, indicative of the existence of a debris disk.

The systems analyzed in this thesis belong to the Class II evolutionary stage, and are generally referred to as protoplanetary disks. The name arises since these accretion disks surrounding Class II pre-main sequence stars are believed to be the birthplace of planets. Many protoplanetary disks possess enough mass<sup>2</sup> and last for a long enough time in order to form planetary systems. In the next section, the main properties of these systems are discussed.

## 1.1 Protoplanetary Disks Properties

The thermal dust continuum emission from circumstellar disks, observed at millimeter and sub-millimeter wavelengths, is mostly optically thin (except for the innermost regions of a protoplanetary disk, which are expected to have high column density). Hence the emission detected at these wavelengths is directly proportional to the total dust mass inside the disk (Beckwith et al., 1990):

$$S_\nu = M_{disk} \frac{\kappa_\nu B_\nu(T_d)}{D^2} \quad (1.1)$$

where  $S_\nu$  is the measured flux density at frequency  $\nu$ ,  $D$  is the distance to the circumstellar disk,  $B_\nu(T_d)$  is the Planck function at frequency  $\nu$  evaluated at the dust temperature  $T_d$ , and  $\kappa_\nu$  corresponds to the dust opacity *per gram of gas* at millimeter and sub-millimeter wavelengths, thus  $M_{disk}$  corresponds to the total gas+dust disk mass.

The mass of many circumstellar disks has been directly measured through observations at long wavelengths. These observations generally adopt a power-law prescription for the circumstellar disk dust opacity:

$$\kappa_\nu = \kappa_{\nu_0} \left( \frac{\nu}{\nu_0} \right)^\beta \quad (1.2)$$

where  $\beta$  corresponds to the spectral index of the dust emissivity. The value of the normalization ( $\kappa_{\nu_0}$ ) depends on the dust grain composition; a widely adopted value is  $\kappa_\nu = 0.1 \text{ cm}^2 \text{ g}^{-1}$  for  $\nu = 1 \text{ THz}$  or  $\lambda = 300 \mu\text{m}$  (Beckwith et al., 1990).

---

<sup>2</sup>The Minimum-Mass Solar Nebula (MMSN; Weidenschilling, 1977; Hayashi, 1981) corresponds to the amount of material necessary at minimum in order to build the planets found in our solar system, from a disk of gas and dust that has solar abundances of hydrogen and helium. Depending on the assumptions regarding the composition of the giant planets cores, the MMSN corresponds to  $0.01\text{--}0.07 M_\odot$  out to a radius of 40 AU.

Several different surveys have measured disk masses in many different star-forming regions, e.g., Andre & Montmerle (1994) and Andrews & Williams (2007a) in  $\rho$ -Ophiuchus, Beckwith et al. (1990) and Andrews & Williams (2005) in Taurus-Auriga, and recently Mann & Williams (2010) in the Orion Nebula Cluster. The derived disk masses are generally in agreement with the mass range of 0.01–0.07  $M_{\odot}$  estimated for the MMSN (Weidenschilling, 1977), although many outliers from this range exist, as can be seen in Figure 1.2. Here, the stellar mass is compared with the circumstellar disk mass for a diverse collection of pre-main sequence stars.

Qualitatively, higher-mass stars seem to be surrounded by heavier disks, in a ratio of  $M_{\star}:M_{\text{disk}} \sim 1:100$ , albeit with a large scatter. And at both ends of this scale this relation breaks down. Circumstellar disks around high-mass O stars have not been detected yet,

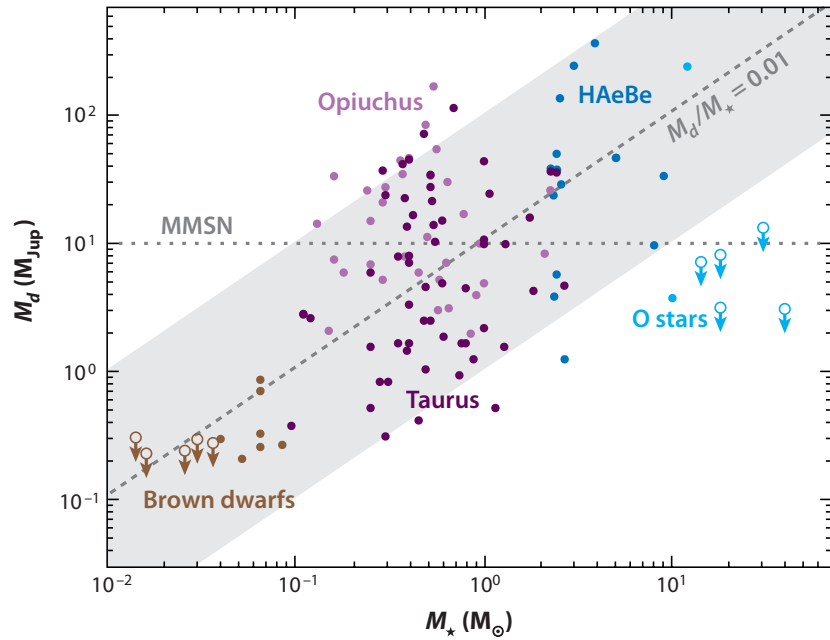


**Figure 1.2:** Circumstellar disk mass versus the mass of the central star (adapted from Williams & Cieza, 2011). Non-detections of the disk (indicated by an arrow symbol) occur at both extremes of the stellar mass range. A circumstellar disk-to-stellar mass ratio of 0.01 is indicated by the dashed diagonal line; over the stellar range of 0.04–10  $M_{\odot}$  most of the disks lie within  $\pm 1$  dex of this correlation (shaded region). Credit: Williams, J. P., & Cieza, L. A., Annual Reviews of Astronomy and Astrophysics, 49, 67, 2011, reproduced with permission © Annual Reviews, Inc.

while sensitivity of current instruments does not allow for the detection (in a reasonable request of observing time) of disks surrounding very low-mass stars. The Atacama Large (sub-)Millimeter Array (ALMA), slated for inauguration in 2013, will change this game by providing orders-of-magnitude improvement in sensitivity to measure masses (and radii) for the faint disk population.

There are several caveats surrounding the circumstellar disk mass derivation from long-wavelength observations. First, calculating the thermal structure of the disk, which can be obtained from theoretical considerations that include heating and cooling mechanisms, is not trivial (see chapter 4). Second, there is an implicit assumption of a gas-to-dust ratio (generally assumed to be 100:1 in mass, comparable to the interstellar gas-to-dust ratio), because long-wavelength observations are only directly probing the dust mass of the disk. And third, a large fraction of the dust mass may be hidden in very large bodies, whose emission is not effectively detected by observations with a wavelength smaller than their size. All of these effects increase the uncertainty in disk masses estimates.

Protoplanetary disk sizes are less uncertain than their masses, since the radius of a disk can be directly measured. However, this can be a difficult task: the disk emission needs to be resolved and in the cold outer disk the emission rapidly drops off. Nevertheless, several protoplanetary disk observations in the dust continuum and CO rotational lines (e.g., Dutrey et al., 1996; Isella et al., 2009; Andrews et al., 2009) have found that circumstellar disks extend to hundreds of AU<sup>3</sup>. A different technique, observations of circumstellar disks silhouettes against the bright background of the Orion Nebula (McCaughrean & O'Dell, 1996; Smith et al., 2005), has provided a direct measurement of the disk extent yielding disk diameters of 100–400 AU (Vicente & Alves, 2005).

Imaging of line emission (e.g., low-level CO rotational lines) for several circumstellar disks has confirmed that the disk material follows a Keplerian velocity profile with radius (Koerner et al., 1993). A significant implication from these studies is that the disk self-gravity must be negligible compared with the star's gravitational pull, hence  $M_{disk} \ll M_*$ . Spectral line imaging can also be used to infer the disk geometry, since the disk rotation directly informs the inclination with respect to the line of sight and the orientation (generally

---

<sup>3</sup>Note however that there are several cases in the literature where the circumstellar disk radius measured from CO observations appear to be larger than the radii measured from dust continuum observations. A discussion regarding this issue is presented in Chapter 4

referred to as position angle) of the projected disk on the sky.

The material composition of the dust grains is another property of protoplanetary disks that has been extensively studied. There are two routes to investigate protoplanetary dust: laboratory analysis of solar system samples and analysis of the infrared spectra of circumstellar disks in young stars (a region of the spectrum rich with emission and absorption resonances of multiple dust species). These methods have yielded insight into the dust composition issue, identifying many different components (for a comprehensive review see [Apai & Lauretta, 2010](#)). [Pollack et al. \(1994\)](#), based on measurements of elemental abundances and theoretical considerations, identified the most abundant species in a prototypical extra-solar dust grain. These are silicates (mainly olivine and pyroxene), carbonaceous materials (mainly organic carbon and graphite) and water ice.

Based on their size, mass, and geometry, it has long been suspected that these circumstellar disks will form planetary systems. The existence of a large number of exoplanets, very different from the planets in our solar system, is now recognized (see [Udry & Santos, 2007](#), for a review), strongly suggesting that many if not all protoplanetary disks do in fact form planets. The physical processes that govern the evolution from a protoplanetary disk into a planetary system are not completely understood. Observationally, the challenge is to understand how this occurs. This thesis focuses on one of the earliest phases of planet formation: the growth of small dust grains into large pebbles. In the following sections I review our current understanding of the grain growth process and the current observational evidence that supports this growth.

## 1.2 Grain Growth in Protoplanetary Disks

In order to understand how planets form, we need to understand the processes that transform microscopic ISM dust grains into twelve-orders-of-magnitude-larger planets. When cloud cores collapse to form stars, sub- $\mu\text{m}$ -sized dust grains from the interstellar medium are part of the collapsing material and become the starting point for further grain growth within the protoplanetary disk. Initially, these sub-micron-sized grains are well coupled to the gas. Their random Brownian motion (as these small dust grains are in thermal equilibrium with the gas) creates a relative velocity between particles that yields plenty of collisions in a very short timescale ([Armitage, 2010](#)). Since the collisions occur at nondestructive ve-

locities (even when including turbulence, [Wurm & Blum, 1998](#)); the sticking probability is very close to one and inevitably, these sub- $\mu\text{m}$ -sized particles will quickly grow in size.

As particles grow, their surface area-to-mass ratio decreases, and they decouple from the gas settling towards the disk mid-plane. The vertical component of the gravitational force from the star is balanced by the aerodynamic gas drag, so the grains settle at terminal velocity ([Weidenschilling, 1977](#)). While settling, these grains sweep up other grains and grow even further. Their rate of coagulation at this point directly increases as their cross section widens, leading to an exponential growth that quickly results in centimeter-sized particles in the disk mid-plane.

Dust coagulation models, that include Brownian motion and dust settling in the presence of turbulence predict that a rapid depletion of  $\mu\text{m}$ -sized grains, and growth of centimeter-sized particles in the disk mid-plane, can be reached in a short timescale (e.g., within  $10^4$  yr, [Dullemond & Dominik, 2005](#)). These short timescales are in disagreement with protoplanetary disk's observed infrared excess and strong millimeter-wave emission, as well as disk lifetimes of a few Myr, which suggest that some amount of fragmentation and/or inefficient sticking needs to be introduced in these models.

However, collisional coagulation stops being efficient around decimeter-sized particles. Large grains will stick after a collision if the relative velocities are low, if sufficient kinetic energy is dissipated during impact, or if sufficient binding energy is available at maximum deformation. In the laboratory, it has been shown that the outcome of a collision between millimeter-sized aggregates is either fragmentation or bouncing, once the impact velocities exceed  $\sim 1 \text{ m s}^{-1}$  ([Blum & Wurm, 2008](#)). Hence, as dust grains decouple from the gas and grow in size, collisional coagulation efficiencies drop once pebble-sized particles are reached.

But a different problem arises when macroscopic dust grains reach the disk mid-plane. Since the gas component of the disk has partial pressure support (i.e., the gravitational force is balanced not only by the centripetal force but also by the pressure gradient) the gas will orbit at a slightly sub-Keplerian velocity for a given distance to the star. However, large grains orbit at Keplerian velocities, and hence will have a relative velocity with respect to the gas, leading them to experience a gas drag that reduces their angular momentum. Thus, large particles rapidly spiral inwards into the star. This is the well-known *radial drift problem* ([Weidenschilling, 1977](#); [Nakagawa et al., 1986](#)). Numerical simulations that

assume typical protoplanetary disks properties, and include radial drift, coagulation and fragmentation of solid particles, have shown that the timescale for radial drift migration is very short (e.g., [Brauer et al., 2008](#), where half of the dust mass is lost in  $\sim 10^5$  yrs). Yet, it is these macroscopic grains that will eventually become the building blocks of planets, and somehow they must be surviving. There is currently an active effort to develop better theoretical models and design more realistic laboratory experiments, but direct observational constraints on particle growth in circumstellar disks are critical to improve our understanding of this astrophysical process

### 1.3 Current Observational Constraints for Grain Growth in Protoplanetary Disks

Evidence supporting the growth of very small grains ( $<$  few  $\mu\text{m}$ ) is provided by infrared spectroscopy of protoplanetary disks. In particular, the silicate feature at  $\lambda \sim 10 \mu\text{m}$  shows a broad range in feature strength, from strongly peaked to weak and flat depending on the grain size. This is illustrated in Figure 1.3, which shows the observed profiles of the  $10 \mu\text{m}$  silicate feature for a selection of different circumstellar disks ([Natta et al., 2007](#)). A strong silicate feature results when grains of small sizes ( $\sim 0.1 \mu\text{m}$ ) are present, which disappears by the time grains have reached sizes of  $\sim 5 \mu\text{m}$ . These results are strongly suggestive of grain growth in protoplanetary disks, but are unable to probe directly the progress of the growth process up to millimeter and centimeter-sized particles, primarily due to their limited wavelength coverage, and the fact that these infrared observations are only probing the outer atmosphere of protoplanetary disks, leaving the inner disk regions unexplored.

Millimeter observations of protoplanetary disks, which trace the thermal continuum emission from dust, can probe the dust population down to the disk mid-plane ([Beckwith et al., 1990](#)). Grain growth can be inferred by measuring the spectral index of the SED at these long wavelengths: parameterizing the dust opacity as a power law (Equation 1.2), the observed emission (Equation 1.1) behaves as  $S_\nu \propto \nu^{2+\beta}$  (assuming the emission arises from optically thin isothermal dust, emitting in the Rayleigh-Jeans limit,  $h\nu \ll k_b T$ , which is generally valid at long wavelengths). In the diffuse interstellar medium, composed mostly of sub-micron-sized grains, the dust opacity spectral index has been measured to be quite

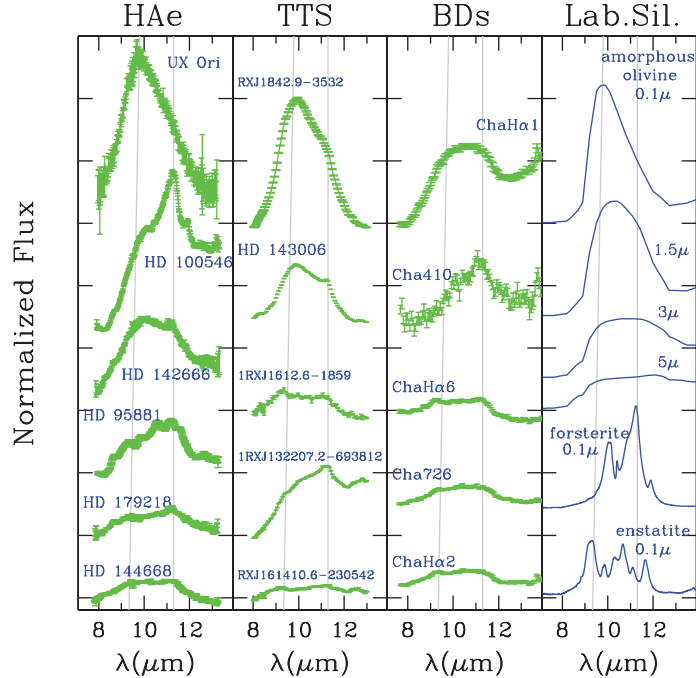


**Figure 1.3:** Observed 10  $\mu\text{m}$  silicate feature profile for Herbig Ae stars (H Ae, from [van Boekel et al., 2005](#)), T-Tauri stars (TTS, from [Bouwman et al., 2008](#)), and brown dwarfs in Chamaeleon ([Apai et al., 2005](#), BDs, from). Flux has been normalized at 8  $\mu\text{m}$ , and displayed on the right are the laboratory silicate profiles for different grain sizes. Figure is adapted from [Natta et al. \(2007\)](#). Credit: A. Natta, reproduced with permission.

steep,  $\beta_{\text{ISM}} \sim 1.5\text{--}2$  ([Weingartner & Draine, 2001](#)). If larger grains are present, the dust emission spectrum will be less steep and this will be reflected in a small value of  $\beta$  compared to  $\beta_{\text{ISM}}$  ([D'Alessio et al., 2001](#)).

Strong observational evidence in support of grain growth has been provided through several surveys of circumstellar disk emission, from sub-millimeter to centimeter wavelengths ([Beckwith & Sargent, 1991](#); [Testi et al., 2001](#); [Calvet et al., 2002](#); [Testi et al., 2003](#); [Natta & Testi, 2004](#); [Wilner et al., 2005](#); [Rodmann et al., 2006](#); [Lommen et al., 2009](#); [Ricci et al., 2010b,a](#)). Figure 1.4 presents a compilation of the values of  $\beta$ , for resolved and unresolved disks surrounding Class 0 YSOs and Class II systems in Taurus and Ophiuchus ([Ricci et al., 2010b](#)). In these studies, a considerably smaller value of the dust opacity spectral index has been measured ( $\beta \lesssim 1$ ), implying a growth of 4 orders of magnitude (from micron-sized grains to centimeter-sized particles).

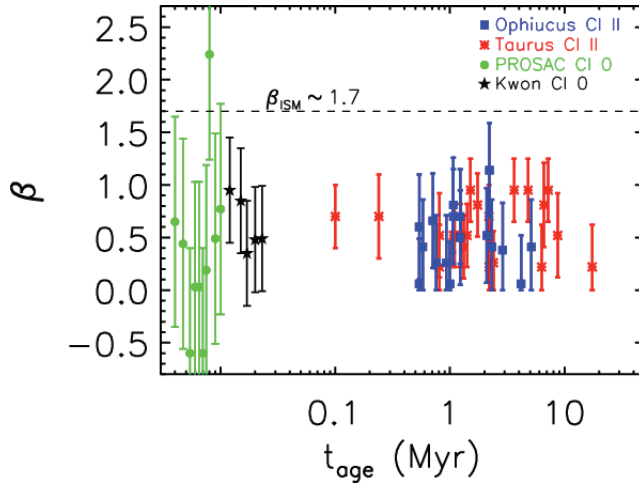


**Figure 1.4:** Comparison of the dust opacity spectral index  $\beta$  with estimated stellar age (Ricci et al., 2010b). The authors derive stellar ages from the Palla & Stahler (1999) pre-main sequence evolutionary models. Class II YSOs measurements from Ricci et al. (2010a,b). Class 0 YSOs are from the PROSAC survey (Jørgensen et al., 2007) and from CARMA observations at 1.3 and 2.7 mm (Kwon et al., 2009). Note that the age estimates for these young objects are much uncertain than for the Class II YSOs. The main point of this figure is that  $\beta \ll \beta_{ISM}$ , which suggests that the grain properties have evolved from their initial conditions. Credit: Ricci et al., Astronomy and Astrophysics, 521, A66, 2010, reproduced with permission © ESO.

The initial grain growth phase in protoplanetary disks is more effectively studied with interferometric observations at multiple millimeter wavelengths (for a review see Natta et al., 2007, and references therein). The problem with single-dish observations at millimeter wavelengths, is that they lack the angular resolution to resolve the disk structure and disentangle what fraction of the emission is optically thick.

Analyses of circumstellar disk observations generally assumes that the dust opacity is constant throughout the disk; the limited angular resolution and sensitivity of these observations have not warranted more sophisticated approaches. However, theory predicts that dust coagulation will be more efficient in the inner disk (Tanaka et al., 2005; Dullemond & Dominik, 2005, 2008; Birnstiel et al., 2010), as higher densities and higher temperatures should result in faster timescales for dust settling within this region. Hence, radial variations in the dust opacity are expected.

The increased sensitivity and improved angular resolution of current interferometers

have enabled the first studies of radial variations of grain growth within circumstellar disks. Observations of disks in Taurus at 1.3 and 2.7 mm with the Combined Array for Research in Millimeter-wave Astronomy (CARMA [Isella et al., 2010](#)) and the Plateau de Bure Interferometer (PdBI [Guilloteau et al., 2011](#)), have constrained  $\beta$  as a function of distance to the central star ( $\beta(R)$ ). One of the best-case examples from these studies is shown in Figure 1.5. In the most favorable cases, these results are only sensitive to large radial variations of the dust opacity spectral index:  $\Delta\beta \sim 0.6 - 0.7$  at  $3\sigma$ , limited not only by poor sensitivity but also by the small wavelength separation between the two bands being observed. This large uncertainty on  $\beta$  arises because the wavelength coverage used to constrain the dust opacity spectral index has a direct effect on its derived uncertainty.

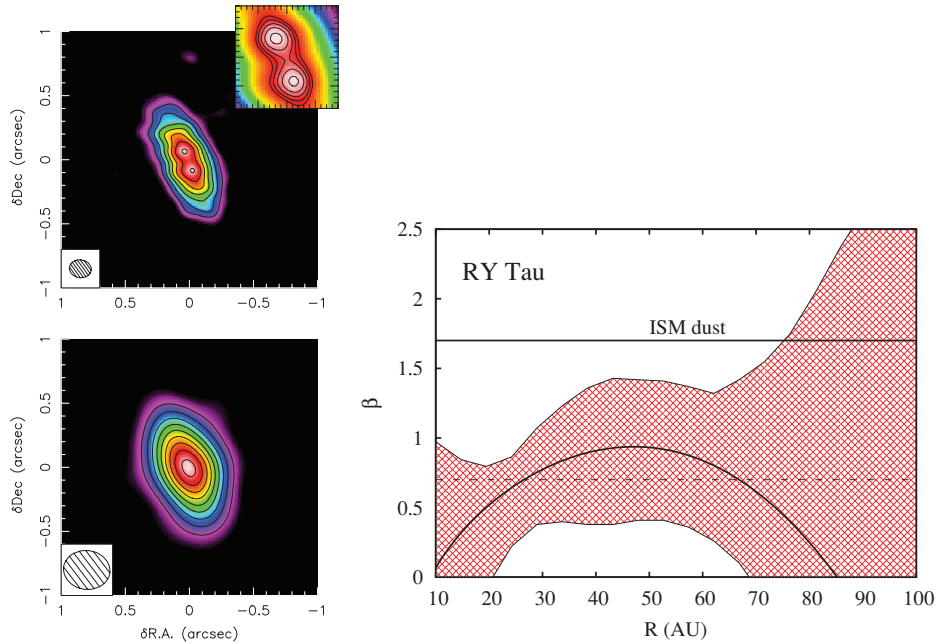


**Figure 1.5:** *Left:* CARMA dust continuum observations of RY Tau at 1.3 mm (top) and 2.8 mm (bottom). Contours are drawn every  $4\sigma$ , with a  $1\sigma$  noise level of  $0.90 \text{ mJy beam}^{-1}$  at 1.3 mm and  $0.28 \text{ mJy beam}^{-1}$  at 2.7 mm. *Right:* Slope of the millimeter dust opacity  $\beta$  as a function of radius for RY Tau. Shaded regions correspond to the  $3\sigma$  constraint in  $\beta(R)$ . The black line inside the shaded region corresponds to the best-fit value for  $\beta(R)$ . For comparison, the global value of  $\beta$  for RY Tau is shown as a horizontal dashed line, while  $\beta_{\text{ISM}} \sim 1.7$  is shown for comparison. Figure adapted from [Isella et al. \(2010\)](#). Credit: A. Isella et al., *Astrophysical Journal*, 714, 1746, 2010, reproduced with permission from AAS.

To first order,  $\beta$  can be constrained by taking the ratio between observations at two different wavelengths, assuming that the dust emission is optically thin and in the Rayleigh-Jeans regime ( $h\nu \ll k_B T$ ), where the observed emission is proportional to the dust emissivity ( $S_\nu \propto \nu^2 \kappa_\nu \propto \nu^{\beta+2}$ ). In this case, the uncertainty in  $\beta$  directly depends on the wavelength separation and the signal-to-noise ratio (SNR) at each wavelength:

$$\beta \pm \Delta\beta = \frac{\log_{10}(S_{\nu_1}/S_{\nu_2})}{\log_{10}(\nu_1/\nu_2)} - 2 \pm \frac{1}{\log_{10}(\nu_1/\nu_2) \ln 10} \left( \frac{1}{\text{SNR}_{\nu_1}^2} + \frac{1}{\text{SNR}_{\nu_2}^2} \right)^{1/2}. \quad (1.3)$$

The  $1\sigma$  uncertainty in  $\beta$  for unresolved high SNR ( $\sim 20$ ) observations at  $\lambda = 1.3$  and 2.8 mm is  $\Delta\beta \sim 0.1$ . By adding high sensitivity long-wavelength ( $\lambda > 7$  mm) as well as short wavelength ( $\lambda < 1$  mm) observations, the uncertainty in the computation of  $\beta$  can be reduced by at least a factor of 3. [Banzatti et al. \(2011\)](#) combined observations of the dust continuum emission that had almost a factor of 10 in wavelength coverage (0.87–7 mm), however, the low signal-to-noise ratio of the long-wavelength observations made this particular study very challenging, so it obtained no better constraints on  $\beta(R)$  than those in [Isella et al. \(2010\)](#) and [Guilloteau et al. \(2011\)](#). To significantly improve these constraints, and effectively compare them to theoretical predictions of grain growth, increased wavelength coverage and enhanced sensitivity are required. The observations presented in my thesis fulfill these two requirements, providing new constraints on the earliest stages of planet formation for a sample of circumstellar disks studied down to  $\sim 20$  AU scales.

## 1.4 Thesis Summary

I aim to constrain the degree of dust evolution and grain growth inside protoplanetary disks by developing an observational program that makes use of multi-wavelength, spatially resolved observations at long wavelengths of circumstellar disks. By studying the dust component of protoplanetary disks we are fundamentally measuring the set of initial conditions for the eventual formation of planets. This thesis consists of the following chapters:

**Chapter 2** introduces the observational program carried out for this thesis, describing the circumstellar disk sample investigated in the following chapters, and explains in detail the necessary calibration steps required to produce a properly calibrated set of observations.

**Chapter 3** describes the CARMA Paired Antennas Calibration System (C-PACS) employed to improve the sensitivity and angular resolution of observations obtained in the extended array configurations. This system was utilized to obtain the high angular resolution observations for the circumstellar disks analyzed on this thesis. A version of this chapter has been published in Pérez et al. (2010).

**Chapter 4** introduces the several different approaches that can be taken to model circumstellar disk observations at millimeter and centimeter wavelengths. This chapter discusses the adopted disk model and its underlying assumptions, used to analyze the interferometric observations presented in chapter 2. I also present the Bayesian approach used to infer and constrain radial variations of the dust opacity spectral index and the maximum grain size of the dust grain population as a function of radius.

**Chapter 5** presents sub-arcsecond angular resolution observations of the circumstellar disk AS 209, which span more than an order of magnitude in wavelength and which were used to investigate radial variations in the dust properties. In this chapter I develop and apply the aforementioned analysis to the first source in our sample. The observational constraints obtained here are compared with predictions from physical models of dust evolution in protoplanetary disks. A version of this chapter has been accepted for publication to the Astrophysical Journal Letters (Pérez et al., 2012, in press).

**Chapter 6** presents the analysis of sub-arcsecond resolution observations of two additional circumstellar disks, CY Tau and Do Ar25. These additional sources were investigated to explore variations in the grain properties for a larger sample of protoplanetary disks. A comparison between the observationally inferred maximum grain size of the dust grain population and theoretical models of grain growth is also presented.

**Chapter 7** discusses the findings of this thesis as well as future prospects in the study of grain growth.

## Chapter 2

# Radio Interferometric Observations of Circumstellar Disks

The circumstellar disks studied in this thesis were observed with three interferometers: the Combined Array for Research in Millimeter-wave Astronomy (CARMA), the Karl G. Jansky Very Large Array (VLA), and the Sub-Millimeter Array (SMA). These diverse telescopes were needed in order to cover the region of the electromagnetic spectrum where circumstellar disk emission is (mainly) optically thin and (mostly) arises from dust thermal emission. At the same time, interferometers—instead of single-dish telescopes—are required in order to spatially resolve protoplanetary disks at the distances of the nearby Taurus and  $\rho$ -Ophiuchus star-forming regions, located at a distance of  $\sim 140$  pc ([Loinard et al., 2008](#)) and  $120 \pm 5$  pc ([Torres et al., 2009, 2012](#)), respectively. The best single-dish telescopes that currently operate at millimeter and sub-millimeter wavelengths can provide angular resolutions of  $10\text{--}15''$ , at best. However, the typical circumstellar disk size corresponds to a few hundred AU, which at the distance of these star-forming regions corresponds to  $\sim 1\text{--}3''$ . Hence, single-dish observations are not well suited to resolve the emission from these circumstellar disks.

The broad range of wavelength coverage presented here—from sub-millimeter to centimeter wavelengths—is of vital importance as well. Observations at long wavelengths ( $>$  few centimeter) can be used to account for any ionized gas emission that may contaminate millimeter-wave observations of the dust thermal emission. Additionally, increasing the wavelength coverage reduces the uncertainty in the derived dust parameters, as, for example, in the computation the dust opacity spectral slope,  $\beta$ , ( $\kappa_\nu \propto \nu^\beta$ ). Hence, the analysis

of these multi-wavelength observations will provide the strongest observational constraints in the characterization of the early growth of dust grains.

This chapter describes the target selection for this study, the telescopes employed to gather these circumstellar disks observations, as well as the observational setup and necessary steps to properly calibrate these multi-wavelength observations, with the goal in mind that these observations will be used to constrain the physical properties of these protoplanetary disks.

## 2.1 Sample Selection

The aforementioned telescopes provide a unique opportunity to spatially resolve circumstellar disks in the nearby Taurus and  $\rho$ -Ophiuchus star-forming regions: thanks to the now possible sub-arcsecond angular resolution of these arrays, we can study circumstellar disks down to spatial scales of  $\sim 20$  AU at the distance of these regions. Furthermore, the young stars with disks in Taurus and  $\rho$ -Ophiuchus have been extensively studied, and a database of stellar parameters as well as broadband photometry, from optical through millimeter wavelengths, is available in the literature. These kind of measurements are essential to assemble detailed disk models that reproduce the observations.

Our group at Caltech began obtaining CARMA observations of circumstellar disks in Taurus, at sub-arcsecond resolution in the 1 and 3 mm atmospheric bands, starting back in 2007 (the first of such studies published in [Isella et al., 2009](#)). Additionally, CARMA started developing a calibration system to improve the quality of observations obtained in the extended array configurations, currently known as the CARMA Paired Antennas Calibration System (C-PACS, [Pérez et al., 2010](#)). This system pairs antennas in the long baselines of the array in order to observe the science target and simultaneously monitor a strong quasar, used to calibrate the delay introduced by atmospheric water vapor.

In early 2008, I conducted the initial tests to establish the feasibility of this technique employing only a single array of antennas. Together with B. A. Zauderer, a graduate student from University of Maryland, we tested the C-PACS calibration method on astronomical sources, investigated different methodologies to apply this technique, and wrote MIRIAD software tasks to calibrate these observations. Also, we conducted the necessary tests to characterize the performance of C-PACS: for angular separations  $\lesssim 5^\circ$  between

the atmospheric calibrator and the science target, improvements in sensitivity (up to a factor of 2 increase in peak flux) and coherence (up to  $\sim 0.95$ ) are possible. A description of the C-PACS technique, its application to astronomical observations, and the resulting enhanced sensitivity and high angular resolution—demonstrated with circumstellar disks observations—were presented in Pérez et al. (2010), which is included in Chapter 3 on this thesis.

Until recently, similar quality observations at  $\lambda > 3$  mm were difficult to obtain, primarily due to the limited sensitivity of the 7 and 10 mm bands of the VLA. Conveniently, the upgrade of the VLA correlator and receivers—to provide orders of magnitude improvement in sensitivity at these long wavelengths—was well underway (Perley et al., 2011). In 2009 our group joined the EVLA<sup>1</sup> Key Science project “Grain growth and sub-structure in protoplanetary disks” (P.I. Claire Chandler, <https://safe.nrao.edu/evla/disks/>). The goals of this collaboration were multifold: to determine the prevalence of cm-sized particles in disks, to establish the location of these large dust grains in protoplanetary disks, to investigate the dependence of particle populations on stellar and disk properties, and to observationally constrain variations of the dust properties across the disk. Sub-arcsecond resolution observations at shorter wavelengths, like those our group had been obtaining with CARMA, were an excellent complement to these VLA high sensitivity observations in order to achieve these goals.

In 2010, as a fourth-year graduate student, I devoted 3 months to the commissioning of the EVLA, as part of the Resident Shared Risk Observation (RSRO) program and as co-investigator on this Key Science Project. During my stay in the Array Operations Center I performed several tests for high-frequency observing, including radio pointing and observing mode tests. I helped diagnose problems with the reference pointing routine that would have hinder future high-frequency observations and I characterized the system behavior when switching between narrow- and wide-bandwidth observing modes. Also, during this EVLA residency I analyzed many of the first 7 and 10 mm astronomical observations as part of our Key Science Project, characterizing the system performance at high frequencies.

A staged approach was employed to achieve the goals of the VLA project. First, multi-frequency photometry in the Q, Ka, K, and C-bands of the VLA (from 7 mm to 6 cm) was

---

<sup>1</sup>During the VLA upgrade, the array was known as the *Expanded Very Large Array (EVLA)*.

obtained. The result of this photometric survey informed the target selection for follow-up higher resolution imaging. The circumstellar disks selected for VLA observations were expected to be brighter than  $200 \mu\text{Jy}$  at 7 mm, from extrapolation of millimeter flux density measurements available in the literature. Sixty young stars in the Taurus and  $\rho$ -Ophiuchus star-forming regions, plus two more from the TW Hydrae association ( $d \sim 50$  pc) and four isolated young Ae stars, were selected based on this criteria; the results of this VLA multi-frequency survey will be presented in Chandler et al. (in preparation).

The circumstellar disk sample analyzed on this thesis, to search for radial variations of the dust properties, was defined by the availability of spatially resolved observations with CARMA and VLA. Such high angular resolution observations can only be obtained for a limited sample of disks, which must be reasonably bright over almost an order of magnitude in wavelength, from  $\sim 1$  to 10 mm. However, circumstellar disk observations at long wavelengths might present contamination arising from continuum emission whose origin is not dust thermal emission (e.g., chromospheric activity or thermal bremsstrahlung from photoevaporative disk winds; [Mundy et al., 1993](#)). Hence, a disk could be bright in the 7 mm and 1 cm bands of the VLA, but a significant fraction of that emission is not arising from dust.

To select a sample of disks where the emission at millimeter wavelengths is dominated by dust, the 6 cm observations from our VLA photometry survey were employed. Assuming that any emission detected at this wavelength is solely arising from processes other than dust thermal emission (since any emission from dust at  $\lambda = 6$  cm will be quite faint and below our RMS sensitivity of  $\sim 10 \mu\text{Jy}$ ), a subsample of disks for which contamination is small at millimeter wavelengths was selected. A compilation of millimeter flux densities ( $\lambda = 0.85\text{--}3.6$  mm) from our entire Taurus and  $\rho$ -Ophiuchus circumstellar disks sample was obtained from the literature and recently updated for this thesis ([Andre & Montmerle, 1994](#); [Osterloh & Beckwith, 1995](#); [Dutrey et al., 1996](#); [Sylvester et al., 1996](#); [Nuernberger et al., 1998](#); [Andrews et al., 2008](#); [Schaefer et al., 2009](#); [Hamidouche, 2010](#); [Isella et al., 2010](#); [Ricci et al., 2010a,b](#); [Guilloteau et al., 2011](#); [Ricci et al., 2012](#); [Harris et al., 2012](#)). These fluxes were scaled to  $\lambda = 3$  mm assuming  $S_\nu \propto \nu^{2+\beta}$  (i.e., optically thin dust emission in the Rayleigh-Jeans domain), characterized by a dust opacity spectral slope of  $\beta = 1$ .

Figure 2.1 compares the extrapolated 3 mm flux densities with the observed 6 cm flux densities, obtained from our photometry survey. Non-detections at  $\lambda = 6$  cm are marked with triangles, binaries/multiples in our sample are colored red, and the disks selected for further analysis on this thesis are colored blue. For a given C-band flux density, assuming optically thick free-free emission with spherical symmetry ( $S_\nu \propto \nu^{0.6}$ ; Reynolds, 1986), I computed the expected emission at 3 mm if only 10% of the total flux density at 1 cm was arising from this free-free contribution detected at 6 cm (blue dashed line); for targets above this line a negligible amount of contamination at millimeter wavelengths is expected.

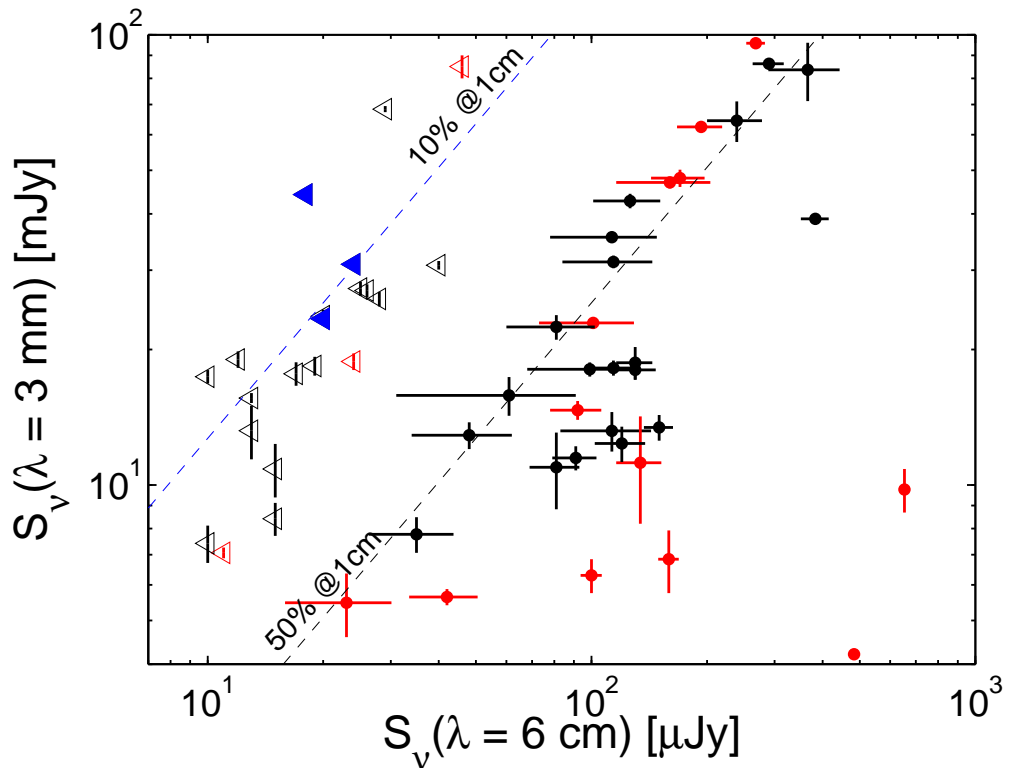


**Figure 2.1:** C-band flux densities ( $\lambda = 6$  cm) vs. millimeter flux densities ( $\lambda = 3$  mm) for the entire Taurus and  $\rho$ -Ophiuchus circumstellar disks sample of the Disks@EVLA collaboration. Non-detections in C-band are indicated by a triangle symbol ( $1\sigma$  upper limit), stars in known binary/multiple stellar systems are colored red. Targets near dashed lines are expected to have free-free emission contamination at 1 cm close to 10% (blue line) and 50% (black line). The 3 protoplanetary disks selected for this study are colored blue.

A total of 13 disks were good candidates for further analysis: they display  $\lesssim 15\%$  contamination at  $\lambda = 1$  cm, are brighter than  $S_\nu \sim 20$  mJy at  $\lambda = 3$  mm (to be imaged with CARMA), and are not known binaries/multiples. However, high resolution imaging in the 7 mm and 1 cm bands of the VLA was performed only for the brightest disks of our sample (as informed by the preliminary photometry), due to limited observing time in the extended array configurations. This excludes 4 candidates which had been successfully imaged with CARMA: LkCa 15, GM Aur, Elias 27 and DM Tau, which were too faint to image at high angular resolution with the VLA<sup>2</sup>. The other 6 disks were both too faint to image with CARMA and VLA in a sensible time request. This resulted in three protoplanetary disks selected to be analyzed for this thesis: AS 209 and DoAr25, in the  $\rho$ -Ophiuchus star-forming region, and CY Tau in the Taurus star-forming region. Coordinates and proper motion for these stars are indicated in Table 2.1, along with their stellar properties in Table 2.2.

**Table 2.1:** Star's coordinates and proper motion

Star	R.A. (J2000)	Dec (J2000)	err(R.A.) [mas]	err(Dec) [mas]	$\mu_\alpha \cos(\delta)$ [mas/yr]	$\mu_\delta$ [mas/yr]	Reference
AS 209	16:49:15.303	-14:22:08.63	2.5	1.5	-7.7 $\pm$ 3.8	-22.8 $\pm$ 2.0	(1)
DoAr 25	16:26:23.676	-24:43:13.90	94	94	3.9 $\pm$ 5.3	-40.3 $\pm$ 5.3	(2)
CY Tau	04:17:33.721	+28:20:46.69	18	15	10.5 $\pm$ 2.4	-24.8 $\pm$ 2.4	(2)

References: (1) [van Leeuwen \(2007\)](#); (2) [Roeser et al. \(2010\)](#)

**Table 2.2:** Stellar properties

Star	Spectral Type	$T_{\text{eff}}$ [K]	$R_\star$ [ $R_\odot$ ]	$L_\star$ [ $L_\odot$ ]	$M_\star$ [ $M_\odot$ ]	References
AS 209	K5	4250	2.3	1.5	0.9	(1,2)
DoAr 25	K5	4250	1.7	0.8	1.0	(1,2)
CY Tau	M2	3430	1.6	0.32	0.6 $\pm$ 0.3	(3,4)

References: (1) [Andrews et al. \(2009\)](#); (2) [Siess et al. \(2000\)](#); (3) [Simon et al. \(2000\)](#); (4) [Hillenbrand & White \(2004\)](#)

---

<sup>2</sup>A current upgrade to increase the total continuum bandwidth of the VLA, from 2 to 8 GHz, will allow to probe a fainter population of disks in the future.

## 2.2 CARMA Observations

The Combined Array for Research in Millimeter-wave Astronomy is an heterogeneous aperture synthesis interferometer comprising 23 antennas: nine 6.1 m telescopes originally from the Berkeley-Illinois-Maryland Association (BIMA), six 10.4 m telescopes originally from the California Institute of Technology/Owens Valley Radio Observatory (OVRO), and eight 3.5 m telescopes originally from the University of Chicago Sunyaev-Zel'dovich Array (SZA). The 15-element array of CARMA, which includes the 10 and 6 m antennas, can be organized into 5 different configurations operating in the 1 and 3 mm atmospheric bands. The range of baseline lengths and angular resolution achieved at each configuration can be found on Table 2.3.

For the purpose of mapping the emission of circumstellar disks in the nearby Taurus and  $\rho$ -Ophiuchus star-forming regions, angular resolutions better than  $\sim 2''$  (corresponding to the typical size of a circumstellar disk of a few hundred AU at the distance of these regions) are required. Hence, the A, B, and C configurations of the CARMA array were employed, which at 107 GHz (2.8 mm) and 230 GHz (1.3 mm) can resolve spatial structures between  $\sim 2''$ – $0.3''$  and  $\sim 1''$ – $0.15''$ , respectively.

Observations employing the most extended array configurations (A and B configurations) made use of the CARMA Paired Antenna Calibration System. Eight antennas from the 15-element array, with receivers working in the 1 or 3 mm bands, are paired with 3.5 m antennas from the 8-element array, which are outfitted with 1 cm receivers. These 3.5 m antennas track a strong calibrator throughout the track and measure the atmospheric delay introduced by variations of the water vapor content on the atmosphere atop the array. Corrections for these atmospheric phase fluctuations are applied during post-processing, and

**Table 2.3:** CARMA configurations and angular resolutions

Configuration	Baseline length	$\theta_{\text{beam}}(1.3 \text{ mm})$	$\theta_{\text{beam}}(2.7 \text{ mm})$
A	250–2000 m	0.15''	0.34''
B	100–1000 m	0.4''	0.86''
C	30–350 m	1.0''	2.1''
D	11–150 m	2.5''	5.2''
E	8–66 m	5.2''	10.9''

only for the baselines of the array which have a pair (generally the longest). A complete description of C-PACS can be found in the following chapter.

The field of view (FOV) for the 15-element array corresponds to

$$\text{FOV} \sim 1' \times \left( \frac{115 \text{ GHz}}{\nu} \right), \quad (2.1)$$

where  $\nu$  is the observing frequency in the operating 1 and 3 mm atmospheric bands. A single pointing towards each target will be sufficient to recover all of the emission since the CARMA FOV is larger than the typical size of a circumstellar disk.

### 2.2.1 Observational setup

Observations in the 1 mm band of the array require stringent weather conditions: low zenith opacities ( $\tau_{230 \text{ GHz}} < 0.3$ ) and a stable atmosphere (with variations of the path length due to atmospheric water vapor  $< 120 \mu\text{m}$ , for a 100 m baseline at 45° elevation during A configuration). The geographic location of CARMA allows for such conditions to be met for a fraction of the total observing time ( $\sim 25\%$  during winter season, when A and B configurations are deployed). For a target transiting at a much lower elevation, such as the circumstellar disks in  $\rho$ -Ophiuchus, atmospheric conditions need to be even better. Because of these constraints most of the CARMA observing time was dedicated to circumstellar disk observations in the 3 mm band.

Observations were obtained with double-sideband single-polarization receivers tuned to a rest frequency of 107 GHz placed in the upper sideband. To optimize the continuum sensitivity, all spectral windows in the correlator were configured to the maximum possible bandwidth: 468.75-MHz-wide windows of 15 channels each, to provide 2.8 GHz of bandwidth for observations before the correlator upgrade in December 2009, and 487.5-MHz-wide windows of 39 channels each, that provide 7.8 GHz of total bandwidth after the upgrade. The integration time per visibility (i.e., the record length) was 30 seconds for C configuration, in order to avoid any time-average smearing. However, for A and B configurations, the record length was kept short (4–10 seconds) in order to sample the atmospheric phase fluctuations as rapidly as possible. A shorter record length was not possible as the number of visibilities that need to be recorded increase linearly with decreasing record length,

increasing dramatically the throughput of the CARMA system. Furthermore, the SNR on the C-PACS calibrator needs to be sufficiently large over each record (see next chapter), hence shortening the integration time per visibility does not imply a better sampling of the atmospheric phase variations.

The observing sequence interleaved observations of a strong calibrator (generally 3 minutes in length) with science target observations, whose duration depended on the array configuration: compact configuration observations were 12–15 minutes in length, and extended configuration observations were 5–10 minutes in length. The duration of the science/calibrator cycle was reduced for extended configurations to diminish the amount of phase error aliased from the “fast” atmospheric phase fluctuations into the fitting of the “slow” phase calibration (Lay, 1997b). This observing sequence repeated throughout the track, which generally proceeded from rise to setting of the science target. Depending on the target elevation a single track could be 4 to 8 hrs long.

Before and/or after the source-calibrator cycle another strong calibrator was observed, in order to measure and correct the receiver and correlator response as a function of frequency, a procedure known as bandpass calibration. To calibrate the flux scale of CARMA observations a planet (Neptune, Uranus or Mars) or a secondary calibrator (3C273 or 3C84) were observed. When a planet was observed, its flux density was inferred from a planetary model provided by the observatory. If a planet was not accessible during a track (elevation  $< 20^\circ\text{--}30^\circ$ ) a secondary flux calibrator was observed; its flux density was obtained from CARMA observations on a different day when both this calibrator and a planet were observed. The uncertainty on the absolute flux calibration was estimated to be  $\sim 10\text{--}15\%$  due to uncertainties in the planetary model and the bootstrapped flux for the secondary flux calibrator.

A summary of our CARMA observations, with a list of targets, phase calibrators, weather conditions and length of the observations, can be found in Table 2.4 and 2.5.

**Table 2.4:** Observing journal for CARMA observations at 2.8 mm

Target	UT Date	Conf.	Phase Calibrator	$\tau_{230 \text{ GHz}}^a$	$\phi_{\text{RMS}}^b [\mu\text{m}]$	Flux Calibrator	$T_b^c [\text{K}]$
AS 209	2010-Jan-28	A	1733-130	0.1	80–200	Neptune	127.6
	2009-Dec-10	B	1733-130	0.4–0.8	100–300	Neptune	127.6
	2010-Mar-22	C	1733-130	0.1–0.15	80–140	Neptune	127.6
DoAr 25	2010-Nov-29	A	1625-254	0.1	100–300	Neptune	127.6
	2010-Nov-30	A	1625-254	0.4	100–300	Neptune	127.6
	2010-Dec-03	A	1625-254	0.5	90–200	Neptune	127.6
	2010-Dec-12	A	1625-254	0.2	250–350	Neptune	127.6
	2010-Jan-06	B	1625-254	0.35–0.45	80–300	Neptune	127.6
	2010-Jan-09	B	1625-254	0.4–0.5	100–200	Neptune	127.6
	2011-Apr-25	C	1625-254	0.3–0.4	80–200	Neptune	127.6
	2012-Jan-19	C	1625-254	0.12	100–300	Neptune	127.6
CY Tau	2010-Feb-15	A	3C 111	0.3	100–300	Uranus	132.5
	2008-Dec-11	B	3C 111	0.3	50–150	Uranus	129.7 <sup>d</sup>
	2011-Dec-29	B	3C 111	0.3	50–150	Uranus	132.5
	2011-Dec-30	B	3C 111	0.3	50–150	Uranus	132.5
	2012-Jan-03	B	3C 111	0.3–0.4	150–300	Uranus	132.5
	2010-Mar-20	C	0336+323	0.1–0.15	100–350	Mars	189.5
	2010-Mar-28	C	3C111, 0336+323	0.15–0.2	100–400	Uranus	132.5
	2012-Feb-08	C	3C 111	0.6–0.9	100–150	Uranus	132.5
	2012-Feb-19	C	3C 111	0.3–0.6	150–400	Uranus	132.5

<sup>a</sup> Zenith opacity at 230 GHz. <sup>b</sup> Path length variations due to atmospheric water vapor, over a 100 m baseline at 45° elevation. <sup>c</sup> Brightness temperature of planet at LO frequency. <sup>d</sup> LO frequency at 111.837 GHz instead of 105 GHz

**Table 2.5:** Observing journal for CARMA observations at 1.3 mm

Target	UT Date	Configuration	Phase Calibrator	$\tau_{230 \text{ GHz}}$	$\phi_{\text{RMS}} [\mu\text{m}]$
CY Tau <sup>1</sup>	2011-Dec-12	A	3C 111	0.2–0.25	60–150
	2009-Jan-05	B	3C 111	0.1	60–150
	2007-Nov-12	C	3C 111	0.5	100–200

<sup>1</sup> Observations from Isella et al. (in preparation). These data were calibrated by A. Isella.

### 2.2.2 Calibration of CARMA interferometric data

The CARMA observations were reduced using the Multichannel Image Reconstruction, Image Analysis and Display (MIRIAD) software package ([Sault et al., 1995](#)). Each night (i.e., each track) was calibrated separately. Malfunctioning antennas, receivers, and/or spectral windows were flagged, as informed by the observer’s log and careful examination of the data. The first step of the calibration consists of inspecting and applying what is known as the *line-length correction*. CARMA has a line-length system that measures the total round trip delay caused by temperature variations of the fiber-optic cables running to each antenna. These variations in cable length are stored in the dataset and can be applied to the data after observations. At this point, application of a *baseline correction* may be necessary, if the position of the antennas were not entered to the online CARMA system at the time of observations, or if the current baseline solution is outdated. These antenna positions are provided by the CARMA observatory.

The next step consists on deriving the *bandpass solution* (i.e., the complex response of the system as a function of frequency) from observations of the bandpass calibrator. Once this correction was applied, a *gain solution* can be determined. These correspond to the complex corrections (also known as gains) that need to be applied to the observations in order to remove any time variable errors that arise from the environment and the instrument itself. Since there is only enough signal to accurately measure these complex corrections (in amplitude and phase) during calibrator observations, gains variations can only be measured and corrected over intervals as long as the source-calibrator cycle. If the amplitude gains change by more than  $\sim 20\%$  from one cycle to the next, or if the phase gains “jump” by more than  $\sim 50^\circ$ , these data are then flagged since it was presumed that the science target will be also affected by such considerably large gain variations. The outlined calibration procedure is iterative, and requires several passes through the data in order to properly flag periods of bad weather in the observations. As a final step, the absolute flux scale of the telescope was calibrated.

### 2.2.3 Astronomical corrections and averaging of CARMA interferometric data

Given the observing date of each calibrated dataset, the proper motion of the star was applied in order to position each circumstellar disk observation at the interferometric phase center (i.e., the source is positioned at the central fringe of the interferometer pattern). The proper motions applied were obtained from different catalogs (van Leeuwen, 2007; Roeser et al., 2010; Zacharias et al., 2010) and are specified in Table 2.1. Since a very narrow range of wavelengths is covered by these CARMA observations ( $\frac{\Delta\lambda}{\lambda} \sim 0.04\text{--}0.08$ ), the calibrated datasets were averaged into a single wideband channel.

The uncertainty on each complex visibility measurement from antennas  $i$  and  $j$  is the noise level  $\sigma$  at the output of the correlator, given by (Thompson et al., 2001)

$$\sigma_{ij} = \frac{1}{\eta_Q} \sqrt{\frac{2k_B^2 T_{\text{sys}}^i T_{\text{sys}}^j}{A_{\text{eff}}^i A_{\text{eff}}^j \Delta\nu t_{\text{int}}}} \quad (2.2)$$

where  $k_B$  is the Boltzmann's constant,  $T_{\text{sys}}^n$  is the system temperature of antenna  $n$ ,  $A_{\text{eff}}^n$  is the effective area of antenna  $n$ ,  $\Delta\nu$  is the bandwidth of the observations,  $t_{\text{int}}$  is the integration time of each visibility, and  $\eta_Q$  is the correlator efficiency factor, related to the loss of information due to the quantization and digitalization of data.

However, the actual noise on a single visibility measurement will be larger than the thermal noise presented on Equation 2.2, since other effects will play a role in degrading these observations. For example, the loss of sensitivity of a particular antenna with bad pointing is alleviated during gain calibration, as the visibility amplitudes measured by this antenna are scaled up by a gain factor larger than 1.0, determined during gain calibration. Hence, the inherent noise of the data from this antenna is also increased by this gain factor, and the theoretical noise of Equation 2.2 should be scaled accordingly. However, the software used for data calibration and analysis, MIRIAD, does not scale the theoretical noise by the measured gains. Thus, in this example, MIRIAD's theoretical noise values will underestimate the uncertainty of the observations causing the uncertainty in the disk model parameters to be also underestimated.

Since different datasets were obtained under different observing conditions, the theoretical visibility noise of each dataset was scaled separately, before combining them into

a single visibility file to be used in the modeling (Chapter 4). The procedure employed here computes the dispersion of the real and imaginary part of the visibilities inside a small region in Fourier space, referred to as *uv-cell*. This cell is large enough to contain sufficient visibility points ( $> 10$ ) to accurately measure the true RMS, but not as large that intrinsic variations of the visibility across the uv-cell may incorrectly increase the RMS noise level. A cell width similar to the antenna size is usually a good choice, since the interferometer is not sensitive to spatial scales smaller than the antenna size. Multiple measurements of the dispersion in the visibilities inside a small uv-cell were obtained. The ratio between this measured dispersion and the theoretical noise was used to compute a scaling factor for the noise in each dataset, which was generally between 1.1–1.5.

The final step was to combine calibrated observations coming from different array configurations and generate a single visibility file (that includes position in the *uv*-plane, real and imaginary part of the visibility, and the weight of each visibility record,  $w_{ij} = 1/\sigma_{ij}^2$ ) to be compared with physical disk models, as it is explained in Chapter 4. As a final check, calibrated visibilities were compared over the spatial frequencies where different array configurations overlap. They were found to agree within the absolute flux scale uncertainty, which is  $\sim 15\%$  for CARMA.

### 2.3 VLA Observations

The Karl J. Jansky Very Large Array is an aperture synthesis interferometer comprising 28 antennas of 25 m diameter. The VLA can be organized into 4 different configurations that contain baselines that range in length from 35 m to 1 km (D configuration) to 680 m to 36.4 km (A configuration). Multiple receivers on each antenna allow the array to operate at any frequency between 1.0 and 50 GHz, with up to 8 GHz bandwidth<sup>3</sup> and full polarization capabilities. To first order, the field of view for the VLA corresponds to the size of the primary beam

$$\text{FOV} \sim 1' \times \left( \frac{45 \text{ GHz}}{\nu} \right), \quad (2.3)$$

---

<sup>3</sup>While the receivers may deliver 8 GHz of IF bandwidth, at the time of our observations the correlator was being commissioned and could not process such large bandwidth. All of our VLA datasets made use of the largest possible bandwidth, which given the correlator restrictions, corresponded to 2 GHz.

where  $\nu$  is the observing frequency in the operating band. Second-order effects that reduce the effective FOV, like bandwidth smearing, are not critical for the high-frequency observations presented here. The large fractional bandwidth of the VLA, particularly at the low-frequency bands where  $\Delta\nu/\nu$  quickly approaches 1, introduces aberrations in the image known as chromatic aberrations. Regions away from the phase tracking center will be distorted when averaging visibilities with a large bandwidth, and this in turn will reduce the effective FOV of the array. However, the observations presented here correspond to the high-frequency bands of the VLA: Q-band (45 GHz, 7 mm) and Ka-band (33 GHz, 9 mm), which do not suffer from this effect since the fractional bandwidth at high frequencies is very small ( $\frac{\Delta\lambda}{\lambda} \sim 0.02\text{--}0.05$ , see Section 2.3.3)

The VLA can be organized into 4 different configurations (A, B, C, D) plus 3 hybrid configurations (DnC, CnB, and BnA) that are optimized to observe targets with declinations lower than  $\delta = -15^\circ$ . During hybrid configurations, the north arm of the array is lengthened to the largest configuration, while the other arms remain at the shorter configuration. This can provide angular resolutions similar to the smaller configuration of the hybrid out to declinations of  $\delta = -30^\circ$ . The range of baseline lengths and angular resolution achieved at each configuration can be found on Table 2.6.

### 2.3.1 Observational setup

The Ka and Q high-frequency bands of the VLA, along with array configurations B, C, BnA and CnB, were employed in order to map the emission of circumstellar disks with angular resolutions better than  $\sim 2''$ . Q-band observations, particularly those with extended array configurations, require stringent weather conditions: low wind speed ( $v_{\text{wind}} \lesssim 5 \text{ m/s}$ ) and a stable atmosphere (with rms variations of the phase due to atmospheric water vapor  $< 7^\circ$ ,

**Table 2.6:** VLA configurations and corresponding angular resolution

Configuration	Baseline length	$\theta_{\text{beam}}(\text{Q-band})$	$\theta_{\text{beam}}(\text{Ka-band})$
A	0.68–36.4 km	0.043''	0.059''
B	0.21–11.1 km	0.14''	0.19''
C	0.035–34 km	0.47''	0.63''
D	0.035–1.03 km	1.5''	2.1''

for a 300 m baseline observing at 11.5 GHz). Note that because of the low frequencies that VLA observes, the atmospheric opacity is typically not a limiting factor. The geographic location of VLA allows for such good conditions to be met for a fraction of the total observing time. For targets located in Taurus ( $\text{RA} = 4^h$ ), Q-band observing can proceed for  $\sim 50\%$  of the total observing time during fall/winter season and only  $\sim 10\text{--}20\%$  during spring/summer season. Since most of our Taurus targets were observed during the spring/summer season, and because the non-fixed VLA configuration schedule rotates, we decided to dedicate most of our observing time to circumstellar disk observations in the Ka-band, with only the faintest objects imaged in Q-band.

VLA observations were obtained employing dual-polarization receivers and two independently tunable basebands centered at 30.5 GHz and 37.5 GHz for Ka-band, and 43 GHz and 47 GHz for Q-band. Each baseband was configured to have eight 128 MHz spectral windows of 64 channels, to provide the most continuum bandwidth per baseband, for a total bandwidth of 2 GHz.

The observing sequence interleaved observations of a strong calibrator (45 sec to few minutes in length) with science target observations, whose duration depended on the array configuration: extended configurations were 1.5–5 minutes in length, compact configurations were 5–10 minutes in length. The observing sequence was repeated throughout the track, which generally proceeded until enough signal is collected on the target: in photometry mode this corresponded to few minutes for a  $\text{SNR} \sim 10$ , while for imaging mode in the most extended configurations a single observation lasted several hours.

Before and/or after the source-calibrator cycle a strong calibrator is observed to determine the bandpass calibration. Also, a known strength calibrator (3C 286) is observed to calibrate the flux scale of the telescope (flux calibration). The record length was 1–5 seconds, in order to avoid time averaging smearing and to also check for any problems arising from the correlator, which was being commissioned at the time. A summary of the VLA observations analyzed for this thesis can be found in Table 2.7.

### 2.3.2 Calibration of VLA interferometric data

The data reduction of VLA observations was performed using the CASA software package. As with the CARMA observations, each track was calibrated separately and malfunctioning

**Table 2.7:** Observing journal for VLA observations in Q- and Ka-band

Name	UT Date	Configuration	Band	API phase RMS <sup>1</sup>	Wind speed
AS 209	2011-Jan-29	CnB	Ka	1.4°	3.5 m/s
	2011-May-15	BnA	Ka	2.5°	2.7 m/s
	2011-May-25	BnA	Ka	3.1°	4.6 m/s
DoAr 25	2011-Jan-23	CnB	Ka	2.5°	2.0 m/s
	2011-May-28	BnA	Ka	4.1°	6.9 m/s
CY Tau	2010-Nov-13	C	Q	1.6°	2.0 m/s
	2011-Apr-05	B	Q	2.8°	6.0 m/s

<sup>1</sup>API: Atmospheric phase interferometer. This is a dedicated 300 m baseline interferometer at the VLA, to quantify the amount of phase fluctuations introduced by the atmosphere.

antennas, receivers, and/or spectral windows were flagged, as informed by the telescope operator’s log and careful examination of the data. Also, the first 5–10 seconds at the beginning of each target observation were flagged, since occasionally antennas will start to record data although they have not acquired the target yet.

The first step of the calibration consists of applying a *baseline correction* if the position of the antennas were not entered to the online system at the time of observations. These antenna positions were provided by the VLA observatory. Afterward, a *bandpass solution* was determined from observations of the bandpass calibrator; this solution was then applied to the dataset. At this point, noisy channels at the edge of each spectral window were flagged and the data were spectrally averaged to a single frequency per spectral window (to reduce the size of the dataset). Next, a *gain solution* was derived from observations of the phase calibrator, at every source-calibrator cycle. Similar to CARMA data calibration, any periods of time where the amplitude gains change by more than  $\sim 20\%$  from one cycle to the next were flagged. This calibration procedure is iterative, and requires several passes through the data in order to properly flag periods of bad weather in the observations. The absolute flux calibration was set from observations of a known-flux standard calibrator. The observatory provides model images for these standard calibrators that encompass its spectral and spatial features (i.e., SED and structure). The VLA staff recommended 3C 286 as the flux calibrator since it is bright at high frequencies and slightly resolved in the most extended array configurations. Employing the model images provided by the observatory, the expected accuracy in the flux calibration is  $\sim 10\%$ .

### 2.3.3 Astronomical corrections and averaging of VLA interferometric data

Given the observed date, each calibrated dataset was corrected by the star’s proper motion, which were obtained from different catalogs (see Table 2.1 in CARMA section). Since a very narrow range of frequencies is averaged for each 1 GHz baseband ( $\frac{\Delta\lambda}{\lambda} \sim 0.02\text{--}0.03$  for Q- and Ka-band, respectively), calibrated datasets were averaged into a single wideband channel: for Ka-band these correspond to two 1-GHz-wide channels, centered at 30.5 GHz ( $\lambda = 9.8$  mm) and 37.5 GHz ( $\lambda = 8.0$  mm), while for Q-band, a single 2-GHz-wide channel centered at 42 GHz ( $\lambda = 7.14$  mm), was obtained.

As explained in Section 2.2.3, the uncertainty of each complex visibility measurement corresponds to the thermal noise at the output of the correlator (Equation 2.2). These observations were obtained during the VLA upgrade (when the telescope was known as the EVLA) and switched power system temperature calibration (which provides the theoretical noise of each visibility) was not available. Hence, the visibility noise values were not stored in the data, and it had to be assumed that all visibilities experienced equal noise (careful attention must be paid then when calibrating EVLA observations, to make sure that a “bad” antenna is not erroneously included, since such antenna will not be down-weighted). The equal noise, used for all visibilities, was computed as the dispersion of the real/imaginary part in the data: since for each visibility the SNR is practically 0, the distribution of the real and imaginary parts of all visibilities should have a Gaussian distribution centered on the mean flux (for the real part) and zero (for the imaginary part). The width of this gaussian corresponds to the noise of each complex visibility point ( $\sigma_{ij}$ ). Because different datasets were obtained under different observing conditions, the equal visibility noise of each dataset was computed separately, before combining them into a single visibility file to be used in the modeling (Chapter 4).

The final step was to combine calibrated observations coming from different array configurations and generate a single visibility file (that includes position in the *uv*-plane, real and imaginary part of the visibility, and the weight of each visibility record,  $w_{ij} = 1/\sigma_{ij}^2$ ) to be compared with physical disk models. As a final check, calibrated visibilities were compared over the spatial frequencies where different array configurations overlap. These were found to agree within the absolute flux scale uncertainty, which is  $\sim 10\%$  for VLA.

## 2.4 SMA Observations

The Submillimeter Array is an aperture synthesis interferometer comprising eight 6 m telescopes. The array can be organized into 4 different configurations that contain baselines that range in length from 8 to 509 m. The field of view for the SMA corresponds to

$$\text{FOV} \sim 0.5' \times \left( \frac{345 \text{ GHz}}{\nu} \right), \quad (2.4)$$

where  $\nu$  is the observing frequency in the operating 0.43, 0.87, and 1.3 mm atmospheric bands. SMA can achieve an angular resolution as high as

$$\theta_{beam} \sim 0.3'' \times \left( \frac{345 \text{ GHz}}{\nu} \right) \quad (2.5)$$

depending on the observing frequency  $\nu$  and the source declination. The SMA observations presented here have been published in [Andrews et al. \(2008, 2009\)](#), where a detailed discussion of the data acquisition, observational setup, and calibration is presented. Hence, I will only present a brief summary of these data.

### 2.4.1 Observational setup and calibration

SMA observations of the dust continuum emission were obtained at 345 GHz (0.88 mm) for 4 circumstellar disks in the star-forming region  $\rho$ -Ophiuchus, with an angular resolution of  $\sim 0.3''$ . These observations were obtained with double-sideband receivers tuned to a local oscillator frequency of 340.755 GHz. Each sideband was configured to have 24 partially overlapping 104 MHz chunks, for a total continuum bandwidth of 4 GHz.

The observing sequence interleaved observations of a strong calibrator with science target observations, with an integration time ratio of 1:2. The duration of the science/calibrator cycle was 8 minutes for the extended configuration, and  $\sim 15\text{--}20$  minutes for compact configurations. Bandpass and flux calibrators were selected from different planets and satellites (Uranus, Jupiter, Saturn, Titan, Callisto) as well as strong quasars (3C 454.3, 3C 279) depending on their availability and array configuration. The typical systematic uncertainty in the absolute flux scale is  $\sim 10\%$ .

This SMA data were flagged and calibrated by [Andrews et al. \(2008, 2009\)](#), employing

the IDL-based MIR software package. A summary of the SMA observations presented in this thesis can be found in Table 2.8.

#### 2.4.2 Astronomical corrections and averaging of SMA interferometric data

Given the observing date, each calibrated dataset was corrected by the star's proper motion, which can be found in Table 2.1. Since at SMA wavelengths a very narrow range of frequencies is being averaged ( $\frac{\Delta\lambda}{\lambda} \sim 0.01$ ), these calibrated datasets were averaged into a single wideband channel.

Following the same procedure outlined in Section 2.2.3, the theoretical noise of the visibilities was scaled to match the actual visibility noise. The scaling factor for the theoretical noise in each dataset was generally between 1.3–1.5, and each dataset was scaled separately. The final step was to combine calibrated observations coming from different array configurations and generate a single visibility file (that includes position in the *uv*-plane, real and imaginary part of the visibility, and the weight each visibility record,  $w_{ij} = 1/\sigma_{ij}^2$ ) to be compared with physical disk models, as described in the next chapter. As a final check, calibrated visibilities were compared over the spatial frequencies where different array configurations overlap. These were found to agree within the absolute flux scale uncertainty.

**Table 2.8:** Summary of SMA observations at 0.88 mm

Target Name	UT Date	Configuration <sup>a</sup>	References
AS 209	2007-Jun-09	V	(1)
	2006-Jun-03	E	
	2006-May-12	C	
DoAr 25	2007-May-26	V	(1,2)
	2007-Jun-17	V	
	2005-Jun-12	C	
	2005-May-08	E	

<sup>a</sup>Baseline lengths range from  $\sim 8$ –70 m in C configuration (compact), to  $\sim 10$ –210 m in E configuration (extended), to about 20–500 m in V configuration (very extended).

References: (1) Andrews et al. (2009); (2) Andrews et al. (2008)

## 2.5 Imaging of Interferometric Data

Calibrated observations from CARMA, SMA and VLA, were imaged (separately) to produce a map of the dust emission at each observed wavelength. These images were not directly used in any subsequent analysis, since performing the analysis in the image domain can be problematic. First and foremost, the actual empirical measurement performed by the interferometer are the complex visibilities, hence any reliable model comparison should be done in the Fourier domain. Second, the image reconstruction process heavily relies on user input. For example, defining the regions where emission is present—in order to proceed with cleaning and deconvolution as explained below—is a subjective art. Consequently, performing the analysis in the image domain may jeopardize the objectivity of this study. Finally, these multi-wavelength observations have different angular resolutions and were obtained under diverse weather conditions which may degrade the expected angular resolution, making it difficult to compare them in the image domain.

Nevertheless, dust continuum maps for each of target observation were created to accompany our analysis in the Fourier domain. The image reconstruction procedure was performed using CASA, and consist on:

(1) **Fourier inversion of the visibilities:** this first step generates the so-called *dirty image*, which is a map of the source intensity distribution on the sky convolved with the point-spread function of the interferometer (also known as *dirty beam*). Before taking the Fourier transform of the visibilities to produce an image, each visibility is assigned a weight, different weighting schemes will produce images with different angular resolution and sensitivity. For the best image SNR each visibility is weighted equally by the inverse of the visibility noise squared ( $w_{ij} = 1/\sigma_{ij}^2$ ), a scheme known as *natural weighting*. This results in low angular resolution, as short  $uv$ -spacings are emphasized w.r.t. long  $uv$ -distances, since generally the  $uv$ -coverage of an interferometer becomes sparser with increasing  $uv$ -distance. To de-emphasize short  $uv$ -spacings, *uniform weighting* can be employed. Here, each  $uv$ -point is weighted by  $w_{ij} = 1/(\rho(u, v)\sigma_{ij}^2)$ , where  $\rho(u, v)$  is the density of visibilities within a  $uv$ -cell centered at  $(u, v)$  with size  $du \times dv$ . Uniform weighting provides the highest angular resolution image for a given the dataset, but the SNR of such image is generally much smaller than a naturally weighted image. An in-between weighting scheme, which was employed on this thesis, is called *robust weighting* (Briggs, 1995), which allow for an smaller PSF

than natural weighting while maintaining a high SNR in the image. This weighting scheme is governed by the *robust parameter*, which varies between  $\text{robust} = 2$  (natural weighting) and  $\text{robust} = -2$  (uniform weighting). The value of the robust parameter was changed for each dataset in order to roughly match the angular resolution of different wavelength observations, if possible.

**(2) Deconvolution of the dirty image through the CLEAN algorithm:** This iterative approach represents the source intensity distribution as a combination of point-sources (known as *cleaned components*), with different flux densities and positions throughout the sky. To find the location and strength of the point-sources that makeup the source emission, the algorithm iteratively removes a single-point source at a time by selecting the strongest peak in the map (in absolute magnitude) over some user-defined region, called the *clean box*. The CLEAN algorithm stops once the remaining largest peak (inside the interest region) is smaller than the user-defined threshold, which I selected to be the noise level in the map. Because the cleaning process can select negative pixels in the map, it is crucial to carefully select the clean box, trying to encompass the source emission and not much of the background.

**(3) Creating the final cleaned image:** This is achieved by convolving the clean components with the ideal synthesized beam, which is just an elliptical Gaussian fitted to the dirty beam. This produces a final deconvolved image for which the dirty beam sidelobes are de-emphasized, known as the *clean image*.

Once a clean dust continuum map was produced, the RMS noise level was measured by selecting a region close to the target with no emission and computing the standard deviation of the flux density in that region of the image. Multi-wavelength maps of the observed emission towards the stars in our sample can be found in Chapter 6.



## Chapter 3

# Atmospheric Phase Correction Using CARMA-PACS: High Angular Resolution Observations of the FU-Orionis Star PP 13S\*

LAURA M. PÉREZ<sup>1</sup>, JAMES W. LAMB<sup>2</sup>, DAVID P. WOODY<sup>2</sup>, JOHN M. CARPENTER<sup>1</sup>, B. ASHLEY ZAUDERER<sup>3</sup>, ANDREA ISELLA<sup>1</sup>, DOUGLAS C. BOCK<sup>4</sup>, ALBERTO D. BOLATTO<sup>3</sup>, JOHN CARLSTROM<sup>5</sup>, THOMAS L. CULVERHOUSE<sup>5</sup>, MARSHALL JOY<sup>6</sup>, WOOJIN KWON<sup>7</sup>, ERIK M. LEITCH<sup>2,5</sup>, DANIEL P. MARRONE<sup>5,8</sup>, STEPHEN J. MUCHOVÉJ<sup>2</sup>, RICHARD L. PLAMBECK<sup>9</sup>, STEPHEN L. SCOTT<sup>2</sup>, PETER J. TEUBEN<sup>3</sup> AND MELVYN C. H. WRIGHT<sup>9</sup>

<sup>1</sup>California Institute of Technology, 1200 East California Blvd, Pasadena, CA 91125

<sup>2</sup>Owens Valley Radio Observatory, California Institute of Technology, Big Pine, CA 93513

<sup>3</sup>Department of Astronomy, University of Maryland, College Park, MD 20742-2421

<sup>4</sup>Combined Array for Research in Millimeter-wave Astronomy, P.O. Box 968, Big Pine, CA 93513

<sup>5</sup>Department of Astronomy and Astrophysics, University of Chicago, 5640 S. Ellis Ave. Chicago, IL 60637

<sup>6</sup>Space Sciences - VP62, NASA Marshall Space Flight Center, Huntsville, AL 35812

<sup>7</sup>Department of Astronomy, University of Illinois, Urbana, IL 61801

<sup>8</sup>Jansky Fellow, National Radio Astronomy Observatory

<sup>9</sup>Astronomy Department, University of California at Berkeley, Berkeley, CA 94720-3411

---

A version of this chapter has been published to the *Astrophysical Journal* ([Pérez et al., 2010](#)). It is reproduced here with permission from AAS.

## Abstract

We present  $0.15''$  resolution observations of the 227 GHz continuum emission from the circumstellar disk around the FU-Orionis star PP 13S\*. The data were obtained with the Combined Array for Research in Millimeter-wave Astronomy1995Sault (CARMA) Paired Antenna Calibration System (C-PACS), which measures and corrects the atmospheric delay fluctuations on the longest baselines of the array in order to improve the sensitivity and angular resolution of the observations. A description of the C-PACS technique and the data reduction procedures are presented. C-PACS was applied to CARMA observations of PP 13S\*, which led to a factor of 1.6 increase in the observed peak flux of the source, a 36% reduction in the noise of the image, and a 52% decrease in the measured size of the source major axis. The calibrated complex visibilities were fitted with a theoretical disk model to constrain the disk surface density. The total disk mass from the best-fit model corresponds to  $0.06 M_{\odot}$ , which is larger than the median mass of a disk around a classical T Tauri star. The disk is optically thick at a wavelength of 1.3 mm for orbital radii less than 48 AU. At larger radii, the inferred surface density of the PP 13S\* disk is an order of magnitude lower than that needed to develop a gravitational instability.

### 3.1 Introduction

Electromagnetic waves from an astronomical radio source suffer distortion from irregularities in the refractivity of the atmosphere ([Thompson et al., 2001](#)). At millimeter and submillimeter wavelengths, the distortions are caused primarily by a turbulent water vapor distribution, though dry air turbulence may also be important under some circumstances ([Stirling et al., 2006](#)). The spatial scales of the turbulence extend to kilometer distances with a power-law spectrum ([Kolmogorov, 1941](#)) that creates atmospheric delay fluctuations on timescales that range from fractions of a second to tens of minutes. The signal degradation is particularly serious for millimeter-wave radio interferometers in extended configurations, where perturbation of phases across the instrument often exceeds many radians. These perturbations can lead to decorrelation (loss of amplitude), distortion of the image, and loss of resolution ([Lay, 1997a](#)).

Different approaches have been employed to overcome the effect of atmospheric delay

fluctuations. A straightforward approach is *self-calibration* (Schwab, 1980), where the visibility phase used to calibrate the data is measured from the actual science target. A model for the source spatial structure is needed and bright sources are required to measure the fringe phase with a high signal-to-noise ratio in a short integration. Two other approaches have been applied to faint targets. In *water vapor radiometry* (Westwater, 1967; Woody et al., 2000), a dedicated radiometer monitors the water vapor emission along the pointing direction of the antenna. In *fast position switching* (Holdaway et al., 1995), the antennas switch rapidly between the science target and a nearby phase calibrator to capture the atmospheric delay fluctuations on time scales longer than the switching cycle time. Both methods probe the atmosphere close to the line-of-sight toward the science target, but have limitations in actual applications. Fast position switching reduces the time spent on source by a factor of  $\sim 2$ , while water vapor radiometry requires a physical model to relate the water line brightness and the path correction, as well as it assumes that refractivity fluctuations are produced only by water vapor.

As an alternative approach, an array of closely *paired antennas* (Asaki et al., 1996, 1998) continuously monitors the atmospheric phase fluctuations by observing a nearby calibrator. Two arrays of antennas are necessary: antennas belonging to the “science array” observe the science target and phase calibrator, while antennas belonging to the “reference array” simultaneously monitor an atmospheric calibrator. Phase correction on the science target and phase calibrator is accomplished by subtracting the visibility phase measured from the atmospheric calibrator on each baseline. An advantage of the paired antenna technique over water vapor radiometry is that it accounts for atmospheric phase fluctuations due to both water vapor and a dry air component.

Between November 2008 and February 2009, the Combined Array for Research in Millimeter-wave Astronomy (CARMA) implemented the CARMA Paired Antenna Calibration System (C-PACS) to correct for atmospheric delay fluctuations on the longest baselines of the interferometer (up to 2 km in length). The goal of C-PACS is to enable routine imaging in the most extended CARMA configurations.

In this paper we describe C-PACS and apply this calibration technique to observations of the circumstellar dust around PP 13S<sup>1</sup>. PP 13S\* is a young pre-main sequence star located

---

<sup>1</sup>PP 13 is a cometary nebula in the list of Parsamian & Petrossian (1979). PP 13S is the southern

in the constellation of Perseus and embedded in the L1473 dark cloud at a distance of  $\sim 350$  pc (Cohen et al., 1983). This object is thought to have experienced a FU-Orionis-type outburst in the past due to a massive accretion episode and is now declining in brightness to a quiescent state (Aspin & Sandell, 2001). The FU-Orionis nature of PP 13S\* has been established based on the highly broadened infrared CO absorption bands (Sandell & Aspin, 1998), the jet-like feature seen in [SII] emission which is characteristic of Herbig-Haro outflows (Aspin & Reipurth, 2000; Aspin & Sandell, 2001), and the consistent dimming and morphology changes observed at near-IR and optical wavelengths over several decades (Aspin & Sandell, 2001). All of these characteristics are common to FU-Orionis objects (Hartmann & Kenyon, 1996). The star, with a bolometric luminosity of  $30 L_\odot$  (Cohen et al., 1983), is surrounded by an extended disk and envelope that contains about  $0.6 M_\odot$  of gas and dust (Sandell & Aspin, 1998). The new CARMA observations will help understand the origin of the FU-Orionis phenomena in PP 13S\* by measuring the distribution of dust continuum emission on spatial scales of  $\sim 50$  AU.

## 3.2 Description of C-PACS

Before presenting the new observations of PP 13S\*, we describe the paired antenna calibration system as implemented at CARMA. We first describe the antenna configuration used for the observations, and outline the basic principles of the technique.

### 3.2.1 CARMA

CARMA is an heterogeneous interferometer comprising 23 antennas: six 10.4 m telescopes from the California Institute of Technology/Owens Valley Radio Observatory (OVRO), nine 6.1 m telescopes from the Berkeley-Illinois-Maryland Association (BIMA), and eight 3.5 m telescopes from the University of Chicago Sunyaev-Zel'dovich Array (SZA). The two most extended array configurations contain baselines that range in length from 100 m to 1000 m (B configuration) and 250 m to 1900 m (A configuration) to achieve an angular resolution of  $0.3''$  and  $0.15''$ , respectively, at an observing frequency of 230 GHz.

---

component containing a red nebula with a bright infrared point source at the apex as designated by Cohen et al. (1983). PP 13S\* corresponds to the embedded star itself, which is obscured by circumstellar material. The northern component, PP 13N, is a T Tauri star.

A schematic of C-PACS is shown in Figure 3.1. C-PACS pairs the eight 3.5 m antennas with selected 6 and 10 m antennas, preferentially on the longer baselines. Typically, a 3.5 m antenna is offset by 20–30 m to the west of a larger antenna. This separation is a compromise between the need to put the antennas as close as possible to probe the same atmospheric path and to avoid shadowing between antennas.

The science array, composed of the 6 m and 10 m antennas, operates in the 1.3 or 3 mm atmospheric windows as requested by the investigator. The reference array, comprising the 3.5 m antennas, operates in the 1 cm window. The observing cycle consists of observations of the science target interleaved with periodic observations of the phase calibrator. Both the

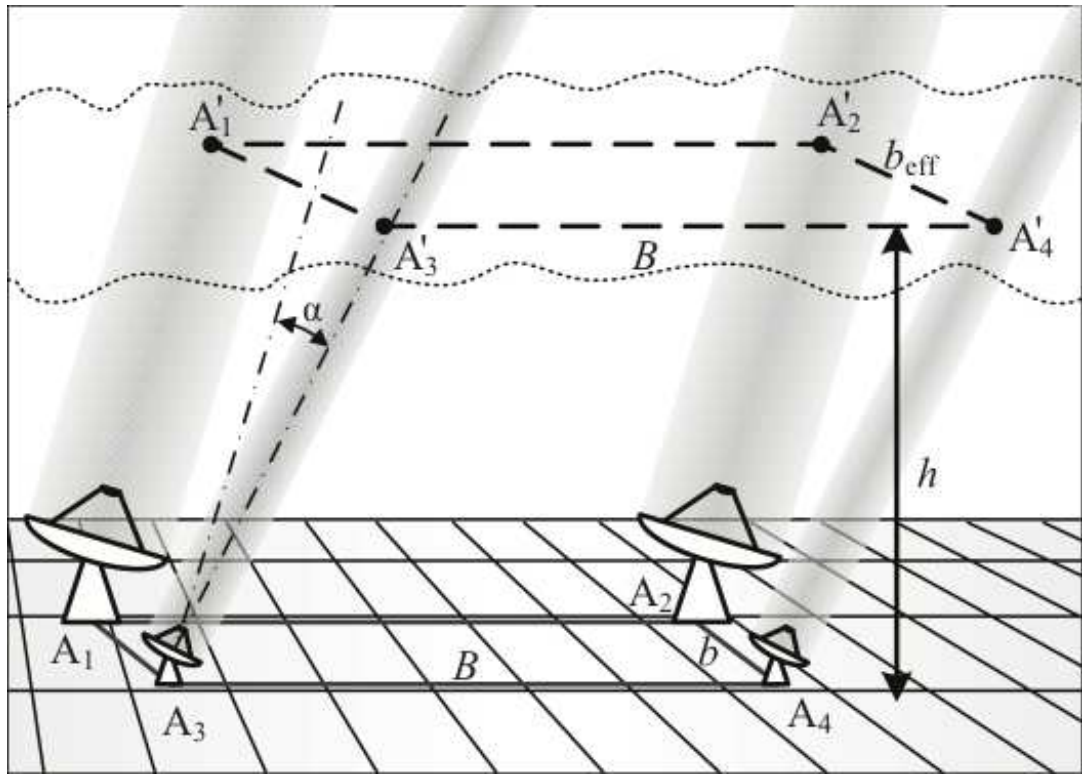


**Figure 3.1:** Schematic of the CARMA Paired Antenna Calibration System. Antennas  $A_1$  and  $A_2$  (in the science array) observe the science target while antennas  $A_3$  and  $A_4$  (in the reference array), offset by a distance  $b$  from the science array, observe a bright atmospheric calibrator. In the turbulent layer at an elevation  $h$  the beams are separated by a distance  $b_{\text{eff}}$  that depends on  $b$ ,  $h$ , and the angular offset between the science and reference sources,  $\alpha$ . If the effective baseline,  $b_{\text{eff}}$ , is much smaller than the science baseline,  $B$ , the delay difference to the reference antennas is a good estimate for the delay difference to the science antennas.

science and reference arrays observe the phase calibrator to measure instrumental phases drifts. Subsequently, the science array observes the science target while the reference array monitors a strong point source (i.e., the “atmospheric” calibrator) close to the science target, to measure the delay introduced by the atmosphere. The atmospheric delay measured by the 3.5 m antennas can then be applied to the science observations.

### 3.2.2 Properties of the atmosphere

It is helpful to have a physical picture to understand the principles of the correction. We suppose the atmosphere to be a pattern of random refractive index variations that is blown across the array at the wind velocity. Furthermore, we assume that the layer is at a height of a couple of kilometers and that the thickness is much less than the height. General experience at this and other sites show that these conditions are often consistent with what is observed. Other conditions can be present, but can often be characterized by two or more layers at different altitudes with separate wind vectors so that only a small change to the analysis is required.

Kolmogorov theory predicts a turbulence distribution with a power-law spectrum from less than a millimeter in size to many kilometers. This results in random delay differences between signals arriving at different antennas that increase with separation as a power-law function ([Tatarskii, 1961](#)). As the pattern moves over the array, the delay differences are observed as temporal fluctuations in the visibility phases. The RMS of the delay depends on the wind speed, but not its direction. Structures smaller in size than the antenna diameter are averaged out and do not contribute to the phase errors. Structures on scales large in comparison with the baseline length are common to the two antennas on the baseline and therefore tend to cancel out. From these theoretical considerations supported by experimental evidence ([Sramek, 1983, 1989](#)), it is found that the resulting delay variance vs baseline length (i.e., the delay structure function) also follows a power law. The theoretical slope of the power law is  $5/3$  and  $2/3$  for two- and three-dimensional Kolmogorov turbulence, respectively.

### 3.2.3 Atmospheric delay corrections

Following the discussion in [Asaki et al. \(1996\)](#), consider two pairs of antennas as shown in Figure 3.1. In the simplest case, we measure the delay difference between the antennas on the reference baseline (i.e., baseline  $A_3 - A_4$  in Figure 3.1) as a function of time. Assuming a non-dispersive atmosphere, the delay on the science baseline (i.e., baseline  $A_1 - A_2$ ) is corrected by applying the delay difference on the reference baseline to the visibility measurement.

The reference and science delays are not identical since the two baselines are not exactly co-located. The relevant distances that determine the efficacy of the delay corrections are not the baseline lengths at the ground, but the distances between the radio beams as they traverse the turbulent layer (i.e.,  $A'_1 - A'_3$  and  $A'_2 - A'_4$  in Figure 3.1). The beam separation at the turbulent layer depends upon the relative positions of the target and reference source in the sky, the height of the turbulent layer, and the configuration of the antennas on the ground. The upper limit to the beam separation is given by

$$d_{\max} = |A_1 - A_2| + \alpha h / \sin(e), \quad (3.1)$$

where  $\alpha$  is the angular separation between the science target and the atmospheric calibrator,  $h$  the height of the turbulence, and  $e$  is the source elevation. Assuming that the turbulent layer is at a height of 1 km (continuous line) or at 2 km (dashed line), Figure 3.2 shows the trajectories of the 3.5 m beam locations relative to the 6 m and 10 m beams for an 8 h observation of PP 13S\* centered on transit with 3C111 as the atmospheric calibrator. As shown in this figure, the choice of 3C111 as the atmospheric calibrator is particularly fortuitous for PP 13S\* since the science and reference beams for most antennas nearly cross within the turbulent zone.

Using phase closure ([Jennison, 1958](#)), the difference ( $\Delta\tau$ ) between the actual delay for the target beams  $A'_1 - A'_2$  and the atmospheric reference beams  $A'_3 - A'_4$  is given by  $\Delta\tau = \tau(A'_1 - A'_2) - \tau(A'_3 - A'_4) = \tau(A'_1 - A'_3) - \tau(A'_2 - A'_4)$ . In a favorable configuration, the beam separations  $A'_1 - A'_3$  and  $A'_2 - A'_4$  will be much less than either the target beam separation  $A'_1 - A'_2$  or the reference beam separation  $A'_3 - A'_4$ . The RMS of the corrected visibilities will be  $\sqrt{2}$  worse than for an array with beam separation  $A'_1 - A'_3$ , which implies that C-PACS will have a performance equivalent to an array that has baseline lengths  $\sim 20-$

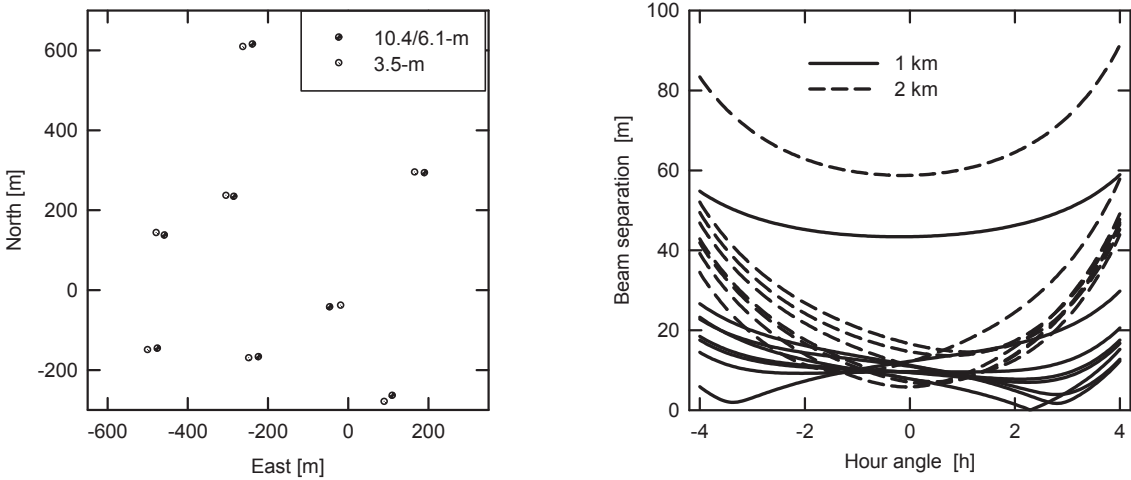


**Figure 3.2:** The left panel shows the locations of the science (10.1 m and 6.4 m) and reference (3.5 m) antennas in the B-configuration of CARMA (circles do not represent the actual antenna diameters). The right panel shows the separation,  $b_{\text{eff}}$ , between the science and reference beams in the turbulent layer for each pair of antennas during the PP 13S\* observations. The continuous (dashed) line corresponds to a turbulent layer at a 1(2) km altitude. For most pairs the configuration is very favorable, giving rise to effective baselines much shorter than the science baseline.

70% larger than the  $A'_1 - A'_3$  beam separation, depending on the structure function exponent. The complete analysis contains additional correlation terms and added uncertainties caused by the finite signal-to-noise for the atmospheric calibrator observations.

### 3.2.4 Atmospheric calibrators

The ability of C-PACS to correct the atmospheric delays is limited by the delays from the short beam spacings  $A'_1 - A'_3$  and  $A'_2 - A'_4$  (see Figure 3.1), instrumental phase drifts on the reference array, and the radiometer noise. The delay errors caused by differences in the beam spacings between the science and reference arrays are given statistically by the structure function  $R(|A'_i - A'_j|)$ . The instrumental errors can be removed by removing a box-car average over the length of the observation, and will contribute negligible delay errors as long as the timescale for the instrumental drifts are large compared to the box-car width. The delay errors due to radiometric phase noise depend on the strength of the source being observed, the receiver properties, and the atmospheric characteristics ([Thompson et al. 2010](#))

al., 2001). The uncertainty in the measured phase from radiometer noise is given by

$$\Delta\phi = \frac{\sqrt{2}k_B T_{\text{sys}}}{\eta_Q A_{\text{eff}} S \sqrt{Bt}} \quad (3.2)$$

where  $k_B$  is the Boltzmann's constant,  $T_{\text{sys}}$  is the system temperature,  $\eta_Q$  is the correlator quantization efficiency,  $A_{\text{eff}}$  is the effective collecting area of the antennas,  $S$  is the flux density of the atmospheric calibrator,  $B$  is the bandwidth of the observations, and  $t$  is the integration time. The measurement uncertainty in the delay is then  $\Delta\phi/(2\pi\nu)$ . The net variance in the delay after applying C-PACS is given by

$$\Delta\tau^2 \approx R(|A'_1 - A'_3|) + R(|A'_2 - A'_4|) + \left( \frac{k_B T_{\text{sys}}}{\eta_Q A_{\text{eff}} S \pi \nu \sqrt{2Bt}} \right)^2 \quad (3.3)$$

The structure function is generally described by a power law with exponents varying from 5/3 to 2/3 depending upon the spacing and thickness of the turbulent layer. The scaling coefficient of the power law also varies depending upon the weather conditions. In order for C-PACS to improve the image quality, the target and reference beams must be close at the turbulent layer such that  $R(|A'_1 - A'_3|) + R(|A'_2 - A'_4|) \ll \lambda^2$ . This requires angular separations  $\lesssim 5^\circ$  for the A and B configuration C-PACS pairings and typical winter weather conditions at the CARMA site. A future publication will use actual measurements to quantify how the quality of the C-PACS correction varies with angular separation between the science target and the atmospheric calibrator (Zauderer et al., in preparation).

The radiometer noise should also contribute much less than a wavelength of delay error for the C-PACS corrections to be successful. For the characteristics of the 3.5 m telescopes and the 1 cm receivers, the radiometer delay error is given by

$$\Delta\tau_{\text{radiometer}} = 1.3 \text{ mm} \left( \frac{S_\nu}{1 \text{ Jy}} \right)^{-1} \left( \frac{t}{1 \text{ s}} \right)^{-1/2} \quad (3.4)$$

Thus, 1.3 mm observations with integration times of  $t = 4$  s (short enough to measure and correct most of the atmosphere fluctuations) require a reference source brighter than  $S \sim 1$  Jy in the 1 cm band. When several atmospheric calibrators are available, the optimum choice between calibrator separation and brightness can be found by minimizing Equation 3.3 for the expected weather conditions.

We combined the SZA 30 GHz calibrator list, the GBT catalog at 1.4 and 5.0 GHz (Condon & Yin, 2001), and the WMAP point source catalog (Wright et al., 2009) to estimate the density of potential C-PACS calibrators. For each source in the GBT catalog, we extrapolated the flux density from 5.0 GHz to 30 GHz by measuring the spectral index  $\alpha$  between 1.4 and 5.0 GHz ( $S_\nu \propto \nu^\alpha$ ). We find that 50% of the sky is within  $5^\circ$  of a point source with flux density greater than 1 Jy at 30 GHz. The number of suitable C-PACS calibrators could be expanded by increasing the sensitivity of the reference array, which would allow us to employ fainter atmospheric calibrators. This could be accomplished by increasing the correlator bandwidth or improving the receiver sensitivity.

### 3.3 Observations and Data Reduction

PP 13S\* is particularly well suited for C-PACS observations since the nearest atmospheric calibrator (3C111) is bright ( $\sim 4$  Jy at 1.3 mm at the time of the observations) and separated by  $1.5^\circ$  from PP 13S\*. Thus the calibrator satisfies the basic criteria needed for successful C-PACS corrections (see Section 3.2.4). In this section, we describe the CARMA observations and data reduction of PP 13S\*.

#### 3.3.1 CARMA 1.3 mm wavelength observations

The 6 m and 10 m antennas were used to obtain 1.3 mm continuum observations of PP 13S\* on UT Dec 5, 2008, in the CARMA B configuration and on UT Jan 18, 2009 in the CARMA A configuration. Double-sideband receivers mounted on each antenna were tuned to a rest frequency of 227 GHz placed in the upper sideband. The correlator was configured with three 468.75-MHz-wide bands to provide 1.41 GHz of continuum bandwidth per sideband. The observing sequence interleaved 3 min observations of 3C111 with 12 min observations of PP 13S\* in B configuration and 4 min in A configuration. The complex visibilities were recorded every 4 s.

Data reduction was performed using the Multichannel Image Reconstruction, Image Analysis and Display (MIRIAD) software package (Sault et al., 1995). Each night of observations was calibrated separately. The calibration consisted of first applying a line-length correction<sup>2</sup> and then a passband correction derived from observations of 3C111. Only these

---

<sup>2</sup>The CARMA line-length system measures the total round trip delay caused by possible mechanical

two calibrations were applied to the millimeter data before proceeding with the C-PACS corrections (see Section 3.3.3). All images that are presented here were formed by inverting the visibility data using natural weighting, and then “cleaning” with the point-spread function (i.e., the “dirty” beam) using a hybrid Högbom/Clark/Steer algorithm ([Högbom, 1974](#); [Clark, 1980](#); [Steer, Dewdney, & Ito, 1984](#)).

### 3.3.2 CARMA 1 cm wavelength observations

The eight 3.5 m antennas were used to obtain 1 cm observations of the atmospheric calibrator simultaneously with the 1.3 mm wavelength observations. Single-sideband receivers mounted on each antenna were tuned to a sky center frequency of 30.4 GHz. For these antennas, a wideband correlator is available that was configured with fourteen 500-MHz-wide bands to provide 7 GHz of continuum bandwidth. Complex visibilities were recorded every 4 s in order to track the rapidly varying atmospheric fluctuations. Single-sideband system temperatures for the 1 cm observations ranged between 35 and 55 K.

The data calibration consisted of applying a time-dependent passband measured from an electronically correlated noise source that was observed every 60 s. This passband was computed and applied on a 60 s timescale to remove any delay variations in the digitizers due to temperature cycling of the air-conditioning that cools the correlator. A passband correction derived from observations of 3C111 was then applied.

### 3.3.3 Applying 1 cm delays to the 1.3 mm data

Phase referencing would normally be performed at this point in the data reduction process to remove the slowly varying phase drift introduced by the instrument. However, a phase calibration computed over a long time interval, and prior to correcting for the “fast” atmospheric delay fluctuations will alias the fast component into a slowly varying error on the phase calibration ([Lay, 1997b](#)). C-PACS can reduce the errors introduced from standard phase calibration techniques by correcting for both fast and slow atmospheric delay fluctuations.

The delays were extracted from the 1 cm wavelength observations of the atmospheric calibrator, and then applied to each corresponding paired baseline in the science array. Only

---

effects and temperature variations of the fiber-optic cables running to each antenna.

eight of the 15 antennas from the science array, those paired with a reference antenna, have the C-PACS correction applied. The delay derived from the reference array is applied to the science target (PP 13S\*) and phase calibrator (3C111) on each record. The delays were computed from the mean phase across all channels in the 1 cm observations divided by the mean frequency. The observed wavelength of 1 cm used for the reference array is longer than the typical atmospheric delay fluctuations, and delay tracking through phase wraps was not a problem.

The atmospheric delays derived from the 1 cm data were applied directly to the 1.3 mm data without any corrections for differences in the observed frequency. This is possible since the dispersion in refractivity of water vapor between centimeter and millimeter wavelengths is less than a few percent ([Hill, 1988](#)) away from the strong atmospheric emission lines, and ionospheric effects are negligible at these frequencies ([Hales et al., 2003](#)). The minimal dispersion of the refractivity has also been verified experimentally from the C-PACS observations (see Section [3.4.1](#)). After applying the delay corrections to the 1.3 mm data on 4 s intervals, a long-interval (10 min) phase calibration is applied to the 1.3 mm data to remove the slow varying instrumental delay difference from the two different arrays.

## 3.4 Application of C-PACS

The effect of the C-PACS on the calibrated phases can be analyzed in several stages. We first compare the phase fluctuations measured toward 3C111 at wavelengths of 1 cm and 1.3 mm to demonstrate that the reference and science arrays are tracing the same atmospheric fluctuations. We then demonstrate that C-PACS yields quantitative improvement in the quality of the PP 13S\* star image. Throughout this section, no absolute flux scale or amplitude calibration are applied to the data in order to evaluate how C-PACS improves the phase stability on the phase calibrator (Section [3.4.1](#)) and PP 13S\* (Section [3.4.2](#)).

### 3.4.1 3C111

Figure [3.3](#) shows the measured fringe phase toward 3C111 for one paired baseline in the B configuration to illustrate the correlation that exists between the phases measured at wavelengths of 1.3 mm and 1 cm. For this figure, the phases measured on the reference

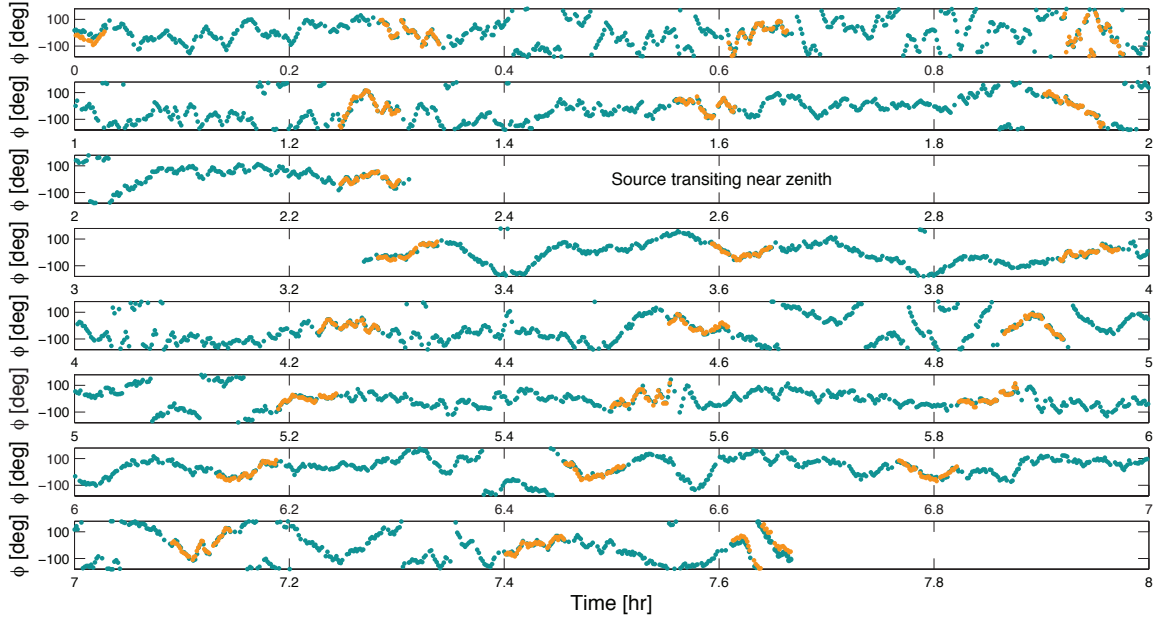


**Figure 3.3:** Visibility phase versus time for the science array (orange) and the reference array (green) measured toward 3C111 on a baseline of length  $\sim 800$  m in B configuration. The phase measured by the reference array at a frequency of 30.4 GHz was scaled to the frequency of the science array (227 GHz) by a factor of 7.5 ( $= 227 \text{ GHz} / 30.4 \text{ GHz}$ ). Each data point indicates the measured phase over a 4 s integration after removing the mean phase computed in 10 min intervals. About 1 h of data are omitted near the middle of the observation when PP 13S\* and 3C111 were transiting at an elevation  $> 80^\circ$  and the tracking of the antennas was poor. The figure demonstrates that the observed phases at 30.4 GHz closely track the phases measured at 227 GHz and can be used to correct the atmospheric fluctuations at higher frequencies.

array were scaled by the ratio of the observed frequencies (227 GHz / 30.4 GHz = 7.5). The correlation between the 1 cm and 1.3 mm phases is evident over the nearly 8 h time period and is present for all paired baselines. In addition, the phases are tracked between the two arrays even though the science array is switching between two sources. These results demonstrate that (1) the 1 cm phases can be used to track the delay fluctuations at higher frequencies, (2) the atmosphere is non-dispersive at these wavelengths such that a linear scale with frequency can be used to predict the phases fluctuations at other wavelengths, and (3) C-PACS can correct the science observations while preserving the link to the phase calibrator observations in the science array.

The observed phases at 227 GHz toward 3C111 on all paired baselines in the A and

B configurations are shown as a function of *uv*-distance<sup>3</sup> in Figure 3.4. The upper panels show the visibility phases measured in 4 s integrations before applying C-PACS corrections, and the middle panels show the visibility phases after applying the corrections. The RMS scatter on the visibility phase before correction is between  $33^\circ$  (at short *uv*-distances) and  $53^\circ$  (at long *uv*-distances) for B configuration and between  $26^\circ$  and  $48^\circ$  for A configuration. After applying the C-PACS correction, the phase scatter is reduced to  $15\text{--}18^\circ$  for correction across all *uv*-distances in both configurations.

Another way to grasp the effect of the C-PACS corrections can be seen on the bottom panels in Figure 3.4, where the coherence value ( $e^{-\phi_{\text{RMS}}^2/2}$ ) is measured over *uv*-distance bins of width  $130 \text{ k}\lambda$ . Before applying the C-PACS corrections, the coherence decreases with increasing baseline length since the longer baselines have larger atmospheric fluctuations.

---

<sup>3</sup>The *uv*-distance is the baseline distance projected perpendicular to the line of sight.

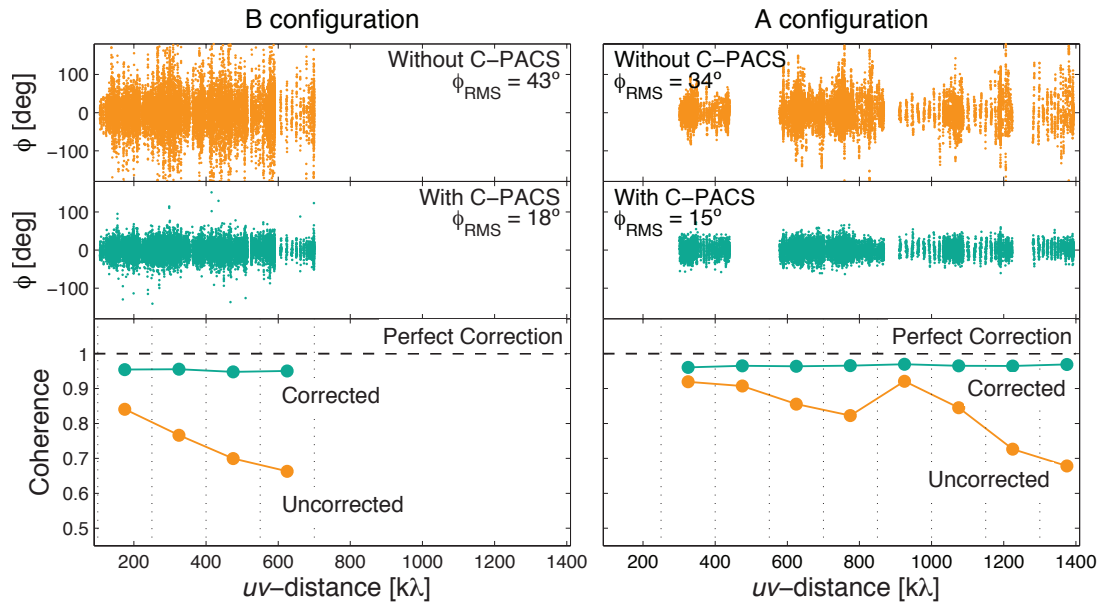


**Figure 3.4:** Visibility phases versus *uv*-distance on all paired baselines for observations of 3C111 in the CARMA B and A configurations. The phases are shown before (top panels) and after (middle panels) applying C-PACS corrections. Each point indicates the measured phase in a 4 s integration after removing the mean phase computed in 10 min intervals. The bottom panels show the coherence calculated over  $130 \text{ k}\lambda$  intervals. Before applying C-PACS, the coherence declines with *uv*-distance as expected for atmospheric phase fluctuations that increase with baseline length. After applying C-PACS, the phase coherence is higher and uniform with baseline length.

After applying the C-PACS corrections, the coherence is uniform with baseline length at a value of  $\sim 95\%$ . The coherence becomes nearly constant with baseline length since C-PACS converts the 200–1800 m baselines into  $\sim 30$ –50 m effective baselines for all paired antennas. While the results shown in Figure 3.4 emphasize the improvement in coherence, C-PACS also improves the visibility phases, which results in higher image fidelity.

### 3.4.2 PP 13S\*

After applying the C-PACS atmospheric delay corrections to the 1.3 mm data, we removed the instrumental delay drifts by phase referencing to the 3C111 observations. Figure 3.5 shows the resulting maps before and after applying the C-PACS corrections for the A and B configurations separately and the combined data sets.

C-PACS improved the image quality for both the A and B configuration maps as measured by the increase in the peak flux, the reduction in the noise level, and the decrease in the observed source size. The improved image quality resulted from correcting the phase fluctuations in the 1.3 mm data. The increase in the source flux and decrease in source size is also illustrated in Figure 3.6, which shows radial profile plots across the 1.3 mm emission toward PP 13S\* along right ascension and declination. In the combined A+B configuration map, the peak flux measured toward PP 13S\* increased from 42.4 mJy to 67.8 mJy (a factor of 1.6) after applying the C-PACS correction. The noise level decreased from  $\sigma = 1.5$  mJy/beam to  $\sigma = 1.1$  mJy/beam, which corresponds to a 36% improvement. The observed full-width-at-half-maximum (FWHM) source size diminished from  $0.41'' \times 0.27''$  to  $0.27'' \times 0.26''$ , or a 52% decrease in the size of the major axis of the 1.3 mm emission.

## 3.5 Properties of the PP 13S\* Circumstellar Disk

Before proceeding to analyze the properties of the dust surrounding PP 13S\*, we must flux calibrate the C-PACS data. The absolute flux calibration was set from observations of Uranus in B configuration and 3C84 in A configuration. The flux density of Uranus was inferred from a planet model, while the flux density of 3C84 was obtained from CARMA observations on a different day when both 3C84 and Uranus were observed. The uncertainty on this calibration is estimated to be 20% due to uncertainties in the planetary model and the

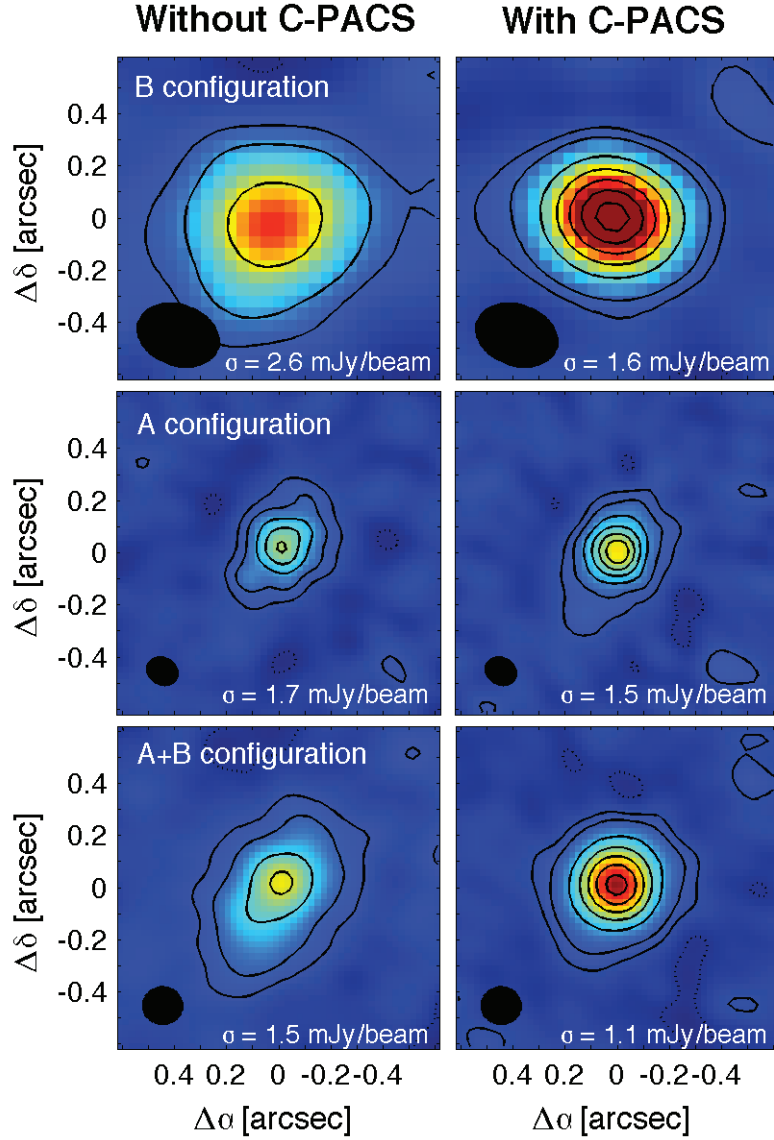


**Figure 3.5:** CARMA 227 GHz continuum images of PP 13S\* before (left) and after (right) C-PACS corrections for data obtained in B configuration (top), A configuration (middle), and B and A configurations combined (bottom). No absolute flux scale or amplitude gain calibration have been applied to the data in order to assess the effect of atmospheric phase corrections only. The color scale range is same for all maps (from -2.4 to 54.8 mJy) such that the measured fluxes can be compared directly. Solid contours are at  $2\sigma$ ,  $5\sigma$  and in increments of  $5\sigma$  thereafter. Dotted contour is at  $-2\sigma$ . For both B and A configurations, applying the C-PACS correction increased the observed peak flux and reduced the observed source size.

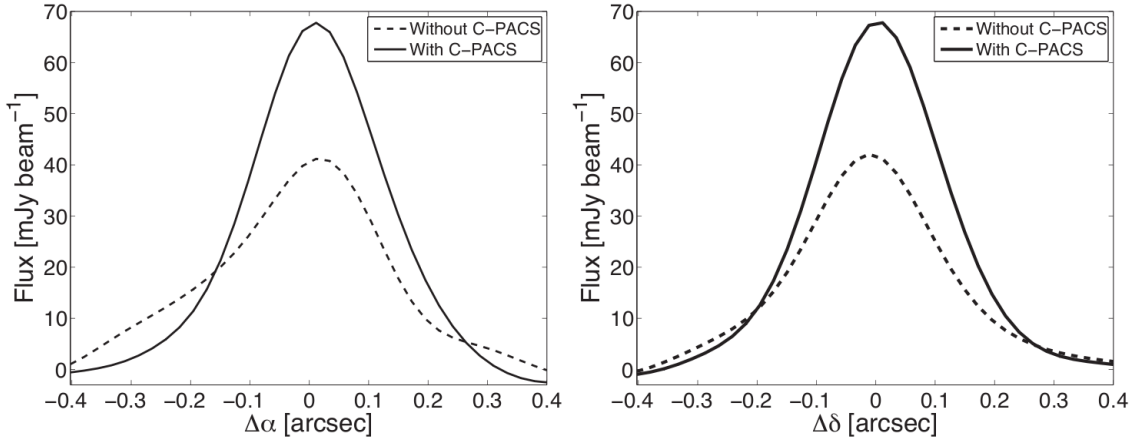


**Figure 3.6:** Observed flux density toward PP 13S\* versus offset in right ascension (left) and declination (right) before and after applying C-PACS corrections. Applying C-PACS corrections increased the peak flux density and decrease the observed source size.

bootstrapped flux for 3C84. The antenna gains as a function of time were then determined from the 3C111 observations.

Figure 3.7 shows the calibrated visibility amplitude observed toward PP 13S\* as a function of baseline length. An unresolved source will have a constant flux density with baseline length. By contrast, the visibility amplitude toward PP 13S\* decreases with increasing baseline length, which suggests that the source is resolved. While the decline in amplitude with baseline length could be explained by a coherence as low as  $\sim 0.2$  on  $\gtrsim 1$  km baselines, the minimum measured coherence on 3C111 at any *uv*-distance was 0.65 even before applying the C-PACS correction (see Figure 3.4). A similar decline in the visibility amplitude for PP 13S\* with baseline length can be seen as well when only a fraction of the data are averaged together (for example, using 1 h of data at a time), indicating that atmospheric decorrelation over long timescales is not giving rise to the amplitude drop at long baselines. Thus, the primary cause of the decrease in amplitudes with increasing baseline length is that the source is resolved.

The FWHM of the 1.3 mm continuum emission toward PP 13S\* is  $0.22'' \times 0.21''$ , which was obtained by fitting a two-dimensional Gaussian to the surface brightness distribution in the combined A+B configuration image after applying the C-PACS corrections and deconvolving the synthesized FWHM beam size of  $0.15'' \times 0.14''$ . The integrated flux density of

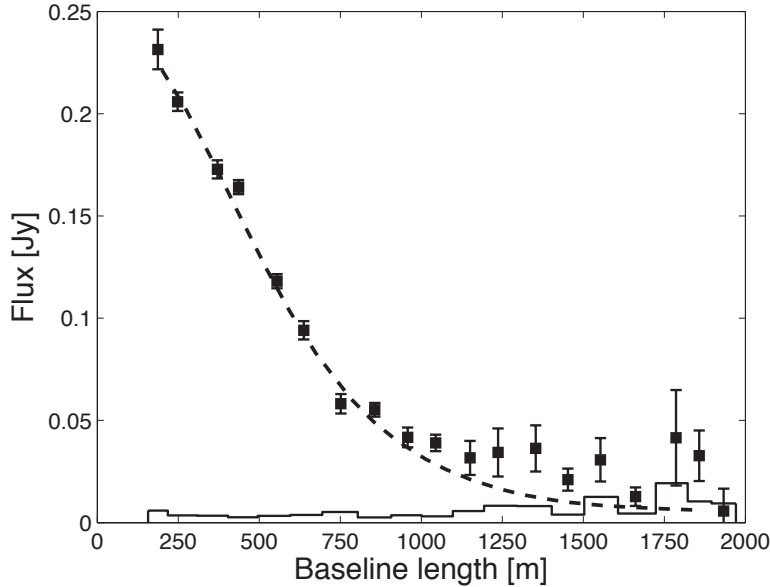


**Figure 3.7:** Observed visibility amplitudes toward PP 13S\* after applying the C-PACS corrections (black points) versus the deprojected baseline length. The errorbars indicate the  $1\sigma$  interval uncertainties, but exclude uncertainties in the flux calibration ( $\sim 20\%$ ). The histogram shows the expected signal for random noise. The dashed line shows the best-fit disk model (see text) to the visibility data. The clear decline in the visibility amplitude with baseline length indicates the dust emission around PP 13S\* has been resolved.

PP 13S\* in the C-PACS corrected image after flux and amplitude calibration is  $241 \pm 48$  mJy, measured by integrating over an aperture of radius  $R_{disk} \sim 1.4 \times \text{FWHM} \sim 0.36''$ , where  $R_{disk}$  is defined to encompass 95% of the emission. The flux observed with CARMA corresponds to about half of the emission measured by single-dish observations (450 mJy at 1.3 mm with a beam size of  $19.5''$  [Sandell & Aspin, 1998](#)). The remaining 1.3 mm flux is presumably contained in an extended envelope larger than  $1.6''$ , which is the largest angular scale probed by the CARMA data.

The presence of a circumstellar disk in PP 13S\* has been previously inferred from several lines of evidence: (i) reflected light along the outflow axis is observed despite the fact that the central object is heavily obscured in the optical ( $A_V \sim 30 - 50$ ; [Cohen et al., 1983](#)), which indicates that the circumstellar material is not spherically symmetric; (ii) infrared absorption bands at  $3 \mu\text{m}$  and  $10 \mu\text{m}$  indicate substantial quantities of cold dust, probably present in an obscured inclined disk ([Cohen et al., 1983; Smith, 1993](#)); and

(iii) the broad  $2.2 \mu\text{m}$  CO overtone absorption feature present in the PP 13S\* spectra (Sandell & Aspin, 1998; Aspin & Sandell, 2001) can be explained by the presence of a massive accreting circumstellar disk (Hartmann & Kenyon, 1996). Nonetheless, without observations of the gas kinematics, we cannot determine if the dust emission detected by CARMA originates from the central cusp of an envelope or from the circumstellar disk that surrounds PP 13S\*. Since the presence of a massive accretion disk has been invoked to explain several characteristics of FU-Orionis objects, we assume that the millimeter continuum emission around PP 13S\* observed by CARMA originates primarily from a circumstellar disk.

To determine the disk properties, we assumed the radial surface density  $[\Sigma(R)]$  can be described by the similarity solution for a viscous accretion disk given by

$$\Sigma(R, t) = \Sigma_t \left( \frac{R_t}{R} \right)^\gamma \exp \left[ -\frac{1}{2(2-\gamma)} \left[ \left( \frac{R}{R_t} \right)^{2-\gamma} - 1 \right] \right], \quad (3.5)$$

where  $\gamma$  is the slope of the disk viscosity ( $\nu(R) \propto R^\gamma$ ), and  $\Sigma_t$  is the surface density at  $R_t$  (Isella et al., 2009). The transition radius is the radius at which the mass flow is zero, such that for  $R < R_t$  the mass flow goes inward and mass is accreted into the disk, and for  $R > R_t$  the mass flow goes outwards as the disk expands to conserve angular momentum.

We assume that the central star has a bolometric luminosity of  $L_{bol} = 30 L_\odot$  (Cohen et al., 1983) and a mass of  $M_* = 1 M_\odot$ . The dust opacity, assumed to be constant throughout the disk, is calculated using compact non-porous spherical grains with fractional abundances from Pollack et al. (1994): 12% silicates, 27% carbonaceous materials and 61% ices. The grain-size distribution is assumed to be a power law ( $n(a) \propto a^{-q}$ ), with slope  $q = 3.5$  and minimum grain size  $a_{min} = 0.05 \mu\text{m}$ . We adopt a dust emissivity index of  $\beta = 1.23$  (derived from a gray-body fit to the spectral energy distribution; Sandell & Aspin, 1998), and a dust-to-gas ratio of 0.01. For these assumed parameters, the implied maximum grain size of the distribution is  $a_{max} = 0.1 \text{ cm}$  and the mass opacity corresponds to  $\kappa_\nu = 0.1 \text{ cm}^2 \text{ g}^{-1}$  at 1.3 mm.

The dust surface density defined in Equation 3.5 was fitted to the observed visibilities using the procedure described in Isella et al. (2009). Figure 3.7 compares the observed and modeled visibility profile for PP 13S\*. The model provides a reasonable fit to the data,

although the observed visibility amplitudes are larger than the model for baselines longer than  $\sim 1$  km. A map of the model was created and subtracted from the observed PP 13S\* map, but no significant residuals ( $> 3\sigma$ ) were found.

The best fit disk model has a disk inclination of  $15^\circ$  (where  $90^\circ$  is defined as an edge-on disk),  $R_t = 13$  AU,  $\Sigma_t = 145 \text{ g cm}^{-2}$ ,  $\gamma = 0.95$ ,  $M_{\text{disk}} = 0.06 M_\odot$ , and  $R_{\text{disk}} = 128$  AU. The mass estimate is larger than the median mass of a Class II circumstellar disk (Andrews & Williams, 2005), and is in agreement with the measured masses around other FU-Orionis objects. For example, Sandell & Weintraub (2001) estimated circumstellar masses (disk and envelope) between  $0.02 M_\odot$  to a few solar masses for a sample of 16 FU-Orionis objects.

Figure 3.8 shows the surface density distribution ( $\Sigma$ ) and the optical depth ( $\tau$ ) as a function of the disk radius. The vertical line marks the separation between the optically thin and thick regimes. We find that the disk becomes optically thick inwards of  $\sim 48$  AU given the assumptions in the model. We caution that the surface density distribution

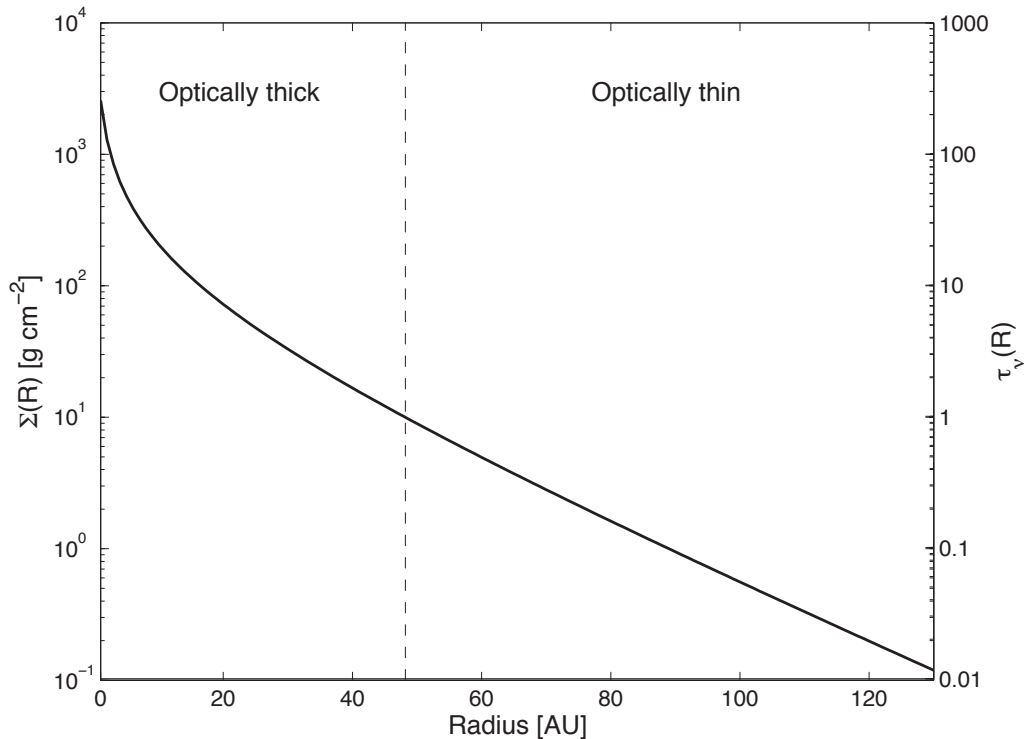


**Figure 3.8:** Model surface density distribution of PP 13S\* as a function of disk radius. The disk optical depth ( $\tau = \Sigma_d(R) \times \kappa_{1.3mm}$ ) was computed assuming a constant dust opacity throughout the disk. The inner region of the disk ( $R < 48$  AU) becomes optically thick at a frequency of 227 GHz.

within this region is poorly constrained not only because of the high optical depth, but because the disk is unresolved for a radius less than 26 AU. The radius where the dust becomes optically thick is large compared to what is found in disks around classical T Tauri stars, where only the inner few astronomical units are opaque at such long wavelengths. Furthermore, the transition radius we find for PP 13S\* is smaller than any of the pre-main sequence circumstellar disks studied by [Isella et al. \(2009\)](#). Thus the circumstellar disk of PP 13S\* is more concentrated than the disks around classical T Tauri stars.

Gravitational instabilities in the disk might be responsible for the enhanced accretion episodes seen in FU-Orionis objects ([Armitage et al., 2001](#)). To investigate if the disk around PP 13S\* is gravitationally unstable, we computed the Toomre's  $Q$  parameter:

$$Q = \frac{c_s \kappa}{\pi G \Sigma(R)}, \quad (3.6)$$

where  $c_s$  is the sound speed and  $\kappa$  is the epicyclic frequency (which is equal to the angular velocity for a Keplerian disk). A disk becomes gravitationally unstable if  $Q \lesssim 1.5$ , as spiral waves develop and mass is transported inwards and momentum is transported outwards ([Lodato & Rice, 2004](#)).

As shown in Figure 3.9, the PP 13\* disk is gravitationally stable to axisymmetric perturbations across all radii for the inferred surface density. The disk surface density would need to be increased by more than an order of magnitude (see dashed line of Figure 3.9) for the disk to develop a gravitational instability. The inferred disk surface density can vary widely depending on the adopted dust properties, as composition, grain-size distribution ( $q$ ,  $a_{min}$ ,  $a_{max}$ ), emissivity index ( $\beta$ ) and dust-to-gas ratio, all affect the resulting opacity. For example,  $\kappa_\nu$  diminishes by 20–30% if ices are ignored from the dust composition, increasing the surface density by the same percentage. Also, flattening the grain-size distribution slope to  $q = 3.0$  gives a 30% increase in the disk mass. Furthermore, we adopted a fixed power law ( $\beta$ ) of the dust opacity law. If  $\beta$  decreases toward the center of the system (as observed in Class 0 sources; [Kwon et al., 2009](#)) we can expect to have larger grains in the circumstellar disk that will reduce the mass opacity and increase the surface density. Despite the uncertainties in the dust properties, it will be difficult to increase the surface density by more than an order of magnitude at a radius  $> 48$  AU where the disk is optically thin, unless the dust properties of PP 13S\* are extraordinarily different from what is found in

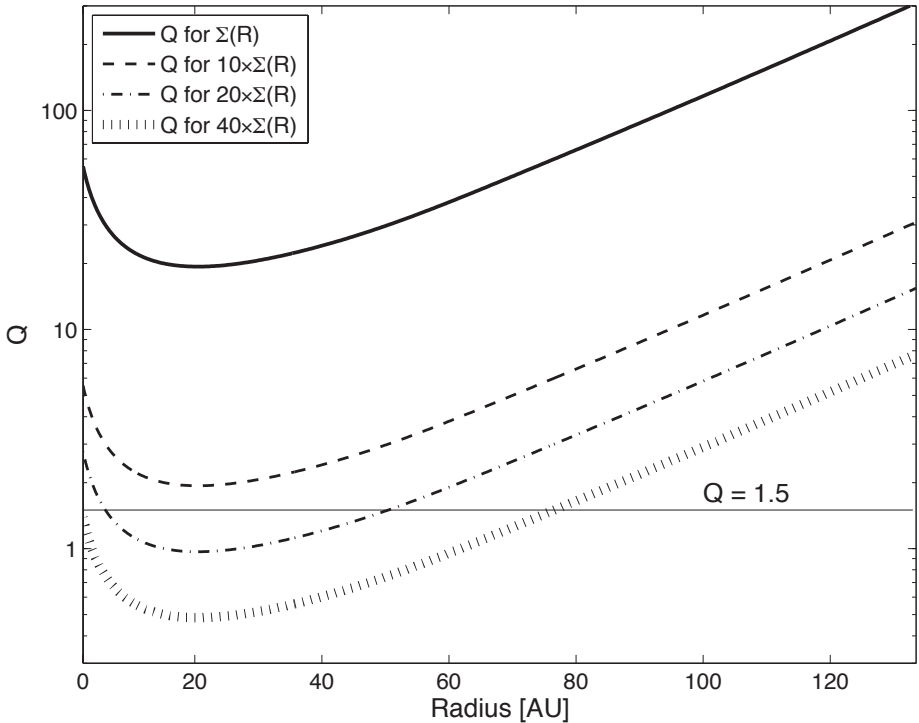


**Figure 3.9:** Toomre’s instability parameter,  $Q$ , plotted for the PP 13S\* disk. The solid line shows the  $Q$  values for the nominal disk model. Dust opacities that are 10, 20 and 40 times larger than the adopted opacities are shown by the dashed, dash-dotted, and vertical-dashed curves, respectively. The  $Q = 1.5$  limit is shown for reference, such that regions with  $Q \lesssim 1.5$  may become gravitational unstable. The disk surface density needs to be an order of magnitude higher than the nominal model in order to form instabilities in the disk.

typical disks ([Andrews & Williams, 2007a,b](#); [Isella et al., 2009](#)).

### 3.6 Conclusions

We have described C-PACS, which uses paired antennas as a means to calibrate the atmospheric phase fluctuations on long interferometric baselines. Specifically, while the 6 and 10 m CARMA antennas observe a science source in the 3 mm or 1 mm atmospheric windows, the 3.5 m CARMA antennas simultaneously observe a nearby atmospheric calibrator in the 1 cm band. The 3.5 m antennas are placed within 30 m of the larger antennas to sample similar atmospheric delay fluctuations. We have applied the calibration technique to

CARMA observations of the circumstellar material around the FU Orionis object PP 13S\*. C-PACS yields quantitative improvement in the image quality of PP 13S\*: the observed peak flux increased by a factor of 1.6, the image noise level decreased by 36%, and the FWHM of the major axis decreased by 52%.

The improvement in the phase error and amplitude coherence provided by the paired antennas technique is a function of the projected beam separation of the antenna pairs at the height of the turbulent layer, and the radiometric noise introduced from the reference array to the science array. Thus, the brightness of the atmospheric calibrator and the angular separation between the atmospheric calibrator and the science target are the main restrictions to the application of this technique for general science observations. Our current estimate requires a calibrator closer than  $5^\circ$  to the science target and brighter than 1 Jy at 30 GHz to correct 1.3 mm observations. Based on existing radio catalogs, we estimate that there are 420 sources that have  $S_\nu > 1$  Jy, such that 50% of the sky can be observed with a suitable calibrator.

With C-PACS, we have obtained  $0.15''$  resolution images of the circumstellar material around PP 13S\* at an observing frequency of 227 GHz. We measure an integrated flux density of 241 mJy at 227 GHz, which is about half of the extended emission detected in a  $19.5''$  beam ([Sandell & Aspin, 1998](#)). We constrain the surface density profile of PP 13S\* using a self-consistent disk model. The main difference in the inferred disk properties compared to disks around other pre-main sequence circumstellar disks is that the dust is more centrally concentrated and there is a larger region that is optically thick at millimeter wavelengths. From analysis of the Toomre  $Q$  parameter, we find that the disk is gravitationally stable over all disk radii unless the disk surface density is underestimated by an order of magnitude or more.

## Acknowledgments

Support for CARMA construction was derived from the Gordon and Betty Moore Foundation, the Kenneth T. and Eileen L. Norris Foundation, the James S. McDonnell Foundation, the Associates of the California Institute of Technology, the University of Chicago, the states of California, Illinois, and Maryland, and the National Science Foundation. Ongoing CARMA development and operations are supported by the National Science Foundation

under a cooperative agreement (grant AST 08-38260), and by the CARMA partner universities. LMP acknowledges support for graduate studies through a Fulbright-CONICYT scholarship. SM gratefully acknowledges support from an NSF Astronomy and Astrophysics Fellowship.

## Chapter 4

# Modeling Circumstellar Disk Observations

To determine the physical conditions inside a protoplanetary disk, one would like to constrain the spatial distribution and temperature of the gas and dust components of the disk, as well as the velocity and magnetic field structure inside it. As explained in Chapter 2, I have gathered continuum observations at multiple millimeter and centimeter wavelengths of several circumstellar disks. With such observations, a model of the disk dust component can be constructed in order to infer its temperature, spatial distribution, and grain growth (the gas component is an exciting line of research, but high sensitivity at high spectral resolution—since lines are few  $\text{km s}^{-1}$  broad—is required to make further progress in this area).

This chapter has three goals: first, explain how radio-wave observations of circumstellar disks can be reproduced using physical models of disk emission (Sections 4.1 and 4.2); second, explain how the parameters that go into these models are constrained, using the tools provided by Bayesian statistics analysis (Section 4.3); and third, describe how radial variations in the dust opacity profile can be inferred and constrained (Section 4.4).

### 4.1 Modeling the Unresolved SED

The presence of circumstellar disks was first inferred by looking at the unresolved spectral energy distribution of nearby young stars ([Mendoza V., 1966](#)). At infrared wavelengths, the unresolved photometry of many young stars shows an excess of emission that is orders of magnitude brighter than the expected emission of the central star. It is currently known that this excess arises from the thermal re-emission of starlight absorbed by dust grains

in the disk. Follow up resolved imaging showed that in fact most stars with this infrared excess harbor a circumstellar disk (Sargent & Beckwith, 1987; O’dell & Wen, 1994). Hence, excess emission in an unresolved SED can readily tell us about the presence of a disk; this has now become a critical selection method to detect circumstellar disks.

The SED of a circumstellar disk can be computed as the sum of the local disk radiation at each annulus of width  $dR$ . In the simple case of an axisymmetric, vertically isothermal ( $T(R, z) = T(R)$ ), and thin disk, the observed SED is given by:

$$F_\nu = \frac{\cos i}{D^2} \int_{R_{in}}^{R_{out}} 2\pi R B_\nu(T_d(R))(1 - e^{-\tau_\nu(R)})dR \quad (4.1)$$

where  $i$  is the disk inclination ( $i = 0$  for a face-on disk),  $D$  corresponds to the distance to the system,  $R_{in}$  and  $R_{out}$  are the disk’s inner and outer radius,  $R$  is the cylindrical distance from the star to a position in the disk,  $B_\nu(T_d)$  is the Planck function evaluated at the disk temperature  $T_d$ , and  $\tau_\nu$  corresponds to the disk’s optical depth. Note that  $\tau_\nu(R) = \tau_\nu^\perp(R)/\cos i$ , where  $\tau_\nu^\perp$  is the vertical optical depth of the disk. This quantity is linearly related to the disk’s opacity per unit mass,  $\kappa_\nu$ , and to the mass surface density of disk material,  $\Sigma$ , ( $\tau_\nu^\perp(R) = \kappa_\nu \Sigma(R)$ ). Then, with a knowledge of the opacity source in a circumstellar disk, one could constrain the disk geometry and the disk structure (i.e.,  $T(R)$ ,  $\Sigma(R)$ ,  $i$ ,  $R_{in}$ ,  $R_{out}$ ) from modeling the SED.

Given reasonable physical conditions inside a protoplanetary disk, the dominant source of opacity is dust since dust grains are able to absorb radiation much more efficiently than gas particles. The gas component of the disk (ions, atoms, molecules and electrons) is the main source of opacity only in the innermost disk regions, where the temperatures are large enough to sublimate dust grains ( $T \gtrsim 1500$  K).

Armed with a knowledge of the SED for a star + disk system, going from the optical to millimeter and centimeter wavelengths, many authors (starting with Beckwith et al., 1990) have inferred the structure of circumstellar disks assuming a simple prescription for  $T_d(R)$  and  $\Sigma(R)$ , as well as a constant dust opacity  $\kappa_\nu$  throughout the disk. A significantly better fit to the observed flatter infrared SED of Class I and Class II YSOs can be obtained if instead of a thin disk, a flared disk geometry, where the disk opening angle increases with radius, is adopted. In such configuration, the star illuminates and heats the disk’s photosphere more efficiently. This energy is then thermally re-radiated by the photosphere, heating

up the highly optically thick and cold inner regions of the disk. A flared disk geometry yields stronger and flatter IR excesses, which reproduces the SED features of Class I and Class II stars (Kenyon & Hartmann, 1987). Note also that a flared disk configuration arises naturally from hydrostatic equilibrium, for a disk that is vertically isothermal and with a temperature profile that goes as  $T(R) \propto R^{-1}$  or shallower (see Section 4.2.1.1).

The ingredients that go into the SED modeling include the emission from the disk given its structure (flared or thin, degree of flaring, disk geometry, theoretical prescriptions for  $T(R)$ ,  $\Sigma(R)$ ), the stellar emission (characterized by  $L_*$ ,  $T_*$ ,  $R_*$  and its distance to us), the dust properties in order to properly model SED features (e.g., the 10  $\mu m$  Silicate feature), and any contribution from an envelope that might absorb or scatter the stellar and disk radiation. In general, SEDs for “star+disk” systems can be well reproduced, however, the spatial distribution of the disk material inferred from SED analysis are not unambiguous: the parameters on Equation 4.1 can be correlated, and different prescriptions can equally well fit the observations. This is why multi-wavelength information about the spatial brightness distribution is fundamental: it breaks this degeneracy by directly resolving the disk structure. And in particular, spatially resolved observations at millimeter and centimeter wavelengths directly trace the mass surface density profile (see next section), making them crucial to properly infer the structure of circumstellar disks.

## 4.2 Modeling Resolved Millimeter- and Centimeter-Wave Observations

Millimeter- and centimeter-wave observations of protoplanetary disks trace the thermal continuum emission from dust grains. These observations probe the dust population down to the disk mid-plane (Beckwith et al., 1990), and when spatially resolved, they trace the radial and azimuthal disk structure (e.g., Isella et al., 2009; Andrews et al., 2011). Studying the wavelength dependence on the radial brightness distribution can inform us about the radial distribution of dust grain properties, and in particular about dust opacity variations across the disk. Consequently, finding an appropriate prescription for the different ingredients that make up the disk emission is critical. This section deals with the particular choices of physical prescriptions made in this thesis, in order to reproduce the observed

circumstellar disk emission at mm and cm wavelengths. The general assumptions are:

- The disk is assumed to be *passive*, i.e., no accretion heating due to viscous dissipation. This is a good approximation for protoplanetary disks that are not actively accreting (those with  $\dot{M} \lesssim 2 \times 10^{-8} M_{\odot}\text{yr}^{-1}$ , Armitage, 2010). For a passive disk the only heating process is absorption of the stellar radiation, which is balanced via radiative losses: the dust reprocess the stellar radiation, re-emitting it at a much longer wavelengths. Here, collisions between gas molecules and dust are ignored as a cooling mechanism, since the collisional cooling rate is generally much smaller than the radiative cooling rate of dust inside protoplanetary disks.
- The timescale for disk and stellar evolution is much longer compared to the time needed for the disk to achieve thermal equilibrium, hence the disk is assumed to be in *steady state*.
- The disk is assumed to be in *hydrostatical equilibrium* between the stellar gravity and the gas pressure, making the disk opening angle increase w.r.t. the distance from the star, i.e., a flared geometry.
- The disk structure follows that of the *two-layer disk approximation* (Chiang & Goldreich, 1997). The boundary between the optically thin disk surface layer and the disk interior defines this model. This boundary corresponds to the height above the disk where the dust is optically thick to the stellar radiation. In this configuration, dust in the disk surface layer absorbs the short-wavelength stellar radiation and re-radiates this energy at longer wavelengths. Because this hot dust layer will be optically thin to its own dust thermal radiation, half of the surface layer emission will be lost to space while the rest will be radiated towards the disk, heating up its interior. Hence, the disk emission is characterized by two components: dust radiation from the surface layer at a temperature  $T_s$  and dust radiation from the disk interior at a temperature  $T_i$ . How the interior and surface temperatures are computed will be discussed in Section 4.2.1.4. Although the *two-layer prescription* is an approximation, the resulting temperature structure is very similar to two- and three-dimensional Monte Carlo radiative transfer models (for a comparison see: Dullemond et al., 2002).

- For the far out regions of the disk, where even the interior becomes optically thin to the stellar radiation, the two-layer model discussed before cannot be defined. Hence, the disk emission will be characterized by a single temperature that smoothly decreases as a power law with radius, which cannot fall below the expected temperature of the outer disk as it is heated by interstellar radiation ( $\sim 10$  K).

The basic equations that define the two-layer disk model have been presented in Chiang et al. (2001) and Dullemond et al. (2001). For the sake of completeness these are introduced here again. The flux density arising from the disk interior corresponds to the sum of the emission arising from each annuli of width  $dR$ :

$$4\pi D^2 F_\nu^i = 4\pi \int_{R_{in}}^{R_{out}} \left(1 - e^{-\tau_\nu^i(R)}\right) B_\nu(T_i(R)) 2\pi R dR \quad (4.2)$$

where it is considered that the radiation leaving the disk interior will be self-attenuated by a  $(1 - e^{-\tau_\nu^i(R)})$  factor. The emission arising from the surface layer, with a column density of material  $\Delta\Sigma$ , corresponds to

$$4\pi D^2 F_\nu^s = 4\pi \int_{R_{in}}^{R_{out}} \left(1 + e^{-\tau_\nu^s(R)}\right) B_\nu(T_s(R)) \Delta\Sigma(R) \kappa_\nu^s 2\pi R dR \quad (4.3)$$

where the subscripts  $i$  and  $s$  denote the dust opacity and optical depth on the *interior* and *surface* of the disk. The goal of the following subsection is to discuss each component that goes into the disk structure model described by equations 4.2 and 4.3.

#### 4.2.1 Ingredients for the disk structure

For a given young star, one (hopefully!) knows its stellar parameters (luminosity, temperature, radius, etc.) as well as its distance and proper motion. Hence, in order to balance out the heating effects from the central star with the cooling effects of the dust, it is necessary to describe the disk structure appropriately. This section has two goals: describe the different aspects that go into characterizing the disk structure, and establish the number of free parameters needed for each prescription that is adopted.

#### 4.2.1.1 Disk geometry

The inner and outer radii of the disk constitute two parameters of the disk model that define the extent of the disk (i.e., how far equations 4.2 and 4.3 need to be integrated). For this thesis, the inner radius is fixed to be equal to the distance where the dust sublimates. Given the stellar luminosity ( $L_\star$ ) and the dust properties (in particular the dust sublimation temperature,  $T_{evap}$ ) the inner disk radius is:

$$R_{in} = \left( \frac{L_\star}{4\pi\sigma T_{evap}^4} \right)^{1/2} = 0.07 \text{AU} \left( \frac{L_\star}{L_\odot} \right)^{1/2} \left( \frac{T_{evap}}{1500 \text{ K}} \right)^{-2} \quad (4.4)$$

which gives a range of inner radii for the stars in this thesis sample of 0.04–0.01 AU. For this thesis, the outer radius of the disk is not a free parameter of the model. It is defined to be as the radius where the disk optical depth to the stellar radiation becomes  $\tau = 0.01$ , which means that for a given surface density profile  $\Sigma(R)$  and for a particular mass opacity  $\kappa_\nu$ , the outer radius can be computed from solving

$$\tau_\nu(R_{out}) = \kappa_\nu \Sigma(R_{out}) \equiv 0.01. \quad (4.5)$$

In general, the choice for the value of  $\tau(R_{out})$  is not critical, as long as it is  $\tau(R_{out}) \ll 1$ . This arises from the fact that the surface density and temperature profiles rapidly decrease with radius in the outer disk (see Sections 4.2.1.2 and 4.2.1.4). Hence, the emission arising from the outer edge of the disk is quite small compared to the inner disk emission, and the flux missed by not integrating equations further than  $R_{out}$  contributes a negligible amount to the total flux.

The aspect ratio of the disk, defined as the ratio between the disk scale height  $H(R)$  and the cylindrical distance from the star to a position in the disk,  $R$ , tell us how much stellar radiation can be intercepted by the disk, and hence it indicates how efficiently the disk is being heated by the central star. For a disk in hydrostatic equilibrium, the vertical pressure gradient in the gas will balance the vertical component of the stellar gravity force. Assuming the equation of state for the gas is  $P = \rho c_s^2$ , where  $\rho$  is the vertical density profile

and  $c_s$  the gas sound speed, the solution for  $\rho(z)$  is found by equating:

$$\text{Stellar gravity along } \hat{z}: \quad \frac{GM_\star}{(R^2 + z^2)} \hat{z} \approx \frac{GM_\star}{R^3} z = \Omega^2 z \quad (4.6)$$

$$\text{Pressure gradient:} \quad \frac{1}{\rho(z)} \frac{dP}{dz} = \frac{c_s^2}{\rho(z)} \frac{d\rho(z)}{z} \quad (4.7)$$

$$\Rightarrow \frac{1}{\rho} \frac{d\rho}{dz} = \frac{\Omega^2}{c_s^2} \quad (4.8)$$

where  $\Omega$  is the Keplerian angular velocity. The approximation of Equation 4.6 is valid when  $z \ll R$ , and in order to derive Equation 4.7 the disk needs to be vertically isothermal (i.e.,  $c_s(R, z) = c_s(R)$ ). This last assumption is justifiable since most of the disk mass is located in the disk interior, which is practically isothermal.

The solution for the vertical density profile (Equation 4.8), has then a simple form described by a Gaussian profile normalized to the surface density distribution at the mid-plane:

$$\rho(z) = \frac{1}{\sqrt{2\pi}} \frac{\Sigma(R)}{H} e^{-\frac{1}{2}(z/H)^2} \quad (4.9)$$

where  $H \equiv \frac{c_s}{\Omega}$  is the disk scale height. The disk's geometrical thickness  $H/R$  defines if the disk is flared or not. Since  $c_s \propto T(R)^{1/2}$ , then

$$\frac{H}{R} \propto \frac{c_s/\Omega}{R} \propto \left( \frac{T(R)}{R} \right)^{1/2}. \quad (4.10)$$

This last equation shows that in order to have a flared disk (i.e.,  $H/R$  increasing with radius) the temperature profile should decrease with radius by  $T(R) \propto R^{-1}$  or shallower. The aspect ratio  $H/R$  for the disks in this thesis were computed as described above, and in principle they could be multiplied by a constant  $\phi$  between  $\phi = 0$  (razor thin disk) and  $\phi = 1$  (fully flared disk), known as the degree of flaring. The degree of flaring most significantly alters the flux emitted by the disk at far-infrared wavelengths: a fully flared disk intercepts more of the stellar radiation producing a stronger infrared excess, and it could be used to match the emission of a particular emission model to the observed SED. Since the observations presented here are not directly probing the wavelength regime most affected by flaring, all of the modeling was done with a fully flared disk (i.e., degree of flaring = 1).

Finally, the inclination ( $i$ ) and position angle (*P.A.*) of the disk in the sky play a significant role in defining the observed disk emission. Although these values do not define the disk structure, they have to be considered as free parameters into the model (except of course when good constraints on  $i$  and *PA* have been obtained through molecular line observations).

Up to this point, describing the disk geometry requires only two free parameters: inclination and position angle, since the degree of flaring, inner disk radius and outer disk radius are fixed or computed as described above.

#### 4.2.1.2 Mass surface density structure

A simple prescription for the surface density distribution of disk material can be given by a power law:

$$\Sigma(R) = \Sigma_0 \left( \frac{R}{R_0} \right)^{-p}, \quad \text{for } R_{in} < R < R_{out} \quad (4.11)$$

where the parameters allowed to vary are the slope of the power law  $p$  and the normalization of the surface density  $\Sigma_0$  (or the normalization radius  $R_0$ , but not both simultaneously). Such a prescription truncates the mass surface density at a radius  $R_{out}$ , which might be appropriate for circumstellar disks in environments with high photoionization/photoevaporation (e.g., proplyds in the Orion Nebula Cloud, [McCaughrean & O'Dell, 1996](#)) or for circumstellar disks in binary YSOs, where a companion is found outside of the disk and can dynamically truncate the outer edge. Otherwise, the disk surface density in the outer disk is expected to taper off smoothly, which might be the case for most circumstellar disks.

[Lynden-Bell & Pringle \(1974\)](#) found that the solution for  $\Sigma(R)$  of a viscously accreting Keplerian disk, subject to the gravity of a massive central object, can be described by a power law combined with an exponential taper at large radii. [Hartmann et al. \(1998\)](#) expanded on this work to show that if the disk viscosity,  $\nu$ , is assumed to be a power law with radius,  $\nu \propto R^\gamma$ , then the solution for the disk surface density is time-independent. Following the work by [Isella et al. \(2009\)](#), where it was shown that the self-similarity solution

found by Lynden-Bell & Pringle can be written as

$$\Sigma(R) = \Sigma_t \left( \frac{R_t}{R} \right)^\gamma \times \exp \left[ -\frac{1}{2(2-\gamma)} \left[ \left( \frac{R}{R_t} \right)^{(2-\gamma)} - 1 \right] \right] \quad (4.12)$$

where  $\Sigma_t$  corresponds to the surface density at radius  $R_t$ , and  $R_t$  is the *transition radius*: the location in the disk where the mass accretion rate changes sign defining a boundary for accretion (for  $R < R_t$  mass flows inward) and expansion (for  $R > R_t$  mass flows outward). Note that in the context of viscous disk evolution, the value of the transition radius will increase with time due to conservation of angular momentum: as matter is accreted onto the star the disk must expand to conserve total angular momentum. This prescription for  $\Sigma(R)$  behaves as a power law for small radii, while at large radii it decreases smoothly in an exponential fashion. Figure 4.1 presents the shape of  $\Sigma(R)$  for different values of  $\gamma$ , at a fixed  $R_t$  and  $\Sigma_t$ .

Although the power-law model has only two free parameters ( $\{\Sigma_0$  or  $R_0$ , and  $p\}$ ), while the similarity solution has three ( $\{\Sigma_t, R_t, \gamma\}$ ), we opted for the similarity solution since it has been successful in explaining an alleged conundrum: the discrepancy between the gas and

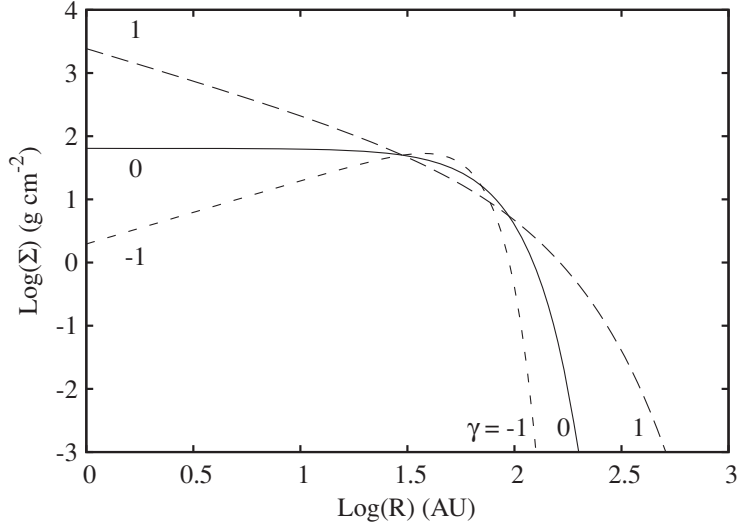


**Figure 4.1:** Surface density profile from the similarity solution of viscous disk evolution (equation 4.12) for  $\gamma = \{-1, 0, 1\}$ . The transition radius and the normalization are fixed at  $R_t = 30$  AU and  $\Sigma_t = 50$  g cm $^{-2}$ .

dust emission at the edge of protoplanetary disks (Hughes et al., 2008). When employing a truncated power law for  $\Sigma(R)$ , the inferred outer radius from dust continuum observations is found to be small compared to the extent inferred from CO molecular line observations, that trace the gaseous component of the disk (e.g., Piétu et al., 2005; Isella et al., 2007). As shown by Hughes et al. (2008), this discrepancy can be apparent, the similarity solution for  $\Sigma(R)$  can simultaneously reproduce the extent of the gaseous and dusty components of several protoplanetary disks. Assuming a constant dust-to-gas ratio, the outer edge density falls smoothly and provides enough column density in CO to produce detectable gaseous emission beyond where dust emission cannot be detected with current sensitivity limits.

More sensitive dust continuum observations have become recently available (Andrews et al., 2011; Isella, Pérez, Carpenter, 2012), where it has been possible to measure the extent of a dusty disk with a tapered surface density profile. Surprisingly, the faint dust emission from the outer edge has not been detected, although current sensitivity now allows it. The interpretation of these observations is that either a different dust-to-gas ratio or decreased dust opacity (due to the radial drift of large solids) is occurring in the outer edges of circumstellar disks. A firm conclusion on this debate can only be put forward once a large sample of protoplanetary disks has been studied with exquisite sensitivity to the dust emission in the far out disk regions. Upcoming ALMA developments will allow for such investigations. Nevertheless, the similarity solution is preferred here over a simple power-law for the surface density profile of our disk model, since this prescription is based on the physics of viscous disk accretion and only adds one extra free parameter compared to the power-law model.

#### 4.2.1.3 Dust properties

For a dust grain of size  $a$ , its cross section for light absorption at wavelength  $\lambda$  is simply given by

$$\sigma(\lambda) = \pi a^2 Q_{ext}(a, \lambda) \quad (4.13)$$

where  $Q_{ext}(a, \lambda)$  corresponds to the extinction efficiency. Besides absorption, light interacts with matter through scattering, causing the direction and/or frequency of the incident light to change. Hence, both absorption and scattering processes are considered in the calculation of  $Q_{ext} = Q_{abs} + Q_{sca}$ . Notice that in the existence of many such dust grains with mass  $m$

and a cross section given by Equation 4.13, we can compute the dust opacity per unit mass of this material as

$$\kappa_\lambda = \frac{\sigma(a, \lambda)}{m} \quad [\text{cm}^2 \text{ gm}^{-1}] \quad (4.14)$$

The value of  $Q_{ext}$  will depend of the optical regime being discussed, described in terms of the size parameter  $x = 2\pi a/\lambda$ . When the particle size is much larger than the wavelength of the light being absorbed, i.e.,  $x \gg 1$ , the extinction efficiency  $Q_{ext}(x \gg 1) \rightarrow 2$ , independent of composition or shape. This result comes from Babinet's theorem, that states that an object will remove light proportional to its projected geometrical surface, and also in the very far-field light will get deflected at the edge of the object through diffraction scattering, whose cross-section is equal to the geometrical cross section. Hence, in the limit of large particles the total cross section of a large interstellar grain (i.e., in the far-field) is twice the geometric cross section. And on this regime, the optical properties of the grain do not depend on wavelength nor material properties (gray absorption).

In the limit of small particles ( $x \ll 1$ ), known as the Rayleigh approximation, scattering becomes inefficient compared to absorption, since in the Rayleigh limit  $Q_{abs} \propto x$  while  $Q_{sca} \propto x^4$ . Hence, the dust opacity per unit mass is dominated by absorption rather than scattering ( $\kappa_\lambda^{abs} = \text{const.}$  while  $\kappa_\lambda^{sca} \propto a^{-3}$ ). In the transition regime, when the particle size is comparable to the wavelength ( $x \sim 1$ ) the calculation of  $Q_{ext}$  requires more sophisticated theories. For spherical grains an exact solution can be found using Mie theory. The dust grains assumed in this thesis have their optical constants computed this way.

To compute the dust opacity  $\kappa_\lambda$ , first a particular dust composition needs to be adopted. In space the most common solids are silicates (minerals with Si-O bonds), carbonaceous materials (e.g., polycyclic aromatic hydrocarbons—PAHs, graphite, organic compounds) and ice (from water, CO, etc.). Hence it is assumed that the protoplanetary disks in our sample contain dust grains whose composition includes these materials. Optical constants (real and imaginary part of the complex refractive index) were obtained from Warren (1984) for water ices (density  $\rho = 0.92 \text{ g cm}^{-3}$ ), from Zubko et al. (1996) for amorphous carbonaceous materials ( $\rho = 1.5 \text{ g cm}^{-3}$ ), and from Semenov et al. (2003) for silicates (in particular olivines,  $\rho = 3.49 \text{ g cm}^{-3}$ ).

Assuming dust grains of a single size  $a = 1.0 \mu\text{m}$ , Figure 4.2 shows the resulting dust opacity for some relevant dust compositions: pure silicates, pure organics, and a mixture

from of carbon, silicates and ice with volume fractional abundances from Pollack et al. (1994), corresponding to: 7.7% Olivine, 29.5% refractory and volatile organics, and 62.8% water ices. This figure illustrates the commonly used assumption, that at wavelengths longer than  $\sim 100 \mu\text{m}$  the dust opacity decreases as a power-law with wavelength:  $\kappa_\lambda \propto \lambda^{-\beta}$ , where  $\beta$  is known as the dust opacity spectral index.

In reality, a distribution of particle sizes will exist, and it is generally assumed to be a power law:  $n(a) \propto a^{-q}$ , for  $a_{min} < a < a_{max}$ , where  $\{a_{min}, a_{max}\}$  are the minimum and maximum grain size of this dust population. Figure 4.3 shows the resulting dust opacity from assuming a distribution of grain sizes with  $a_{min} = 0.005 \mu\text{m}$ ,  $a_{max} = 1 \text{ cm}$ ,  $q = 3.5$ , for the same dust compositions presented above. Again, the opacity decreases at long wavelengths with a power-law-like behavior (for  $\lambda \gtrsim 100 \mu\text{m}$ ) for all the different dust mixtures presented here and for a maximum grain size of 1 cm.

Now, for a fixed dust composition,  $\kappa_\lambda$  will depend on the minimum and maximum grain size of the dust grain population, and on the grain size distribution slope  $q$ . It is well known that  $a_{min}$  has a negligible effect on  $\kappa_\lambda$  for  $\lambda \gg 100 \mu\text{m}$ , as long as  $a_{min} \ll a_{max}$  (see Natta et al., 2007). Figure 4.4 assumes a fixed composition, as presented in Pollack et al. (1994), and a fixed slope  $q = 3.5$  (as found for ISM grains; e.g., Mathis et al., 1977). On the left panel of Figure 4.4 the value of  $a_{min}$  is varied between 0.005 to 100  $\mu\text{m}$ , keeping  $a_{max}$  fixed to 1 cm. On the right panel of the same figure,  $a_{min}$  is fixed to 0.005  $\mu\text{m}$  and  $a_{max}$  is allowed to vary between 100  $\mu\text{m}$  to 1 cm. This figure illustrate the point that fixing the value of *minimum grain size* will not produce a large effect when computing  $\kappa_\lambda$ , as long as  $a_{min} \ll a_{max}$  (left panel). On the other hand, as the maximum grain size of the dust population is increased, the slope of the dust opacity diminishes (right panel), hence the measured value of  $\beta$  is strongly related to the maximum size of the dust grain population.

But the relation between  $a_{max}$  and  $\beta$  is not as direct as it may seem: it is degenerate with the slope of the grain size distribution  $q$ . Figure 4.5 presents the resulting value of  $\beta$  (ordinate) from adopting different maximum grain sizes (abscissa) for a fixed dust composition. Here, different curves show the impact of assuming different values of  $q$ , for the slope of the grain size distribution. Even for the extreme case of steep grain size distribution with  $q = 4.0$ , a low value of  $\beta$  ( $\beta \lesssim 1$ ) is indicative of a dust population for which grains have attained at least millimeter dimensions, if not a larger size.

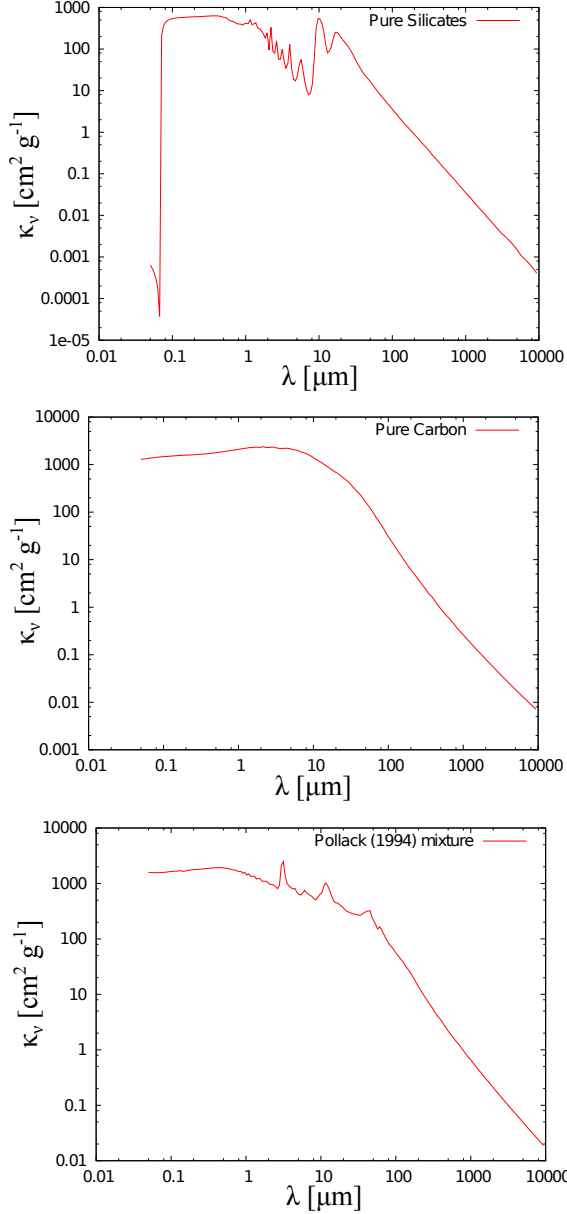


**Figure 4.2:** Dust opacity  $\kappa_\nu$  for different grain compositions and a fixed particle size ( $a = 1.0 \mu\text{m}$ ). Note that at long wavelengths  $\kappa_\lambda \propto \lambda^{-\beta}$  for these diverse dust mixtures. (carbonaceous materials from Zubko et al. (1996), silicates from Semenov et al. (2003), dust mixture from Pollack et al. (1994)).

#### 4.2.1.4 Temperature structure

Since the timescale for stellar evolution, disk evolution, and planet formation, are much longer than the time it takes for the disk material to achieve thermal equilibrium, we can

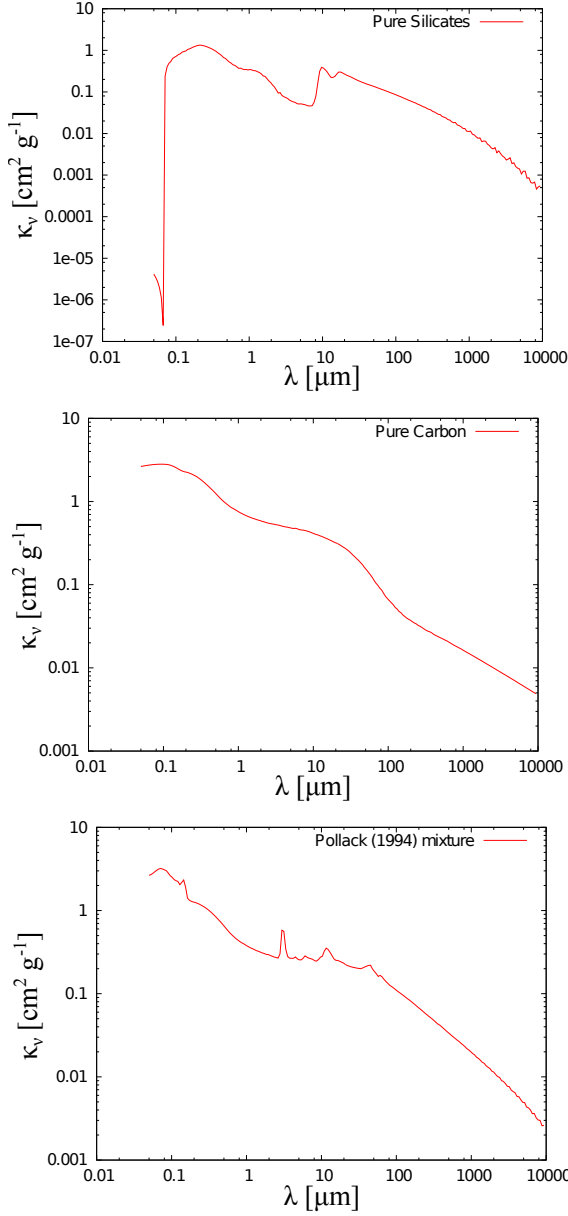


**Figure 4.3:** Dust opacity  $\kappa_\nu$  for different grain compositions and a distribution of particle sizes  $n(a) \propto a^{-q}$  with  $a_{min} = 0.005 \mu\text{m}$ ,  $a_{max} = 1 \text{ cm}$ ,  $q = 3.5$ . Note that at long wavelengths  $\kappa_\lambda \propto \lambda^{-\beta}$  for these diverse dust mixtures (carbonaceous materials from Zubko et al. (1996), silicates from Semenov et al. (2003), dust mixture from Pollack et al. (1994)).

assume that the temperature profile of the disk is set by the balance between heating and cooling processes. This balance depends on the preferred structure of the disk. For this thesis, the two-layer disk approximation developed by Chiang & Goldreich (1997) is

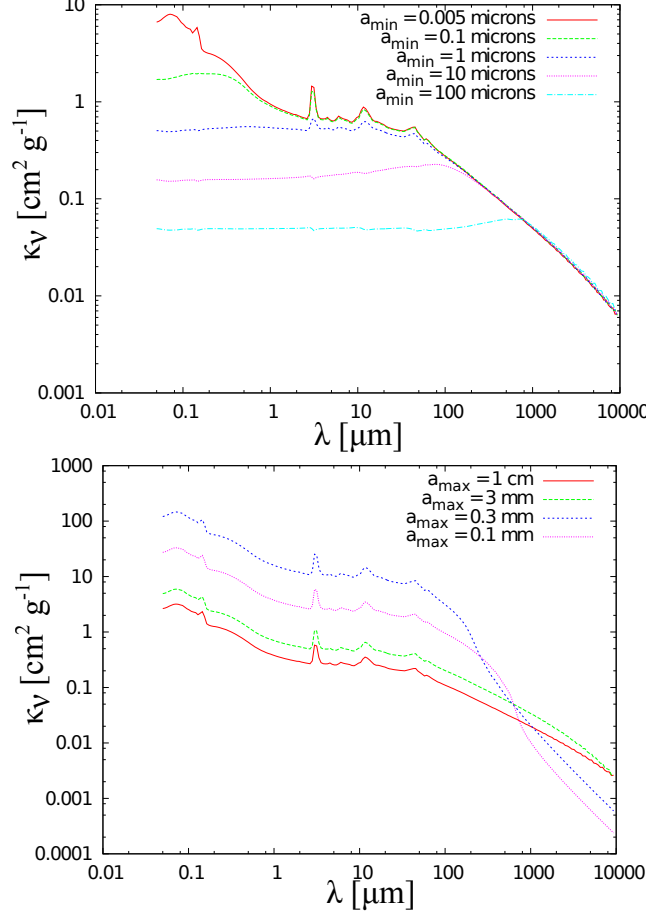


**Figure 4.4:** Dust opacity  $\kappa_\nu$  for the same grain composition (Pollack 1994) and a distribution of particle sizes  $n(a) \propto a^{-q}$  with  $q = 3.5$ . Left panel: the value of  $a_{\max}$  is fixed to 1 cm, while  $a_{\min}$  varies between 0.005 to 100  $\mu\text{m}$ . Right panel: the value of  $a_{\min}$  is fixed to 0.005  $\mu\text{m}$ , while  $a_{\max}$  varies between 100  $\mu\text{m}$  to 1 cm. Note that at long wavelengths the value of  $\beta$  is related to the maximum grain size of the dust grain population (carbonaceous materials from Zubko et al. (1996), silicates from Semenov et al. (2003), dust mixture from Pollack et al. (1994)).

adopted. This approximation consist of a passive flared disk, whose surface is irradiated by the central star, and whose interior is heated through the re-emission of the stellar radiation by the dust in the disk upper layers.

The iterative method employed to compute the temperature structure of the two-layer disk model, devised and presented by Dullemond et al. (2001), is briefly discussed. At a

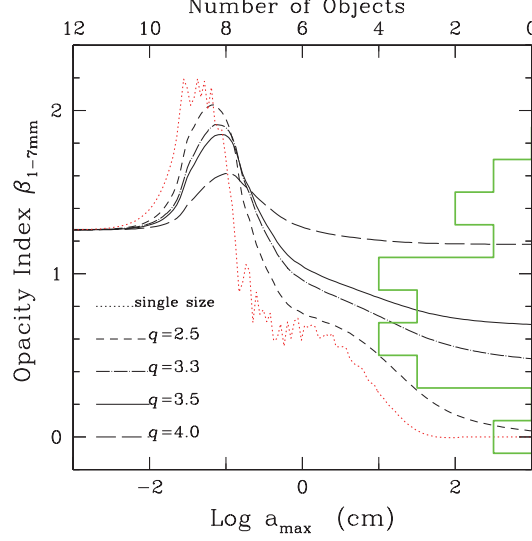


**Figure 4.5:** Dust opacity spectral index  $\beta$  as a function of  $a_{max}$  for a fixed grain composition and a distribution of particle sizes  $n(a) \propto a^{-q}$ , (Natta et al., 2007). Different curves portray different values of the grain-size distribution slope  $q$ . Note that small values of the opacity spectral slope ( $\beta \lesssim 1$ ) are indicative of the existence of grains with sizes  $\gtrsim 1$  cm in the grain population. Credit: A. Natta, reproduced with permission.

distance  $R$  from the star, the stellar flux impinging onto the disk is given by

$$F_{irr}^* = \sin(\alpha) \frac{L_*}{4\pi R^2} = \sin(\alpha) \sigma T_*^4 \frac{R_*^2}{R^2} \quad (4.15)$$

where  $\alpha$  is the grazing angle at which the radiation impinges onto the disk surface,  $\sigma$  is the Stefan-Boltzmann constant, and it is assumed that the star emits with a black-body spectrum at a temperature  $T_*$ . Within the framework of the two-layer disk model, the disk surface is defined as the layer of material that is optically thin to the stellar radiation, hence the temperature of the dust in the surface layer is simply given by

$$\frac{1}{4\pi R^2} \int_0^\infty 4\pi R_*^2 \kappa_\nu \pi B_\nu(T_*) d\nu = 4\pi \int_0^\infty \pi \kappa_\nu B_\nu(T_s) d\nu \quad (4.16)$$

where the heating and cooling of the dust grains in the disk surface layer, at a distance  $R$  from the central star, is balanced without including any optical depth effects since  $\tau \lesssim 1$  in

the surface layer. Employing the *Planck mean opacity*

$$\kappa_P(T) \equiv \frac{\int_0^\infty \kappa_\nu B_\nu(T) d\nu}{\int_0^\infty B_\nu(T) d\nu} \quad (4.17)$$

(which is the average opacity, weighted by the Planck function at temperature T), an expression for the dust temperature in the surface of the disk is derived from Equation 4.16

$$T_s = \left( \frac{\kappa_P(T_*)}{\kappa_P(T_s)} \right)^{1/4} \left( \frac{R_*}{2R} \right)^{1/2} T_*. \quad (4.18)$$

This equation can be solved by an iterative procedure: first make an initial guess for  $T_s$ , then compute the Plank mean opacity at this temperature ( $\kappa_P(T_s)$ ), and then solve for  $T_s$  using Equation 4.18. Use the new computed value for  $T_s$  to find  $\kappa_P(T_s)$ , solve Equation 4.18 again, and repeat this procedure until it converges. This takes a few iterations for a tolerance value of few percent on  $T_s$ .

The main assumption of the two-layer disk model is that exactly half of the reprocessed flux is directed downwards and will eventually heat up the disk interior, while the other half is re-radiated upwards and lost into space. This assumption is used to compute the dust temperature for the disk mid-plane. Since the disk interior might be optically thin to the radiation coming from the disk surface, only a fraction  $\psi_s$  of the surface flux will be absorbed by the interior, where  $\psi_s = 1$  if the interior is completely optically thick to the disk surface emission. Hence, the flux absorbed by the disk interior will be

$$F_{abs}(\text{Int}) = \psi_s \frac{F_{irr}^*}{2}. \quad (4.19)$$

The flux emitted by the disk interior at a temperature  $T_i$  is

$$F_{em}(\text{Int}) = \int_0^\infty \pi B_\nu(T_i)(1 - e^{-\Sigma\kappa_i}) d\nu \quad (4.20)$$

$$= \psi_i \sigma T_i^4 \quad (4.21)$$

with

$$\psi_i = \frac{\int_0^\infty B_\nu(T_i)(1 - e^{-\Sigma\kappa_i}) d\nu}{\int_0^\infty B_\nu(T_i) d\nu} \quad (4.22)$$

where the term  $(1 - e^{-\Sigma\kappa_i})$  is included to account for the case where the disk interior is not

optically thick to its own radiation. Hence, for a fully optically thick disk  $\psi_i = 1$  and the emission from the interior is just simply  $F_{em}(\text{Int}) = \sigma T_i^4$ . In radiative equilibrium, we have that  $F_{abs}(\text{Int}) = F_{em}(\text{Int})$ , and we can compute the temperature where the disk interior can emit as much as it can absorbs:

$$T_i = \left( \frac{\sin(\alpha)}{2} \frac{\psi_s}{\psi_i} \right)^{1/4} \left( \frac{R_*}{R} \right)^{1/2} T_*. \quad (4.23)$$

An expression for  $\psi_s$  is now derived by noting that if the surface layer of the disk has a surface density  $\Delta\Sigma$  and is at a temperature  $T_s$ , the total flux emitted by this layer corresponds to

$$F_{em}(\text{Surf}) = \int_0^\infty 4\pi \Delta\Sigma \kappa_\nu B_\nu(T_s) d\nu. \quad (4.24)$$

Only a fraction  $\frac{1}{2}(1 - e^{-\Sigma\kappa_\nu})$  is absorbed by the disk interior, hence the absorbed flux by the interior from the reprocessed emission of the surface layer is

$$F_{abs}(\text{Int}) = \int_0^\infty 2\pi \Delta\Sigma \kappa_\nu B_\nu(T_s)(1 - e^{-\Sigma\kappa_\nu}) d\nu \quad (4.25)$$

$$= \psi_s F_{em}(\text{Surf}) \quad (4.26)$$

with

$$\psi_s = \frac{\int_0^\infty \kappa_\nu B_\nu(T_s)(1 - e^{-\Sigma\kappa_i}) d\nu}{\int_0^\infty \kappa_\nu B_\nu(T_s) d\nu}. \quad (4.27)$$

The value of  $\psi_s$  can be found by replacing Equation 4.18 into this last equation. To find the interior temperature  $T_i$  from Equation 4.23 an estimate for  $\psi_i$  needs to be made, which in turn depends on  $T_i$ . Again, an iterative procedure is used to compute a solution for Equation 4.23, where  $\alpha$ , the grazing angle to the disk, is calculated using the numerical procedure outlined by Chiang et al. (2001). This iterative calculation of the disk interior's temperature converges after a few iterations.

The assumptions implicit to the two-layer disk model breaks down for the far out regions of the disk, where the surface density of material drops significantly and even the disk interior becomes optically thin to the stellar radiation. When this condition is met, the disk emission is now characterized by a single temperature profile that smoothly decreases as a power law with radius, that cannot fall below the expected temperature of the outer

disk as it is heated by interstellar radiation ( $T_{out} = 10$  K)

$$T(R) = \left( T_0^4 \left( \frac{R}{R_0} \right)^{4q} + T_{out}^4 \right)^{1/4} \quad (4.28)$$

where  $T_0$  and  $R_0$  correspond to the value of the interior temperature and radius for the last step of the iteration under the two-layer disk model, and  $q$  is the slope of  $T_i$  for the last 10 steps.

Once the surface density profile  $\Sigma(R)$ , the dust composition and the disk geometry are set, the calculation of the temperature profile as presented here does not introduce any other free parameters to the model. When fitting our observations with the preceding disk structure model and a fixed dust composition, we have a total of 5 free parameters:  $\{i, PA\}$ , that describe the disk geometry, and  $\{\Sigma_t, R_t, \gamma\}$  that describe the surface density profile.

### 4.3 Disk Structure Fitting Through Markov Chain Monte Carlo

The previous section discussed the components necessary to describe the structure of a circumstellar disk:  $\Sigma, \kappa_\nu, T$ , and the geometry of the disk. This section describes the Markov-Chain Monte Carlo procedure used to find the circumstellar disk model that best describes our observations. This procedure has been presented and used to model circumstellar disk observations in [Isella et al. \(2009\)](#).

#### 4.3.1 Finding the best-fit model to our data

With the preceding prescription for the disk temperature, mass surface density and dust opacity, a model can be constructed for the disk surface brightness distribution, that depends on the stellar properties and the disk parameters described before. A set of these parameters  $P_1, \dots, P_N$  (with  $N = 5$  for our circumstellar disk prescription) define a single *state*  $\mathbf{x}$  of the model:  $\mathbf{x}\{P_1, \dots, P_N\}$ . From the modeled disk brightness distribution an image is produced, making sure that the significant spatial scales of the disks are covered. Then, the Fourier transform of this image is taken, in order to obtain modeled visibilities that are sampled in the same  $uv$ -points as the original observations. The model that best reproduces our

observations is found by comparing modeled and observed visibilities by means of the  $\chi^2$ :

$$\chi^2 = \sum_i \frac{(\text{Re}_i^{Obs} - \text{Re}_i^{Mod})^2 + (\text{Im}_i^{Obs} - \text{Im}_i^{Mod})^2}{\sigma_i^2} \quad (4.29)$$

where the real and imaginary part of each observed and modeled visibility are  $\text{Re}^{Obs}$ ,  $\text{Im}^{Obs}$ , and  $\text{Re}^{Mod}$ ,  $\text{Im}^{Mod}$ , and each visibility point is weighted by its thermal noise  $\sigma_i$  (see Chapter 2). To find the best-fit values and the confidence intervals for the parameters in our model, a Bayesian approach is adopted.

Bayes' theorem allows us to determine the probability that our hypothesis is true given the observed data (i.e., the probability of the state  $\mathbf{x}$  given our set of observations  $\mathbf{D}$ :  $p(\mathbf{x}|\mathbf{D})$ ), by computing the probability that we would have observed the measured data *if* our hypothesis was true,  $p(\mathbf{D}|\mathbf{x})$ , and the known prior probability distribution of the model parameters,  $p(\mathbf{x})$ . Bayes theorem in essence can be expressed as:

$$\text{prob}(hypothesis|data, I) \propto \text{prob}(data|hypothesis, I) \times \text{prob}(hypothesis, I), \quad (4.30)$$

where  $I$  represents any relevant background information that we might know.

The  $\chi^2$  distribution is sampled by varying the input parameters  $P_1, \dots, P_N$  and the best-fit model found as the one that minimizes  $\chi^2$ . The problem is that sampling the parameter space by brute-force becomes a difficult feat (even for small  $N$ ), hence more sophisticated algorithms, as the Markov Chain Monte Carlo (MCMC) method, are needed.

A Markov Chain is a sequence of states in which each state uses the previous one(s) to transit to the next state. A MCMC method randomly samples the prior probability distribution of the system states (let's call it  $f(x)$ , where  $x$  corresponds to a particular state) while it uses the guidance from the previous states to generate a new one (so we advance from state  $x_n$  to state  $x_{n+1}$  given by the transition probability  $p(x_{n+1}|x_n)$ ). One important property of this chains is that if a reversible Markov chain is designed (such that  $f(x)p(x|x') = f(x')p(x'|x)$ ), then this chain will eventually converge to the original distribution of the system states  $f(x)$  (Gilks et al., 1995).

In some particular problem, we are interested in computing the probability of the state  $\mathbf{x} = \{P_1, \dots, P_N\}$  given our set of observations  $\mathbf{D}$  (i.e.,  $p(\mathbf{x}|\mathbf{D})$ ). The joint probability for

the model parameters  $\mathbf{x}$  and the observed data  $\mathbf{D}$  can be expanded as:

$$p(\mathbf{x}, \mathbf{D}) = p(\mathbf{x})p(\mathbf{D}|\mathbf{x}) = p(\mathbf{D})p(\mathbf{x}|\mathbf{D}) \quad (4.31)$$

where  $p(\mathbf{D}|\mathbf{x})$  corresponds to the probability of the observed data  $\mathbf{D}$  given the model parameters  $\mathbf{x}$  (i.e., the likelihood of  $\mathbf{x}$ ) and  $p(\mathbf{x})$  is the prior probability distribution of the model parameters. If we create a Markov chain whose equilibrium distribution is equal to the posterior probability of the model parameters (i.e.,  $f(\mathbf{x}) = p(\mathbf{x}|\mathbf{D})$ ), from Equation 4.31 we can write:

$$f(\mathbf{x}) = p(\mathbf{x}|\mathbf{D}) \propto p(\mathbf{x})p(\mathbf{D}|\mathbf{x}) \quad (4.32)$$

It can be shown that if the error distribution of the observed data is Gaussian, then the probability of drawing the observed values given a certain model  $\mathbf{x}$ ,  $p(\mathbf{D}|\mathbf{x})$ , is proportional to  $e^{-\chi^2(\mathbf{x})/2}$ . And if the prior of possible states  $\mathbf{x}$  is uniform ( $p(\mathbf{x}) = 1, \forall \mathbf{x}$ ), we can re-write the last equation as:

$$f(\mathbf{x}) = p(\mathbf{x}|\mathbf{D}) \propto e^{-\chi^2(\mathbf{x})/2}. \quad (4.33)$$

From these we can conclude that:

- The posterior probability of the state  $\mathbf{x}$  given our set of observations  $\mathbf{D}$  is proportional to the distribution of  $\chi^2(\mathbf{x})$  values as  $e^{-\chi^2(\mathbf{x})/2}$ .
- The state that maximizes  $p(\mathbf{x}|\mathbf{D})$  corresponds to the state that minimizes  $\chi^2(\mathbf{x})$ .
- The MCMC algorithm samples the posterior distribution given the prior and the observational data. Many realizations are required to reach the equilibrium distribution of the system states  $f(x)$ , which is equivalent to the posterior probability  $p(\mathbf{x}|\mathbf{D})$ . Then, marginalizing over all but one parameter can be used to obtain the probability distribution of the parameter of interest, and find its best-fit value and uncertainty.

### 4.3.2 Uncertainties in model parameters

Having found the appropriate set of best-fit parameters by minimizing the  $\chi^2$  statistic, the issue now is finding the confidence intervals for each parameter. [Avni \(1976\)](#) showed that for a given significance level  $\alpha$ , the region of confidence correspond to all model parameters

that produce a  $\chi^2$  value less than:

$$\chi^2(\alpha) = \chi^2_{min} + \Delta\chi^2(\alpha, N_{dof}) \quad (4.34)$$

where  $\Delta\chi^2$  is the difference above the minimum  $\chi^2$  for  $N_p$  parameters at a given significance level  $\alpha$ .

In principle, the difference above the minimum  $\chi^2$  could be used to find the confidence intervals. However, the number of degrees of freedom in our nonlinear model might not be constant during the fit. For example, if two parameters are correlated, then the fit might be “driven” by one of the two parameters and the actual number of parameters will be smaller than  $N_P$ . Thus, this method will not be used to estimate the uncertainty in our model parameters.

Remembering that the MCMC fitting algorithm provides the posterior probability distribution of the model parameters, we can obtain the probability distribution of each parameter through marginalization. Then, finding the confidence intervals for each parameter consist in identifying a region in the PDF for which the parameter  $P_i$  has the same probability at its extremes, and for which the total probability (area under the curve) corresponds to the significance level  $\alpha$ . The confidence interval ( $\sigma_{low} \leq P_i \leq \sigma_{up}$  with significance  $\alpha$ ) for the parameter  $P_i$  is given by:

$$p(\sigma_{low}|\mathbf{D}) = p(\sigma_{up}|\mathbf{D}) \text{ and } \int_{\sigma_{low}}^{\sigma_{up}} p(P_i|\mathbf{D}) dP_i = \alpha \quad (4.35)$$

In the case of a Normal probability distribution for the parameter  $P_i$ , the confidence interval will be symmetric w.r.t. the best-fit value (i.e.,  $\sigma_{low} = \sigma_{up} = \sigma_{P_i}$ ), and the uncertainty on  $P_i$  will be given by the standard deviation of this Gaussian probability distribution. Examples of the derived uncertainties in the model parameters can be found in Figures 5.3 of Chapter 5.

### 4.3.3 Uncertainties for $\Sigma(R)$ and $T(R)$

To estimate the uncertainty of  $\Sigma(R)$  and  $T(R)$  at each radius  $R$ , which are necessary to estimate the constraints on  $\beta(R)$  (next section), one could think of the following ways:

1. Using  $\Delta\chi^2$ : as explained before, this cannot be done with a nonlinear model since the

number of parameters will be an ill-defined quantity.

2. Using the parameter uncertainties  $\sigma_{P_i}$ : Since we defined the surface density as a function of the parameters:  $\Sigma(R) = f(P_1, \dots, P_N, R)$ , we could use the error estimated for each parameter  $\sigma_{P_i}$  to compute the envelope of functions that contains all the  $\Sigma(R)$  within  $\pm\sigma_{P_i}$ . This could be done in principle if the parameters are uncorrelated with each other, but that is generally not the case. Doing this we will overestimate the uncertainty in the surface density as a function of radius.
3. Analytical propagation of errors: Since the MCMC procedure has “measured” the parameters  $P_1, \dots, P_N$ , and  $\Sigma(R)$  has an analytical form described by Equation 4.12 we could in principle propagate the uncertainty in the measured variables to determine the uncertainty in the dependent variable  $\Sigma(R)$ . It is important to consider that some of the model parameters might be correlated, which means that we will need to consider the covariance between these parameters when computing the uncertainty on  $\Sigma(R)$ . But for estimating the uncertainty on  $T(R)$ , this method would not work, since we do not have an analytical form that describes  $T(R)$  as a function of the model parameters  $P_i$ .
4. Probability distribution for  $\Sigma(R)$ : A sufficiently well sampled MCMC chain will reach the equilibrium distribution, that corresponds to the posterior probability distribution  $p(P_1, \dots, P_N | \mathbf{D})$ . For each realization of the chain (i.e., for a given set of parameters  $P'_1, \dots, P'_N$ ), the functional form of  $\Sigma(R)$  can be used to calculate  $\Sigma'(R) = f(P'_1, \dots, P'_N, R)$ , and the corresponding  $T'(R)$  given this  $\Sigma'(R)$  can be computed as explained in Section 4.2.1.4. Then,  $\Sigma(R)$  and  $T(R)$  calculated this way will have an associated value of  $\chi^2(P'_1, \dots, P'_N)$  for each realization of the chain. Hence, for each disk radius  $R$  a probability distribution can be computed using the  $\chi^2$  distribution corresponding to all possible values of  $\Sigma(R)$  and  $T(R)$  given our MCMC chain. Then, for a significance level  $\alpha$  we can use Equation 4.35 to compute the confidence interval for  $\Sigma(R)$  and  $T(R)$ . We repeat this for all radius between  $R_{min}$  and  $R_{max}$  and we can obtain the uncertainty on  $\Sigma$  and  $T$  as a function of radius. This is the route taken on this thesis to estimate the confidence intervals on the mass surface density and temperature profiles from our models.

## 4.4 Monte Carlo Fitting of Radial Variations of $\beta$

To reproduce the multi-wavelength observations presented in Chapter 2, the disk emission model described in the preceding sections was employed. Since the ultimate goal is to determine if variations in the dust opacity across each circumstellar disk are present, this final section describes how variations in the dust opacity slope  $\beta$  are constrained as a function of radius, using a Monte Carlo fitting technique.

The first step is to compile a SED for the circumstellar disk currently being modeled, that extends from far-IR to cm wavelengths. At that point, with a particular grain mixture and dust composition, the maximum grain size ( $a_{max}$ ) and the slope of the grain distribution ( $q$ ) that best reproduces the unresolved SED are found. Then, assuming a *constant dust opacity* throughout the disk, each wavelength is fitted *separately* with the physical model described before. The net result is that a constraint on  $\Sigma(R)$  and  $T(R)$  is obtained for each observation and at different wavelengths.

The best-fit surface density and temperature profiles inferred in this manner might be different for each wavelength if the assumption of a constant dust opacity with radius is not valid (Isella et al., 2010). This arises naturally, since the temperature and mass distribution should not depend on wavelength, while the dust opacity does. When the best-fit parameters found for the each multi-wavelength observations indicate a differing  $\Sigma(R)$  and  $T(R)$  for each wavelength, it is concluded that there must be some variation of  $\kappa_\nu$  with radius that is not accounted for, since the initial assumption of the modeling is that  $\kappa_\nu$  has a constant value with radius.

At the wavelengths our observations probe the dust emission is mostly optically thin<sup>1</sup> and in the Rayleigh-Jeans domain<sup>2</sup> (hence  $B_\nu(T) \propto T$ ) Thus, our observations directly constrain the product  $\kappa_\lambda \times \Sigma \times T$ , where all these physical quantities depend on the distance to the star  $R$ , but only the dust opacity depends on the observed wavelength  $\lambda$ . The modeling presented above, assuming a constant dust opacity with radius and fitting each wavelength separately, may result in a wavelength-dependent  $\Sigma_\lambda(R)$  and  $T_\lambda(R)$ , which is unphysical but

---

<sup>1</sup>Except for the innermost regions of the disk.

<sup>2</sup>The assumption of circumstellar disk emission in the Rayleigh-Jeans domain might not be accurate enough, particularly for the cold outer disk at sub-millimeter wavelengths, where  $h\nu \sim k_B T$ . The discussion regarding this particular assumption is deferred for Chapter 5.

telling: the assumption of a constant  $\kappa_\lambda$  with radius is not warranted by the observations.

Expanding on the work presented in Isella et al. (2010), if  $\bar{\kappa}_\lambda(R)$ ,  $\bar{\Sigma}(R)$ , and  $\bar{T}(R)$  are the *true* but unknown disk physical quantities, then variations of the dust opacity with radius can be inferred from

$$\kappa_\lambda \times \Sigma_\lambda(R) \times T_\lambda(R) = \bar{\kappa}_\lambda(R) \times \bar{\Sigma}(R) \times \bar{T}(R), \quad (4.36)$$

where the right-hand side of this equation corresponds to the true disk properties and the left-hand side encompasses the constraints found for the disk modeling at each wavelength. Taking the ratio of Equation 4.36 for two different wavelengths,  $\lambda_1$  and  $\lambda_2$ , and adopting the power-law behavior for the dust opacity at long wavelengths,  $\kappa_\lambda \propto \lambda^{-\beta}$ , it follows that

$$\left(\frac{\lambda_1}{\lambda_2}\right)^{\beta(R)} = \left(\frac{\lambda_1}{\lambda_2}\right)^{\beta_C} \times \frac{\Sigma_{\lambda_1}(R)T_{\lambda_1}(R)}{\Sigma_{\lambda_2}(R)T_{\lambda_2}(R)} \quad (4.37)$$

were  $\beta_C$  corresponds to the spectral slope of the assumed constant dust opacity with radius. From this equation is easy to re-derive Equation (9) from Isella et al. (2010), which gives uses a very useful prescription to constraint the radial variations of the opacity spectral slope ( $\Delta\beta(R) = \beta(R) - \beta_C$ ) in dual-wavelength observations:

$$\Delta\beta(R) = \log^{-1} \left[ \frac{\lambda_1}{\lambda_2} \right] \times \log \left[ \frac{\Sigma_{\lambda_1}(R)T_{\lambda_1}(R)}{\Sigma_{\lambda_2}(R)T_{\lambda_2}(R)} \right] \quad (4.38)$$

This last equation shows that in logarithmic space  $\Delta\beta(R)$  is the slope of a straight line at points  $\{x = \log(\lambda), y = \log(\Sigma_\lambda(R)T_\lambda(R))\}$ . Hence, to measure at each radius  $\Delta\beta(R)$  with our set of multi-wavelength observations, we find the slope of a straight line—in a least-square sense—that fits our constraints on the product  $\Sigma_\lambda(R) \times T_\lambda(R)$ , found using the procedure described in Section 4.3.

The actual constraints on  $\Delta\beta(R)$  are found in a more sophisticated way, making use of the Bayesian approach that the modeling method is based upon. First, note that the result of the MCMC minimization algorithm is a sampled posterior probability distribution of our model parameters, i.e., for each sampled model state we have the probability of that state being true given our observations (see Section 4.3.1). Hence, at each disk radius, PDF for the product  $\Sigma_\lambda(R) \times T_\lambda(R)$  is constructed. This PDF will be different for each wavelength

that has been modeled. In the following, I refer to this PDF as  $PDF(\lambda, R)$ .

The Monte Carlo fitting for  $\Delta\beta(R)$  is performed at each radius  $R$ , in the following way:

- The  $PDF(\lambda, R)$  is randomly sampled (in a Monte Carlo sense), and random values of the product  $\Sigma(R) \times T(R)$  for each wavelength are obtained,
- Then, the best-fit straight line that goes through the points  $\{x = \log(\lambda), y = \log(\Sigma_\lambda(R)T_\lambda(R))\}$  for the observed wavelengths is found. The slope of this best-fit line will correspond to  $\Delta\beta(R)$  for the particular random sampling of  $\Sigma(R) \times T(R)$ .
- These last two steps are repeated enough times such that a PDF for  $\Delta\beta(R)$  is constructed.
- Then, the best-fit value of  $\Delta\beta$  at a radius  $R$  corresponds to the peak of this PDF. The confidence intervals at  $1\sigma$ ,  $2\sigma$ , and  $3\sigma$  are derived from the region of the distribution that contains 68.3%, 95.5%, and 99.7% of all samples at equal probability (as described in Section 4.3.2 for the uncertainties of the model parameters).
- These series of steps are performed for all radii sampled by our observations, in order to obtain a best-fit value and inferred constraints on  $\beta(R) = \beta_C + \Delta\beta(R)$  for each circumstellar disk in this thesis.

## 4.5 Maximum Likelihood Estimate Method to Constrain the value of $a_{max}(R)$

To derive equations 4.37 and 4.38, the assumption of  $\kappa_\lambda \propto \lambda^{-\beta}$  must be satisfied. However, for  $a_{max} \sim 0.1\text{--}1$  mm this approximation may break down (Draine, 2006), as illustrated in Chapter 5, right panel of Figure 5.7. Therefore, rather than inferring the value of the maximum grain size from the constraints found for  $\beta(R)$ ,  $a_{max}$  can be directly constrained by fitting an specific dust opacity  $\bar{\kappa}_\lambda$  to the observational constraints already found for the product  $\kappa_\lambda \times \Sigma_\lambda \times T_\lambda$  at each radius. For a fixed dust composition and grain-size distribution slope,  $q$ , the values of  $a_{max}$  and  $\bar{\Sigma} \times \bar{T}$  that satisfy Equation 4.36 are found, with that last equation (4.36) now written as

$$\kappa_\lambda \Sigma_\lambda(R) T_\lambda(R) = \bar{\kappa}_\lambda(a_{max}(R)) \bar{\Sigma}(R) \bar{T}(R) \quad (4.39)$$

where the right-hand side corresponds to our model (with parameters  $a_{max}$  and  $\bar{\Sigma} \times \bar{T}$ ), and where the left-hand side has been constrained by the modeling of our multi-wavelength observations (i.e., a PDF for the product  $\kappa_\lambda \times \Sigma_\lambda(R) \times T_\lambda(R)$  is available).

At each radius  $R$ , a two-dimensional grid of parameters  $\{a_{max}, \bar{\Sigma} \times \bar{T}\}$  is defined. At each point in the grid, the value of the product  $\bar{\kappa}_\lambda(a_{max}) \times \bar{\Sigma} \times \bar{T}$  is obtained for each wavelength. Then, for each set of parameters in the grid, the probability that such measurement will have occurred (given our observational constraints on the left-hand side of Equation 5.4) is computed. This way, the likelihood function for the parameters  $\{a_{max}, \bar{\Sigma}\}$  is constructed. Thus, the best-fit values for  $a_{max}$  and  $\bar{\Sigma}$  are those that maximize the likelihood, while the confidence intervals on this two parameters are obtained from the marginalized likelihood function.

The analysis of a multi-wavelength set of observations of circumstellar disks, that span more than an order of magnitude in wavelength, is presented in the next two chapters (Chapter 5 and 6). The observational constraints on  $\beta(R)$  and  $a_{max}(R)$  presented in those chapters were obtained with the methods and model described here.



## Chapter 5

# Constraints on the Radial Variation of Grain Growth in the AS 209 Circumstellar Disk

LAURA M. PÉREZ<sup>1</sup>, JOHN M. CARPENTER<sup>1</sup>, CLAIRE J. CHANDLER<sup>2</sup>, ANDREA ISELLA<sup>1</sup>,  
 SEAN M. ANDREWS<sup>3</sup>, LUCA RICCI<sup>1</sup>, NURIA CALVET<sup>4</sup>, STUARTT A. CORDER<sup>5</sup>,  
 ADAM T. DELLER<sup>6</sup>, CORNELIS P. DULLEMOND<sup>7</sup>, JANE S. GREAVES<sup>8</sup>,  
 ROBERT J. HARRIS<sup>3</sup>, THOMAS HENNING<sup>9</sup>, WOOJIN KWON<sup>10</sup>, JOSEPH LAZIO<sup>11</sup>,  
 HENDRIK LINZ<sup>7</sup>, LEE G. MUNDY<sup>12</sup>, ANNEILA I. SARGENT<sup>1</sup>, SHAYE STORM<sup>12</sup>,  
 LEONARDO TESTI<sup>13,14</sup>, AND DAVID J. WILNER<sup>3</sup>

<sup>1</sup>California Institute of Technology, 1200 East California Blvd, Pasadena, CA 91125, USA

<sup>2</sup>National Radio Astronomy Observatory, P.O. Box O, Socorro NM 87801, USA

<sup>3</sup>Harvard-Smithsonian Center for Astrophysics, 60 Garden Street, Cambridge, MA 02138, USA

<sup>4</sup>University of Michigan, 830 Dennison Building, 500 Church Street, Ann Arbor, MI 48109, USA

<sup>5</sup>Joint ALMA Observatory, Av. Alonso de Córdova 3107, Vitacura, Santiago, Chile

<sup>6</sup>The Netherlands Institute for Radio Astronomy (ASTRON), 7990-AA Dwingeloo, The Netherlands

<sup>7</sup>Heidelberg University, Center for Astronomy, Albert Ueberle Str 2, Heidelberg, Germany

<sup>8</sup>University of St. Andrews, Physics and Astronomy, North Haugh, St Andrews KY16 9SS

<sup>9</sup>Max-Planck-Institut für Astronomie, Königstuhl 17, 69117 Heidelberg, Germany

<sup>10</sup>University of Illinois, 1002 West Green St., Urbana, IL 61801, USA

<sup>11</sup>Jet Propulsion Laboratory, California Institute of Technology, 4800 Oak Grove Dr, Pasadena, CA 91106

<sup>12</sup>University of Maryland, College Park, MD 20742, USA

<sup>13</sup>European Southern Observatory, Karl Schwarzschild str. 2, 85748 Garching, Germany

<sup>14</sup>INAF-Osservatorio Astrofisico di Arcetri, Largo E. Fermi 5, 50125 Firenze, Italy

## Abstract

We present dust continuum observations of the protoplanetary disk surrounding the pre-main sequence star AS 209, spanning more than an order of magnitude in wavelength from 0.88 to 9.8 mm. The disk was observed with sub-arcsecond angular resolution ( $0.2'' - 0.5''$ ) to investigate radial variations in its dust properties. At longer wavelengths, the disk emission structure is notably more compact, providing model-independent evidence for changes in the grain properties across the disk. We find that physical models which reproduce the disk emission require a radial dependence of the dust opacity  $\kappa_\nu$ . Assuming that the observed wavelength-dependent structure can be attributed to radial variations in the dust opacity spectral index ( $\beta$ ), we find that  $\beta(R)$  increases from  $\beta < 0.5$  at  $\sim 20$  AU to  $\beta > 1.5$  for  $R \gtrsim 80$  AU, inconsistent with a constant value of  $\beta$  across the disk (at the  $10\sigma$  level). Furthermore, if radial variations of  $\kappa_\nu$  are caused by particle growth, we find that the maximum size of the particle-size distribution ( $a_{max}$ ) increases from sub-millimeter-sized grains in the outer disk ( $R \gtrsim 70$  AU) to millimeter and centimeter-sized grains in the inner disk regions ( $R \lesssim 70$  AU). We compare our observational constraint on  $a_{max}(R)$  with predictions from physical models of dust evolution in protoplanetary disks. For the dust composition and grain-size distribution investigated here, our observational constraints on  $a_{max}(R)$  are consistent with models where the maximum grain size is limited by radial drift.

### 5.1 Introduction

The growth of sub-micron-sized dust grains into millimeter and centimeter-sized particles is a fundamental component of the planet formation process (Beckwith et al., 2000; Natta et al., 2007). Grain growth directly affects the optical properties of dust particles (Henning & Stognienko, 1996; D'Alessio et al., 2001), with composition and temperature having a lesser impact (Henning & Mutschke, 1997; Semenov et al., 2003; Boudet et al., 2005). At long wavelengths, the slope  $\alpha$  of the spectral energy distribution (SED,  $\nu S_\nu \propto \nu^{\alpha+1}$ ) can be related to the spectral index of the dust opacity  $\beta$  ( $\kappa_\nu \propto \nu^\beta$ ), in particular  $\beta = \alpha - 2$  for optically thin warm dust (Beckwith & Sargent, 1991; Miyake & Nakagawa, 1993). The millimeter dust opacity slope for small interstellar medium (ISM) dust grains is  $\beta_{ISM} \sim 1.7$  (Li & Draine, 2001). A smaller value of  $\beta$  is measured if larger millimeter-sized grains are

present (D’Alessio et al., 2001; Draine, 2006).

Observations of dust in disks from sub-mm to cm wavelengths (Testi et al., 2001; Calvet et al., 2002; Testi et al., 2003; Natta & Testi, 2004; Wilner et al., 2005; Rodmann et al., 2006; Lommen et al., 2009; Ricci et al., 2010b,a) have provided strong evidence for grain growth in disks. These results, obtained mainly from spatially unresolved observations, assumed a constant dust opacity (i.e., constant  $\beta$ ) throughout the disk. However, theoretical models of dust transport, fragmentation, and size evolution in protoplanetary disks predict that the average size of grains varies with the distance to the central star (hereafter referred to as radius, Dullemond & Dominik, 2005; Birnstiel et al., 2010). Hence, radial variations in the dust opacity slope are expected.

The increased sensitivity and angular resolution of current interferometers has enabled the first studies of radial variations of grain growth within circumstellar disks. Observations of disks in Taurus at 1.3 and 3 mm with CARMA<sup>1</sup> (Isella et al., 2010) and PdBI<sup>2</sup> (Guilloteau et al., 2011), have constrained  $\beta$  as a function of radius. However, these results are only sensitive to radial variations larger than  $\Delta\beta \sim 0.6\text{--}0.7$  at  $3\sigma$  in the best cases, limited by the small wavelength separation between the two bands being observed. Increased wavelength coverage has been obtained by adding cm-wave observations (Banzatti et al., 2011), but the low signal-to-noise ratio, before the Karl G. Jansky Very Large Array (VLA) upgrade, made such studies challenging. To significantly improve these constraints, and effectively compare them to theoretical predictions of grain growth, increased wavelength coverage and enhanced sensitivity are required.

Here we present the first results of a program that combines spatially resolved observations from sub-millimeter to centimeter wavelengths, to constrain radial variations of grain growth within circumstellar disks. The pre-main sequence star AS 209, also known as V1121 Oph, is a classical K5 T-Tauri star with high accretion rate ( $1.3 \times 10^{-7} M_{\odot} \text{yr}^{-1}$ , Johns-Krull et al., 2000). AS 209 is isolated from the main  $\rho$ -Ophiuchus cloud ( $\alpha = 16^{\text{h}}49^{\text{m}}15.3^{\text{s}}$ ,  $\delta = -14^{\circ}22'08.7''$ ) at a distance of  $131 \pm 50$  pc (van Leeuwen, 2007). Resolved 0.88 mm continuum observations reveal a smooth radial density structure down to  $0.3'' \sim 40$  AU (Andrews et al., 2009, 2010). We obtained additional spatially resolved observations at  $\lambda > 0.88$  mm, to study grain growth inside the AS 209 disk.

---

<sup>1</sup>Combined Array for Research in Millimeter-wave Astronomy

<sup>2</sup>Plateau de Bure Interferometer

## 5.2 AS 209 Observations

Submillimeter Array (SMA) observations at 0.88 mm were obtained between May 2006 and June 2007, in C, E, and V configurations ( $\sim 0.3''$  resolution), with total continuum bandwidth of 4 GHz. Its integrated flux density is  $577 \pm 60$  mJy at 0.88 mm. Andrews et al. (2009) presented a detailed discussion of the observations and data reduction.

CARMA observations at 2.8 mm were obtained between December 2009 and March 2010, in C, B, and A configurations spanning baselines of 30–1800 m ( $\sim 0.5''$  resolution), with total continuum bandwidth of 8 GHz. Its integrated flux density is  $40 \pm 6$  mJy at 2.8 mm. Atmospheric conditions were good, with zenith opacities  $\tau_{230\text{ GHz}} \leq 0.15$ , except for B configuration observations where  $\tau_{230\text{ GHz}} \sim 0.4$ . Data were calibrated using the Multichannel Image Reconstruction, Image Analysis and Display (MIRIAD) software package (Sault et al., 1995).

VLA observations at 8.0 and 9.8 mm (Ka-band) were obtained between Jan–May 2011 (project AC982), in CnB and BnA configurations, spanning baselines of 350 m to 36.4 km ( $\sim 0.2''$  resolution). Two 1 GHz basebands centered at 30.5 and 37.5 GHz provided 2 GHz of continuum bandwidth. At 8.0 and 9.8 mm the integrated flux density of AS 209 is  $1.2 \pm 0.1$  and  $0.7 \pm 0.1$  mJy, respectively. Data were calibrated using the Common Astronomy Software Applications (CASA).

For all datasets, quasar observations interspersed between science target observations were used to calibrate the complex antenna gains. Absolute flux calibration was obtained by observing Neptune for CARMA, Uranus and Titan for SMA, and 3C286 for VLA. For each telescope, calibrated visibilities coming from different configurations were corrected for proper motion (van Leeuwen, 2007) and compared over the spatial frequencies where these configurations overlap; these were found to agree within the absolute flux scale uncertainty ( $\sim 10 - 15\%$ ). Fourier inversion of the visibilities and cleaning of the dirty image to produce dust emission map, were performed using CASA.

The synthesized dust continuum maps for the AS 209 circumstellar disk are found in Figure 5.1. Each map extends  $4''$  by  $4''$ , corresponding to 500 AU at the adopted distance. A Briggs weighting scheme with a robust parameter of 0.7 was used to image SMA and CARMA observations, while VLA data were mapped with natural weighting. The image properties of these observations, together with the source photometry (obtained by fitting

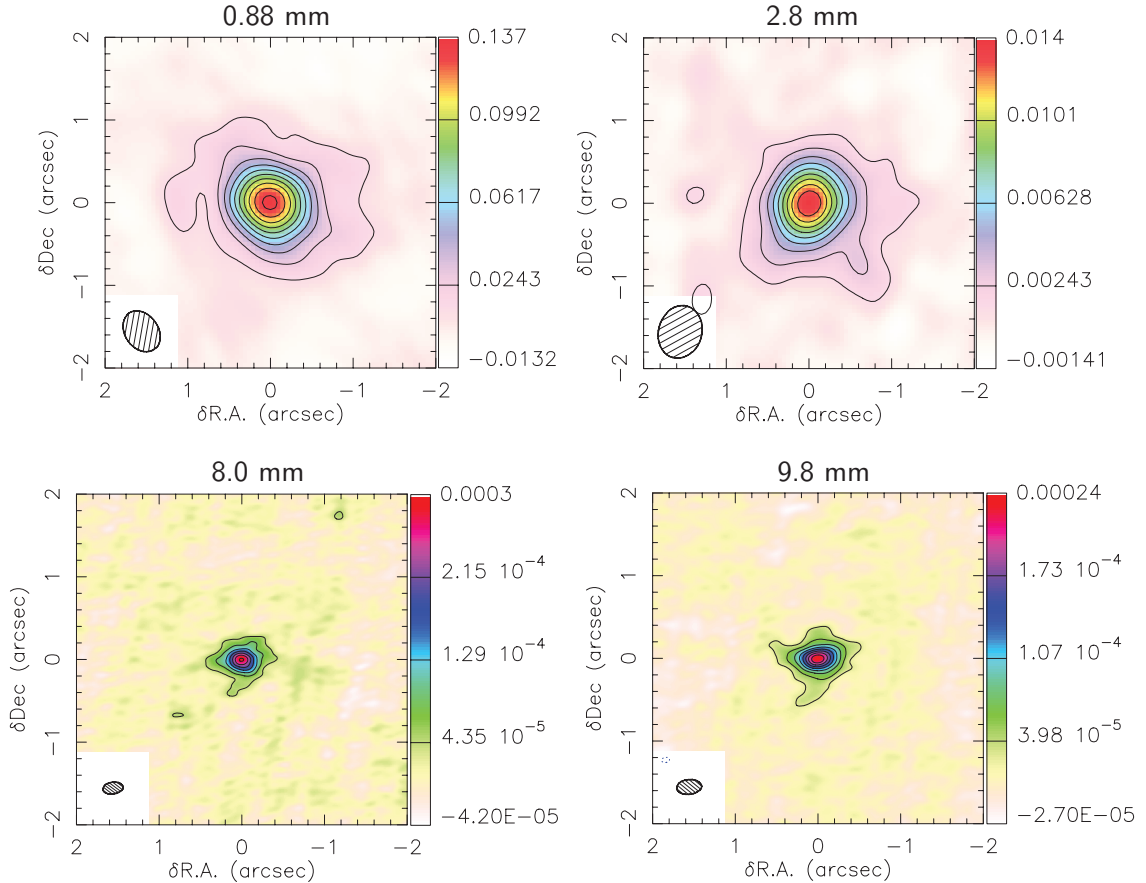


**Figure 5.1:** Aperture synthesis images of the continuum emission towards the young star AS 209, observed with SMA (0.88 mm), CARMA (2.8 mm) and VLA (8.0 and 9.8 mm, datasets imaged together with multi-frequency synthesis). For all panels, the colorbar units are Jy beam $^{-1}$ . Contours are drawn at  $3\sigma$  intervals (6 $\sigma$  for VLA observations), where  $\sigma$  is the RMS noise level on each map (see Table 5.1).

an elliptical Gaussian to each observation) and deconvolved sizes, can be found on Table 5.1.

### 5.3 Observational Results

Figure 5.2 presents the normalized real/imaginary part of the correlated emission from AS 209, as a function of spatial frequency (*uv*-distance), for each wavelength. The real part of the visibility will be constant with increasing spatial frequency for an unresolved point-source. In contrast, for AS 209 we measure a declining profile with increasing *uv*-distance, indicative of spatially resolved emission at all wavelengths. Furthermore, the short-wavelength emission (0.88, 2.8 mm) diminishes faster than the long-wavelength emission (8.0, 9.8 mm). Therefore, the long-wavelength emission has a more compact structure than the emission detected at short wavelengths.

Before interpreting these observational results in terms of spatial variations of grain properties, we explore other explanations for the differing amplitude profiles: (1) seeing affecting high-frequency observations would have to be  $> 1.2''$  at 0.88 mm ( $\times 10$  larger than the observed seeing; Andrews et al., 2009), (2) optically thick emission at short wavelengths: modeling of these observations (§5.4) shows that  $\tau < 1$  over the scales studied. Consequently, we conclude that the long-wavelength emission comes from a smaller region than the short-wavelength emission.

Before proceeding, we account for continuum emission not arising from dust, such as free-free emission from photoevaporative stellar winds. Such emission originates close to the star (within 10 AU for TW Hya, Pascucci et al., 2011), appearing as a point source at the

**Table 5.1:** Properties of the aperture synthesis imaging of AS 209

Telescope	$\lambda$ [mm]	Integrated Flux [mJy]	Image rms noise [mJy/beam]	Synthesized beam ['']	Beam P.A. [°]
SMA	0.88	$577 \pm 60$	4.4	$0.53'' \times 0.40''$	35.0
CARMA	2.8	$40 \pm 6$	0.47	$0.64'' \times 0.52''$	-16.2
VLA	8.0	$1.2 \pm 0.1$	0.014	$0.24'' \times 0.14''$	97.9
VLA	9.8	$0.7 \pm 0.1$	0.009	$0.31'' \times 0.18''$	95.7

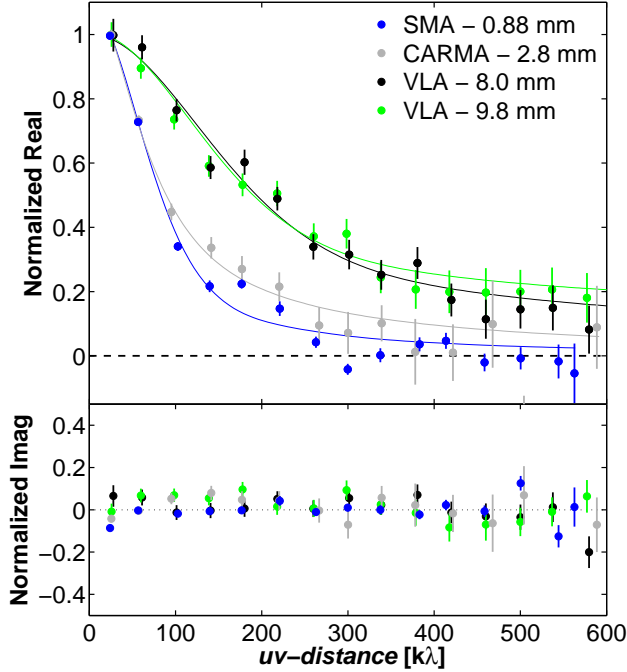


**Figure 5.2:** Real and imaginary part of the bin-averaged visibilities from AS 209 as a function of spatial frequency (*uv*-distance). Disk visibilities have been normalized by the measured flux density between *uv*-distances of 0–40 [ $k\lambda$ ], and deprojected assuming PA =  $86^\circ$ ,  $i = 38^\circ$  (Andrews et al., 2009). Filled circles and errorbars: correlated emission observed at different wavelengths, continuous lines: best-fit at each wavelength.

resolution of our observations. Indeed, in addition to the resolved emission detected with the VLA, we detect a point-like component (at *uv*-distances  $> 900 k\lambda$ ) with a flux density of  $0.08 \pm 0.02$  mJy (8 mm) and  $0.10 \pm 0.02$  mJy (9.8 mm), corresponding to  $\sim 7\%$  and  $\sim 14\%$  of the total emission at these wavelengths. However, VLA observations at 5.2 cm from the Disks@EVLA collaboration<sup>3</sup> (Chandler et al., in prep) place a  $3\sigma$  upper limit of  $72 \mu\text{Jy}$ , suggesting that the point-like emission at 8 and 9.8 mm may be dust emission. Nonetheless, we conservatively assume that this point-like emission is a free-free component, including it in models described next.

---

<sup>3</sup><https://safe.nrao.edu/evla/disks/>

## 5.4 Modeling Results

Observations were analyzed using the disk emission model described in [Isella et al. \(2009\)](#). The disk structure follows the two-layer disk approximation ([Chiang & Goldreich, 1997](#)), defined by the boundary between the disk surface layer (optically thin to the stellar radiation) and the disk interior (optically thick to the stellar emission). The disk is passively heated by the AS 209 star ( $L_\star = 1.5 L_\odot$ ,  $T_\star = 4250$  K,  $M_\star = 0.9 M_\odot$ , [Andrews et al., 2009](#)). Dust in the disk surface absorbs the stellar radiation and re-radiates this energy at longer wavelengths. Because this hot dust layer will be optically thin to its own thermal radiation, half of the surface layer emission will be radiated outwards while the rest will be radiated towards the disk, heating up its interior.

For the density structure, we employ the self-similar solution for a viscous accretion disk ([Lynden-Bell & Pringle, 1974](#))

$$\Sigma(R) = \Sigma_t \left( \frac{R_t}{R} \right)^\gamma \times \exp \left[ -\frac{1}{2(2-\gamma)} \left[ \left( \frac{R}{R_t} \right)^{(2-\gamma)} - 1 \right] \right] \quad (5.1)$$

where  $\Sigma_t$  corresponds to the surface density at radius  $R_t$ . This  $\Sigma(R)$  prescription behaves as a power law for small radii, decreasing exponentially at large radii.

We compute the dust opacity  $\kappa_\nu$  using Mie theory, assuming a population of compact spherical grains larger than  $a_{min} = 0.01 \mu\text{m}$ , in a power-law distribution of sizes,  $n(a) \propto a^{-q}$  for  $a_{min} < a < a_{max}$ . Optical constants for the astrophysical grains components were obtained from [Semenov et al. \(2003\)](#), [Zubko et al. \(1996\)](#), and [Warren \(1984\)](#). Fractional abundances were adopted from [Pollack et al. \(1994\)](#), in volume: 8% silicates, 30% organics, 62% water ice). Recent revisions for the solar oxygen abundance ([Asplund et al., 2009](#)) reduce this amount of water-ice. However, the effect on the disk modeling is minimal, with a difference in the disk structure constraints well within their uncertainties, as shown by [Isella et al. \(2010\)](#).

The best-fit model to a single wavelength observation is found through  $\chi^2$  minimization with 3 free parameters that describe the surface density ( $\Sigma_t, R_t, \gamma$ ), since the disk geometry is fixed to  $i = 38^\circ$  and PA=  $86^\circ$  based on molecular line observations ([Andrews et al., 2009](#)). The  $\chi^2$  probability distribution is sampled by varying the free parameters, generating a model state and comparing this state to the data in Fourier space, following the Markov

Chain Monte Carlo (MCMC) method described in [Isella et al. \(2009\)](#).

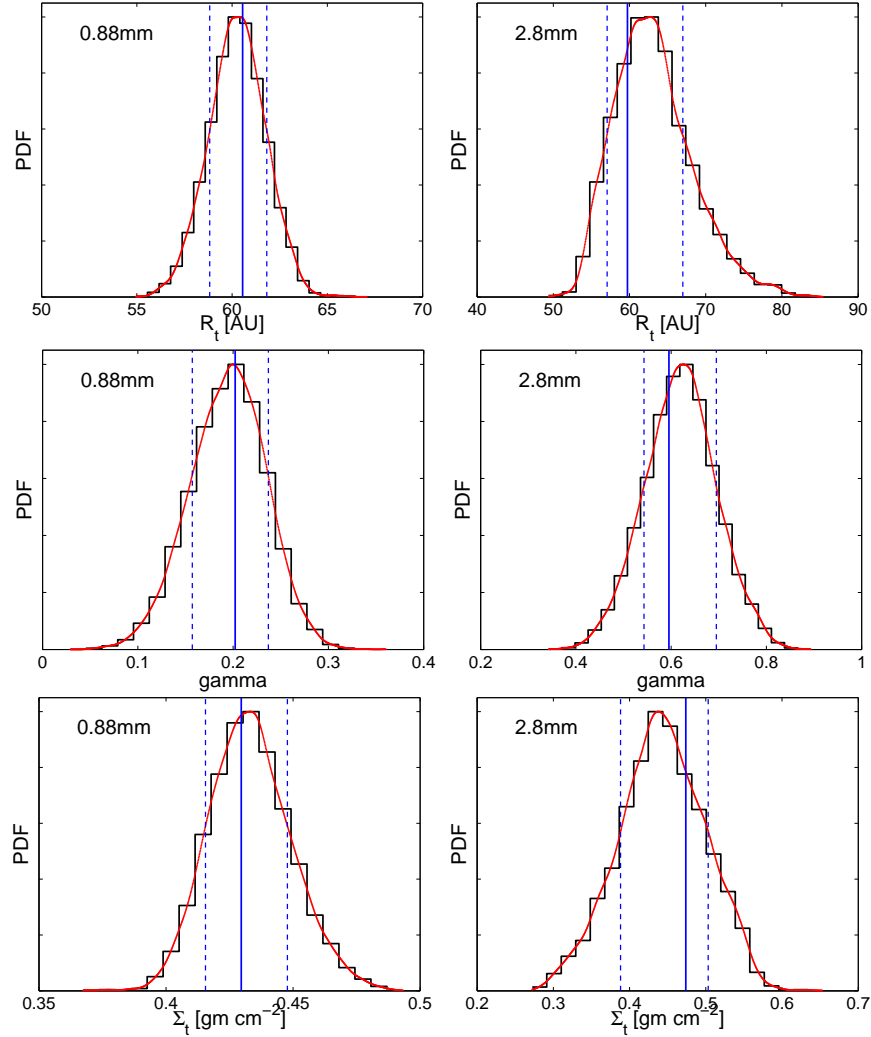
For this initial model fit, we select the maximum grain size ( $a_{max}$ ) and grain-size distribution slope ( $q$ ) that best fits the unresolved SED from sub-mm to cm wavelengths. For AS 209, these correspond to  $q = 3.5$ ,  $a_{max} = 1.3$  mm, resulting in  $\beta = 1.0$  between 0.88 and 8.0 mm. Then, assuming a *constant dust opacity* throughout the disk, each wavelength is fitted *separately* with the physical model described here. We obtain best-fit  $\Sigma(R)$  and  $T(R)$  profiles, that will be different for each wavelength if the assumption of a radially constant dust opacity is not valid ([Isella et al., 2010](#)).

Table 5.2 presents the best-fit model parameters, corresponding to those that minimize the  $\chi^2$ , and the  $1\sigma$  constraints for the 3-parameter fit to these multi-wavelength observations. The marginalized probability distribution function for each model parameter, constrained separately by each wavelength observation, is presented in Figure 5.3 for the short-wavelength observations (0.88 mm, left; 2.8 mm, right), and in Figure 5.4 for the long-wavelength observations (8.0 mm, left; 9.8 mm, right). The best-fit model visibility profiles at each wavelength are shown as continuous lines in Figure 5.2. Maps of the observed emission, with corresponding best-fit model and residual emission maps are shown in Figure 5.5.

Figure 5.6 shows the best-fit and  $3\sigma$  constraints on  $T(R)$  and the disk optical depth  $\tau_\lambda(R) = \kappa_\lambda \Sigma(R)$ , inferred from modeling each observation separately. As can be seen in this figure, a differing  $\Sigma(R)$  and  $T(R)$  was inferred for each wavelength when  $\kappa_\lambda$  is assumed to be constant with radius. We constrain  $R_t$  to be large for the short-wavelength emission

**Table 5.2:** Best-fit model parameters and constraints for AS 209

$\lambda$	$R_t$	$\gamma$	$\Sigma_t$
[mm]	[AU]		[gm cm $^{-2}$ ]
0.88	$61^{+1}_{-2}$	$0.20^{+0.03}_{-0.05}$	$0.43^{+0.02}_{-0.01}$
2.8	$60^{+7}_{-3}$	$0.60^{+0.10}_{-0.05}$	$0.47^{+0.03}_{-0.09}$
8.0	$24^{+1}_{-3}$	$0.36^{+0.09}_{-0.18}$	$1.75^{+0.39}_{-0.21}$
9.8	$26^{+2}_{-4}$	$0.31^{+0.15}_{-0.18}$	$1.97^{+0.47}_{-0.31}$



**Figure 5.3:** Marginalized probability distribution functions for the 3 model parameters ( $\Sigma_t, R_t, \gamma$ ) that define the AS 209 disk emission at 0.88 mm (left) and 2.8 mm (right). On each panel: *black histograms* correspond to the empirical PDF, *red curves* are the kernel smoothing density estimate obtained from the empirical PDF as described in section 3, *vertical lines* correspond to the best-fit value for each parameter (continuous line) and  $1\sigma$  confidence interval obtained from the marginalized PDF (dashed lines). The y-axis numerical values are inconsequential, and are intentionally left out.

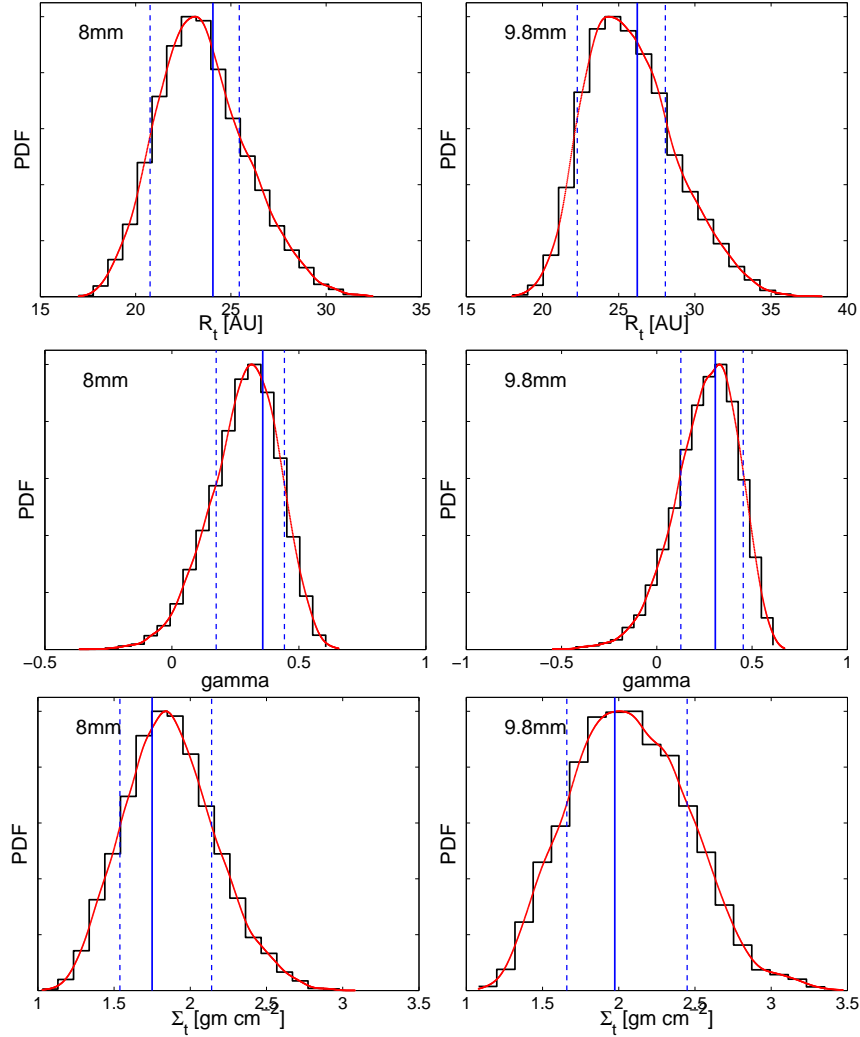


**Figure 5.4:** Marginalized probability distribution functions for the 3 model parameters ( $\Sigma_t, \gamma$ ) that define the AS 209 disk emission at 8.0 mm (left) and 9.8 mm (right). Colors and curve descriptions are the same as those in Figure 5.3.

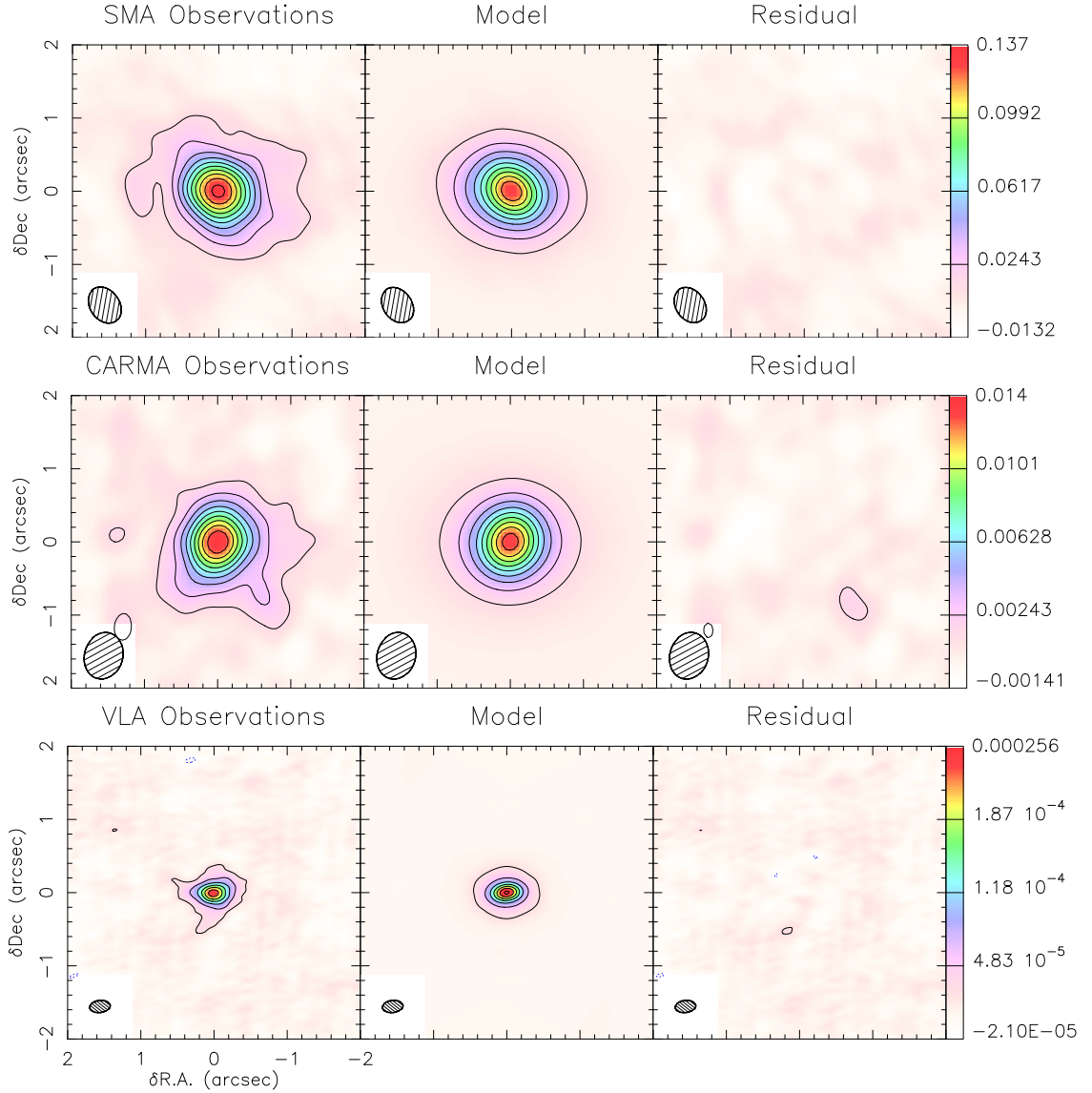


**Figure 5.5:** Continuum emission towards AS 209, observed at 0.88 mm (top panels), 2.8 mm (middle panels) and 8.0 and 9.8 mm (combined through multi-frequency synthesis, bottom panels). Each observation, accompanied by the best-fit disk emission and a residual map obtained by subtracting the best-fit model from the observations, used Briggs weighting with  $\text{robust} = 0.7$  (SMA, CARMA), while VLA data used natural weighting. Contours start at  $-3\sigma$ , stepping by  $3\sigma$  (CARMA, SMA) and  $6\sigma$  (VLA), where  $\sigma$  is the RMS noise on each map:  $\sigma_{\text{SMA}} = 4.4 \text{ mJy/beam}$ ,  $\sigma_{\text{CARMA}} = 0.47 \text{ mJy/beam}$ ,  $\sigma_{\text{VLA}} = 0.01 \text{ mJy/beam}$ .

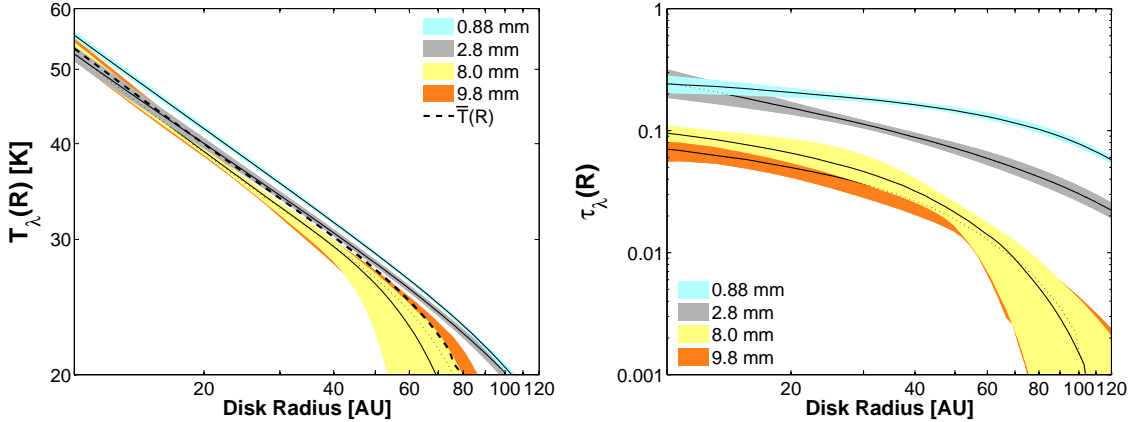


**Figure 5.6:** *Top:*  $T_\lambda(R)$  inferred from separate modeling of our multi-wavelength observations, assuming a constant dust opacity with radius. *Bottom:* Optical depth  $\tau_\lambda(R) = \kappa_\lambda \times \Sigma_\lambda(R)$  inferred from separate modeling of multi-wavelength observations, assuming a radially constant  $\kappa_\lambda$ . Colored regions:  $3\sigma$  confidence interval constrained by our observations, continuous line: best-fit model, dashed line on left panel: average temperature profile. The different  $\Sigma(R)$  and  $T(R)$  profiles for each wavelength portray a varying dust opacity with radius, and because of this, none of them is the true surface density and temperature profile of the disk.

( $R_t = 61 \pm 2$  AU from 0.88 mm and  $R_t = 60 \pm 6$  AU from 2.8 mm), while a small  $R_t$  is inferred at long-wavelengths ( $R_t = 24 \pm 3$  AU from 8 mm,  $R_t = 26 \pm 4$  AU from 9.8 mm). We note that the derived temperature profiles differ by  $< 4$  K for  $R < 70$  AU, and by  $\lesssim 10$  K for  $R > 70$  AU.

Since the disk is optically thin (right panel, Figure 5.6), the observed emission will depend directly upon the dust opacity and the disk mass:  $S_\lambda \propto \kappa_\lambda \times \Sigma \times B_\lambda(T)$ . Hence, our observations constrain the product  $\kappa_\lambda \times \Sigma \times B_\lambda(T)$ , where all these physical parameters ( $\kappa_\lambda, \Sigma, T$ ) depend on the disk radius, but only the dust opacity depends on the observed wavelength. The modeling presented above, assuming a constant dust opacity with radius and fitting each wavelength separately, has resulted in a wavelength-dependent  $\Sigma_\lambda(R)$  and  $T_\lambda(R)$ , which is unphysical but telling: the assumption of a constant  $\kappa_\lambda$  with radius is likely incorrect. Radial variations of the dust opacity are required to reconcile the differing visibility profiles (real part vs.  $uv$ -distance, Figure 5.2) and the wavelength-dependent  $\Sigma_\lambda(R)$  and  $T_\lambda(R)$  (Figure 5.6).

## 5.5 Discussion

### 5.5.1 Radial variations of $\beta$

Expanding on the work presented in Isella et al. (2010), if the *true* but unknown disk physical quantities are  $\bar{\kappa}_\lambda(R)$ ,  $\bar{\Sigma}(R)$ , and  $\bar{T}(R)$ , then at each wavelength

$$\kappa_\lambda \Sigma_\lambda(R) B_\lambda(T_\lambda(R)) = \bar{\kappa}_\lambda(R) \bar{\Sigma}(R) B_\lambda(\bar{T}(R)) \quad (5.2)$$

where the right-hand side of this equation corresponds to the true disk properties, and the left-hand side encompasses the constraints found from our multi-wavelength observations. Taking the ratio of equation 5.2 for  $\lambda_1 \neq \lambda_2$ , and assuming that at long wavelengths  $\kappa_\lambda \propto \lambda^{-\beta}$ , we obtain

$$\Delta\beta(R) = \log^{-1} \left[ \frac{\lambda_1}{\lambda_2} \right] \times \log \left[ \frac{\Sigma_{\lambda_1} B_{\lambda_1}(T_{\lambda_1}) / B_{\lambda_1}(\bar{T})}{\Sigma_{\lambda_2} B_{\lambda_2}(T_{\lambda_2}) / B_{\lambda_2}(\bar{T})} \right] \quad (5.3)$$

where  $\Sigma_\lambda$ ,  $T_\lambda$ , and  $\bar{T}$  depend on the radius  $R$ . Equation 5.3 is a useful prescription to constrain radial variations of the opacity spectral slope ( $\Delta\beta(R) = \beta(R) - \beta_C$ ) in dual-wavelength observations. Here  $\beta_C$  corresponds to the spectral slope of the assumed radially constant dust opacity.

In the Rayleigh-Jeans regime (when  $hc/\lambda \ll k_B T$ ,  $k_B$ : Boltzmann constant), knowledge of  $\bar{T}(R)$  to derive  $\Delta\beta(R)$  is unnecessary since  $B_\lambda(T) \propto T$ . However, in the cold outer disk and at short wavelengths, the Rayleigh-Jeans assumption is ill-founded (e.g.,  $h\nu \sim k_B T$  for  $T = 20$  K at 0.88 mm). Consequently, we require an estimate of  $\bar{T}(R)$ . Since the temperature profiles inferred from each wavelength ( $T_\lambda(R)$ ) are not very different, we average them to deduce  $\bar{T}(R)$  (dashed line on Figure 5.6).

Equation 5.3 shows that in logarithmic space  $\Delta\beta(R)$  is the slope of a line that goes through points  $\{x = \log(\lambda), y = \log[\Sigma_\lambda B_\lambda(T_\lambda)/B_\lambda(\bar{T})]\}$ , with  $y$  evaluated at radius  $R$ . Hence, to measure  $\Delta\beta(R)$  we find the slope of a straight line—in a least-square sense—that fits our constraints on the product  $\Sigma_\lambda \times B_\lambda(T_\lambda)/B_\lambda(\bar{T})$  from our set of multi-wavelength observations. To set confidence intervals on  $\Delta\beta(R)$ , we make use of the Bayesian approach upon which our modeling is based. Since the result of the MCMC algorithm is a fully sampled posterior probability distribution function (PDF) for all the model parameters,

we construct a PDF of the product  $\Sigma_\lambda \times B_\lambda(T_\lambda)/B_\lambda(\bar{T})$  at each radius  $R$  and for each wavelength. Random samples of these PDFs are taken at each wavelength, the slope of the line through points  $\{x = \log(\lambda), y = \log[\Sigma_\lambda \times B_\lambda(T_\lambda)/B_\lambda(\bar{T})]\}$  at a radius  $R$ , is computed. This slope corresponds to one random sampling of  $\Delta\beta(R)$ . Hence, the PDF for  $\Delta\beta(R)$  is constructed by performing a large number of random samples. The peak of this PDF is the best-fit value of  $\Delta\beta$  at radius  $R$ . Confidence intervals are derived from the region of the PDF that contains 68.3%, 95.5% and 99.7% of all samples at equal probability ( $1\sigma$ ,  $2\sigma$ , and  $3\sigma$ ).

Figure 5.7 presents the constraints on the radial variation of  $\beta$  obtained from our multi-wavelength observations. The values of  $\beta$  allowed by our observations are significantly different than  $\beta_{ISM} \sim 1.7$ , for  $R \lesssim 70$  AU. Furthermore, we find a gradient on  $\beta(R)$  inconsistent with a constant value at the  $10\sigma$  level.

### 5.5.2 Radial variations of $a_{max}$

To derive equation 5.3, the assumption of  $\kappa_\lambda \propto \lambda^{-\beta}$  must be satisfied. We caution that for  $a_{max} \sim 0.1$ –1 mm this approximation may break down (Draine, 2006), as illustrated in Figure 5.7 (right). Therefore, rather than inferring  $a_{max}(R)$  from  $\beta(R)$ , we constrain it

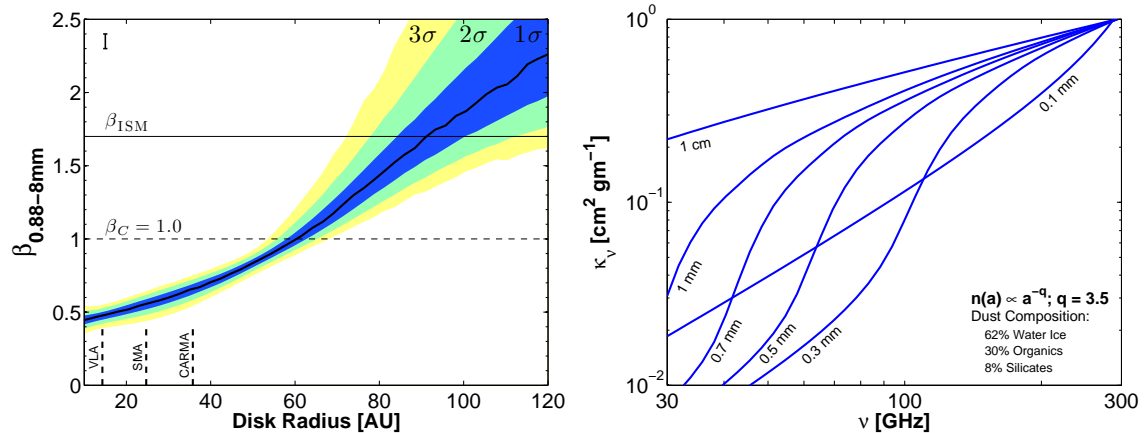


**Figure 5.7:** *Left:* Dust opacity spectral slope,  $\beta$ , vs. radius, inferred from multi-wavelength observations of the AS 209 disk. Black line: best-fit  $\beta(R)$ , colored areas: confidence interval constrained by our observations. Vertical dashed-lines indicate the spatial resolution of our observations, error-bar in top-left corner indicates additional systematic uncertainty on  $\beta(R)$  arising from amplitude calibration uncertainty. *Right:* Dust opacity (normalized at 300 GHz) for  $a_{max}$  between 0.1–10 cm. Note that the power-law assumption,  $\kappa_\nu \propto \nu^\beta$ , breaks down for (sub-)mm-sized grains.

directly by fitting a specific dust opacity  $\bar{\kappa}_\lambda$  to the constraints on the product  $\kappa_\lambda \times \Sigma_\lambda \times B_\lambda(T_\lambda)$  at each radius. With a knowledge of  $\bar{T}(R)$ , and for a fixed set of dust properties (composition and grain-size distribution), we estimate the values of  $a_{max}$  and  $\bar{\Sigma}$  that satisfy equation 5.2, now written as

$$\kappa_\lambda \Sigma_\lambda(R) \frac{B_\lambda(T_\lambda(R))}{B_\lambda(\bar{T}(R))} = \bar{\kappa}_\lambda(a_{max}(R)) \bar{\Sigma}(R) \quad (5.4)$$

where the right-hand side corresponds to our model (with parameters  $a_{max}$  and  $\bar{\Sigma}$ ), and the left-hand side has been constrained by our multi-wavelength observations (i.e., we have a PDF for the product  $\kappa_\lambda \times \Sigma_\lambda(R) \times \frac{B_\lambda(T_\lambda(R))}{B_\lambda(\bar{T}(R))}$ ).

At each radius  $R$ , we constructed a two-dimensional grid of parameters  $\{a_{max}, \bar{\Sigma}\}$ . At each point in the grid, we compute the product  $\bar{\kappa}_\lambda(a_{max}) \times \bar{\Sigma}$  at each wavelength. We then find the probability that such measurement will have occurred (given our observational constraints on the left-hand side of Equation 5.4), and construct the likelihood function of the parameters  $\{a_{max}, \bar{\Sigma}\}$ . Best-fit values for  $a_{max}$  and  $\bar{\Sigma}$  are found by maximizing the likelihood, confidence intervals are obtained from the marginalized likelihoods.

Figure 5.8 presents our constraints on  $a_{max}(R)$  and  $\bar{\Sigma}(R)$  for two representative values of  $q$ . The same composition presented in §5.4 is assumed, however a different dust mixture will influence the derived  $a_{max}(R)$ . For a composition that includes updated oxygen abundances, the inferred maximum grain size decreases by a factor of two, which is well within the uncertainties of this derivation given other unknowns parameters (e.g., grain-size distribution slope). Across the disk, grains have grown at least up to  $\sim 0.5$  mm, with small grains present in the outer disk and large grains in the inner disk.

We compare our observational constraints with theoretical models of grain growth, employing the approximations presented in Birnstiel et al. (2012) for the evolution of  $a_{max}$  with radius. Since the true  $\bar{\Sigma}(R)$  profile constrained by our observations depends on the assumed value of  $q$  (see Figure 5.8), these theoretical prescriptions will depend on  $q$  as well. Our observational constraints on  $a_{max}$  are consistent with a *radial-drift-limited* grain population, where the head-wind felt by dust particles makes them spiral towards the star. A *fragmentation dominated* population, where the turbulent relative motion of particles causes collisions that either grow or fragment these grains, seems incompatible for standard

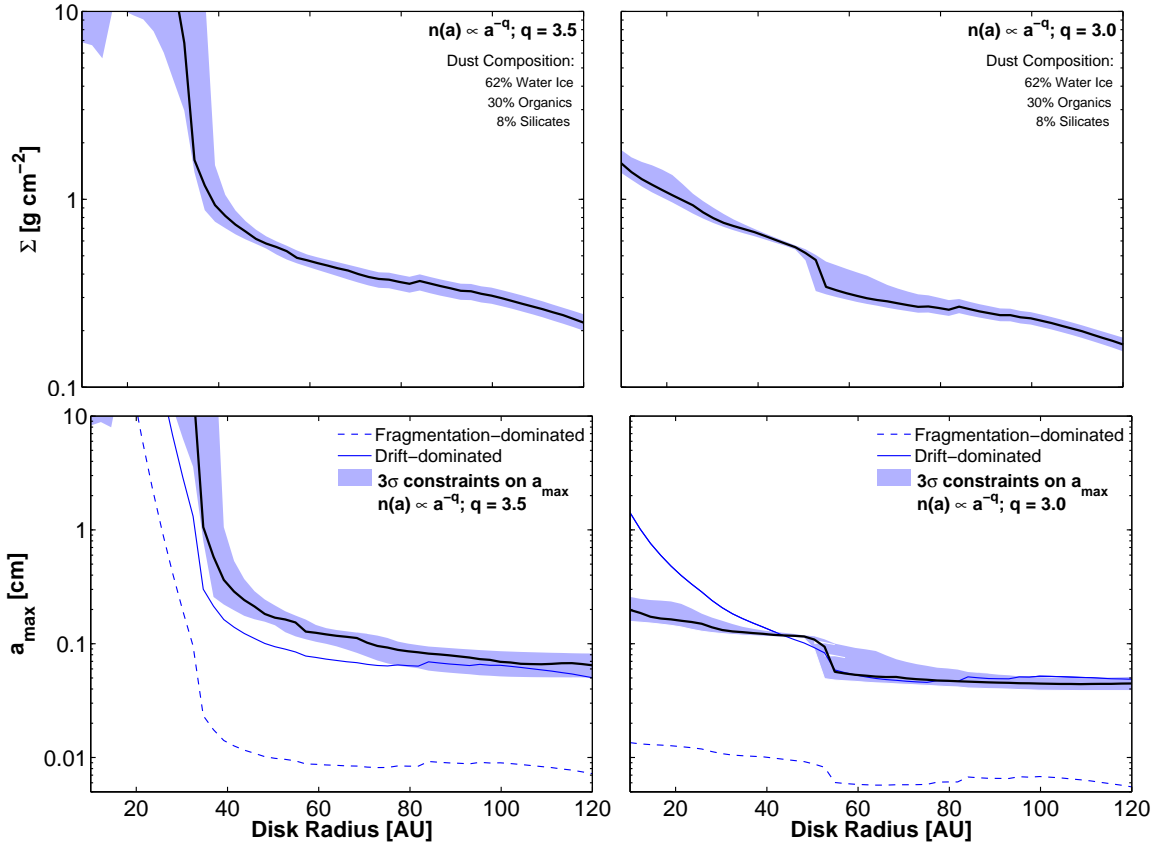


**Figure 5.8:** Surface density (top) and maximum grain size as a function of radius (bottom), for two grain size distributions:  $q = 3.5$  (left),  $q = 3.0$  (right). Black line: best-fit, shaded region:  $3\sigma$  confidence interval. Assumed grain properties are specified in figure legend. We compare our observational constraints with theoretical grain evolution models (Birnstiel et al., 2012), that include fragmentation and radial drift.

values of the turbulence parameter ( $\alpha_t = 0.01$ , Shakura & Sunyaev, 1973), fragmentation threshold velocity ( $u_t = 10$  m/s, Blum & Wurm, 2008), and 100:1 gas-to-dust ratio. These curves represent barriers that prevent grains for further size increase, hence, the smaller of the two is considered the upper limit to growth. However, the parameters that go into deriving the fragmentation limit are very uncertain, while the physics and parameters in radial drift are better established. Either no fragmentation barrier exists (for a low-turbulence disk,  $\alpha_t < 0.01$ , the maximum collision speed never reaches the fragmentation threshold velocity in AS 209, making fragmentation impossible) or the gas-to-dust ratio is  $\sim \times 10$  larger, allowing for the fragmentation-limited barrier to be consistent with our  $a_{\max}(R)$  constraint.

### 5.5.3 Summary

We have obtained multi-wavelength spatially-resolved observations at 0.88, 2.8, 8.0, and 9.8 mm of the AS 209 circumstellar disk. These observations reveal a wavelength-dependent structure, explained as radial variations of the dust opacity across the disk. We find a change in  $\Delta\beta > 1$  between the inner ( $\sim 20$  AU) and outer ( $\sim 120$  AU) disk, inconsistent with a constant  $\beta$  value. This gradient in  $\beta(R)$  implies that a significant change in the dust properties as a function of radius must exist. We interpret this gradient as a decrease in the maximum grain size with radius: going from several centimeters or more in the inner disk to sub-mm-sized grains in the outer disk. When compared with theoretical models of dust size evolution (Birnstiel et al., 2012), we find that our observational constraint on  $a_{max}(R)$  agrees with a radial drift-dominated population, for reasonable values of the composition, grain-size distribution, and disk properties.

## Acknowledgments

We acknowledge T. Birnstiel for useful discussions. A.I., J.M.C., L.M.P acknowledge support from NSF award AST-1109334. The National Radio Astronomy Observatory is a facility of the National Science Foundation operated under cooperative agreement by Associated Universities, Inc. Support for CARMA construction was derived from the states of California, Illinois, and Maryland, the James S. McDonnell Foundation, the Gordon and Betty Moore Foundation, the Kenneth T. and Eileen L. Norris Foundation, the University of Chicago, the Associates of the California Institute of Technology, and the National Science Foundation. Ongoing CARMA development and operations are supported by the National Science Foundation under a cooperative agreement, and by the CARMA partner universities. The SMA is a joint project between the Smithsonian Astrophysical Observatory and the Academia Sinica Institute of Astronomy and Astrophysics, funded by the Smithsonian Institution and Academia Sinica. Part of this research was carried out at the Jet Propulsion Laboratory, Caltech, under a contract with the National Aeronautics and Space Administration.

## Chapter 6

# Grain Growth in the Circumstellar Disks of DoAr 25 and CY Tau

The analysis of sub-arcsecond resolution observations of two circumstellar disks, CY Tau and DoAr 25, are presented here. These additional sources were investigated to explore variations in the grain properties for a larger sample of protoplanetary disks. A comparison between the observationally inferred maximum grain size of the dust grain population and theoretical models of grain growth is also presented.

### 6.1 DoAr 25

DoAr 25<sup>1</sup> is a pre-main sequence K5 star located in the L1688 dark cloud, the main cloud of the larger rho-Ophiuchus molecular cloud complex. The distance to this cloud has been measured to be  $120 \pm 5$  pc, from VLBI astrometry of two members of the cloud (Loinard et al., 2008). Analysis of the Hipparcos catalog of trigonometric parallaxes have found slightly larger values of the distance to L1688; e.g., Mamajek (2008) determined its distance to be  $131 \pm 3$  pc employing seven cloud members. For this study, a distance to DoAr 25 of 125 pc is adopted.

This young star (3.8 Myr of age, Andrews et al., 2009) is surrounded by a bright disk at sub-millimeter wavelengths ( $S_\nu = 0.563 \pm 0.003$  Jy at  $880 \mu\text{m}$ , Andrews et al., 2009), and has a low mass accretion rate ( $< 2 \times 10^{-10} M_\odot \text{ yr}^{-1}$  Natta et al., 2006). Spitzer IRS spectra from Olofsson et al. (2009) and McClure et al. (2010) reveal a disk with a flat spectrum

---

<sup>1</sup>also known as GY92 17, WSB 29, and WLY 1-34

between 10–30 microns (Figure 6.1), and a small excess over the stellar photosphere between 1–15  $\mu\text{m}$ , which may be indicative of the existence of a small inner hole. However, previous high angular resolution observations have not been able to reveal this cavity in the dust continuum emission (Andrews et al., 2009, 2008)

A detailed analysis of multi-wavelength resolved observations of the dust continuum emission towards DoAr 25 is presented. These observations constrain any radial variations of the dust properties that might be present in the DoAr 25 circumstellar disk. In addition, these observational constraints are compared with theoretical models that consider dust growth and disk evolution.

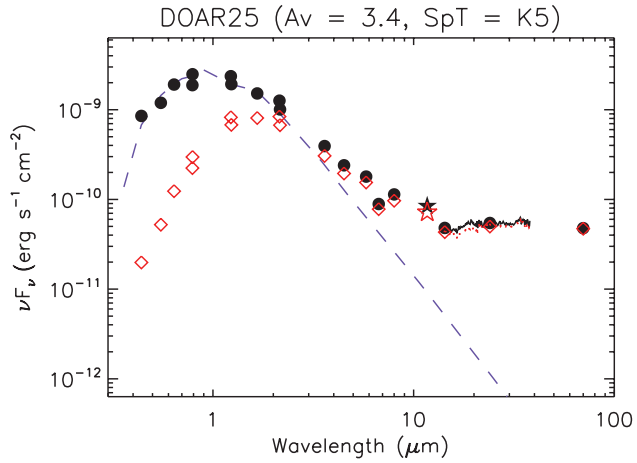


**Figure 6.1:** Spectral energy distribution of DoAr 25 from McClure et al. (2010): Empty squares and dotted lines represent the original, extinguished data, while filled circles and solid lines are the extinction-corrected data. Optical photometry is mainly from Wilking et al. (2005); Platais et al. (1998); Bouvier & Appenzeller (1992); Monet et al. (2003). Near-infrared photometry is from the DENIS Consortium and 2MASS surveys. Mid-infrared data are from ISO (Bontemps et al. 2001), the c2d 2007 December data release, and the IRS spectra presented in McClure et al. (2010). Photospheres are calculated from the Kenyon & Hartmann (1995) colors and are indicated by dashed lines. Credit: McClure, et al. 2010, Astrophysical Journal, Supplement, 188, 75, reproduced with permission from AAS.

### 6.1.1 Observational results

The synthesized dust continuum maps for the circumstellar disk of DoAr 25, obtained at 0.88 mm with the SMA, 2.8 mm with CARMA, and 8.0 and 9.8 mm with the VLA, are found in Figure 6.2. Each map extends  $4''$  by  $4''$ , corresponding to 500 AU at the adopted distance. Observations of DoAr 25 at 2.8 mm made use of the Paired Antennas Calibration System, to correct for atmospheric radio-seeing at the longest baselines of the array. The improvement of the observations from the extended array configurations is presented in subsection 6.1.2.

For imaging VLA observations a natural weighting scheme was adopted (i.e., each visibility weighted by the inverse of its thermal noise squared, or a robust parameter of 2.0), obtaining a beam size close to  $0.2''$ . For CARMA and SMA a Briggs weighting scheme is employed, with a robust parameter of 0.7 for SMA and 0.3 for CARMA, since these observations lacked the long baselines (compared to the VLA) necessary for high-angular resolution imaging with natural weighting. The image properties of these observations, together with the source photometry (obtained by fitting an elliptical Gaussian to each observation) and deconvolved sizes, can be found on Table 6.1.

Figure 6.3 presents the real and imaginary part of the visibility as a function of  $uv$ -distance for each wavelength. Each visibility has been deprojected by the disk's inclination and position angle inferred from the disk modeling (see next section), before averaging into  $uv$ -bins with a width of  $50 k\lambda$ . Also, each visibility bin has been normalized by the measured flux at the first  $uv$ -bin, between  $0 - 50 k\lambda$ . Given the decline of the real part of the visibility profile at each wavelength, much similar to the AS 209 disk, the circumstellar disk emission from DoAr 25 is resolved from 0.88 to 9.8 mm. Furthermore, since the short-wavelength

**Table 6.1:** Properties of the aperture synthesis imaging of DoAr 25

Telescope	$\lambda$ [mm]	Integrated Flux [mJy]	Image rms noise [mJy/beam]	Synthesized beam ['']	Beam P.A. [°]
SMA	0.88	$514 \pm 20$	3.6	$0.48'' \times 0.34''$	16.0
CARMA	2.8	$30.0 \pm 1.2$	0.26	$0.66'' \times 0.34''$	-179.7
VLA	8.0	$1.16 \pm 0.06$	0.019	$0.23'' \times 0.16''$	69.3
VLA	9.8	$0.65 \pm 0.03$	0.011	$0.31'' \times 0.20''$	74.1

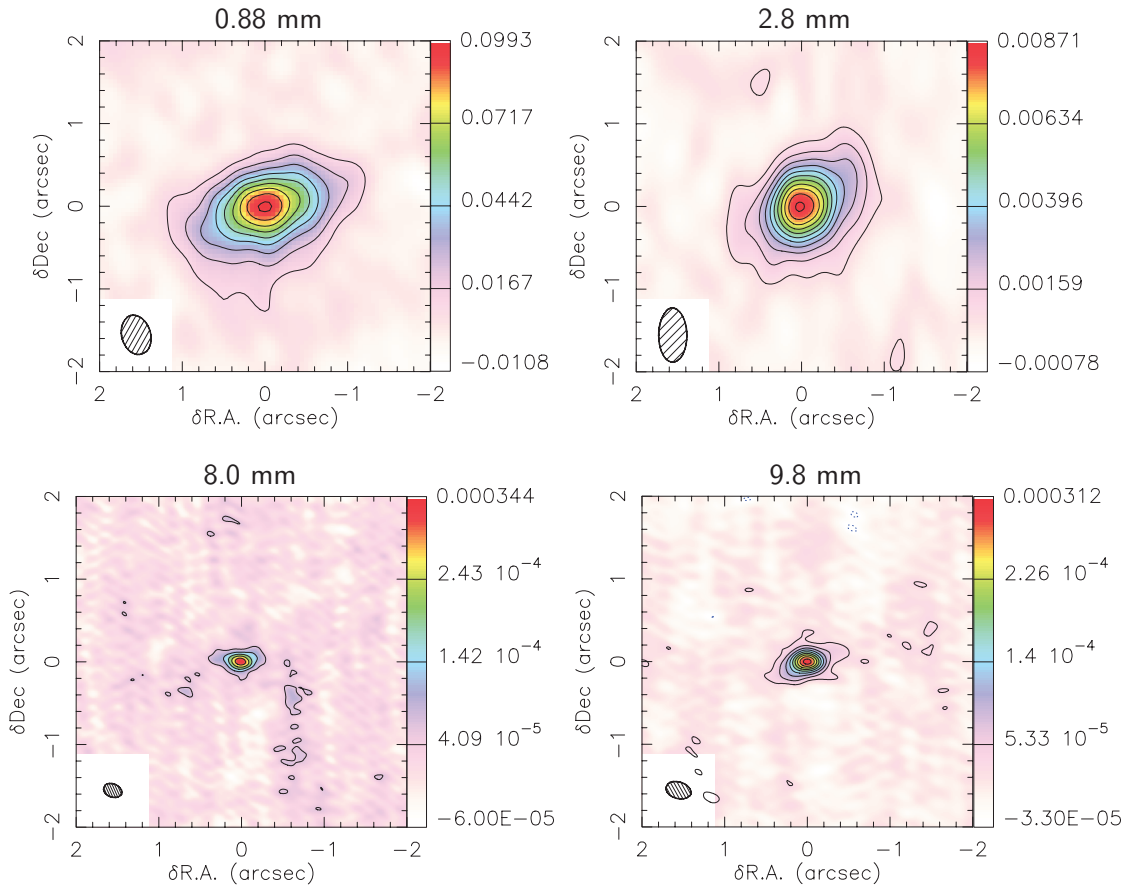


**Figure 6.2:** Aperture synthesis images of the continuum emission towards the young star DoAr 25, observed with SMA (0.88 mm, top left panel), CARMA (2.8 mm, top right panel) and VLA (8.0 mm, bottom left; 9.8 mm bottom right panel). For all panels, the colorbar units are Jy beam<sup>-1</sup>, and contours are drawn at 3 $\sigma$  intervals, where  $\sigma$  is the RMS noise level on each map (see Table 6.1).

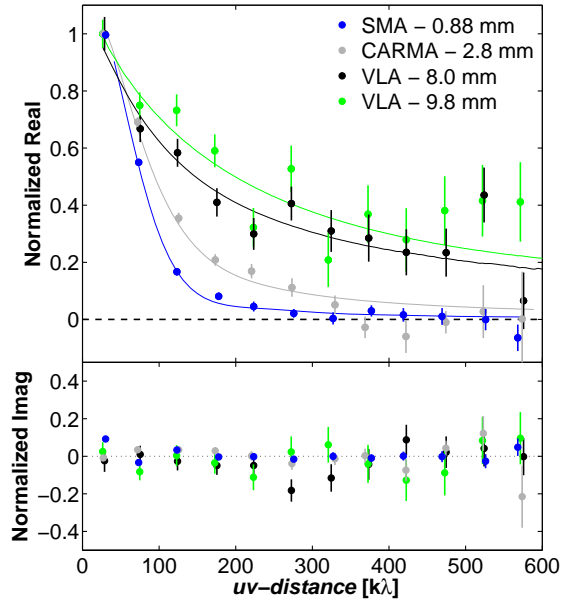


**Figure 6.3:** Normalized real and imaginary part of the correlated emission from DoAr 25 as a function of spatial frequency (*uv*-distance). The visibilities from the disk have been deprojected assuming a position angle of  $\sim 110^\circ$  and inclination of  $\sim 60^\circ$ , as derived from the disk emission modeling. Each bin has been normalized by the measured flux between *uv*-distances of 0 – 50 [ $k\lambda$ ]. Filled circles and error bars of different color correspond to the correlated real and imaginary parts of the emission observed at different wavelengths (0.88 mm: blue, 2.8 mm: gray, 8.0 mm: black). Continuous lines: best-fit disk emission model at each wavelength.

emission (traced by the 0.88 mm and 2.8 mm) is more extended than the long-wavelength emission (traced by the VLA observations), these data suggest the existence of a wavelength-dependent structure, as it was found for AS 209. In the next section, this peculiar aspect of the DoAr25 disk will be explained as radial variations of the dust properties across the circumstellar disk.

The possibility of the long-wavelength measurement being contaminated by free-free emission from photoevaporative stellar winds is also considered. VLA observations at 6 cm (C-band) from the Disks@EVLA collaboration, were employed to constraint the amount of contamination. DoAr 25 is not detected at 6 cm, with an RMS of 18  $\mu$ Jy. Extrapolating the  $3\sigma$  upper limit at C-band to the wavelengths of the Ka-band observations, and assuming optically thick free-free emission ( $S_\nu \propto \nu^{0.6}$ ), a contribution of at most 10% and 15% at 8.0 and 9.8 mm would be expected. However, unlike for AS 209, a significant point-like

component in the largest  $uv$ -distances sampled by our observations is not detected (at 8.0 mm, a flux density of  $0.13 \pm 0.09$  mJy for spatial frequencies larger than  $1125\text{ k}\lambda$  is detected, while at 9.8 mm a flux density of  $0.0 \pm 0.03$  mJy for spatial frequencies larger than  $920\text{ k}\lambda$  is measured). Hence, no free-free contribution was included in the modeling of these observations.

### 6.1.2 The effect of C-PACS in the DoAr25 disk

C-PACS was employed for the tracks obtained in the two most extended configurations of CARMA, in order to improve the radio-seeing of our observations. As noted before, the improvement obtained by the paired antennas technique strongly depends on the calibrator strength and separation to the science target. For DoAr 25, a calibrator just  $1.2^\circ$  away was available, whose centimeter-wave flux density was about  $\sim 1 - 2$  Jy during the time period of our CARMA observations.

Figure 6.4 and 6.5 present the images of the calibrated CARMA observations before and after applying the C-PACS correction, to illustrate the range of improvement that C-PACS can provide. Despite the varied weather conditions (listed in Chapter 2), after application of C-PACS the DoAr 25 observations are generally improved, with a diminished RMS noise level in the map, and a larger source peak flux and improved coherence. The best-weather A-configuration observations (third row, Figure 6.4), reveal a double-peaked feature in the center of the disk, typical of circumstellar disks with cleared inner regions. Unfortunately, this particular feature is barely resolved at the limit of available angular resolution and it is not seen in the other multi wavelength observations. Hence, the DoAr 25 observations were modeled without a vacated inner hole; the disk inner radius,  $R_{in}$ , is left as the dust sublimation radius, defined in Chapter 4.

### 6.1.3 Modeling of dust continuum emission

The multi-wavelength observations of DoAr 25 were analyzed using the disk emission model described in Section 3. Similar to the analysis of the AS 209 disk, the dust opacity  $\kappa_\nu$  is computed assuming a grain population of compact spherical grains larger than  $a_{min} = 0.01\text{ }\mu\text{m}$ , in a power-law distribution of sizes,  $n(a) \propto a^{-q}$  for  $a_{min} < a < a_{max}$ , and whose composition follows that of Pollack et al. (1994). To begin modeling of these observations,

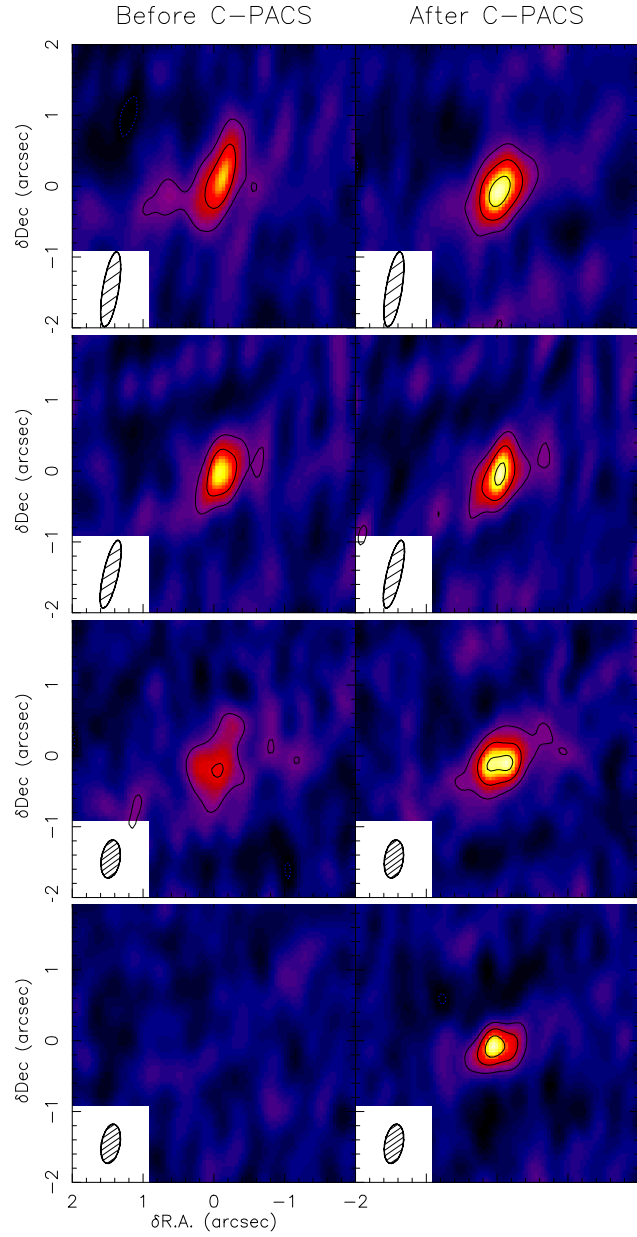


**Figure 6.4:** Comparison between gain calibrated CARMA A-configuration observations without C-PACS calibration (left panels) and with C-PACS calibration (right panels). Each row corresponds to different dates of observations (from top to bottom dates are: 2010-Nov-29, 2010-Nov-30, 2010-Dec-03, 2010-Dec-12). Contours start at  $-3\sigma$  and step by  $3\sigma$ , where  $\sigma$  correspond to the RMS noise level in the map. The improvement in the image RMS varies between 10–30%, with an increase in the signal-to-noise ratio (due to improved coherence) by factors of 1.3–10.

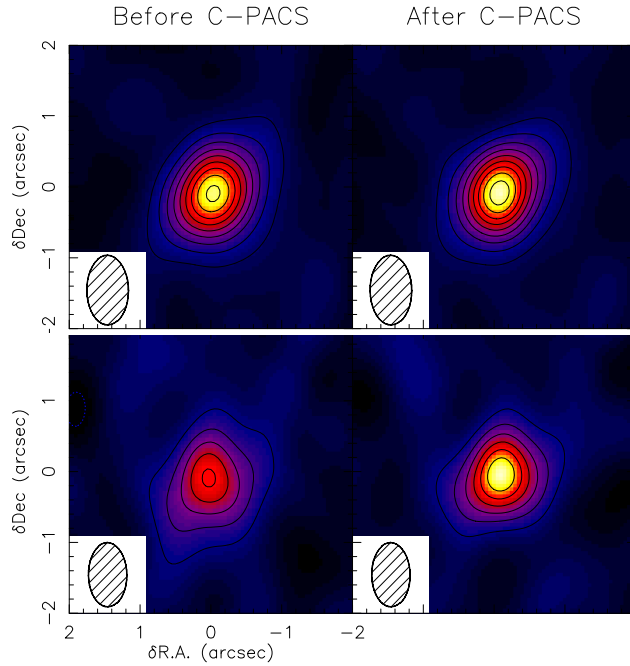


**Figure 6.5:** Comparison between gain calibrated CARMA B-configuration observations without C-PACS calibration (left panels) and with C-PACS calibration (right panels). Each row corresponds to different dates of observations (top: 2010-Jan-06, bottom: 2010-Jan-09). Contours start at  $-3\sigma$  and step by  $3\sigma$ , where  $\sigma$  correspond to the RMS noise level in the map. The improvement in the image RMS varies 10–15%, with an increase in the signal-to-noise ratio (due to improved coherence) by factors of 1.2–2.

the maximum grain size and grain-size distribution slope that best reproduces the unresolved SED, from sub-mm to cm wavelengths, was selected. For DoAr 25, these correspond to  $q = 3.5$ ,  $a_{max} = 1.5$  mm, which results in a opacity spectral slope  $\beta = 0.91$  between 0.88 and 8.0 mm.

Each wavelength is fitted separately assuming a constant dust opacity throughout the disk. As opposed to the model constraints derived for AS 209, in the case of DoAr 25 there are no molecular line observations that have previously constrained the disk geometry. Hence, the modeling of these observations and the  $\chi^2$  minimization is performed with two additional parameters, besides  $\{\Sigma_t, R_t, \gamma\}$ , that describe the disk geometry ( $i$  and *P.A.*). During the initial modeling of the long-wavelength observations (8.0 and 9.8 mm), the value of  $\gamma$  was constrained to be between  $\gamma = 1$ –2.5, while the values of  $R_t$  and  $\Sigma_t$  were rather unconstrained. It happens that when  $\gamma = 2$ , the prescription for the disk surface density

$\Sigma(R)$  (see Equation 4.12) becomes a power law of the form:  $\Sigma(R) = \Sigma_t \left(\frac{R}{R_t}\right)^2$ . With such a power-law prescription, the parameters  $\Sigma_t$  and  $R_t$  are naturally correlated and is not possible to constrain them simultaneously; one of them needs to be fixed while the other is let to vary. Since the surface density for DoAr 25, as traced by observations with  $\lambda = 8.0, 9.8$  mm, has a power-law-like behavior with  $\gamma$  approaching a value of 2, it was decided that for these long-wave observations, the transitional radius value ( $R_t$ ) was fixed and only four parameters were varied: those that describe the surface density profile ( $\Sigma_t, \gamma$ ) and those that describe the disk geometry ( $i, P.A.$ ).

Table 6.2 presents the best-fit model parameters, corresponding to those that minimize the  $\chi^2$ , and the  $1\sigma$  constraints for the 5-parameter fit to the short-wavelength observations and the 4-parameter fit to the long-wavelength data. The marginalized probability distribution function (PDF) for each model parameter, constrained separately by each wavelength observation, is presented in Figure 6.6 for 0.8 mm, Figure 6.7 for 2.8 mm, and Figure 6.8 for 8.0 mm (left) and 9.8 mm (right). The deprojected real and imaginary parts of the visibility profiles, for each of the best-fit model observations at different wavelengths, is presented in Figure 6.3 (continuous lines) in conjunction with the observed visibility profiles. Maps of the observed emission at each wavelength, with corresponding best-fit model and map of residual emission are shown in Figure 6.9.

From each separate model fitting a best-fit surface density and temperature profiles ( $\Sigma(R)$  and  $T(R)$ ) were obtained. These might be different for each wavelength if the assumption of a constant dust opacity with radius is not valid. Figure 6.10 shows the best-fit and

**Table 6.2:** Best-fit model parameters and constraints for DoAr 25

$\lambda$ [mm]	$i$ [°]	P.A. [°]	$R_t$ [AU]	$\gamma$	$\Sigma_t$ [gm cm $^{-2}$ ]
0.88	$61.6 \pm 1.2$	$109_{-2}^{+1}$	$63 \pm 2$	$-0.12_{-0.04}^{+0.07}$	$0.57_{-0.03}^{+0.02}$
2.8	$58.0_{-2.4}^{+2.5}$	$118 \pm 3$	$51_{-3}^{+2}$	$0.33_{-0.06}^{+0.08}$	$0.66_{-0.05}^{+0.06}$
8.0	$60_{-19}^{+8}$	$105_{-18}^{+14}$	$50^a$	$1.02_{-0.06}^{+0.11}$	$0.43_{-0.05}^{+0.04}$
9.8	$78_{-4}^{+3}$	$113 \pm 5$	$70^a$	$1.47_{-0.15}^{+0.14}$	$0.26_{-0.04}^{+0.03}$

<sup>a</sup> Parameter fixed to this value during modeling

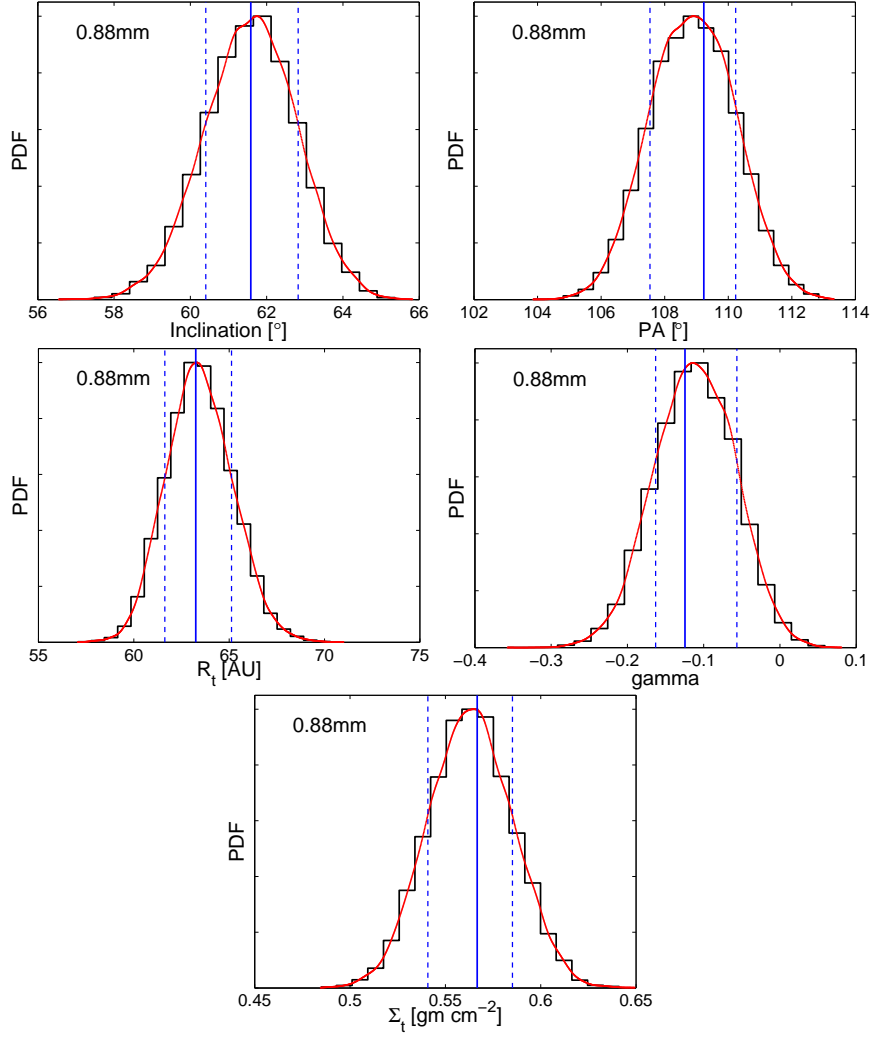


**Figure 6.6:** Marginalized probability distribution functions for the 5 model parameters ( $i, P.A., \Sigma_t, R_t, \gamma$ ) that define the disk emission at 0.88 mm for DoAr 25. On each panel: *black histograms* correspond to the empirical PDF, *red curves* are the kernel smoothing density estimate obtained from the empirical PDF as described in section 3, *vertical lines* correspond to the best-fit value for each parameter (continuous line) and  $1\sigma$  confidence interval obtained from the marginalized PDF (dashed lines). The y-axis numerical values are inconsequential, and are intentionally left out.

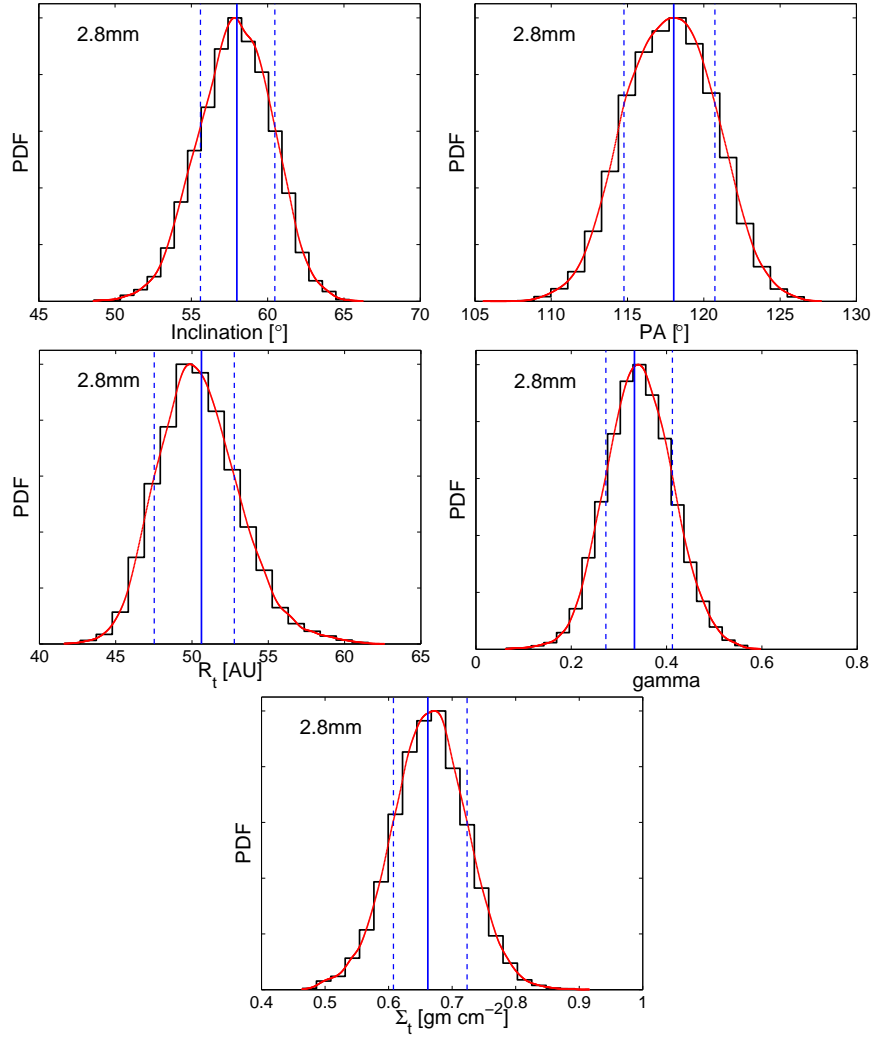


**Figure 6.7:** Marginalized probability distribution functions for the 5 model parameters ( $i$ , P.A.,  $\Sigma_t$ ,  $R_t$ ,  $\gamma$ ) that define the disk emission at 2.8 mm for DoAr 25. Colors and curve descriptions are the same as those in Figure 6.6.

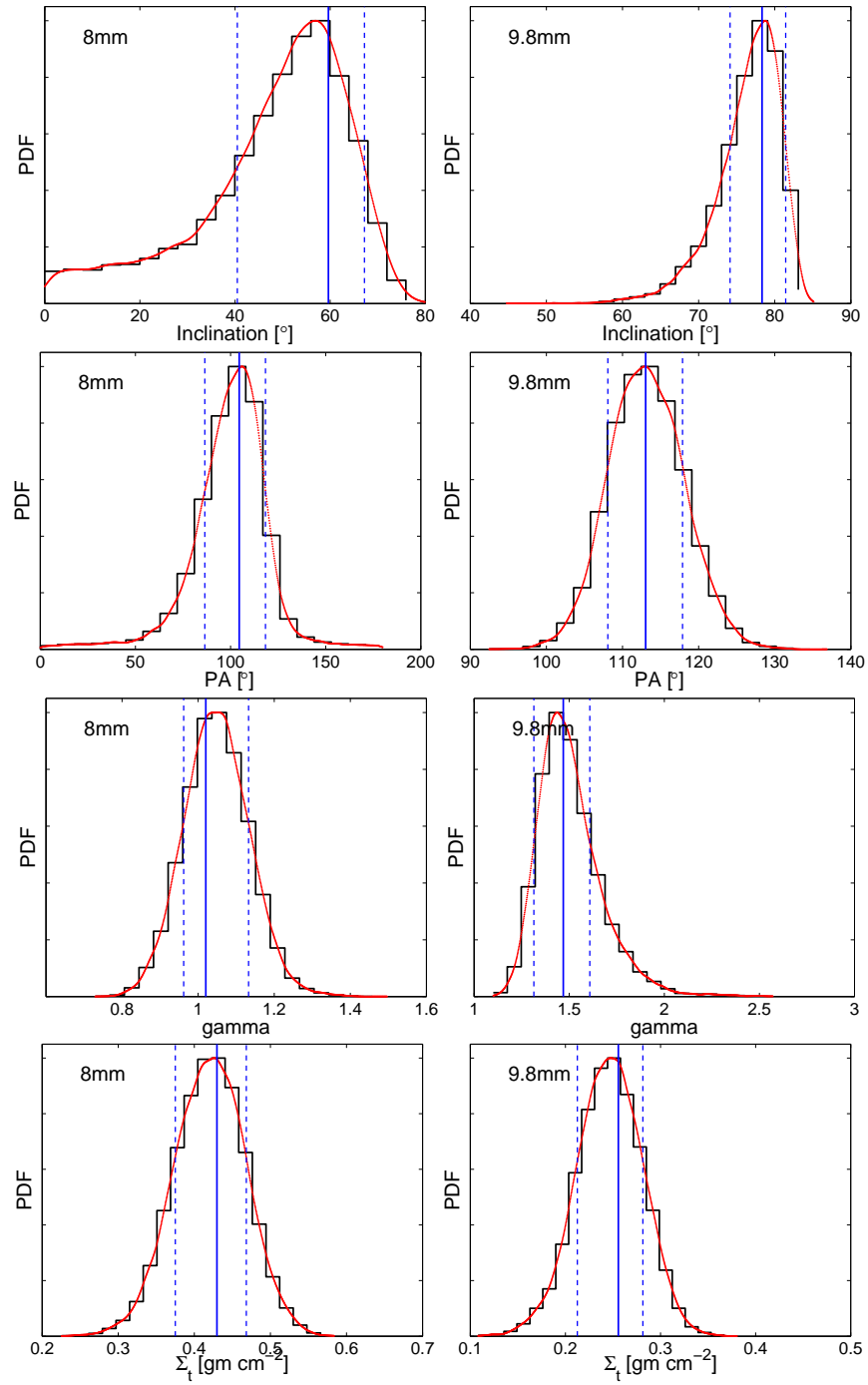


**Figure 6.8:** Marginalized probability distribution functions for the 4 model parameters ( $i, P.A., \Sigma_t, \gamma$ ) that define the disk emission at 8.0 and 9.8 mm for DoAr 25. Colors and curve descriptions are the same as those in Figure 6.6.

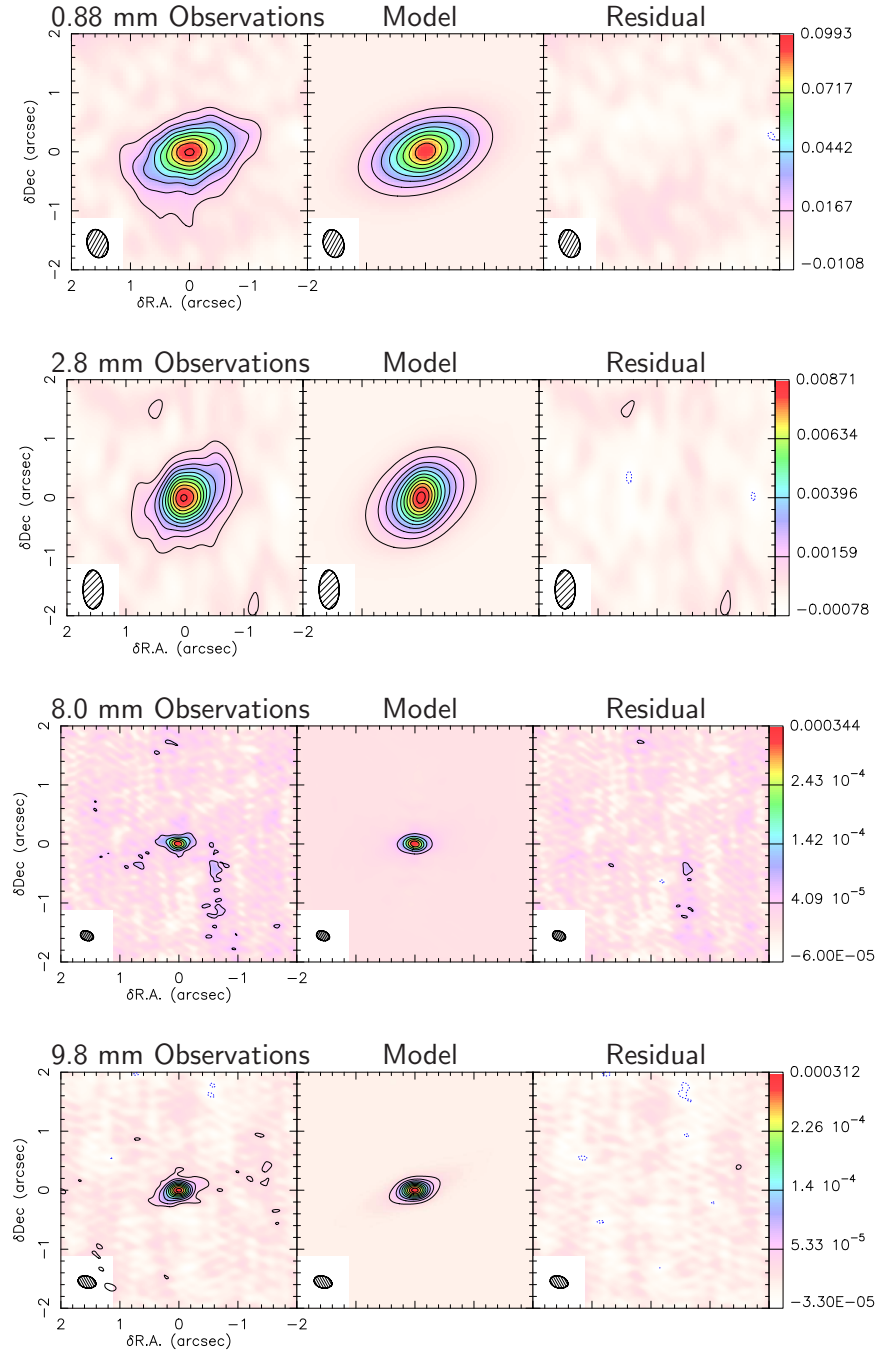


**Figure 6.9:** Modeling of the dust continuum emission towards DoAr 25, as observed with SMA (0.88 mm, top panels), CARMA (2.8 mm, second row of panels) and VLA (8.0 and 9.8 mm, last-two bottom panels). Each observation is accompanied by the best-fit disk emission, and a residual map obtained by subtracting the best-fit model from the observations in the Fourier domain. Maps were obtained using Briggs weighting with robust = 0.7 (0.88 mm) and robust = 0.3 (2.8 mm) to match observed beam size, while the VLA data used natural weighting. Contours start at  $-3\sigma$ , stepping by  $3\sigma$ , where  $\sigma$  is the RMS noise on each map (Table 6.1).

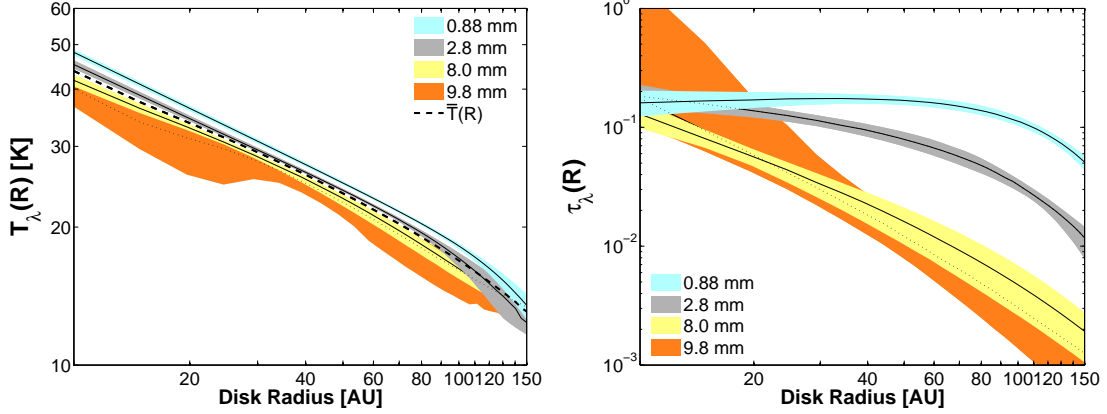


**Figure 6.10:** *Left:*  $T_\lambda(R)$  inferred from separate modeling of our multi-wavelength observations, assuming a constant dust opacity with radius. *Right:* Optical depth  $\tau_\lambda(R) = \kappa_\lambda \times \Sigma_\lambda(R)$  inferred from separate modeling of multi-wavelength observations, assuming a radially constant  $\kappa_\lambda$ . Colored regions:  $3\sigma$  confidence interval constrained by our observations, continuous line: best-fit model, dashed line on left panel: average temperature profile, assumed to be  $\bar{T}(R)$ . The different  $\Sigma(R)$  and  $T(R)$  profiles for each wavelength portray a varying dust opacity with radius, and because of this, none of them is the true surface density and temperature profile of the disk.

$3\sigma$  constraints on the temperature  $T(R)$  (left) and the disk optical depth  $\tau_\lambda(R) = \kappa_\lambda \times \Sigma(R)$  (bottom), inferred from modeling each observations separately, and where  $\kappa_\lambda$  was assumed to be constant with radius. Note that the best-fit temperature profiles from these multi-wavelength observations are practically the same, differing by  $< 3$  K for  $R > 25$  AU, and by  $< 8$  K inside 25 AU. Also note that the dust emission is optically thin at all wavelengths for  $R > 20$  AU, this will be the case even if our model computes a mid-plane dust temperature off by an order of magnitude. Finally, note that the model is consistent with an optically thick region at 9.8 mm inwards of  $\sim 11$  AU, at a  $3\sigma$  level, however this region is well inside the attained angular resolution at this wavelength.

Modeling of the 0.88 and 2.8 mm data resulted in surface density profiles that are flat in the inner disk regions (perhaps accounting for an inner disk hole). This flat profile can be seen on the left panel of Figure 6.10 for  $\lambda = 0.88, 2.8$  mm, and in the inferred best-fit value of  $\gamma$  that is close to zero at both wavelengths. However, the modeling of VLA observations at 8.0 and 9.8 mm present a completely different picture. The inferred  $\Sigma(R)$  profile were strongly peaked and resulted in a best-fit  $\gamma$  value close to 1 for 8.0 mm and 1.5 for 9.8 mm

(with a long tail towards values of  $\gamma > 1.5$ , see Figure 6.8). Again, it is evident that the short-wavelength emission traces a different structure in the dust than the long-wavelength observations.

Since the emission is optically thin (right panel, Figure 6.10), the observed emission will depend directly upon the dust opacity and the disk mass:  $S_\nu \propto \kappa_\nu \times \Sigma \times B_\nu(T)$ . Hence, our observations constrain the product  $\kappa_\nu \times \Sigma \times B_\nu(T)$ , where all these physical parameters ( $\kappa_\nu, \Sigma, T$ ) depend on the disk radius, but only the dust opacity depends on the observed wavelength. The modeling presented above, assuming a constant dust opacity with radius, and fitting each wavelength separately, portrays a different  $\Sigma(R)$  inferred for each wavelength, signifying that the assumption of a radially constant dust opacity is not permitted. Radial variations of the dust opacity are required to reconcile the differing visibility profiles (real part vs.  $uv$ -distance, Figure 6.3) and the wavelength-dependent  $\Sigma_\lambda(R)$  and  $T_\lambda(R)$  (Figure 6.10).

#### 6.1.4 Radial variations of the dust opacity

As with the case of the AS 209 circumstellar disk, there is observational evidence that radial variations in the dust properties exist in the disk surrounding DoAr 25. These are interpreted as changes in the dust opacity spectral index  $\beta$  with radius. Following the same Bayesian approach outlined in the previous chapter, the observational constraints on  $\beta(R)$  obtained for DoAr 25 are presented in Figure 6.11. The values of  $\beta$  allowed by these multi-wavelength observations are significantly different than  $\beta_{\text{ISM}} \sim 1.7$ , for  $R \lesssim 80$  AU, and are consistently below the ISM value of  $\beta$  throughout the disk extent. Furthermore, we found a gradient on  $\beta(R)$  inconsistent with a constant value of  $\beta$  at the  $15\sigma$  level.

As shown before, the constraint in  $\beta(R)$  depends on the assumption that the dust opacity follows a power-law with frequency,  $\kappa_\nu \propto \nu^\beta$ , which might not necessarily be the case. Rather than inferring  $a_{\max}(R)$  from  $\beta(R)$ , the variations in the dust properties, particularly  $a_{\max}$ , can be directly constrained without this assumption. With the premise that radial variations of  $\kappa_\lambda$  are only caused by changes in the maximum grain size with radius, the range of allowed maximum grain sizes can be estimated by fitting a specific dust opacity  $\bar{\kappa}_\lambda$ —that is dependent on  $a_{\max}$ —to the constraints on the product  $\kappa_\nu \times \Sigma_\lambda \times B_\nu(T_\lambda)$  at each radius. Figure 6.12 presents the constraints found for  $a_{\max}(R)$  and  $\bar{\Sigma}(R)$  for DoAr25,

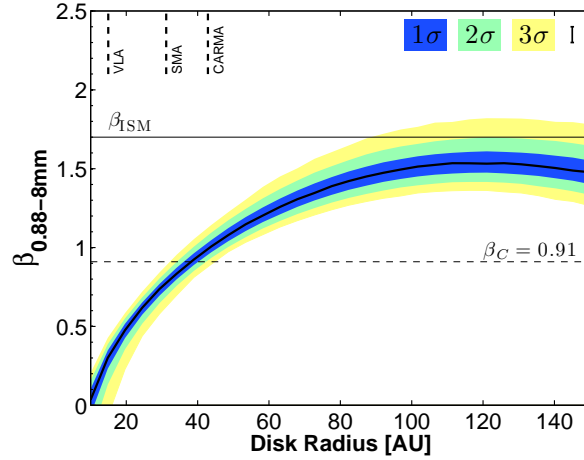


**Figure 6.11:** Dust opacity spectral slope,  $\beta$ , as a function of radius, inferred from multi-wavelength observations of the DoAr 25 disk. Black line: best-fit  $\beta(R)$ , colored areas: confidence interval constrained by our observations. Vertical dashed-lines indicate the spatial resolution of our observations. The errorbar in top-right corner indicates additional systematic uncertainty on  $\beta(R)$  arising from amplitude calibration uncertainty.

assuming the same dust composition as in section 6.1.3, and for two representative grain size distribution slopes ( $q = 3.5$  left,  $q = 3.0$  right). Across the disk, grains have grown at least up to  $\sim 0.3$  mm, with small grains present in the outer disk and large grains in the inner disk.

These observational constraints on  $a_{max}(R)$  are compared with Birnstiel et al. (2010) theoretical models of grain growth evolution, employing the approximations presented in Birnstiel et al. (2012) for the evolution of  $a_{max}$  with radius. These theoretical prescriptions will depend on the adopted grain size distribution slope,  $q$ , since our constraint on the surface density with radius depends on  $q$  as well. For DoAr 25, we find a consistent agreement between our observational constraint on the maximum grain size and the growth barrier imposed by radial drift of macroscopic particles, at least up to  $\sim 90$  AU. Farther out in the disk, for  $R > 90$  AU, our observational constraint is well above the radial drift barrier, with dust grains in the outer disk that have managed to somehow overcome this growth barrier.

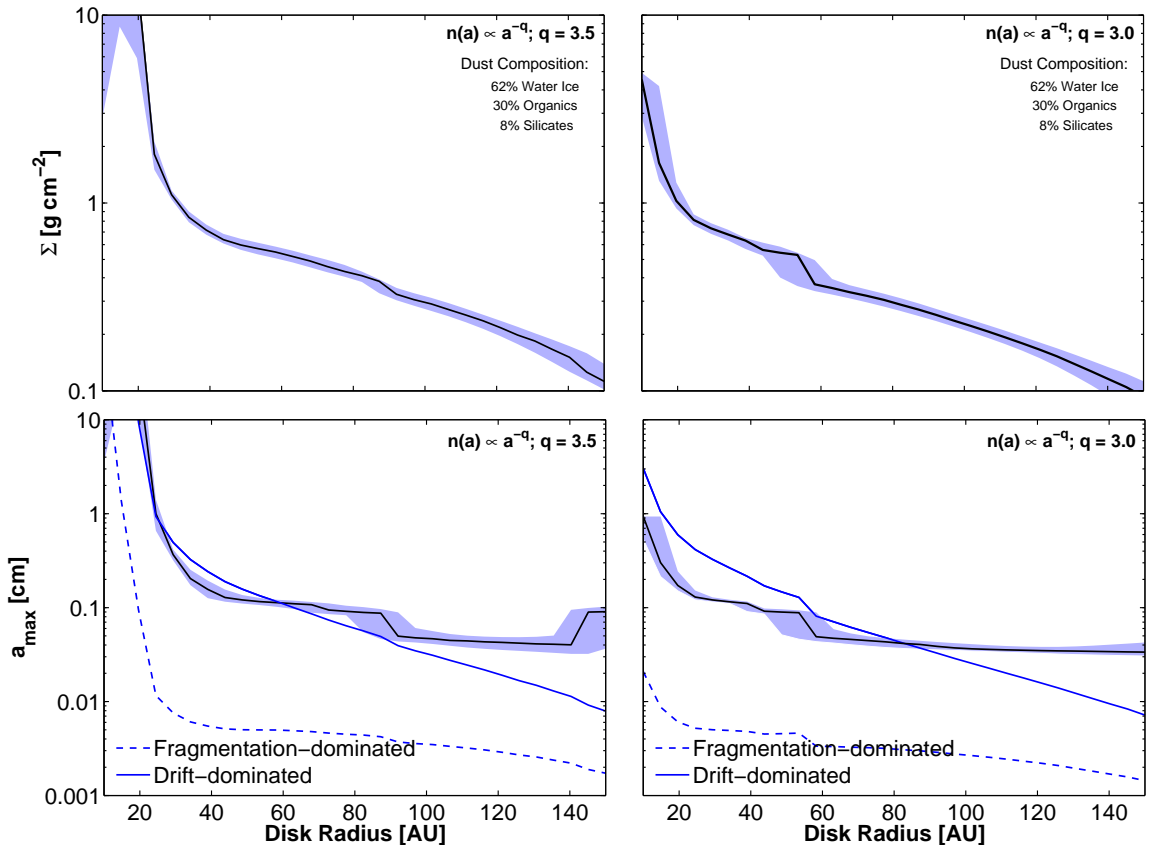


**Figure 6.12:** Surface density (top) and maximum grain size as a function of radius (bottom), for two grain size distributions:  $q = 3.5$  (left),  $q = 3.0$  (right) in the DoAr 25 disk. Black line: best-fit, shaded region:  $3\sigma$  confidence interval. Assumed grain properties are specified in figure legend. We compare our observational constraints with theoretical grain evolution models (Birnstiel et al., 2012), that include fragmentation and radial drift.

## 6.2 CY Tau

CY Tau is a pre-main sequence M2 star, located in the Taurus star-forming region, at a distance of  $\sim 140$  pc (Loinard et al., 2008). This young star ( $2.3 \pm 0.4$  Myr old, Bertout et al., 2007), has been studied by Guilloteau et al. (2011) in an attempt to constrain radial variations of  $\beta$  in a dual frequency survey using observations at 1.3 and 2.7mm (Figure 6.13, left) with the Plateau de Bure Interferometer (PdBI). Both a power-law surface density profile ( $\Sigma(R) = \Sigma_0(R/R_0)^p$ ) and a viscous-disk evolution similarity solution for  $\Sigma(R)$  (equation 4.12) were reasonable fits to their data (Figure 6.13, right).

The region of the disk inwards of their effective angular resolution ( $\sim 50$  AU at 1.3 mm and  $\sim 100$  AU at 2.7 mm) are inaccessible, nevertheless, an attempt to constrain radial variations of  $\beta$  is conducted. Two different parameterizations of the dust opacity spectral slope are employed: one where  $\beta(R)$  has a logarithmic dependance with radius (motivated by power-law surface density profiles), and another ad-hoc functional form that is *fixed* on its extremes to  $\beta = 0$  at  $R = 0$  (representative of large grains) and  $\beta = 1.7$  at large radii

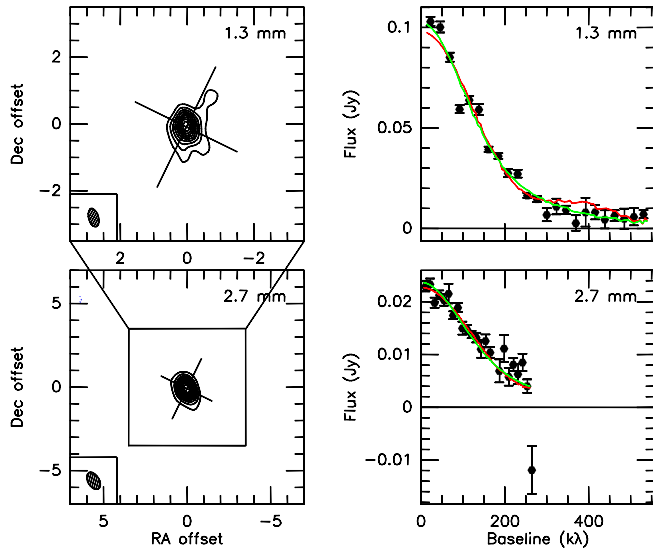


**Figure 6.13:** Adapted from Guilloteau et al. (2011). *Left:* CY Tau observations at 1.3 and 2.7 mm with PdBI. All contours are drawn at  $4\sigma$  ( $\sigma = 3.3$  mJy beam $^{-1}$  at 1.3 mm,  $\sigma = 1.6$  mJy beam $^{-1}$  at 2.7 mm). *Right:* Deprojected and circularly averaged visibilities for each wavelength (red: best-fit for power-law  $\Sigma(R)$ , green: best-fit for similarity solution  $\Sigma(R)$ ). Credit: S. Guilloteau, et al., Astronomy and Astrophysics, 529, A105, 2011, reproduced with permission ©ESO.

(representative of small ISM grains). The constraints on  $\beta$  vs. radius (at the  $1\sigma$  level) found for CY Tau are shown in Figure 6.14 (blue color: logarithmic dependance of  $\beta$  with radius, red color: ad-hoc functional form for  $\beta(R)$ , green color: allowed values outside of the outer disk radius). Given the closeness in frequency of the two wavelength studied, the lack of long baselines at 2.7 mm (see 2.7 mm visibility profile in Figure 6.13), and disregarding the ad-hoc functional form that imposes a variation of  $\beta$  with radius, the  $\beta(R)$  constraints obtained in Guilloteau et al. (2011) are consistent with a constant value of  $\beta$  at the  $3\sigma$  level for CY Tau.

In the following, a detailed analysis of multi-wavelength resolved observations of the dust continuum emission towards CY Tau, from 1.3 mm to 7.1 mm, is presented. Different from the work presented in Guilloteau et al. (2011), an agnostic approach regarding the variations of  $\beta$  with radius is taken, where no functional form for  $\beta(R)$  is assumed. In addition, the observational constraints obtained for CY Tau are compared with theoretical models that consider dust growth and disk evolution.

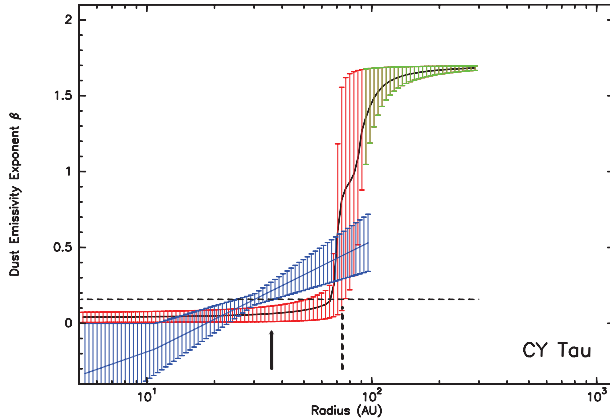


**Figure 6.14:** Adapted from Guilloteau et al. (2011): Constraints on the variations of the dust emissivity index  $\beta$  with radius. The red hatched area indicate the allowed range of values using a prescription where  $\beta(R)$  is *fixed* on its extremes to  $\beta = 0$  at  $R = 0$  (representative of large grains) and  $\beta = 1.7$  at large radii (representative of small ISM grains). The blue hatched area uses the power law prescription for  $\Sigma(R)$  and is truncated at the outer radius found in the power law model. Credit: S. Guilloteau, et al., Astronomy and Astrophysics, 529, A105, 2011, reproduced with permission ©ESO.

### 6.2.1 Observational results

The synthesized dust continuum maps for CY Tau’s circumstellar disk, obtained at 1.3 and 2.8 mm with CARMA, and 7.1 mm with the VLA, are found in Figure 6.15. Each map extends  $4''$  by  $4''$ , corresponding to 560 AU at the adopted distance. For imaging the 1.3 mm CARMA observations as well as the 7 mm VLA observations, a natural weighting scheme was adopted (i.e., a robust parameter of 2.0), obtaining a beam size close to  $0.25''$ . For 2.8 mm CARMA observations a Briggs weighting scheme is employed, with a robust parameter of  $-1.0$ , since these observations lacked the long baselines (compared to the VLA) necessary for high angular resolution imaging with natural weighting. The image properties of these observations, together with the source photometry (obtained by fitting an elliptical Gaussian to each observation) and deconvolved sizes, can be found on Table 6.3.

Figure 6.16 presents the real and imaginary part of the visibility as a function of  $uv$ -distance for each wavelength. Each visibility has been deprojected by the disk’s inclination and position angle inferred from the disk modeling (see next section), before averaging into  $uv$ -bins with a width of  $40 \text{ k}\lambda$ . Also, each visibility bin has been normalized by the measured flux at the first  $uv$ -bin, between  $0 - 40 \text{ k}\lambda$ . Given the decline of the real part of the visibility profile at each wavelength, much similar to the AS 209 and DoAr 25 disk, the circumstellar disk emission from CY Tau is resolved from 1.3 to 7.1 mm. Furthermore, since the short-wavelength emission (traced by the CARMA 1.3 and 2.8 mm observations) is more extended than the long-wavelength emission (traced by the VLA 7.1 mm observations), these data suggest the existence of a wavelength dependent structure, as it was found for both AS 209 and DoAr 25. In the next section, this wavelength-dependent structure will be explained

**Table 6.3:** Properties of the aperture synthesis imaging of CY Tau

Telescope	$\lambda$	Integrated Flux	Image rms noise	Synthesized beam	Beam P.A.
	[mm]	[mJy]	[mJy/beam]	[ $''$ ]	[ $^{\circ}$ ]
CARMA	1.34	$113 \pm 7$	0.65	$0.27'' \times 0.24''$	-69.2
CARMA	2.8	$24.9 \pm 0.5$	0.37	$0.38'' \times 0.32''$	88.2
VLA	7.14	$1.65 \pm 0.03$	0.019	$0.35'' \times 0.26''$	88.2

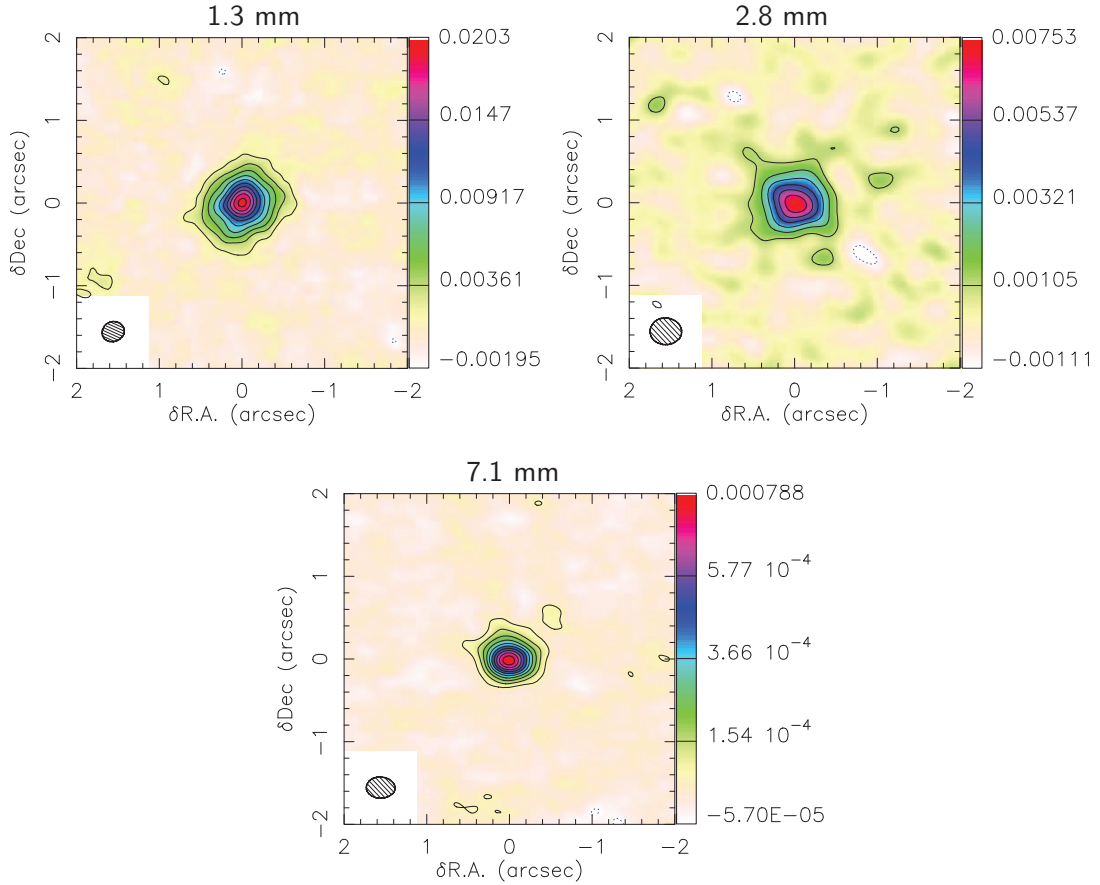


**Figure 6.15:** Aperture synthesis images of the continuum emission towards the young star CY Tau, observed with CARMA (1.3 and 2.8 mm, top panels) and VLA (7.0 mm, bottom panel). For all panels, the colorbar units are  $\text{Jy beam}^{-1}$ . Contours are drawn at  $3\sigma$  intervals, where  $\sigma$  is the RMS noise level on each map (see Table 6.3).

as radial variations of the dust properties across the circumsellar disk of CY Tau.

Free-free contamination at the 7.1 mm observations was deemed negligible. VLA observations at 6 cm (C-band) from the Disks@EVLA collaboration, were employed to constraint the amount of contamination. CY Tau is not detected at 6 cm, with an RMS of  $20 \mu\text{Jy}$ . Extrapolating the  $3\sigma$  upper limit at C-band to the wavelengths of the Q-band observations, and assuming optically thick free-free emission ( $S_\nu \propto \nu^{0.6}$ ), a contribution of at most 12% at 7.1 mm would be expected. However, unlike for AS 209, a significant point-like component in the largest  $uv$ -distances sampled by the VLA observations is not detected (at 7.1 mm, a flux density of  $-0.4 \pm 0.4 \text{ mJy}$  for spatial frequencies larger than  $980 \text{ k}\lambda$  is measured).

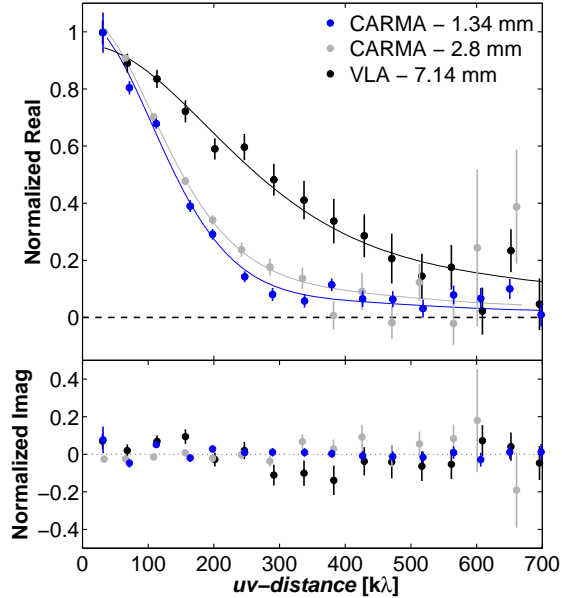


**Figure 6.16:** Normalized real and imaginary part of the correlated emission from CY Tau as a function of spatial frequency (*uv*-distance). The visibilities from the disk have been deprojected by the position angle and inclination derived from the disk emission modeling (see Table 6.4). Each bin has been normalized by the measured flux between *uv*-distances of 0–40 [ $k\lambda$ ]. Filled circles and error bars of different color correspond to correlated real and imaginary part of the emission observed at different wavelengths (1.3 mm: blue, 2.8 mm: gray, 7.1 mm: black). Continuous lines: best-fit disk emission model at each wavelength.

Hence, no free-free contribution was included in the modeling of these observations.

### 6.2.2 Modeling of dust continuum emission

The multi-wavelength observations of CY Tau were analyzed using the disk emission model described in Section 3. As in the analysis of AS 209 and DoAr 25 circumstellar disks, the dust opacity  $\kappa_\nu$  is computed assuming a grain population of compact spherical grains larger than  $a_{min} = 0.01 \mu\text{m}$ , in a power-law distribution of sizes,  $n(a) \propto a^{-q}$  for  $a_{min} < a < a_{max}$ , and whose composition follows that of Pollack et al. (1994). To begin modeling of these observations, the maximum grain size and grain size distribution slope that best reproduces the unresolved SED, from sub-mm to cm wavelengths, was selected. For CY Tau, these correspond to  $q = 3.5$ ,  $a_{max} = 2.5 \text{ mm}$ , which results in a opacity spectral slope  $\beta = 0.8$  between 1.3 and 7.1 mm.

Each wavelength is fitted separately assuming a constant dust opacity throughout the disk. The modeling of these observations and the  $\chi^2$  minimization is performed with 5 parameters: three describing the surface density  $\{\Sigma_t, R_t, \gamma\}$ , and two that describe the disk geometry ( $i$  and  $P.A.$ ). During the modeling of the long-wavelength observations (7.14 mm), the P.A. of the disk remained unconstrained, since the inclination of the disk is very close to face-on. The best way forward was to fix the value of this parameter at this wavelength (to the best-fit value found at the intermediate wavelength, 2.8 mm), while the others parameters are let to vary.

The marginalized probability distribution function (PDF) for each model parameter, constrained separately by each wavelength observation, is presented in Figure 6.17 for 1.3 mm, Figure 6.18 for 2.8 mm, and Figure 6.19 for 7.1 mm. Table 6.4 presents the best-fit model parameters, corresponding to those that minimize the  $\chi^2$ , and the  $1\sigma$  constraints for the 5-parameter fit to the short-wavelength observations and the 4-parameter fit to the long-wavelength data. The deprojected real and imaginary parts of the visibility profiles for each of the best-fit model observations at different wavelengths was presented in Figure 6.16 (continuous lines) in conjunction with the observed visibility profiles. Maps of the observed emission at each wavelength, with corresponding best-fit model and map of residual emission are shown in Figure 6.20.

**Table 6.4:** Best-fit model parameters and constraints for CY Tau

$\lambda$	$i$	P.A.	$R_t$	$\gamma$	$\Sigma_t$
[mm]	[ $^\circ$ ]	[ $^\circ$ ]	[AU]		[gm cm $^{-2}$ ]
1.3	$35.1^{+3.2}_{-4.5}$	$138^{+7}_{-8}$	$34^{+1}_{-2}$	$0.05^{+0.06}_{-0.08}$	$1.25^{+0.09}_{-0.07}$
2.8	$17^{+0}_{-16}$	$161^{+19}_{-154}$	$31 \pm 1$	$0.2^{+0.09}_{-0.06}$	$2.21^{+0.13}_{-0.09}$
7.1	$0 \pm 20$	$161^a$	$16 \pm 2$	$0.4 \pm 0.2$	$5.3^{+0.9}_{-1.1}$

<sup>a</sup> Parameter fixed to this value during modeling

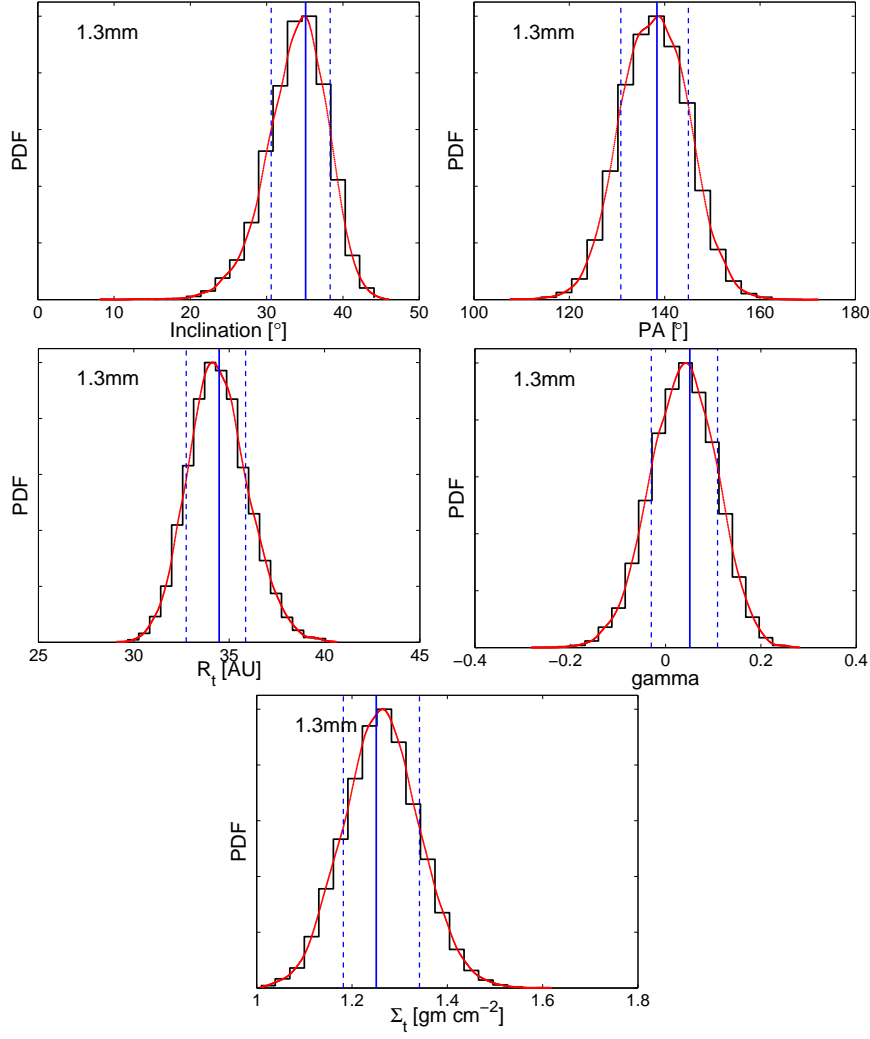


**Figure 6.17:** Marginalized probability distribution functions for the 5 model parameters ( $i$ , P.A.,  $\Sigma_t$ ,  $R_t$ ,  $\gamma$ ) that define the disk emission at 1.3 mm for CY Tau. On each panel: *black histograms* correspond to the empirical PDF, *red curves* are the kernel smoothing density estimate obtained from the empirical PDF as described in section 3, *vertical lines* correspond to the best-fit value for each parameter (continuous line) and  $1\sigma$  confidence interval obtained from the marginalized PDF (dashed lines). The y-axis numerical values are inconsequential, and are intentionally left out.

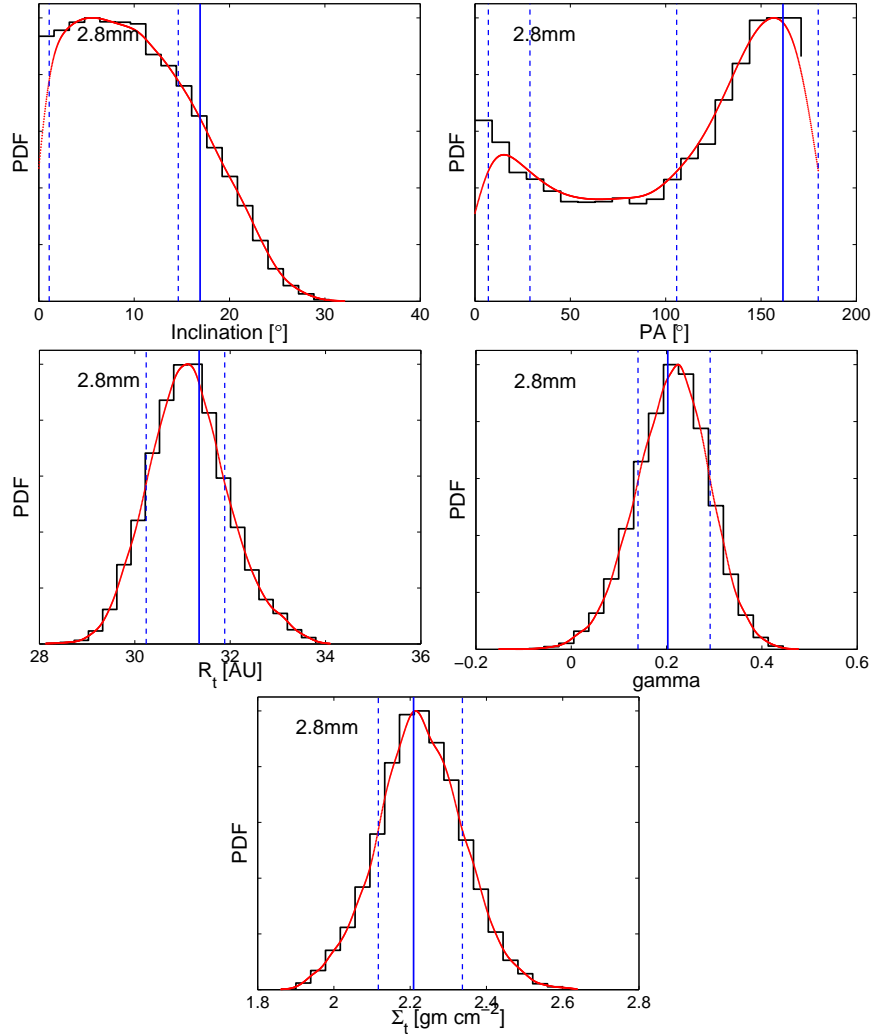


**Figure 6.18:** Marginalized probability distribution functions for the 5 model parameters ( $i$ ,  $P.A.$ ,  $\Sigma_t$ ,  $R_t$ ,  $\gamma$ ) that define the disk emission at 2.8 mm for CY Tau. Colors and curve descriptions as in Figure 6.17.

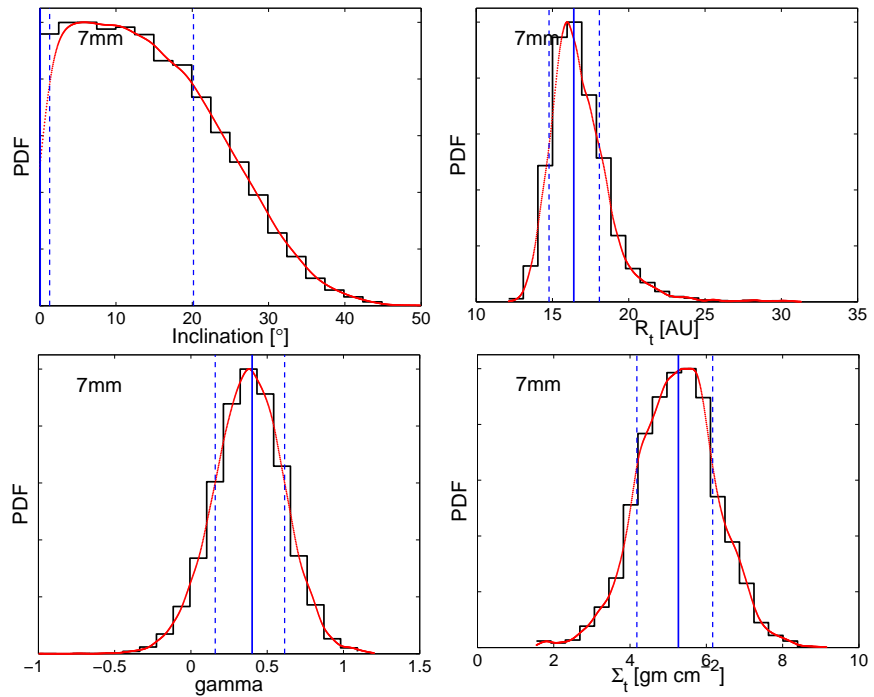


**Figure 6.19:** Marginalized probability distribution functions for the 4 model parameters  $(i, R_t, \Sigma_t, \gamma)$  that define the disk emission at 7.1 mm for CY Tau. Colors and curve descriptions as in Figure 6.17.

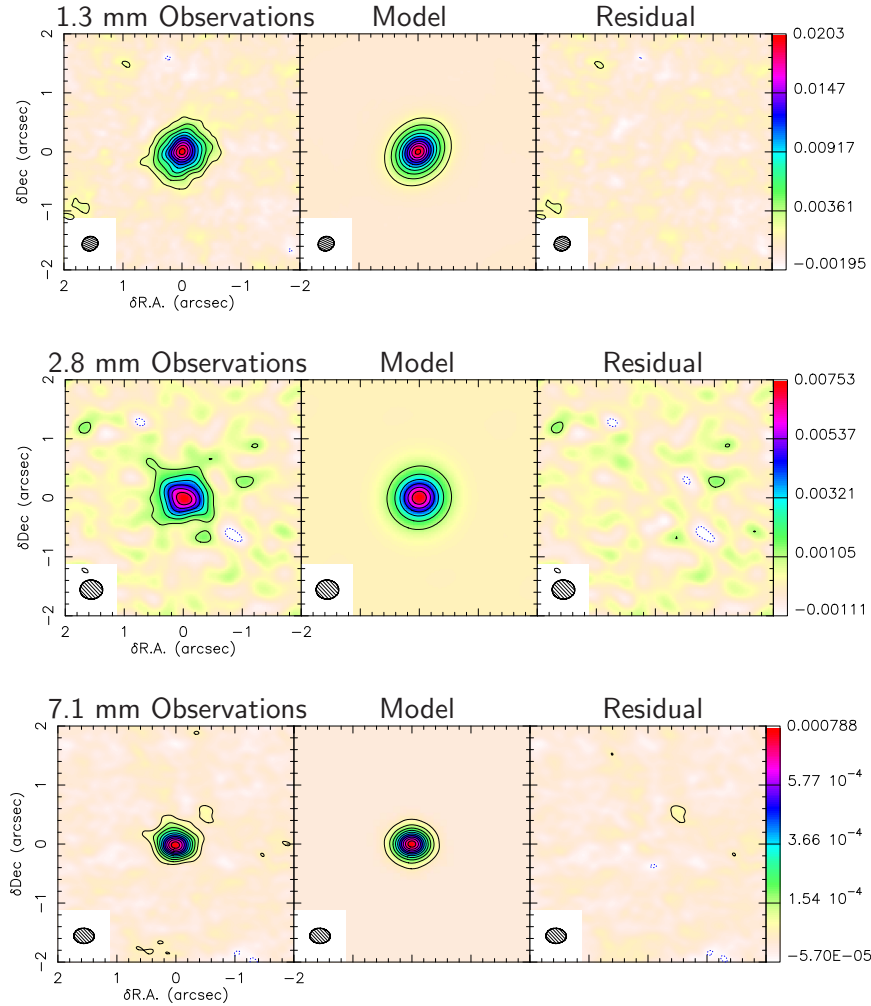


**Figure 6.20:** Modeling of the dust continuum emission towards CY Tau, as observed with CARMA at 1.3 mm (top panels) and 2.8 mm (middle panels) and VLA (7.1 mm, bottom panels). Each observation is accompanied by the best-fit disk emission, and a residual map obtained by subtracting the best-fit model from the observations in the Fourier domain. Maps were obtained using natural weighting for  $\lambda = 1.3$  mm and  $\lambda = 7.1$  mm, while a Briggs weighting scheme with robust = -1.0 for  $\lambda = 2.8$  mm, was used to try to match the observed beam sizes. Contours start at  $-3\sigma$ , stepping by  $3\sigma$ , where  $\sigma$  is the RMS noise on each map (Table 6.3).

From each separate model fitting a best-fit  $\Sigma(R)$  and  $T(R)$  profiles were obtained. These might be different for each wavelength if the assumption of a constant dust opacity with radius is not valid. Figure 6.21 shows the best-fit and  $3\sigma$  constraints on the temperature  $T(R)$  (left) and the disk optical depth  $\tau_\lambda(R) = \kappa_\lambda \times \Sigma(R)$  (right), inferred from modeling each observations separately, and where  $\kappa_\lambda$  was assumed to be constant with radius. Note that the best-fit temperature profiles from these multi-wavelength observations are similar, differing by  $< 3$  K for  $R < 55$  AU, and by  $< 6$  K for  $R > 55$  AU. Also note that the dust emission is optically thin at all wavelengths, this will be the case even if our modeling computes a mid-plane dust temperature that is incorrectly large by a factor of  $\sim 5$ .

The modeling presented above, assuming a constant dust opacity with radius and fitting each wavelength separately, portrays a different  $\Sigma(R)$  and  $T(R)$  inferred for each wavelength, signifying that the assumption of a radially constant dust opacity is not permitted. Radial variations of the dust opacity are required to reconcile the differing visibility profiles (real part vs.  $uv$ -distance, Figure 6.16) and the wavelength-dependent  $\Sigma_\lambda(R)$  and  $T_\lambda(R)$  (Figure 6.21).

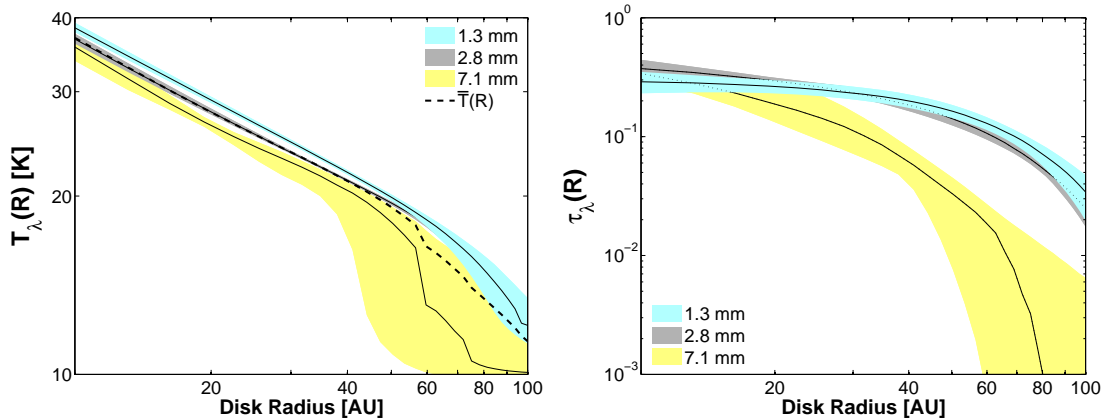


**Figure 6.21:** *Left:*  $T_\lambda(R)$  inferred from separate modeling of our multi-wavelength observations, assuming a constant dust opacity with radius. *Right:* Optical depth  $\tau_\lambda(R) = \kappa_\lambda \times \Sigma_\lambda(R)$  inferred from separate modeling of multi-wavelength observations, assuming a radially constant  $\kappa_\lambda$ . Colored regions:  $3\sigma$  confidence interval constrained by our observations, continuous line: best-fit model, dashed line on left panel: average temperature profile, assumed to be  $\bar{T}(R)$ . The different  $\Sigma(R)$  and  $T(R)$  profiles for each wavelength portray a varying dust opacity with radius, and because of this, none of them is the true surface density and temperature profile of the disk.

### 6.2.3 Radial variations of the dust opacity

As with the case of the circumstellar disks surrounding AS 209 and DoAr 25, there is observational evidence that radial variations in the dust properties are established in the circumstellar disk of CY Tau. These radial variations are interpreted as changes in the dust opacity spectral index  $\beta$  with radius, following the same Bayesian approach outlined before. The observational constraints on  $\beta(R)$  obtained for CY Tau are presented in Figure 6.22. The values of  $\beta$  allowed by these multi-wavelength observations are significantly different (and below) the ISM value of the dust opacity slope for  $R \lesssim 50$  AU. Furthermore, a gradient on  $\beta(R)$  inconsistent with a constant value of  $\beta$  at the  $7\sigma$  level is revealed.

Rather than inferring  $a_{max}(R)$  from  $\beta(R)$  (since this will depend on the assumption that the dust opacity follows a power-law with frequency,  $\kappa_\nu \propto \nu^\beta$ ), radial variations of  $a_{max}$  were directly constrained without this assumption, following the same procedure outlined in previous sections. However, for CY Tau a grain-size distribution with a power-law slope of  $q = 3.5$  was not able to fit our data in a reasonable fashion, requiring unphysically steep jumps of  $a_{max}$ , which are not expected to occur in a narrow range of disk radii. Hence only the constraints obtained for  $q = 3.0$  are considered.

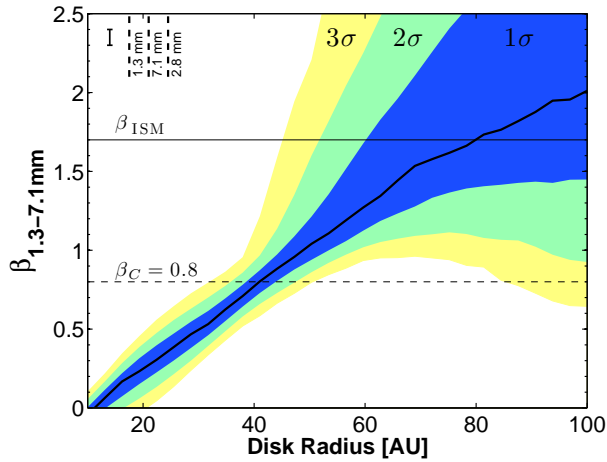


**Figure 6.22:** Dust opacity spectral slope,  $\beta$ , as a function of radius, inferred from multi-wavelength observations of the CY Tau disk. Black line: best-fit  $\beta(R)$ , colored areas: confidence interval constrained by our observations. Vertical dashed-lines indicate the spatial resolution of our observations. The errorbar in top-right corner indicates additional systematic uncertainty on  $\beta(R)$  arising from amplitude calibration uncertainty.

Figure 6.23 presents these constraints for  $a_{max}(R)$  and  $\Sigma(R)$  for CY Tau, assuming the same dust composition as in section 6.2.2, and for a grain size distribution slopes  $q = 3.0$ . For disk radii between 50–70 AU, solutions with a substantially large value of  $a_{max}$  (and hence a large  $\Sigma(R)$  value) were a possible fit to our data (within  $3\sigma$ ). However, this region of the parameter space (shown in light-blue, Figure 6.23) is disconnected from the main region where  $3\sigma$  constraints on  $a_{max}$  are continuous with radius (shown in darker blue, Figure 6.23). Hence, we disregard the  $a_{max}$  solutions in the *disconnected* region based on the fact that any solution that attempts to go through this region will be discontinuous. Across the disk, grains have grown at least up to  $\sim 0.4$  mm, with small grains present in the outer disk and large grains in the inner disk.

These observational constraints on  $a_{max}(R)$  are compared with Birnstiel et al. (2010) models of grain growth evolution, employing the approximations presented in Birnstiel et al. (2012) for the evolution of  $a_{max}$  with radius. For CY Tau, we find an agreement between our observational constraint on the maximum grain size and the growth barrier imposed by radial drift of macroscopic particles, at least up to  $\sim 70$  AU. Farther out in the disk, for  $R \gtrsim 70$  AU, our observational constraint is above the radial drift barrier, with dust grains in the outer disk that have managed to somehow overcome this growth barrier.

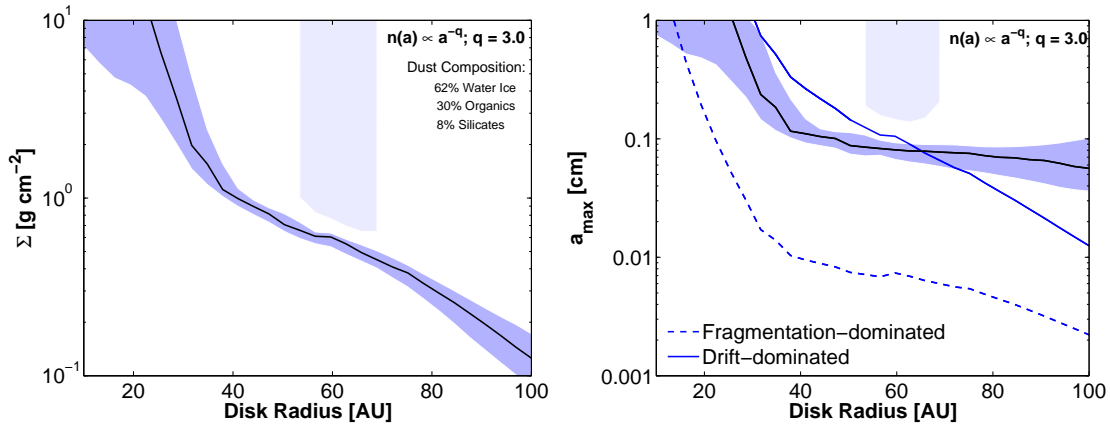


**Figure 6.23:** Surface density (left) and maximum grain size as a function of radius (right), for the CY Tau disk. Black line: best-fit, shaded region:  $3\sigma$  confidence interval. Assumed grain properties are specified in figure legend. We compare our observational constraints with theoretical grain evolution models (Birnstiel et al., 2012), that include fragmentation and radial drift.

## Chapter 7

### Conclusions and Future Work

The first observational constraints in dust grain growth, that attempted to resolve radial variations of the dust properties, appeared less than two years ago ([Isella et al., 2010](#); [Banzatti et al., 2011](#); [Guilloteau et al., 2011](#)). These investigations did not occur earlier since only recently it has become possible to resolve circumstellar disk structures down to several tens to AU, at long enough wavelengths where the emission becomes (mostly) optically thin. However, given the limited wavelength coverage and the lack of sensitivity of these studies, stringent constraints on the changes of the dust opacity spectral index,  $\beta$ , with increasing distance from the star, were not possible to obtain. Up until then, radial variations of  $\beta$  were expected to occur inside circumstellar disks, as informed by several theoretical considerations. But observationally this had not yet been conclusively proven until the inception of this thesis.

#### 7.1 General Results from This Thesis

The observational constraints presented here have allowed us for the first time to clearly assert that a constant value of the dust opacity is not warranted, at least for the sample of circumstellar disks that has been carefully examined. Furthermore, a gradient in  $\beta(R)$  is necessary in order to explain our observations, with low values of  $\beta$  in the inner regions of the disk, and large values of  $\beta$  in the outer disk. Such  $\beta(R)$  gradients have been proposed in the past. For example, [Birnstiel et al. \(2010\)](#) predict that value of  $\beta$  is expected to change from  $\beta \lesssim 0.5$  for  $R \sim 20$  AU increasing to  $\beta \gtrsim 2.5$  for  $R \gtrsim 80$  AU for typical disk properties. The improved constraints on  $\beta(R)$  obtained on this thesis can be appreciated in Figure 7.1.

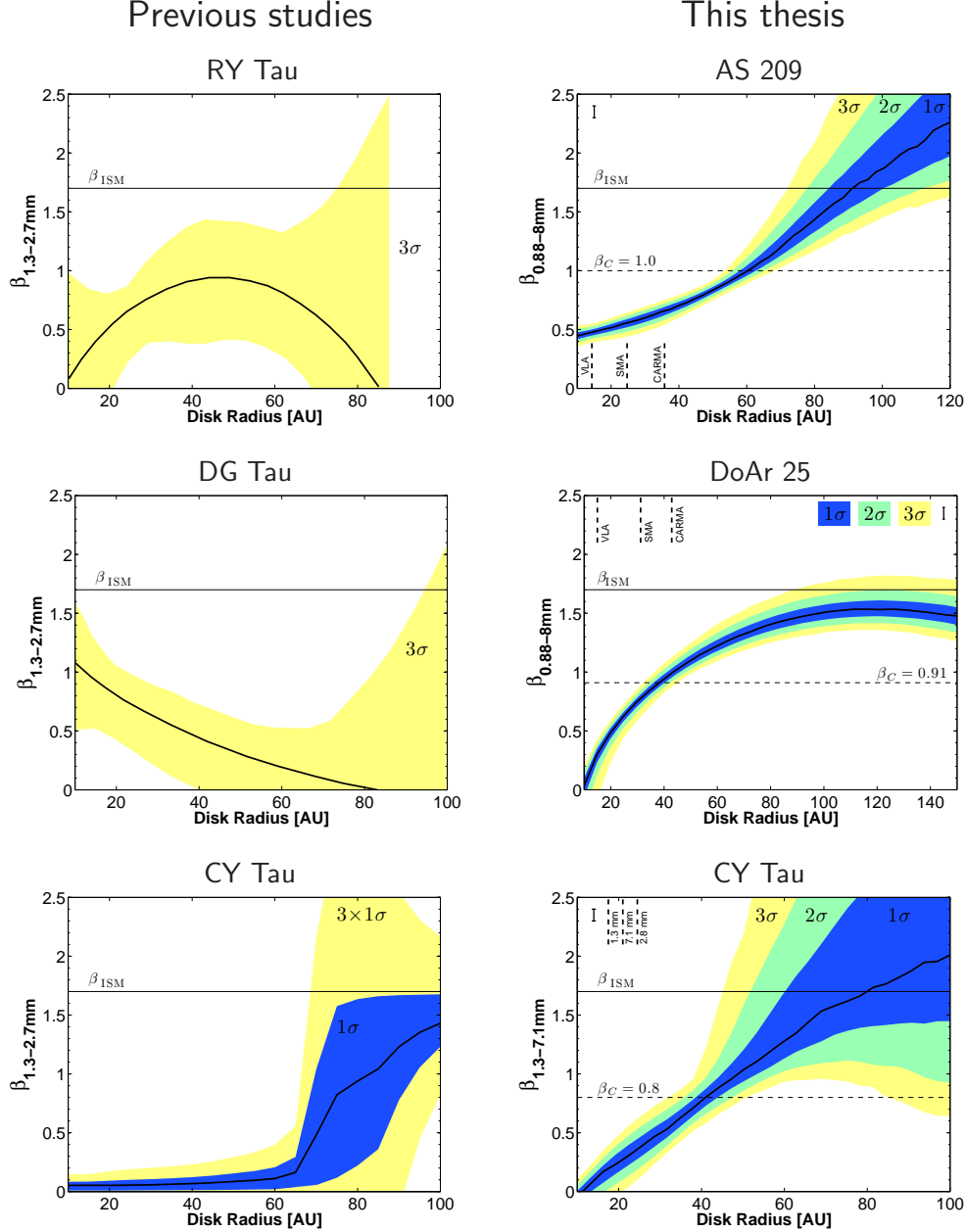


**Figure 7.1:** Observational constraints for the dust opacity spectral index  $\beta$  as a function of radius for 5 different circumstellar disks. *Left:*  $\beta(R)$  constraints from previous studies for the protoplanetary disks surrounding RY Tau and DG Tau (Isella et al., 2010) and CY Tau (Guilloteau et al., 2011). *Right:*  $\beta(R)$  constraints from this thesis, for the protoplanetary disks surrounding AS 209 (Pérez et al., 2012, in press), and DoAr 25 and CYTau (Pérez et al., in preparation). The addition of long wavelength VLA observations as well as the increased sensitivity of CARMA, SMA and the VLA made possible to obtain these stringent constraints.

Additionally, since it has been now appreciated that the approximation of the dust opacity being a power law with frequency ( $\kappa_\nu \propto \nu^\beta$ ) is not warranted when the maximum grain size of the population is between  $a_{max} \sim 0.1\text{--}10$  mm (see Figure 5.7), a different approach was taken on this thesis. Leaving everything else fixed (i.e., fixed dust composition and fixed grain-size distribution), a direct fit for  $a_{max}$  vs. radius was obtained for each protoplanetary disk. This allowed for the first time to compare observational constraints of radial  $a_{max}$  variations with simple theoretical predictions of grain growth, that include two fundamental processes: collisional coagulation, including fragmentation, and radial drift of solids through interactions with the gaseous disk.

A compilation of the results obtained on this thesis for the radial variation of the maximum grain size of the dust population, assuming standard values for the protoplanetary disks characteristics, is shown in Figure 7.2. These results seem to favors models where radial drift is the dominant process limiting the growth of grains. However, the appropriate next step is to investigate whether such simple models can actually reproduce the measured brightness profiles at the observed wavelengths. Grain growth simulations, that start from the derived protoplanetary disks parameters from our modeling, need to be performed for each one of our targets. This will be a topic for future investigations.

## 7.2 Future Work: Studying Grain Growth with ALMA

A small fraction of protoplanetary disks display a deficit of near-IR flux indicating a lack of material close to the star, while substantial emission at longer wavelengths indicates that the outer disk remains massive (Strom et al., 1989). These so-called transitional disks are thought to be intermediate systems between young ( $\sim 1\text{--}10$  Myr) optically thick protoplanetary disks and old ( $> 10$  Myr) optically thin debris disks, where significant disk evolution has occurred.

The lack of inner disk material in transitional disks can be caused by a variety of mechanisms: *grain growth* beyond sizes where emission is efficient (Dullemond & Dominik, 2005), *photoevaporation* driven by the central star (Clarke et al., 2001), or *dynamical clearing* by a young planet or a low-mass stellar companion (Skrutskie et al., 1990; Ireland & Kraus, 2008). However, photoevaporation can be dismissed as the origin of the cleared cavity in some stars, due to their large disk mass, large cavity size, and high accretion rates—all

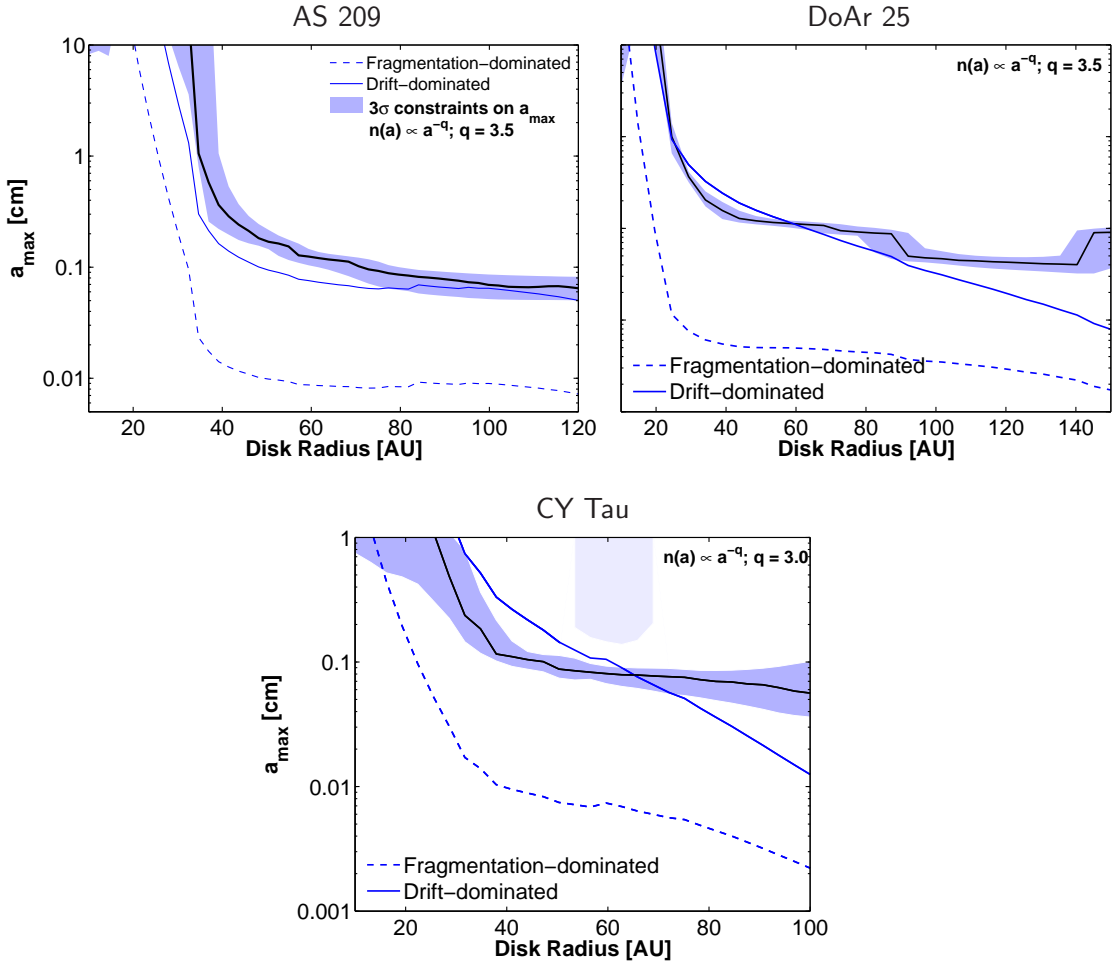


**Figure 7.2:** Compilation of the obtained constraints on the maximum grain size as a function of radius ( $a_{\max}$ ), for three circumstellar disks: AS 209, DoAr 25 and CY Tau. The black line corresponds to the best-fit  $a_{\max}(R)$ , while the shaded region indicates the  $3\sigma$  confidence interval. These observational constraints were compared with theoretical grain evolution models (Birnstiel et al., 2012), that include fragmentation (dashed line) and radial drift of solids (solid line). In all of the disks studied the radial drift barrier seemed to be the dominant limitation for the growth of grains. However, it remains to be shown that these simple prescriptions can actually reproduce the measured brightness profiles at all of the observed wavelengths.

characteristics which are not expected when photo evaporation is proceeding (Alexander & Armitage, 2007). By selecting a subset of transition disks with large inner holes, large disk masses, and high accretion rates, we can rule out photo-evaporation, which leaves grain growth or dynamical clearing as the likely origin of inner disk holes.

Observationally, distinguishing between these mechanisms has been difficult. The case of LkCa 15, a young K5 star located in the Taurus region, is very illustrative of the problem of pre-ALMA observations. Figure 7.3 presents CARMA observations in the 1.3 mm band, with an angular resolution of  $0.2''$  (Isella, Pérez, Carpenter, 2012).

Although sub-arcsecond resolution is achieved, the inner hole structure can be equally well constrained by two different parameterizations of the surface density profile: a smooth  $\Sigma(R)$  (with a gradual density decrease towards the star) or a truncated  $\Sigma(R)$  (with a sharp density decrease at the inner hole radius). These two different parameterizations may arise from the two mechanisms discussed above. Dust coagulation is more efficient in the dense inner disk, thus, as particles grow their opacity diminishes leading to observed inner cavities. Models of grain growth predict a continuous radial variation of the dust opacity within the disk (e.g., Birnstiel et al., 2010), whose observational signature corresponds to a gradual transition between the inner and outer disk structure. By contrast, a massive planet is expected to produce a sharp truncation in the inner disk due to dynamical interactions between the young planet and the disk (Bryden et al., 1999; Wolf et al., 2007). During the planet formation process, the orbiting companion creates a tidal barrier to the inflow of gas and dust. The observational signature of this dust-clearing mechanism is a steep transition between the inner and outer disk.

Figure 7.4 compares the real part of the correlated flux measured by CARMA, as a function of the baseline length, with the best-fit solution found for a truncated inner disk and for a smooth inner disk. In the right panel of Figure 7.4, the difference between the

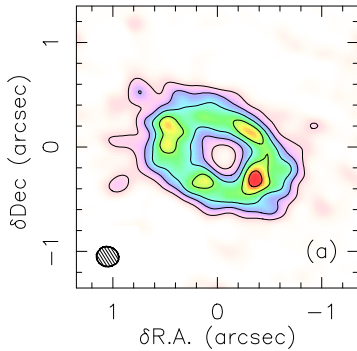


**Figure 7.3:** CARMA aperture synthesis image of the 1.3 mm dust continuum emission toward LkCa 15 (beam FWHM =  $0.21'' \times 0.19''$ ;  $\sigma_{RMS} = 0.4$  mJy/beam). Contours are drawn every  $3\sigma$ .

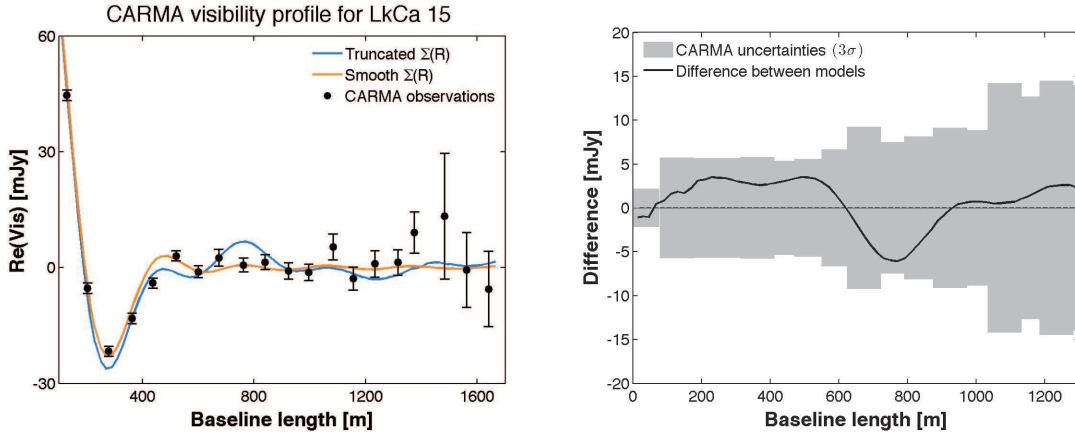


**Figure 7.4:** *Left panel:* Observed CARMA visibility profile for LkCa 15 at 1.3 mm (black points) compared with the best-fit models for a truncated (blue) and a smooth (orange) surface density profile. The real part of the correlated flux has been deprojected to account for the disk geometry. *Right panel:* Difference in the visibility profile between the smooth and truncated surface density models (solid line), compared to the sensitivity of CARMA observations (shaded region). This figure demonstrates that the sensitivity of current observations limits our ability to identify the structure of the inner hole and infer the physical process responsible for the cavity in LkCa 15.

smooth and truncated models is shown. Compared with the  $3\sigma$  uncertainties of the CARMA observations (shaded region), it is impossible to distinguish between the two models.

To demonstrate the potential of ALMA, I simulated observations of the LkCa 15 disk using the best-fit solutions found from the CARMA data. Simulated 450  $\mu$ m images were produced using both the truncated and smooth surface density models (Figure 7.5). The structural differences between the two models are evident in these images: the smoothly varying  $\Sigma(R)$  shows trace amounts of emission in the inner disk that is detectable with ALMA, while the inner region in the truncated disk model is devoid of emission and resolved. More quantitatively, Figure 7.6 shows the visibility profiles that ALMA would observe for the two different models (left panel), where the colored regions indicate the  $3\sigma$  measurement uncertainties from the simulated observations. In the right panel of Figure 7.6, the difference between the smooth and truncated models is computed. The  $3\sigma$  uncertainties of the simulated ALMA observations (shaded region) are small enough that we can clearly distinguish between a truncated and smoothly varying density profiles.

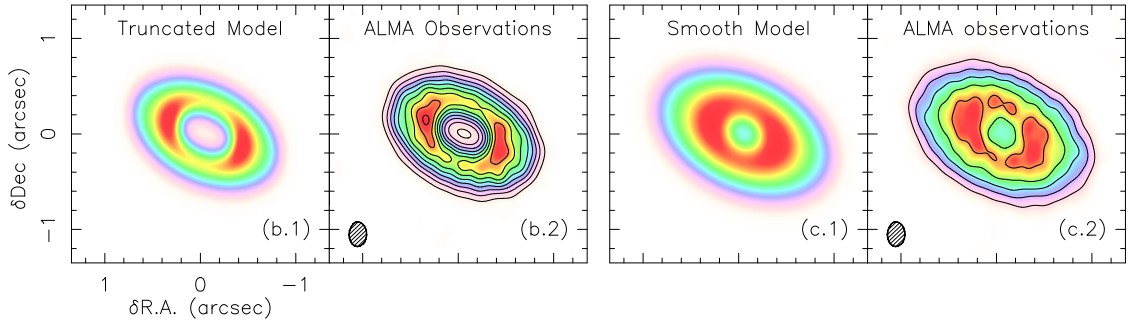


**Figure 7.5:** Simulated ALMA Early Science observations of LkCa 15, for a disk model where the density is sharply truncated at a finite radius and the inner disk is clear of dust (panels b.1 and b.2), and for a smoothly varying density distribution that peaks at a finite radius (panels c.1 and c.2). Contours are drawn every  $10\sigma$ , with  $\sigma = 1.5 \text{ mJy beam}^{-1}$  the RMS noise level in the map. These ALMA simulations assume a 30 min on source integration and the default weather conditions for Band 9.

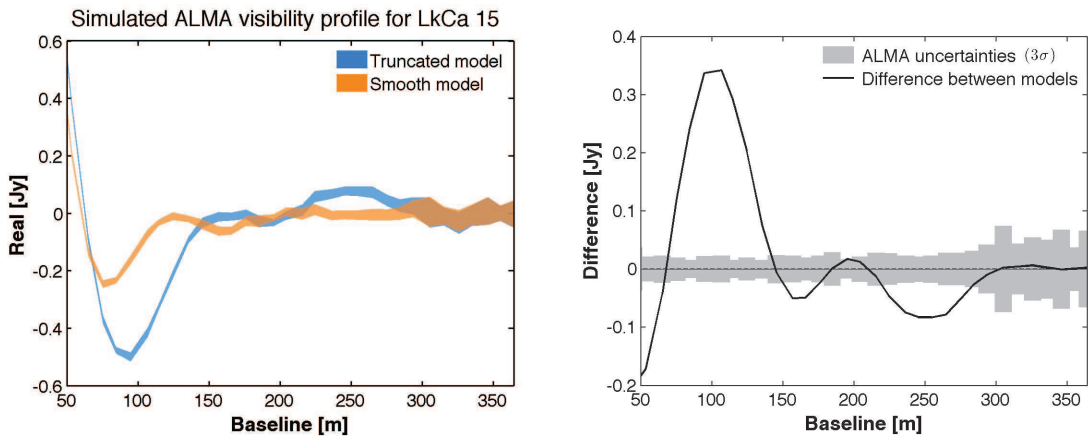


**Figure 7.6:** *Left panel:* Simulated ALMA visibility profile for LkCa 15 at  $450 \mu\text{m}$  in the extended configuration, assuming a truncated (blue) and a smooth (orange) surface density profile. The span of the shaded region represents the  $3\sigma$  uncertainty level derived from the simulated observations. *Right panel:* Difference in the visibility profile between the smooth and truncated surface density models (solid line), compared to the sensitivity of ALMA observations (shaded region).

I authored a successful ALMA Cycle-0 proposal, to resolve the inner regions of five protoplanetary disks, which were selected based on the criteria defined above. These 5 disks have all been resolved at mm wavelengths with either CARMA or SMA ([Andrews et al., 2011](#); [Brown et al., 2008](#); [Isella, Pérez, Carpenter, 2012](#)). The top panel in Figure 7.7 shows the SMA 880  $\mu\text{m}$  images for each disk, the inner disk cavity is resolved in each case, but just as with the example above a robust identification of the inner disk sharpness is not possible with this data. This future ALMA Early Science 450  $\mu\text{m}$  observations will detect trace amounts of dust in the inner depleted regions. Analysis of the ALMA visibility data will reveal if the inner edge of the disk is sharply truncated (favoring dynamical sculpting by a planet), or if the inner edge varies smoothly with radius (favoring accelerated grain growth in the inner disk). Also, although some of these disks show apparent azimuthal asymmetries, these structures are not statistically significant ( $< 3\sigma$  where  $\sigma$  is the RMS noise level in the map, [Andrews et al., 2011](#)). Future ALMA observations will be much more sensitive to disk asymmetries—if they exist.

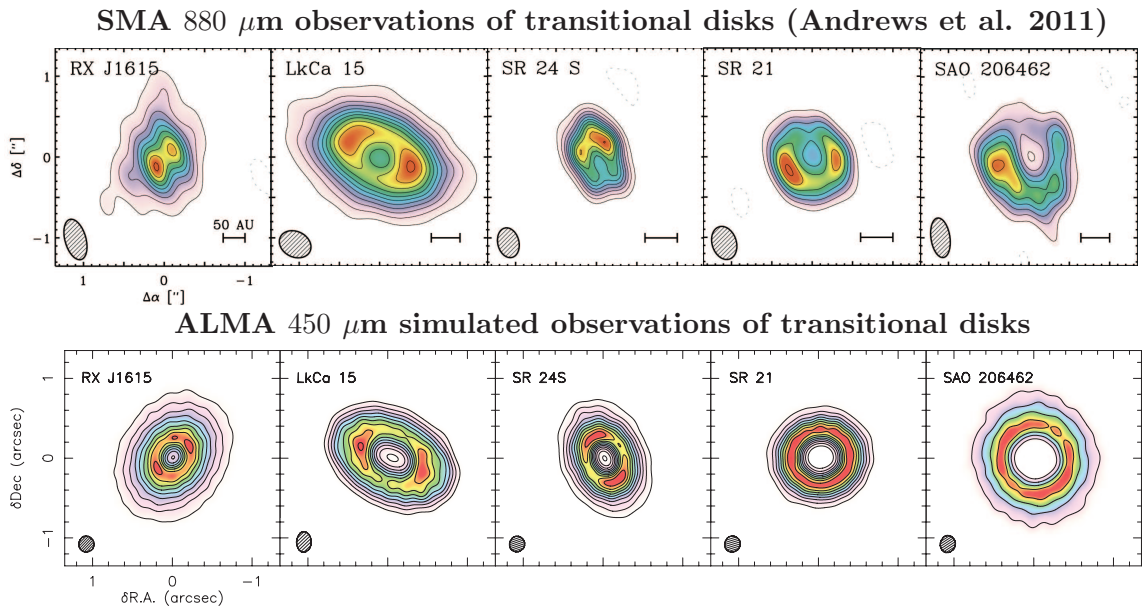


**Figure 7.7:** Observed (top) and simulated (bottom) images of the 5 transitional disks to be observed with ALMA Early Science. Each panel is 2.7'' on a side, and a 50 AU scale bar is shown for reference. *Top:* SMA images at 880  $\mu\text{m}$  (from [Andrews et al., 2011](#)). Contours are drawn every  $3\sigma$  and the smallest beam FWHM is  $\sim 0.4''$ . *Bottom:* Simulated ALMA images at 450  $\mu\text{m}$ . Contours are drawn every  $10\sigma$  (5 $\sigma$  for SR 24 S), and the beam FWHM is  $\sim 0.20''$ .

### 7.3 And the Future is Here: ALMA Early Science Observations of Transitional Disks

In October 11, 2012 I was notified that the first two disks of our sample had been observed in the extended array configuration (baselines between 20 – 400 m). Figure 7.8 presents the synthesized maps at  $\lambda = 0.45$  mm for the dust continuum emission towards SAO 206462 and SR 21. The first thing to notice is the evident asymmetries in both these protoplanetary disks, which are detected at a very significant level: at  $\sim 60\sigma$  for SAO 206462 and at  $\sim 120\sigma$  for SR 21, where  $\sigma$  is the RMS noise level in the image. The strongly peaked asymmetry seen in the south-west of SAO 206462 is consistent with recent scattered light observations of this object (Muto et al., 2012). The second thing to notice is that although the asymmetries are somewhat similar in both disks, the depleted inner cavities are not. For SAO 206462 only a small amount of dust is detected in the inner disk and the cavity seems to be quite large. In contrast, the inner cavity of SR 21 seems to be either smaller than that of SAO 206462 (and hence not entirely resolved by this observations) or it is not entirely depleted. These two striking features (asymmetries and inner cavities) need to be further investigated. Unfortunately, the simple analysis presented before might not be all that appropriate for these two targets, since it assumed that these circumstellar disks will be axisymmetric (a fair—although conservative—assumption given what was known before these ALMA observations).

There is no doubt we are witnessing a crucial process taking place inside these protoplanetary disks, and theorists are eager with possible explanations. For example, asymmetries may arise from planet-disk interactions that excite spiral density waves in the disk surface density (for a review see Kley & Nelson, 2012) or symmetry may be lost due to large-scale anticyclonic vortices that form at the boundary between the low-viscosity disk mid-plane (so-called “dead zone”) and the highly ionized and viscously accreting upper disk layers (e.g., Regály et al., 2012). It remains to be shown what of the several possibilities is more likely to explain these new high sensitivity circumstellar disk observations.

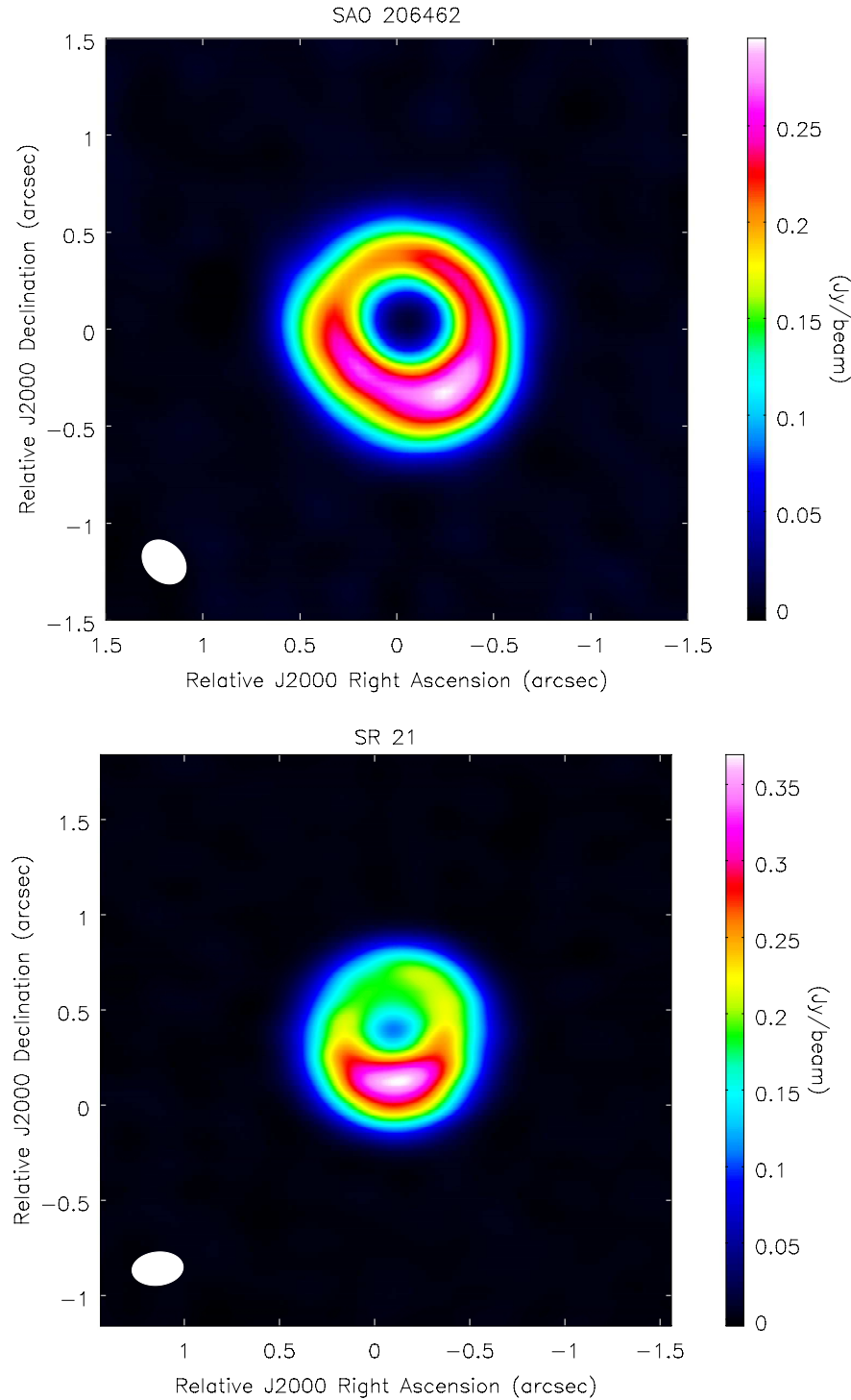


**Figure 7.8:** ALMA Early Science observations (not simulations!) of the transitional disks surrounding SAO 206462 (top) and SR 21 (bottom), observed at  $450\text{ }\mu\text{m}$  in the extended array configuration with an angular resolution of  $\sim 0.2''$  ( $\sim 25\text{ AU}$  at the distance of these objects). These ALMA Early Science observations provide an unique opportunity to study the structure of protoplanetary disks with possible planetary companions.

## Bibliography

- Acke, B., & van den Ancker, M. E. 2004, *Astronomy and Astrophysics*, 426, 151
- Adams, F. C., Lada, C. J., & Shu, F. H. 1987, *Astrophysical Journal*, 312, 788
- Apai, D., Pascucci, I., Bouwman, J., et al. 2005, *Science*, 310, 834
- Alexander, R. D., & Armitage, P. J. 2007, *Monthly Notices of the Royal Astronomical Society*, 375, 500
- Andre, P., & Montmerle, T. 1994, *Astrophysical Journal*, 420, 837
- Andre, P., Ward-Thompson, D., & Barsony, M. 1993, *Astrophysical Journal*, 406, 122
- Andrews, S. M., & Williams, J. P. 2005, *Astrophysical Journal*, 631, 1134
- Andrews, S. M., & Williams, J. P. 2007, *Astrophysical Journal*, 671, 1800
- Andrews, S. M., & Williams, J. P. 2007b, *Astrophysical Journal*, 659, 705
- Andrews, S. M., Hughes, A. M., Wilner, D. J., & Qi, C. 2008, *Astrophysical Journal, Letters*, 678, L133
- Andrews, S. M., Liu, M. C., Williams, J. P., & Allers, K. N. 2008, *Astrophysical Journal*, 685, 1039
- Andrews, S. M., Wilner, D. J., Hughes, A. M., Qi, C., & Dullemond, C. P. 2009, *Astrophysical Journal*, 700, 1502
- Andrews, S. M., Wilner, D. J., Hughes, A. M., Qi, C., & Dullemond, C. P. 2010, *Astrophysical Journal*, 723, 1241
- Andrews, S. M., Wilner, D. J., Espaillat, C., et al. 2011, *Astrophysical Journal*, 732, 42

- Apai, D. A., & Lauretta, D. S. 2010, Protoplanetary Dust: Astrophysical and Cosmochemical Perspectives
- Armitage, P. J., Livio, M., & Pringle, J. E. 2001, Monthly Notices of the Royal Astronomical Society, 324, 705
- Armitage, P. J. 2010, *Astrophysics of Planet Formation*, by Philip J. Armitage, pp. 294. ISBN 978-0-521-88745-8 (hardback). Cambridge, UK: Cambridge University Press, 2010.,
- Asaki, Y., Saito, M., Kawabe, R., Morita, K.-I., & Sasao, T. 1996, Radio Science, 31, 1615
- Asaki, Y., Shibata, K. M., Kawabe, R., Roh, D.-G., Saito, M., Morita, K.-I., & Sasao, T. 1998, Radio Science, 33, 1297
- Aspin, C., & Reipurth, B. 2000, Monthly Notices of the Royal Astronomical Society, 311, 522
- Aspin, C., & Sandell, G. 2001, Monthly Notices of the Royal Astronomical Society, 328, 751
- Asplund, M., Grevesse, N., Sauval, A. J., & Scott, P. 2009, Annual Reviews of Astronomy and Astrophysics, 47, 481
- Avni, Y. 1976, Astrophysical Journal, 210, 642
- Banzatti, A., Testi, L., Isella, A., et al. 2011, Astronomy and Astrophysics, 525, A12
- Beckwith, S. V. W., & Sargent, A. I. 1991, Astrophysical Journal, 381, 250
- Beckwith, S. V. W., Sargent, A. I., Chini, R. S., & Guesten, R. 1990, Astronomical Journal, 99, 924
- Beckwith, S. V. W., Henning, T., & Nakagawa, Y. 2000, Protostars and Planets IV, 533
- Bertout, C., Siess, L., & Cabrit, S. 2007, Astronomy and Astrophysics, 473, L21
- Birnstiel, T., Ricci, L., Trotta, F., et al. 2010, Astronomy and Astrophysics, 516, L14
- Birnstiel, T., Dullemond, C. P., & Brauer, F. 2010, Astronomy and Astrophysics, 513, A79

- Birnstiel, T., Klahr, H., & Ercolano, B. 2012, *Astronomy and Astrophysics*, 539, A148
- Blum, J., & Wurm, G. 2008, *Annual Reviews of Astronomy and Astrophysics*, 46, 21
- Boudet, N., Mutschke, H., Nayral, C., et al. 2005, *Astrophysical Journal*, 633, 272
- Bouvier, J., & Appenzeller, I. 1992, *Astronomy and Astrophysics, Supplement*, 92, 481
- Bouwman, J., Henning, T., Hillenbrand, L. A., et al. 2008, *Astrophysical Journal*, 683, 479
- Brauer, F., Dullemond, C. P., & Henning, T. 2008, *Astronomy and Astrophysics*, 480, 859
- Briggs, D. S. 1995, Ph.D. Thesis, New Mexico Institute of Mining and Technology
- Brown, J. M., Blake, G. A., Qi, C., Dullemond, C. P., & Wilner, D. J. 2008, *Astrophysical Journal, Letters*, 675, L109
- Bryden, G., Chen, X., Lin, D. N. C., Nelson, R. P., & Papaloizou, J. C. B. 1999, *Astrophysical Journal*, 514, 344
- Calvet, N., D'Alessio, P., Hartmann, L., et al. 2002, *Astrophysical Journal*, 568, 1008
- Chiang, E. I., & Goldreich, P. 1997, *Astrophysical Journal*, 490, 368
- Chiang, E., & Youdin, A. N. 2010, *Annual Review of Earth and Planetary Sciences*, 38, 493
- Chiang, E. I., Joung, M. K., Creech-Eakman, M. J., et al. 2001, *Astrophysical Journal*, 547, 1077
- Clark, B.G. 1980, *Astronomy and Astrophysics*, 89, 377
- Clarke, C. J., Gendrin, A., & Sotomayor, M. 2001, *Monthly Notices of the Royal Astronomical Society*, 328, 485
- Cohen, M., Aitken, D. K., Roche, P. F., & Williams, P. M. 1983, *Astrophysical Journal*, 273, 624
- Condon, J. J., & Yin, Q. F. 2001, *Publications of the Astronomical Society of the Pacific*, 113, 362
- D'Alessio, P., Calvet, N., & Hartmann, L. 2001, *Astrophysical Journal*, 553, 321

- Dauphas, N., & Chaussidon, M. 2011, Annual Review of Earth and Planetary Sciences, 39, 351
- Draine, B. T. 2006, *Astrophysical Journal*, 636, 1114
- Dullemond, C. P., & Dominik, C. 2005, *Astronomy and Astrophysics*, 434, 971
- Dullemond, C. P., & Dominik, C. 2008, *Astronomy and Astrophysics*, 487, 205
- Dullemond, C. P., Dominik, C., & Natta, A. 2001, *Astrophysical Journal*, 560, 957
- Dullemond, C. P., van Zadelhoff, G. J., & Natta, A. 2002, *Astronomy and Astrophysics*, 389, 464
- Dutrey, A., Guilloteau, S., Duvert, G., et al. 1996, *Astronomy and Astrophysics*, 309, 493
- Evans, N. J., II, Dunham, M. M., Jørgensen, J. K., et al. 2009, *Astrophysical Journal*, Supplement, 181, 321
- Gilks, W. R., Best, N. G., & Tan, K. K. C. 1995, *Journal of the Royal Statistical Society, Series C (Applied Statistics)* 44, 4, 455
- Guilloteau, S., Dutrey, A., Piétu, V., & Boehler, Y. 2011, *Astronomy and Astrophysics*, 529, A105
- Högblom, J. A. 1974, *Astronomy and Astrophysics*, Supplement, 15, 417
- Hales, S., Hills, R., Robson, Y., Richer, J., Delgado, G., Otrola, A., Radford, S. 2003, ALMA Memo 459
- Hamidouche, M. 2010, *Astrophysical Journal*, 722, 204
- Harris, R. J., Andrews, S. M., Wilner, D. J., & Kraus, A. L. 2012, *Astrophysical Journal*, 751, 115
- Hartmann, L., & Kenyon, S. J. 1996, *Annual Reviews of Astronomy and Astrophysics*, 34, 207
- Hartmann, L., Calvet, N., Gullbring, E., & D'Alessio, P. 1998, *Astrophysical Journal*, 495, 385

- Hayashi, C. 1981, Progress of Theoretical Physics Supplement, 70, 35
- Henning, T., & Mutschke, H. 1997, Astronomy and Astrophysics, 327, 743
- Henning, T., & Stognienko, R. 1996, Astronomy and Astrophysics, 311, 291
- Hernández, J., Hartmann, L., Megeath, T., et al. 2007, Astrophysical Journal, 662, 1067
- Hill, R. J. 1988, IEEE Transactions on Antennas and Propagation, 36, 423
- Hillenbrand, L. A., & White, R. J. 2004, Astrophysical Journal, 604, 741
- Hillenbrand, L. A. 2005, arXiv:astro-ph/0511083
- Holdaway, M.A., Radford, S. J. E., Owen, F. N., Foster, S. M. 1995, MMA Memo 139
- Hughes, A. M., Wilner, D. J., Qi, C., & Hogerheijde, M. R. 2008, Astrophysical Journal, 678, 1119
- Ireland, M. J., & Kraus, A. L. 2008, Astrophysical Journal, Letters, 678, L59
- Isella, A., Testi, L., Natta, A., et al. 2007, Astronomy and Astrophysics, 469, 213
- Isella, A., Carpenter, J. M., & Sargent, A. I. 2009, Astrophysical Journal, 701, 260
- Isella, A., Carpenter, J. M., & Sargent, A. I. 2010, Astrophysical Journal, 714, 1746
- Isella, A., Pérez, L. M., & Carpenter, J. M. 2012, Astrophysical Journal, 747, 136
- Jennison, R. C. 1958, MNRAS, 118, 276
- Johns-Krull, C. M., Valenti, J. A., & Linsky, J. L. 2000, Astrophysical Journal, 539, 815
- Jørgensen, J. K., Bourke, T. L., Myers, P. C., et al. 2007, Astrophysical Journal, 659, 479
- Kenyon, S. J., & Hartmann, L. 1987, Astrophysical Journal, 323, 714
- Kenyon, S. J., & Hartmann, L. 1995, Astrophysical Journal, Supplement, 101, 117
- Kitamura, Y., Momose, M., Yokogawa, S., et al. 2002, Astrophysical Journal, 581, 357
- Kley, W., & Nelson, R. P. 2012, Annual Reviews of Astronomy and Astrophysics, 50, 211

- Koerner, D. W., & Sargent, A. I. 1995, *Astronomical Journal*, 109, 2138
- Koerner, D. W., Sargent, A. I., & Beckwith, S. V. W. 1993, *Icarus*, 106, 2
- Kolmogorov, A. 1941, *Akademiiia Nauk SSSR Doklady*, 30, 301
- Kwon, W., Looney, L. W., Mundy, L. G., Chiang, H.-F., & Kemball, A. J. 2009, *Astrophysical Journal*, 696, 841
- Kwon, W., Looney, L. W., & Mundy, L. G. 2011, *Astrophysical Journal*, 741, 3
- Lada, C. J., & Wilking, B. A. 1984, *Astrophysical Journal*, 287, 610
- Lay, O. P. 1997, *Astronomy and Astrophysics, Supplement*, 122, 535
- Lay, O. P. 1997b, *Astronomy and Astrophysics, Supplement*, 122, 547
- Li, A., & Draine, B. T. 2001, *Astrophysical Journal*, 554, 778
- Lodato, G., & Rice, W. K. M. 2004, *Monthly Notices of the Royal Astronomical Society*, 351, 630
- Loinard, L., Torres, R. M., Mioduszewski, A. J., & Rodríguez, L. F. 2008, *Astrophysical Journal, Letters*, 675, L29
- Lommen, D., Maddison, S. T., Wright, C. M., et al. 2009, *Astronomy and Astrophysics*, 495, 869
- Lynden-Bell, D., & Pringle, J. E. 1974, *Monthly Notices of the Royal Astronomical Society*, 168, 603
- Mamajek, E. E. 2008, *Astronomische Nachrichten*, 329, 10
- Mann, R. K., & Williams, J. P. 2010, *Astrophysical Journal*, 725, 430
- Mathis, J. S., Rumpl, W., & Nordsieck, K. H. 1977, *Astrophysical Journal*, 217, 425
- McCaughrean, M. J., & O'Dell, C. R. 1996, *Astronomical Journal*, 111, 1977
- McClure, M. K., Furlan, E., Manoj, P., et al. 2010, *Astrophysical Journal, Supplement*, 188, 75

- Mendoza V., E. E. 1966, *Astrophysical Journal*, 143, 1010
- Miyake, K., & Nakagawa, Y. 1993, *Icarus*, 106, 20
- Monet, D. G., Levine, S. E., Canzian, B., et al. 2003, *Astronomical Journal*, 125, 984
- Mundy, L. G., McMullin, J. P., Grossman, A. W., & Sandell, G. 1993, *Icarus*, 106, 11
- Muto, T., Grady, C. A., Hashimoto, J., et al. 2012, *Astrophysical Journal, Letters*, 748, L22
- Nakagawa, Y., Sekiya, M., & Hayashi, C. 1986, *Icarus*, 67, 375
- Natta, A., & Testi, L. 2004, *Star Formation in the Interstellar Medium: In Honor of David Hollenbach*, 323, 279
- Natta, A., Testi, L., & Randich, S. 2006, *Astronomy and Astrophysics*, 452, 245
- Natta, A., Testi, L., Calvet, N., et al. 2007, [arXiv:astro-ph/0602041v1](https://arxiv.org/abs/0706.0204)
- Nuernberger, D., Brandner, W., Yorke, H. W., & Zinnecker, H. 1998, *Astronomy and Astrophysics*, 330, 549
- O'dell, C. R., & Wen, Z. 1994, *Astrophysical Journal*, 436, 194
- Olofsson, J., Augereau, J.-C., van Dishoeck, E. F., et al. 2009, *Astronomy and Astrophysics*, 507, 327
- Osterloh, M., & Beckwith, S. V. W. 1995, *Astrophysical Journal*, 439, 288
- Palla, F., & Stahler, S. W. 1999, *Astrophysical Journal*, 525, 772
- Parsamian, E. S., & Petrossian, V. M. 1979, *Soobshcheniya Byurakanskoy Observatorii Akademii Nauk Armyanskoy SSR* Erevan, 51, 12
- Pascucci, I., Sterzik, M., Alexander, R. D., et al. 2011, *Astrophysical Journal*, 736, 13
- Pérez, L. M., Lamb, J. W., Woody, D. P., et al. 2010, *Astrophysical Journal*, 724, 493
- Pérez, L. M., Carpenter, J. M., Chandler, C. J., et al. 2012, [arXiv:1210.5252 \[astro-ph.SR\]](https://arxiv.org/abs/1210.5252)

- Perley, R. A., Chandler, C. J., Butler, B. J., & Wrobel, J. M. 2011, *Astrophysical Journal, Letters*, 739, L1
- Piétu, V., Guilloteau, S., & Dutrey, A. 2005, *Astronomy and Astrophysics*, 443, 945
- Platais, I., Girard, T. M., Kozhurina-Platais, V., et al. 1998, *Astronomical Journal*, 116, 2556
- Pollack, J. B., Hollenbach, D., Beckwith, S., et al. 1994, *Astrophysical Journal*, 421, 615
- Regály, Z., Juhász, A., Sándor, Z., & Dullemond, C. P. 2012, *Monthly Notices of the Royal Astronomical Society*, 419, 1701
- Reynolds, S. P. 1986, *Astrophysical Journal*, 304, 713
- Ricci, L., Testi, L., Natta, A., et al. 2010, *Astronomy and Astrophysics*, 512, A15
- Ricci, L., Testi, L., Natta, A., & Brooks, K. J. 2010, *Astronomy and Astrophysics*, 521, A66
- Ricci, L., Trotta, F., Testi, L., et al. 2012, *Astronomy and Astrophysics*, 540, A6
- Rodmann, J., Henning, T., Chandler, C. J., Mundy, L. G., & Wilner, D. J. 2006, *Astronomy and Astrophysics*, 446, 211
- Roeser, S., Demleitner, M., & Schilbach, E. 2010, *Astronomical Journal*, 139, 2440
- Sandell, G., & Aspin, C. 1998, *Astronomy and Astrophysics*, 333, 1016
- Sandell, G., & Weintraub, D. A. 2001, *Astrophysical Journal, Supplement*, 134, 115
- Sargent, A. I., & Beckwith, S. 1987, *Astrophysical Journal*, 323, 294
- Sault, R. J., Teuben, P. J., & Wright, M. C. H. 1995, *Astronomical Data Analysis Software and Systems IV* (ASP Conf. Ser. 77), ed. R. A. Shaw, H. E. Payne, & J. J. E. Hayes (San Francisco, CA:ASP), 433
- Schaefer, G. H., Dutrey, A., Guilloteau, S., Simon, M., & White, R. J. 2009, *Astrophysical Journal*, 701, 698

- Schwab, F. R. 1980, Proceedings of the International Society for Optical Engineering, 231, 18
- Semenov, D., Henning, T., Helling, C., Ilgner, M., & Sedlmayr, E. 2003, Astronomy and Astrophysics, 410, 611
- Shakura, N. I., & Sunyaev, R. A. 1973, Astronomy and Astrophysics, 24, 337
- Siess, L., Dufour, E., & Forestini, M. 2000, Astronomy and Astrophysics, 358, 593
- Simon, M., Dutrey, A., & Guilloteau, S. 2000, Astrophysical Journal, 545, 1034
- Skrutskie, M. F., Dutkewitch, D., Strom, S. E., et al. 1990, Astronomical Journal, 99, 1187
- Smith, N., Bally, J., Licht, D., & Walawender, J. 2005, Astronomical Journal, 129, 382
- Smith, R. G. 1993, Monthly Notices of the Royal Astronomical Society, 264, 587
- Sramek, R. A. 1983, VLA Test Memo, No. 143
- Sramek, R. A. 1989, VLA Test Memo, No. 175
- Steer, D. G., Dewdney, P. E., & Ito, M. R. 1984, Astronomy and Astrophysics, 137, 159
- Stirling, A., Richer, J., Hills, R., & Pardo, J. 2006, Proceedings of the International Society for Optical Engineering, 6267, 63
- Strom, K. M., Strom, S. E., Edwards, S., Cabrit, S., & Skrutskie, M. F. 1989, Astronomical Journal, 97, 1451
- Sylvester, R. J., Skinner, C. J., Barlow, M. J., & Mannings, V. 1996, Monthly Notices of the Royal Astronomical Society, 279, 915
- Tanaka, H., Himeno, Y., & Ida, S. 2005, Astrophysical Journal, 625, 414
- Tatarskii, V. I. 1961, Wave Propagation in a Turbulent Medium (New York: Dover)
- Testi, L., Natta, A., Shepherd, D. S., & Wilner, D. J. 2001, Astrophysical Journal, 554, 1087
- Testi, L., Natta, A., Shepherd, D. S., & Wilner, D. J. 2003, Astronomy and Astrophysics, 403, 323

- Thompson, A. R., Moran, J. M., & Swenson, G. W., Jr. 2001, "Interferometry and synthesis in radio astronomy by A. Richard Thompson, James M. Moran, and George W. Swenson, Jr. 2nd ed. New York: Wiley, c2001.xxiii, 692 p. : ill. ; 25 cm. "A Wiley-Interscience publication." Includes bibliographical references and indexes. ISBN : 0471254924
- Torres, R. M., Loinard, L., Mioduszewski, A. J., & Rodríguez, L. F. 2009, *Astrophysical Journal*, 698, 242
- Torres, R. M., Loinard, L., Mioduszewski, A. J., et al. 2012, *Astrophysical Journal*, 747, 18
- Udry, S., & Santos, N. C. 2007, *Annual Reviews of Astronomy and Astrophysics*, 45, 397
- van Boekel, R., Min, M., Waters, L. B. F. M., et al. 2005, *Astronomy and Astrophysics*, 437, 189
- van Leeuwen, F. 2007, *Astronomy and Astrophysics*, 474, 653
- Vicente, S. M., & Alves, J. 2005, *Astronomy and Astrophysics*, 441, 195
- Warren, S. G. 1984, *Applied Optics*, 23, 1206
- Weidenschilling, S. J. 1977, *Monthly Notices of the Royal Astronomical Society*, 180, 57
- Weingartner, J. C., & Draine, B. T. 2001, *Astrophysical Journal*, 548, 296
- Westwater, E. R. 1967, ESSA Technical Report IER 30-ITSA 30
- White, R. J., & Hillenbrand, L. A. 2004, *Astrophysical Journal*, 616, 998
- Williams, J. P., & Cieza, L. A. 2011, *Annual Reviews of Astronomy and Astrophysics*, 49, 67
- Wilking, B. A., Meyer, M. R., Robinson, J. G., & Greene, T. P. 2005, *Astronomical Journal*, 130, 1733
- Wilner, D. J., D'Alessio, P., Calvet, N., Claussen, M. J., & Hartmann, L. 2005, *Astrophysical Journal, Letters*, 626, L109
- Wolf, S., Moro-Martín, A., & D'Angelo, G. 2007, *Planetary and Space Science*, 55, 569

Woody, D. J., Carpenter, J., & Scoville, N. 2000, in ASP Conf. Ser. 217, Imaging at Radio Through Submillimeter Wavelengths, ed. J. G. Mangum & S. J. E. Radford (San Francisco: ASP), 31

Wright, E. L., et al. 2009, *Astrophysical Journal, Supplement*, 180, 283

Wurm, G., & Blum, J. 1998, *Icarus*, 132, 125

Zacharias, N., Finch, C., Girard, T., et al. 2010, *Astronomical Journal*, 139, 2184

Zacharias, N., Finch, C. T., Girard, T. M., et al. 2012, *VizieR Online Data Catalog*, 1322, 0

Zubko, V. G., Mennella, V., Colangeli, L., & Bussoletti, E. 1996, *Monthly Notices of the Royal Astronomical Society*, 282, 1321